

**Evaluating Degradation Mechanisms in Next-generation Electrode Chemistries**

by

Zilai Yan

Submitted in partial fulfilment of the requirements  
for the degree of Doctor of Philosophy

at

Dalhousie University  
Halifax, Nova Scotia  
November 2021

© Copyright by Zilai Yan, 2021

*Energy is the only universal currency*

*Never waste any of it*

## TABLE OF CONTENT

LIST OF TABLES .....	vi
LIST OF FIGURES .....	vii
ABSTRACT .....	xvi
LIST OF ABBREVIATIONS AND SYMBOLS USED.....	xvii
ACKNOWLEDGEMENTS.....	xxii
CHAPTER 1 INTRODUCTION .....	1
1.1 Motivation.....	1
1.2 Lithium-Ion Batteries.....	5
1.3 Common Cell Designs .....	5
1.4 Anode Materials.....	8
1.5 Cathode Materials .....	11
1.6 Electrolytes .....	12
1.7 Solid Electrolyte Interphases .....	14
1.8 Characterizations of Electrolyte Reactivity .....	16
1.8.1 The Measurement of Post-first-cycle Irreversible Capacity .....	16
1.8.2 Electrochemical Impedance Spectroscopy .....	21
1.8.3 Other Characterization Methods.....	23
CHAPTER 2 Lifetime as the Key Parameter for Rechargeable Batteries: Potassium-ion Batteries as An Example.....	25
2.1 Introduction.....	25
2.2 Battery Cost Model.....	27
2.3 Results and Discussion .....	29
2.4 Conclusions.....	39
CHAPTER 3 EXPERIMENTAL TECHNIQUES.....	41
3.1 Cell Construction .....	41
3.1.1 Half Cells .....	41
3.1.2 Conventional Symmetric Cells .....	42
3.1.4 Quasi-three-electrode Double Half-cells .....	43

3.2 Electrochemical Measurements .....	44
3.2.1 Cycling Tests .....	44
3.2.2 Electrochemical Impedance Spectroscopy .....	44
3.3 Scanning Electron Microscope .....	49
3.4 Ion Milling .....	50
3.5 X-Ray Diffraction .....	51
CHAPTER 4 Understanding Interfacial Impedance Growth in Porous Electrodes Containing Blended Active Materials .....	54
4.1 Introduction.....	54
4.2 Experimental.....	55
4.3 Theoretical Model.....	57
4.4 Results and Discussion .....	61
4.5 Conclusions.....	69
CHAPTER 5 Understanding Degradation Patterns in Li Cells with Si-Alloy Negative Electrodes.....	70
5.1 Introduction.....	70
5.2 Experimental.....	72
5.3 A Li Inventory Model.....	75
5.4 Anode Degradation Behavior in Symmetric Cells.....	83
5.5 The Measurement of SEI Growth and Repair.....	88
5.6 Conclusions.....	101
CHAPTER 6 Current-corrected Cycling Strategies for True Electrode Performance Measurement and Prolonged Cell Cycle Life.....	103
6.1 Introduction.....	103
6.2 Experimental.....	105
6.3 Results and Discussion .....	106
6.4 Conclusions.....	118
CHAPTER 7 Conclusions and Future Work .....	120
7.1 Conclusions.....	120
7.2 Future Work.....	122
7.2.1 Mechanical Failure Analysis of Alloy/graphite Blended Electrodes.....	122
7.2.2 Optimization of Alloy Material and Electrolyte towards Slow SEI Growth.....	122

7.2.3 Decoding Capacity Fade and Coulombic Efficiency in Li Cells .....	123
7.2.4 Kinetics Analysis of Electrode Materials at High Rates.....	125
BIBIOGRAPHY .....	127
A- APPENDIX A Supplementary Information for Chapter 2 .....	143
B- APPENDIX B Details of the Cost Models .....	149
C- APPENDIX C Supplementary Information for Chapter 4 .....	169
D- APPENDIX D Supplementary Information for Chapter 5 .....	179
E- APPENDIX E Supplementary Information for Chapter 6.....	191
F- APPENDIX F Copyright Permission .....	196

## LIST OF TABLES

Table 1.1 Specifications of battery test equipment [23]. .....	19
Table 3.1 Cathode materials used to compare current LIB with potential KIB technologies. ....	35
Table 4.1 The baseline value for inhomogeneous transmission line. ....	62
Table 5.1 Li inventory of a hypothetical symmetric cell for its first cycle. * .....	79
Table 5.2 Li inventory of a hypothetical symmetric cell for its post-first cycle. * .....	80
Table B.1 The battery systems used in the Chapter 3. ....	149
Table B.2 Modifications of different battery systems in BatPac model (part one). ....	150
Table B.3 Modifications of different battery systems in BatPac model (part two). ....	154
Table B.4 Cost details for different battery systems in BatPac model (part one). ....	159
Table B.5 Cost details for different battery systems in BatPac model (part two). ....	164
Table D.1 Specific surface areas (in $\text{m}^2 \text{g}^{-1}$ ) of powders used in this study [27]. ....	188
Table E. 1 Rietveld refinement results for synthesized $\text{LiNiO}_2$ . ....	193

## LIST OF FIGURES

Figure 1.1 Schematic of a Li-ion battery. The brown, green, and red balls represent C, Li, and O atoms, respectively. The balls occupying the octahedral sites (bonded with O atoms) represent transition metal(s). Here, the occupation of these balls is 60% Ni, 20% Co, and 20% Mn. .... 5

Figure 1.2 A schematic diagram of (a) pouch-type cell (showing an electrode/separator stack with cell tabs protruding from the electrodes), and (b) coin-type cell. .... 6

Figure 1.3 Electrode stacking configurations in (a) full cell, (b) half cell, and (c) symmetric cell. 7

Figure 1.4 The main degradation mechanisms of Si anodes due to their large volume changes during cycling. Reprinted with permission from ref [5]. Copyright 2016 Springer Nature. .... 8

Figure 1.5 (a) Field emission scanning electron microscope image of an ion polished cross section of a 3M L-20772 V6 alloy particle. Surrounding darker regions are graphite. (b) TEM image of particle edge of the alloy particle. Reprinted with permission from ref [50]. Copyright 2014, IOP Publishing. .... 9

Figure 1.6 (a) Cycling performance of uncalendered and calendered 3M Si-alloy (V6) electrodes. (b) Cycling performance of uncalendered and calendered V6/MAG-E electrodes with different MAG-E contents (by weight ratio). MAG-E is one commonly used graphite for LIBs. Reproduced with permission from ref [51]. Copyright 2014, IOP Publishing. .... 10

Figure 1.7 Schematic presentation of polyhetero microphase SEI. Reprinted with permission from ref [30]. Copyright 2017, IOP Publishing. .... 15

Figure 1.8 One single-electron mechanism for EC reacting with  $\text{Li}^+$  and  $e^-$ . Reprinted with permission from ref [97]. Copyright 2005 American Chemical Society ..... 16

Figure 1.9 Illustrations about the CE calculations at  $i^{\text{th}}$  cycle of (a) full cells, (b) half cells with anode electrodes, (c) half cells with cathode electrodes, (d) symmetric cells.  $Q_d(i)$  and  $Q_c(i)$  are the discharge capacity and the charge capacity at  $i^{\text{th}}$  cycle, respectively..... 17

Figure 1.10 The absolute value of the potential across a resistor with a positive and negative current of equal magnitude alternating every six minutes before (top panel) and after (bottom panel) calibration. The red arrows represent an error in current equality of 1 part in 10,000. Reprinted with permission from ref [98]. Copyright 2012, Aaron Smith. .... 19

Figure 1.11 An illustration of the construction pathways for making (a) a conventional symmetric cell and (b) a DHC. Reprinted with permission from ref [28]. Copyright 2018, Elsevier. .... 20

Figure 2.1 (a) Cost breakdown for LNMC/G and KNMC/G batteries. Purchased items include cell hardware, module hardware, and battery jacket. Supporting systems are battery and thermal management systems. Other costs include direct labor summary, variable overhead, general, sales, administration, research and development, depreciation, profit, and warranty. (b) Total cost, available energy, mass, and volume for the LNMC/G and KNMC/G batteries. .... 30

Figure 2.2 A summary of the capital cost of KIBs with selected cathode active materials (coupled with the graphite anode [133]). Cathode prices were estimated with a range. The capital cost of a LIB with Li-NMC622 as cathode (its price was set to \$17 kg<sup>-1</sup>) is presented as reference (red dashed line). Selected K cathodes are divided into three groups: hexacyanometalates (green), *i.e.* K<sub>2</sub>MnFe(CN)<sub>6</sub> [127] and K<sub>1.75</sub>Mn[Fe(CN)<sub>6</sub>]<sub>0.93</sub>·H<sub>2</sub>O [140]; layered oxides (black), *i.e.* K<sub>0.5</sub>MnO<sub>2</sub> [137], KCrO<sub>2</sub> [138], K<sub>0.6</sub>CoO<sub>2</sub> [139], and K<sub>0.65</sub>Fe<sub>0.5</sub>Mn<sub>0.5</sub>O<sub>2</sub>[136]; polyanionic compounds (orange), *i.e.* KVPO<sub>4</sub>F [141]. Where known, raw material costs are shown as a best-case price scenario..... 33

Figure 2.3 Effect of the KIB cycle life on annualized capital cost: (a) 1000 cycles, (b) 200 cycles, (c) 750 cycles, and (d) 1500 cycles. Four fictional cathodes (cycling potential at 50% state of charge, reversible capacity, density) were selected for exploring this effect: Cathode A (3 V, 100 mAh g<sup>-1</sup>, 2.5 g cm<sup>-3</sup>), Cathode B (4 V, 150 mAh g<sup>-1</sup>, 3 g cm<sup>-3</sup>), Cathode C (4.5 V, 170 mAh g<sup>-1</sup>, 4.5 g cm<sup>-3</sup>), and Cathode D (5 V, 200 mAh g<sup>-1</sup>, 5 g cm<sup>-3</sup>). Cathode prices were given with a range. The LNMC/G battery with a cycle life of 1000 was used as reference. .... 36

Figure 3.1 Exploded view of (a) a coin-type half cell and (b) a coin-type conventional symmetric cell. .... 41

Figure 3.2 Exploded view of (a) a double half-cell with a connection to the battery test system and (b) a quasi-three-electrode double half-cell with a connection to the battery test system and an extra voltmeter. .... 43

Figure 3.3(a) A representative Nyquist plot, obtained from the EIS. (b) An illustration of the connection between the EIS analyzer and electrochemical cell. (c) An equivalent circuit used to describe (b)..... 46

Figure 3.4 (a) A schematic shows an electrode particle, the SEI layer, and the electrolyte. (b) An equivalent circuit used to describe (a).  $Z_w$ ,  $R_s$ ,  $C$ , and  $R_{Ely}$  represent Warburg impedance, the resistance at the electrode/electrolyte interface, the capacitance at the electrode/electrolyte interface, and the electrolyte resistance, respectively..... 48

Figure 3.5 A schematic showing the operating principle of ion milling. .... 51

Figure 3.6 Schematic diagram of Bragg scattering from lattice planes in a solid. .... 52

Figure 4.1 (a) Cross-sectional SEM image of Si-alloy/graphite (31.8 wt.% graphite content) blended electrodes. The irregularly shaped particles are Si-alloy. Flake-like particles are graphite. (b) An illustration of a porous electrode containing a blend of active materials (black and grey particles) in electrolyte. The active materials are electronically

connected through carbon black (black lines) while the void space among solid materials is filled with electrolyte for  $\text{Li}^+$  ion diffusion. The lithium ion diffusion path and electronic path are represented with red and blue arrows, respectively. .... 58

Figure 4.2 (a) An equivalent circuit for porous electrodes containing blended active materials consisting of a mixture of type A and type B active particles.  $R_{ion}$  and  $R_e$  represent the ionic resistance in electrolyte and the electronic resistance in CB, respectively.  $Z_A$  and  $Z_B$  represent the interfacial impedance of two different active materials. The circuits for  $Z_A$  and  $Z_B$  are presented on the right.  $R_{c(n)}$ ,  $R_{s(n)}$ , and  $C_{(n)}$  represent the contact resistances between CB and the  $n^{\text{th}}$  active particle, the  $n^{\text{th}}$ /electrolyte interfacial resistance, and the capacitance of the double layer that is created at the  $n^{\text{th}}$ /electrolyte interface, respectively. (b) A simplified transmission line model circuit with four particle links ( $n = 1-4$ , each particle being either of type A or B). (c) An illustration of the calculation of  $Z_{ITLM}(\omega)$  after considering the electrodes comprised of parallel ITLMs on a current collector. .... 60

Figure 4.3 (a) A typical EIS spectrum of lithiated anode electrodes in the symmetric cells made here (a graphite electrode is used here as an example). (b) EIS spectra generated from ITLM simulation results. The  $Z_{ITLM}(\omega)$  changes when  $R_{ion}$ ,  $R_e$ ,  $R_c$ , or  $R_s$  increase by 32 times. The parameter values for the baseline are presented in Table 4.1. The inset in (b) shows an expanded view of (b). .... 62

Figure 4.4 (a) Nyquist plots of graphite electrodes with various loading masses, measured at the 1<sup>st</sup> cycle in symmetric cells. (b) Plots of  $R_{tei}$  versus  $m_{areal}^{-1}$ . A linear fit was used to show the trend between  $R_{tei}$  and  $m_{areal}^{-1}$ . .... 64

Figure 4.5 Nyquist plots for (a) graphite, (b) Si-alloy, and (c) Si-alloy/graphite (31.8 wt.% graphite content) blended electrodes measured at different cycles. The inset in (c) shows an expanded view. (d) The relative interfacial resistance vs. cycle number of these three electrodes. The relative interfacial resistances were calculated on the basis of  $R_{tei}$  values at different cycles, after normalizing by the first cycle  $R_{tei}$ . .... 65

Figure 4.6 (a) A summary of the relative interfacial resistance growth of graphite, Si-alloy, and graphite/Si-alloy blended electrodes with different graphite contents at 20<sup>th</sup> cycle. (b) Plots of  $R_{ITL}$  versus  $R_{sB}$  with different ratios of the two particle types. Particle A has a constant interfacial impedance and particle B has a larger interfacial impedance. The value for all parameters, except  $R_{sB}$ , is presented in Table 4.1. The solid bands for each particle ratio reveal the range in  $R_{ITL}$  values caused by the different particle arrangements. Question marks can be either A or B of the particle interfacial impedance, including two resistors and a capacitor as shown on the right of Figure 4.2(a). (c) The distribution of ITLMs in simulated electrodes with different particle B content, which varies from 10% to 90%. (d) Normalized ITLM interfacial impedance growth with increasing particle B content.  $k$  represents the ratio of  $R_{sB} / R_{sA}$ , and ranges from 2 to 50. The value of all parameters, except  $R_{sA}$  and  $R_{sB}$ , is presented in Table 4.1. The value of  $R_{sA}$  was set as 800 M $\Omega$  to give a baseline of  $R_{ITLM} = 40 \Omega$ , which is close to the measured data. .... 68

Figure 5.1 (a) An example of potential curves of a symmetric cell during discharge and individual contributions from electrode A and electrode B. (b) An example of potential curves of

a Si-based anode material and graphite in half cell. As shown, unlike graphite, Si-based anode materials often have considerable capacity above typical upper cut-off potentials. Illustrations of the main reaction, side reactions, and the reaction for excess capacity at (c) electrode A and (d) electrode B that occur during the  $i^{th}$  symmetric cell discharge. The capacities for each reaction during a single symmetric cell discharge/charge process are labelled in brackets. *Li-Eld*, *Eld*, and *Elyt* stand for lithiated electrode, delithiated electrode, and electrolyte, respectively. .... 77

Figure 5.2  $Si_{80}W_{20}$  DHC (a) Charge and discharge capacity and (b) accumulated inventory-change reaction capacity versus cycle number of the pre-lithiated electrode (electrode A), and pre-delithiated electrode (electrode B). The specific capacity of electrode A and B were calculated with respect to their corresponding active material mass. To acquire the electrode inventory-change rate for each cycle, it was assumed that electrode A and B have achieved the same average specific steady state reaction rate during these cycles, as applied in equation (5.3). .... 82

Figure 5.3 (a) Potential curves of a  $Si_{80}W_{20}$  half cell. The grey area represents the excess capacity above 0.9 V. Potential curves of (b) a  $Si_{80}W_{20}$  QDHC and (c) the pre-delithiated  $Si_{80}W_{20}$  electrode in the QDHC. The inset in (c) shows an expanded view of potential curves above 0.8 V. The dashed line represents the intended upper cut-off potential. (d) The upper endpoint potential and released accumulated excess capacity of the prelithiated  $Si_{80}W_{20}$  electrode during cycling. .... 84

Figure 5.4 (a) Capacity versus cycle number of  $Si_{80}W_{20}/G$  20/50 electrodes cycled in a QDHC and a half cell. Potential curves of the  $Si_{80}W_{20}/G$  20/50 (b) QDHC and (c) half cell. The insets in (b) and (c) show the corresponding lower endpoint potential versus cycle number. Only in this experiment, SFG6L was used as the graphite material. .... 86

Figure 5.5 (a) Potential curves of a  $Si_{80}W_{20}/G$  20/50 QDHC at various cycles. The inset in (a) shows an expanded view of potential curves above 0.8 V. A summary of (b) upper endpoint potential and (c) accumulated excess capacity versus cycle number of  $Si_{80}W_{20}$ , graphite, and various  $Si_{80}W_{20}/G$  electrodes in QDHCs. (d) Accumulated excess capacity of  $Si_{80}W_{20}$  in various  $Si_{80}W_{20}/G$  blended electrodes when cycled in QDHCs, with a comparison to a neat  $Si_{80}W_{20}$  electrode. .... 89

Figure 5.6 (a-c) Capacity and (d-f) corresponding accumulated inventory-change reaction capacity versus cycle number of  $Si_{80}W_{20}/G$  20/50,  $Si_{80}W_{20}/G$  10/60, and  $Si_{80}W_{20}/G$  5/65 electrodes in DHCs, respectively. The DHCs were cycled with a constant C-rate protocol. In the legends, C represents carbonaceous materials, including graphite and carbon black. A and B represent electrode A and B, respectively. The inventory-change reaction capacity is analyzed only from cycle 21 to 50, since during these cycles the blended electrodes have negligible excess capacity increase and mechanical failure. 96

Figure 5.7 Accumulated specific SEI growth on  $Si_{80}W_{20}$  per  $Si_{80}W_{20}$  mass, versus cycle number of  $Si_{80}W_{20}/G$  20/50,  $Si_{80}W_{20}/G$  10/60, and  $Si_{80}W_{20}/G$  5/65 DHCs cycled with a constant C-rate protocol. (b) A summary of the average SEI growth on  $Si_{80}W_{20}$  per cycle per  $Si_{80}W_{20}$  mass in these electrodes (between the 21<sup>st</sup> and 50<sup>th</sup> cycle). .... 98

- Figure 5.8 Capacity versus cycle number of graphite and Si<sub>80</sub>W<sub>20</sub>/G 20/50 electrodes in DHCs at (a) 45 °C and (b) 60 °C. The DHCs were cycled with a constant C-rate protocol. (c) The accumulated specific SEI growth on Si<sub>80</sub>W<sub>20</sub> per Si<sub>80</sub>W<sub>20</sub> mass versus cycle number for Si<sub>80</sub>W<sub>20</sub>/G 20/50 electrodes at 30 °C, 45 °C and 60 °C. (d) A summary of the average specific SEI growth on carbonaceous materials and on Si<sub>80</sub>W<sub>20</sub> per cycle at different temperatures. The average fade at 60 °C was evaluated between cycles 21 and 30. Error bars for Si<sub>80</sub>W<sub>20</sub> at 60 °C were calculated as the range of six samples. The other error bars were calculated as the range of four samples. .... 99
- Figure 6.1 (a) Lithiation capacity, (b) the actual cycling rate, and (c) the applied current density of graphite electrodes in half cells cycled with CCGC and TGC protocols. In each 50 cycles, the graphite electrodes were first cycled at the rate of C/20, followed by 49 cycles at the rate of C/3 between 5 mV and 0.9 V. The dQ/dV curves of the graphite electrodes at indicated cycle number, cycled with (d) TGC and (e) CCGC protocols. Arrows indicate how the differential capacity peaks of graphite are shifted between C/20 and C/3 cycling rates. .... 107
- Figure 6.2 (a) Lithiation capacity and (b) the actual cycling rate of graphite electrodes cycled at different rates using CCGC and TGC. .... 110
- Figure 6.3 (a) Delithiation capacity (top panel) and capacity retention (bottom panel) of LiNiO<sub>2</sub> electrodes cycled on the basis of TGC and CCGC. The initial cycle was set at the rate of C/20, followed by the cycling at C/2 rate. The actual cycling rate for LiNiO<sub>2</sub> electrodes under TGC at the second delithiation is C/1.4. (b) Average overpotential of the LiNiO<sub>2</sub> electrodes cycled by TGC and CCGC. The dQ/dV curves between 2<sup>th</sup> and 300<sup>th</sup> cycle of the LiNiO<sub>2</sub> electrodes (c) TGC and (d) CCGC. Later cycles are towards either green or orange..... 113
- Figure 6.4 (a) Lithiation capacity of Si electrodes cycled with TGC and CCGC. The initial cycle was set at the rate of C/20 between 5 mV-1.5 V. The following cycles were set at C/4 between 5 mV-0.9 V. The actual cycling rate for Si electrodes under TGC at the second lithiation is C/3.9. (b) Average lithiation potential of the Si electrodes cycled by TGC and CCGC. .... 114
- Figure 6.5 (a) Capacity and (b) capacity retention of the Li-ion pouch cells cycled at 30 °C on the basis of TGC and CCGC. Cells were charged at the rate of 1C, trickled until the current below C/5, then discharged at C/2 rate. A power outage occurred near the ~300<sup>th</sup> cycle. (c) Capacity and (d) capacity retention of the Li-ion pouch cells cycled at 45 °C on the basis of TGC and CCGC. For these cells, in every 100 cycles, cells were initially charged and discharged at C/5 rate, then charged at 2C rate, held at the upper potential limit until the current dropped below C/2, and then discharged at C/2 rate for the following 99 cycles. .... 116
- Figure A.1 Nyquist plots for aged MAG-E electrodes in (a) 1M LiPF<sub>6</sub>/EC:DEC and (b) 0.5M KPF<sub>6</sub>/EC:DEC. The electrode mass loadings of each cell have been presented in the figures. .... 146

Figure A.2 Cost breakdown of KIBs with selected cathodes with the LNMC/G as reference. The dash bars represent the cost increases due to the price increase of K cathodes from their lower to their upper price limits. ....	147
Figure A.3 Cycling performance of graphite anodes in DHCs with selected electrolytes. The specific capacity of DHCs was calculated with respect to the active material mass in the pre-lithiated electrode. ....	148
Figure C.1 Monte Carlo simulation to investigate the effect of parameters on the IES spectra of blended electrodes. All parameters were randomized between 0-1000 $\Omega$ or 0-1000 F, except the content of the two different particles, which was randomized between 0-100%. 100,000 trials were made to explore the major contribution to the overall interfacial resistance growth. 5000 ITLs were used for the simulation of $Z_{ITLM}$ . These results show that $R_{SA}$ and $R_{SB}$ , related to the interfacial resistance of particle A and B, have a strong correlation to the semicircle(s) growth. ....	170
Figure C.2 The impedance growth in the four-particle-linked ITL containing one particle B, which can have an increased interfacial resistance ( $R_{SB}$ ). Four possible transmission lines have been presented in (a-d) along with the increase of $R_{SB}$ in particle B. ....	171
Figure C.3 The impedance growth in the four-particle-linked ITL containing two B particles, which can have an increased interfacial resistance ( $R_{SB}$ ). Six possible transmission lines have been presented in (a-f) along with the increase of $R_{SB}$ in particle B. ....	172
Figure C.4 The impedance growth in the four-particle-linked ITL containing three B particles, which can have an increased interfacial resistance ( $R_{SB}$ ). Four possible transmission lines have been presented in (a-f) along with the increase of $R_{SB}$ in particle B. ....	173
Figure C.5 Cross-sectional SEM images of Si-alloy/graphite (31.8 wt.% graphite content) blended electrodes, (a) pristine and (b) electrochemically lithiated to the state of charge of ~50% after 20 cycles. These two electrodes in pristine condition have a similar thickness. The volume expansion of the Si-alloy/graphite blended electrode at the state of charge of ~50% is ~30%. This result agrees within 19% of a direct measurement of the volume expansion as measured with a micrometer. ....	174
Figure C.6 The Nyquist plot of Si-alloy/graphite blended electrodes with various graphite contents at the 1 <sup>st</sup> cycle (left column) and at the 20 <sup>th</sup> cycle (right column). ....	175
Figure C.7 Cross-section SEM image of a handmixed Si-alloy/graphite blended electrode (54.5 wt.% graphite content) purposely made to have a poor particle distribution. The slurry was hand-mixed about five minutes or just until all the particles were dispersed in water. The bright irregularly-shaped particles are Si-alloy and the dark flake-like particles are graphite. Agglomerations of Si-alloy and graphite particles are shown in the red and blue dotted line regions, respectively. ....	176
Figure C.8 (a) Simulated distribution of extremely-poor-dispersed electrodes when the content of particle B is 50%, compared to the distribution of well-dispersed electrodes. (b)	

Normalized overall interfacial impedance growth in extremely-poor-dispersed electrodes, in comparison to well dispersed electrodes.  $k = R_{sB}/R_{sA}$ . ..... 177

Figure C.9 The Nyquist plots of Si-alloy/graphite blended electrodes made with two different mixing processes: mixed in planetary (left column, good dispersion) and mixed by hand (right column, poor dispersion). The impedance was measured at the first fully discharge state (C/20). Electrodes with three different graphite contents were tested. Results show the interfacial impedance between electrodes made with the different mixing processes is similar for electrodes having the same composition. Please note that the axes represents the areal impedance multiplied by the mass loading. The reason for using this type of impedance is to exclude variations caused by the mass loading, as described in the main manuscript. .... 178

Figure D.1 (a) XRD pattern of synthesized  $\text{Si}_{80}\text{W}_{20}$ . (b) SEM image of  $\text{Si}_{80}\text{W}_{20}$ . (c) Cross-sectional SEM image of  $\text{Si}_{80}\text{W}_{20}$  and corresponding energy-dispersive X-ray spectroscopy (EDS) maps of (d) Cu, (e) Si, and (f) W elements. .... 179

Figure D.2 Exploded views of (a) a DHC and (b) a QDHC with connections to battery test systems. (c) Capacity versus cycle number of graphite electrodes cycled in DHCs and QDHCs. The electrodes were composed of 90 wt% graphite (MAG-E), 2 wt% CB, and 8 wt% poly(vinylidene fluoirde) (PVDF) (HSV 900, KYNAR). The mass loading of the graphite electrodes was  $\sim 2.7 \text{ mg cm}^{-2}$ , or 3.7 mg per disk electrode. (d) Irreversible capacity rate versus cycle number of the graphite electrodes evaluated in DHCs and QDHCs. The irreversible capacity rate was calculated using the discharge capacity fade between consecutive cycles, per cycle time and per the total electrode mass in each symmetric cell. The average irreversible capacity rates between the 41<sup>th</sup> and the 50<sup>th</sup> cycle measured using DHC and QDHC are shown in (d). The difference in irreversible capacity rates observed for DHCs and QDHCs can also be estimated from the charger system specifications. Considering that the charger's potential sense leads have a high impedance of  $10^{12} \Omega$  and that the average potential of graphite is 0.1 V, this corresponds to aleakage current of  $10^{-13} \text{ A}$ . The results indicate the additional connection has a very small, but measureable impact on cell capacity. Nevertheless, caution has been taken in this work by not using QDHCs for coulometric studies. .... 180

Figure D.3 (a) The specific capacity versus cycle number of  $\text{Si}_{80}\text{W}_{20}$  electrodes in a QDHC (symmetric cell) and a half cell. (b) Capacity retention versus cycle number of aged  $\text{Si}_{80}\text{W}_{20}$  electrodes in half cells. The half cells were cycled between 5 mV and 2.5 V while the QDHCs were cycled between  $\pm 2.5 \text{ V}$ . Potential curves of the prelithiated  $\text{Si}_{80}\text{W}_{20}$  electrode in the QDHC (c) between 1<sup>st</sup> and 9<sup>th</sup> cycles, and (d) between 9<sup>th</sup> and 21<sup>st</sup> cycles. The insets in (c) and (d) show expanded views of the potentials above 2.4 V and 2.45 V, respectively. .... 181

Figure D.4 (a) Capacity of the  $\text{Si}_{80}\text{W}_{20}/\text{G} 20/50$  electrode before (black) and after (blue) 50 cycles in QDHCs with cut-off potentials of  $\pm 2.5 \text{ V}$ . The capacity before cycling in QDHCs was obtained in the pre-lithiation process for symmetric cell preparation. (b) A summary of capacity fade in QDHCs and mechanical failure of the  $\text{Si}_{80}\text{W}_{20}/\text{G} 20/50$  electrodes in QDHCs and half cells. The electrode mechanical failure in symmetric cells was

determined by conducting an additional discharge/charge cycle on the individual half-cells that make up the QDHCs. The capacity loss due to mechanical failure was then equated to the difference between the charge capacities of the individual half-cells before and after symmetric cell cycling. The capacity loss due to electrode mechanical failure in half cells was determined as the difference in capacities between the initial and the 51<sup>st</sup> cycle charge capacity. .... 182

Figure D.5 Differential capacity of (a) graphite, (b) Si<sub>80</sub>W<sub>20</sub>/G 5/65, (c), Si<sub>80</sub>W<sub>20</sub>/G 20/50, and (d) Si<sub>80</sub>W<sub>20</sub>/G 35/35 QDHCs at differential cycles, as indicated. .... 183

Figure D.6 Capacity versus cycle number of (a) Si<sub>80</sub>W<sub>20</sub>, (c) Si<sub>80</sub>W<sub>20</sub>/G 20/50, (e) Si<sub>80</sub>W<sub>20</sub>/G 10/60, and (g) Si<sub>80</sub>W<sub>20</sub>/G 5/65 electrodes cycled in half cells with different lower cutoff potentials, including 5 mV, 60 mV, and 80 mV, while the upper cutoff potential for these cells was set to 0.9 V except for the first cycle. Cells were initially cycled between 5 mV and 1.5 V at C/20 rate, then cycled at C/5 rate, trickled to C/20 for sequent cycles. Corresponding capacity retention versus cycle number for these cells are shown in (b), (d), (f), and (h), respectively. The capacity retention was calculated on the basis of the second cycle discharge capacity. .... 184

Figure D.7 Alloy capacity versus cycle number of Si<sub>80</sub>W<sub>20</sub> cycled to 5 mV in the blended electrodes as indicated. The data extracted from Figure D.6. The alloy capacity is calculated assuming constant graphite capacities which are 336 mAh g<sup>-1</sup>. .... 185

Figure D.8 (a) Capacity and (b) capacity retention versus cycle number of Si<sub>80</sub>W<sub>20</sub>/G 20/50 electrodes cycled in half cells with a lower cutoff potential of 80 mV at different temperatures. (c) Capacity of the Si<sub>80</sub>W<sub>20</sub>/G 20/50 electrode before (black) and after (blue) 50 cycles in DHCs (symmetric cells) at 60 °C. The capacity before cycling in DHCs was obtained in the pre-lithiation process for symmetric cell preparation. The result indicates no mechanical failure is observed when elevated temperature is applied. (d) Differential capacity curves of Si<sub>80</sub>W<sub>20</sub>/G 20/50 electrodes before and after cycling in symmetric cell at 60 °C, showing that little change has occurred after the cycling process. .... 186

Figure D.9 (a) Capacity and (b) time per cycle versus cycle number of Si<sub>80</sub>W<sub>20</sub> electrodes cycled in DHCs with a constant current constant voltage (CCCV) cycling protocol and a constant C-rate CCCV cycling protocol. (c) Capacity retention and (d) time per cycle versus cycle number of graphite and various ratio of Si<sub>80</sub>W<sub>20</sub>/G electrodes cycled in DHCs with a constant C-rate CCCV protocol. .... 187

Figure D.10 (a) Charge and discharge capacity versus cycle number of DHC containing graphite electrodes. The constant C-rate CCCV cycling protocol is used. (b) Accumulated side reaction capacity versus cycle number of the graphite/graphite DHC (symmetric cell), pre-lithiated electrode (electrode A), and pre-delithiated electrode (electrode B). The specific capacities of electrode A and B were calculated with respect to their corresponding active material mass, assuming that electrode A and B have achieved the same average specific steady state reaction rate between the 21<sup>st</sup> and 50<sup>th</sup> cycle and have

the same average specific reaction rate during these cycles, as applied in equation (5.3). .....	188
Figure D.11 Si <sub>75</sub> W <sub>25</sub> was prepared as a similar way for Si <sub>80</sub> W <sub>20</sub> , but with different stoichiometric ratio of Si and W. (a) Capacity of Si <sub>75</sub> W <sub>25</sub> /G 20/50 electrodes cycled in DHC with the constant C-rate CCCV cycling protocol. (b) A summary of average SEI growth capacity per cycle and average SEI growth capacity per cycle over reversible capacity on Si <sub>75</sub> W <sub>25</sub> , with a comparison of Si <sub>80</sub> W <sub>20</sub> .....	189
Figure D.12 Capacity of (a) SiO/G 20/50 and (b) SiO/G 10/60 electrodes before (black) and after (blue) 50 cycles in DHCs (symmetric cells) at 30 °C. The capacity before cycling in DHCs was obtained in the pre-lithiation process for symmetric cell preparation. No mechanical failure is observed for SiO/G 20/50 and SiO/G 10/60 electrodes when cycled in DHCs.....	189
Figure D.13 Capacity of (a) SiO/G 20/50 and (c) SiO/G 10/60 electrodes cycled in DHCs with the constant C-rate CCCV cycling protocol. The corresponding accumulated side reaction capacity was shown in (b) and (d), respectively. A summary of (e) average SEI growth capacity per cycle on SiO and (f) average SEI growth capacity per cycle per SiO reversible capacity. Values for Si <sub>80</sub> W <sub>20</sub> electrodes are shown for comparison.....	190
Figure E.1 Illustrated the relationship between the capacity retention and the cycling rate at each cycle, if the cycling current is set to be constant while the cell capacity fades linearly. The initial cycling rate is set to be C/5.....	191
Figure E.2 (a) XRD pattern and Rietveld refinement of synthesized LiNiO <sub>2</sub> . Inset of (a) is crystal structure of the LiNiO <sub>2</sub> . Blue, red, and black balls represent Li, O, and Ni atoms, respectively. (b) SEM image of the synthesized LiNO <sub>2</sub> . .....	192
Figure E.3 The dQ/dV curves of the graphite electrodes at indicated cycle number, cycled by TGC protocol.....	193
Figure E.4 Illustration of the calculation of the average overpotential at each cycle. (b) The calculated average overpotential of the graphite electrodes cycled under CCGC and TGC. In each 50 cycles, the graphite electrodes were first cycled at the rate of C/20, followed by 49 cycles at the rate of C/3 between 5 mV and 0.9 V.....	194
Figure E.5 (a) Initial potential curves and (b) corresponding differential capacity (dQ/dV) curves of Si electrodes under CCGC and TGC. The initial cycle was set at the rate of C/20 between 5 mV-1.5 V. ....	194
Figure E.6 (a-d) The dQ/dV curves of two Si electrode cells cycled with TGC at the indicated cycles. (e) The dQ/dV curves of cycles 1 (black) to 60 (orange) of a Si electrode cell cycled with CCGC. Both CCGC cycled Si electrode cells in this study had nominally identical dQ/dV curves.....	195

## ABSTRACT

Electrode degradation is one of the major obstacles hindering the implementation of new electrode chemistries into practical batteries. In this thesis, studies regarding the electrode degradation of some next-generation electrode materials have been explored, based on impedance and coulometry analysis. The impedance growth at Si-alloy and graphite blended electrodes were examined using symmetric cells. An inhomogeneous transmission line of active particles was developed to model this binary system. Both theoretical and experimental results show a small portion of low interfacial impedance particles can suppress the electrode interfacial impedance in blended electrodes. The next project is focused on the understanding of anode capacity fade in symmetric cells. A Li inventory model was proposed to interpret this fade in symmetric cells. A feasible approach to measure the solid-electrolyte-interphase growth, which results from the electrolyte reduction, was proposed. In the last project, an advanced galvanostatic cycling technology, termed current-corrected galvanostatic cycling, was proposed, in which each cycle's current is adjusted to maintain a constant cycle duration based on the measured capacity of previous cycles. This method enables the measurement of true electrode/cell performance because unnecessary polarization is avoided.

## LIST OF ABBREVIATIONS AND SYMBOLS USED

AFM	Atomic force microscopy
BMF	Polyethylene blown microfiber
CB	Carbon black
CE	Coulombic efficiency
CCCV	Constant current constant voltage
CCGC	Current-corrected galvanostatic cycling
DEC	Diethylene carbonate
DHCs	Double half-cells
EC	Ethylene carbonate
EES	Electrochemical energy storage
EIS	Electrochemical impedance spectroscopy
EMC	Ethyl methyl carbonate
EQCM	Electrochemical quartz crystal microbalance
FEC	Fluoroethylene carbonate
FESEM	Field emission scanning electron microscope
HPC	High precision charger
ITLs	Inhomogeneous transmission lines
ITLM	Inhomogeneous transmission line model
KIB	K-ion battery
LCO	LiCoO <sub>2</sub>
LIB	Li-ion battery

LiPAA	Lithium polyacrylate
Na-CMC	Sodium carboxymethyl cellulose
NCA	$\text{LiNi}_{1-y-z}\text{Co}_y\text{Al}_z\text{O}_2$
NIB	Sodium-ion battery
NMC	$\text{LiNi}_x\text{Mn}_y\text{Co}_z\text{O}_2$
NMC622	$\text{LiNi}_{0.6}\text{Mn}_{0.2}\text{Co}_{0.2}\text{O}_2$
NMC811	$\text{LiNi}_{0.8}\text{Mn}_{0.1}\text{Co}_{0.1}\text{O}_2$
NMP	N-methyl-2-pyrrolidone
PAA	Poly(acrylic acid)
PVDF	Polyvinylidene difluoride
QDHCs	Quasi-three-electrode double half-cells
SEI	Solid electrolyte interphase
SEM	Scanning electron microscopy
RE	Reference electrode
TEM	Transmission electron microscopy
TGC	Traditional galvanostatic cycling
VC	Vinylene carbonate
XRD	X-ray diffraction
XPS	X-ray photoelectron spectroscopy
$C_{(n)}$	The capacitance of the double layer created at the $n^{\text{th}}$ particle/electrolyte interface, F
$\Delta C(i)$	Charge capacity fade per cycle,
$\Delta D(i)$	Discharge capacity fade per cycle

$q$	Side reaction capacity occurring at the formation cycling
$q_{EC}(i)$	Excess capacity
$q_{MF}(i)$	Capacity consumed by the electrode mechanical failure at $i^{th}$ cycle
$q_{SEI}(i)$	Capacity consumed by SEI growth and repair via chemical reactions at $i^{th}$ cycle
$q_{SEI}(i)'$	Capacity consumed by SEI growth and repair via electrochemical reactions at $i^{th}$ cycle
$Q(i)$	Reversible capacity at $i^{th}$ cycle
$Q_0$	Initial reversible capacity in prelithiated electrode
$R_{ion}$	Ionic path resistance through electrolyte
$R_e$	Electronic path resistance through carbon black or other conductive additives
$R_{c(n)}$	The contact resistance between carbon black and $n^{th}$ active particle
$R_{s(n)}$	$n^{th}$ particle/electrolyte interfacial resistance
$R_{ITL}$	Calculated interfacial resistance of an inhomogeneous transmission line
$R_{ITLM}$	Estimated overall interfacial resistance from the inhomogeneous transmission line model
$R_{semi}$	Measured semicircle(s) resistance from conventional symmetric cells
$R_{tei}$	Measured total electrode/electrolyte interfacial resistance
$V(\omega, t)$	Alternating voltage signal
$I(\omega, t)$	Current response
$Z_{(n)}$	Interfacial impedance of the $n^{th}$ particle
$Z_{ITL}(\omega)$	Calculated impedance of an inhomogeneous transmission line

$Z_{ITLM}(\omega)$	Estimated electrode overall impedance from the inhomogeneous transmission line model
$Z_{sym}$	Measured impedance in conventional symmetric cells
$Z_{el}$	Measured electrode impedance
$Z(Im)$	Imaginary part of measured or calculated impedance
$Z(Re)$	Real part of measured or calculated impedance
$Z(\omega)$	The impedance of a cell
$Z_{capacitor}(\omega)$	The impedance of a capacitor
$Z_{Inductor}(\omega)$	The impedance of an inductor
$Z_{Resistor}(\omega)$	The impedance of a resistor
$Z_{cor}$	Corrected impedance
$Z_{eld}$	Electrode impedance
$Z_{elyt}$	Electrolyte impedance
$Z_{EIS-sym}$	EIS system impedance
$Z_{total}$	Total impedance
$i$	Cycle number
$j$	The imaginary unit
$k$	The ratio of interfacial resistance between particle B and particle A, $R_{SB}/R_{SA}$
$\omega$	The frequency of input signal
$n$	Particle index, where $n$ can be 1, 2, 3, 4, each particle being of type A, or B
$m$	The $m$ ITL in from the inhomogeneous transmission line model
$\varphi$	Phase shift between the current response and the alternating voltage
$t$	Time

$N$	The number of inhomogeneous transmission lines in the model
$m_{areal}$	Mass loading
$de$	Delithiation, used as superscript
$li$	Lithiation, used as superscript
$A, B$	Type of particles or electrodes, used as subscript

## ACKNOWLEDGEMENTS

With over a thousand cells made and many projects failed, it is gladly to have some nice works done at the end. I would like to acknowledge my supervisor Dr. Mark Obrovac for the opportunity to study here. I am grateful for the guidance he provided. His meticulous attitude during the planning and development of this thesis project has been very much appreciated.

I would like to thank my committee members, Dr. Lukas Swan, Dr. Laurent Kreplak, and Dr. Mita Dasog for their advice on this thesis. I would like to thank Dr. Chongyin Yang to fill up Dr. Mita's absence as a thesis reader. I would like to thank Dr. Miran Gaberscek as the thesis external examiner.

I would like to thank all the members of the Obrovac lab, past and present.

## CHAPTER 1 INTRODUCTION

### 1.1 Motivation

Li-ion battery (LIB) technology has become indispensable in portable device and electric vehicle applications, due to its advantages of high energy density, rapid charge/discharge capability, and relatively long service lifetime [1,2]. However, state-of-the-art LIB technology is challenged by the ever-increasing demand for higher energy-density and lower cost rechargeable batteries [3–5]. At present, a mainstream approach to pursue this demanding target is through developing new electrode materials [5–7].

Graphite and  $\text{LiCoO}_2$  (LCO) are the dominating negative electrode (anode) and positive electrode (cathode) materials, respectively, currently used in high-energy LIBs for small consumer electronic devices. Ni-rich layered oxides, such as  $\text{LiNi}_{1-x-y}\text{Mn}_x\text{Co}_y\text{O}_2$  (NMC) and  $\text{LiNi}_{1-x-y}\text{Co}_x\text{Al}_y\text{O}_2$  (NCA), as well as olivine based cathodes, such as  $\text{LiFePO}_4$  (LFP), are gaining dominance in grid storage and automotive applications. Graphite has an overall outstanding electrochemical performance, including high specific/volumetric capacity ( $372 \text{ mAh g}^{-1}/ 719 \text{ Ah L}^{-1}$ ), superior cycle life, low average lithiation/delithiation potential ( $\sim 0.1 \text{ V}$ ), low hysteresis, and high coulombic efficiency (CE) [8]. Si-based materials have been extensively studied as very promising candidates for anode materials, mainly due to its high theoretical specific/volumetric capacity ( $3579 \text{ mAh g}^{-1}/ 2194 \text{ Ah L}^{-1}$ ), relatively low average lithiation/delithiation potential ( $\sim 0.4 \text{ V}$ ) of Si [9]. On the basis of these two features, Si-based anodes have great potential to improve cell energy density, theoretically up to 34% [8].

LCO has a theoretical capacity of  $274 \text{ mAh g}^{-1}$  when charged to 5.1 V. However, the LCO is commonly designed to charge to 4.2 V in full cell ( $\sim 0.5$  per LCO or delivered reversible capacity of  $137 \text{ mAh g}^{-1}$ ), to avoid a lattice distortion between hexagonal and monoclinic phase transition

that likely leads to the capacity degradation of LCO [10]. NMC and NCA have attracted great attention in both industry and academia because of reduced cost via reduced Co content [11]. Ni-rich (over 80% Ni) layered oxides have especially high gravimetric capacities (*e.g.*,  $\sim 200 \text{ mAh g}^{-1}$  for  $\text{LiNi}_{0.8}\text{Mn}_{0.1}\text{Co}_{0.1}\text{O}_2$  (NMC811) [12]) when charged to 4.3 V, which is frequently used as the key metric for claiming higher energy density over 4.2 V LCO. LFP is even lower in cost, but comes with challenges of low energy density, poor electrical conductivity, and slow Li-diffusion.

The pathway of new electrode materials into practical LIBs is often hindered by the severe degradation reactions during cell operation, leading to shortened battery service life. The amount of active material may decrease, mainly induced by structural degradation (the reversibility of the active material to host Li fails) and mechanical failure (the active material loses electrical contact to the electrode) [13]. Due to the strong oxidative/reductive nature of cathode/anode surfaces, electrolyte decomposition may also occur, as another major cause of cell failure [14]. To improve the Si-based anode performance in practical cells, efforts have been made, including the design of Si alloys, co-utilization of graphite, and the use of advanced binders and electrolytes [8,15–17]. For Ni-rich cathode materials, the stabilization strategy includes elemental doping, the implementation of single-crystal particles, and the use of core-shell structures [18].

Even though much progress has been made to reduce degradation mechanisms that lead to capacity fade, providing battery lifetimes with Si-based and Ni-rich materials (with high nickel content of  $>60\%$ ) that are comparable to conventional Li-ion cells remains a challenge. For example, Si-based materials generally undergo the large volume change during cycling, causing damage to stabilized interface between electrode and electrolyte and consequently resulting in accelerated electrolyte decomposition [19–21].

The characterization of the mechanisms leading to cell capacity fade is important. In cells where mechanical or structural failure of the active material is not significant, cell capacity fade due to electrolyte decomposition reactions can be quantified by electrochemical measurements. Such measurements need to be extremely accurate and precise, since the capacity contributed from such reactions are dwarfed in comparison to the total reversible capacity [22]. This necessitates the use of high precision chargers (HPC) for such measurements, especially when half-cells are used [23,24]. Irreversible capacity loss from electrolyte decomposition reactions can be convoluted, to some extent, with signals from the active material loss [25].

Even though HPCs are a powerful tool to study electrolyte reactivity, their high cost (about \$4000 per channel) limits their use. Another feasible approach to evaluate electrolyte reactivity is by using a standard charger to measure the capacity fade of symmetric cells. Symmetric cells are constructed using two identical electrodes (one previously lithiated and one delithiated) [26]. The capacity fade of symmetric cells during cycling is directly related to the electrode CE. By cycling such symmetric cells, the electrolyte reactivity of graphite electrodes has been precisely measured [27]. However, conventional symmetric cells are intricate, difficult to assemble, and perfect alignment between two identical electrodes is difficult to achieve. To address these issues, double half-cells (DHCs) have been developed, consisting of two Li half-cells having identical working electrodes [27,28]. As a result, DHCs provide a more accurate coulombic measurement than the conventional symmetric cells and are easier to assemble.

Electrolyte decomposition reactions not only alter cell capacity, but also can change the interfacial impedance between the electrode and the electrolyte because of the deposition of decomposition products on electrode surface [29]. The deposited interfacial layer is widely termed as the solid electrolyte interphase (SEI) layer [30]. Electrochemical impedance spectroscopy (EIS)

provides a non-destructive approach to characterize the SEI contribution to interfacial impedance. Previous studies have shown that EIS spectra can vary considerably when electrodes are at different electrochemical potentials or when different electrolyte compositions are used [31–34]. By analyzing these spectra, the interfacial impedance in each case can be extracted to estimate the quality of the SEI layer [35]. Generally, it is believed that a lower interfacial impedance represents a more effective SEI [36].

In order to develop next generation electrode materials for commercial LIBs having a relatively long service lifetime, it is crucial to suppress their high electrolyte reactivity. To accomplish this requires reliable and efficient methods to measure the electrolyte reactivity and characterize the SEI layer on electrodes. In this thesis, a brief overview of LIBs, especially the electrode/electrolyte interface, is given in Chapter 1. Chapter 2 demonstrates the importance of lifetime on rechargeable batteries, using potassium-ion batteries (a trending next-generation battery chemistry) as an example. With the importance of battery lifetime established, the remainder of the thesis focuses on methods to quantitatively measure and model battery degradation mechanisms that contribute to reduce battery lifetime. In Chapter 3, the experimental tools used in this thesis and the related principles are discussed. Chapter 4 investigates interfacial impedance growth on Si-alloy/graphite blended electrodes. Chapter 5 provides interpretation of the capacity fade in symmetric cells. Additionally, strategies to evaluate the electrolyte reactivity are discussed. Chapter 6 provides a modified cycling protocol to collect the true electrochemical performance of electrode under designed rate. A summary of this thesis will be provided in Chapter 7, as well as a description of future work.

## 1.2 Lithium-Ion Batteries

The first commercially successful LIBs were marketed by Sony in 1991, using a coke anode,  $\text{LiCoO}_2$  (a layered oxide material) cathode, and a  $\text{Li}^+$  conducting electrolyte [37]. Figure 1.1 shows a schematic of a Li-ion battery. In battery fabrication, anode and cathode materials are coated onto a Cu current collector and an Al current collector, respectively. The Cu and Al current collectors can be connected to an external circuit to enable the battery charge/discharge process. A porous separator between the anode and cathode is used to prevent the battery from shorting internally. During charge, by an applied external current or potential,  $\text{Li}^+$  ions are removed from the cathode and inserted into the anode. This process is reversed during discharge, where  $\text{Li}^+$  ions move back from the anode to the cathode.

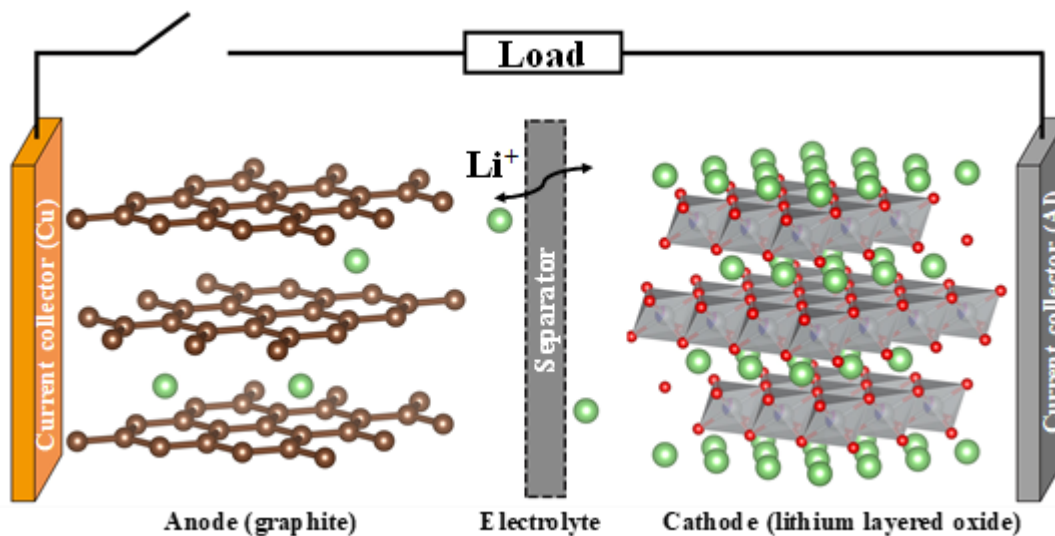


Figure 1.1 Schematic of a Li-ion battery. The brown, green, and red balls represent C, Li, and O atoms, respectively. The balls occupying the octahedral sites (bonded with O atoms) represent transition metal(s). Here, the occupation of these balls is 60% Ni, 20% Co, and 20% Mn.

## 1.3 Common Cell Designs

An electrochemical cell is the basic unit of a LIB. In some applications, like cellphones, a battery may comprise only one cell. In large-scale applications, such as electric vehicles, multiple cells are assembled into a battery. These cells are connected in parallel and/or serially by

interconnecting circuits, assembled into a protective frame, and operated through a battery management system and often additionally a thermal management system [38]. The use of different cell designs can result in changes in battery performance, including energy density, safety, reliability, and cost, even if similar electrode chemistries are used [5].

Pouch-type cells, shown in Figure 1.2(a), are one of the most common commercial LIB cell types. Typically, electrode materials are coated on both sides of the current collectors. The double-sided electrodes and separators are then either wound or stacked and then sealed with electrolyte into a cell pouch. Tabs on the electrodes protruding from the pouch facilitate the passage of current into the cell. Pouch-type cells can be designed with various cell dimensions to fit the space requirements of different applications. Other commonly used commercial LIB cell types are cylindrical-type cells and prismatic-type cells.

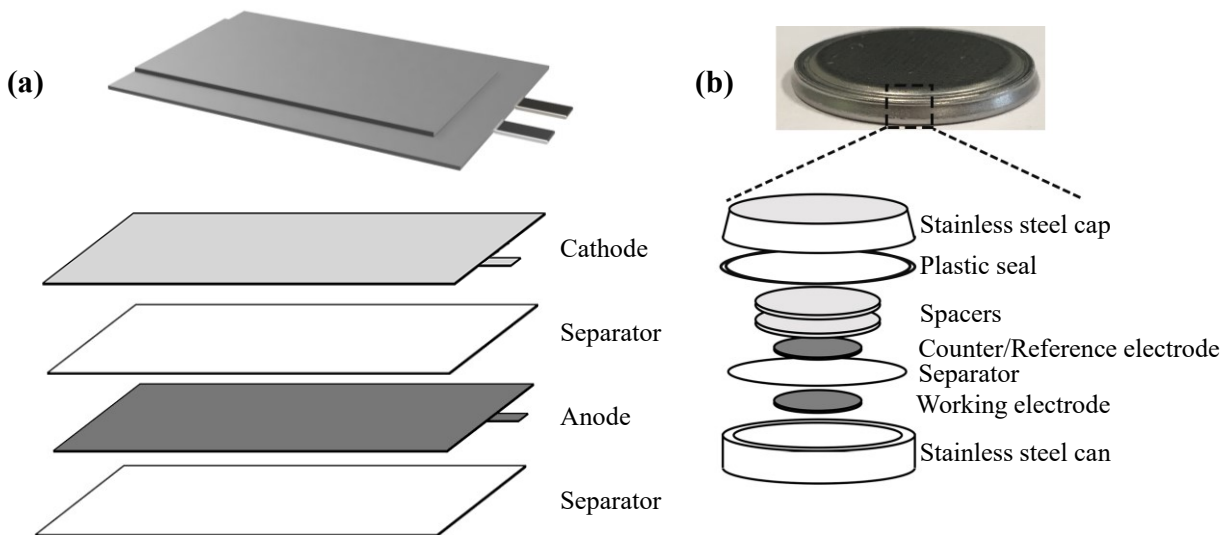


Figure 1.2 A schematic diagram of (a) pouch-type cell (showing an electrode/separator stack with cell tabs protruding from the electrodes), and (b) coin-type cell.

For academic battery researchers, coin-type cells are one of the most widely used cell types, having similar cell components (Figure 1.2(b)) to the aforementioned commercial cell formats [39]. The benefits of using coin-type cells include easy assembly, high reproducibility, and a small-

quantity requirement of electrode materials [40]. Three major coin cell configurations are commonly used: full cells, half cells, and symmetric cells. In a full cell, two different working electrodes, a cathode and an anode, are included. A coin-type full cell is often used as a LIB prototype for academic study [41]. In half cells, one working electrode is used, paired with a disk of Li metal as a reference/counter electrode. Half cells are important for investigating the basic electrochemical performance of electrode materials of interest, such as their potential profiles, specific/volumetric capacities, cyclability, and rate capability [42,43]. In symmetric cells, two identical working electrodes are included. Symmetric cells are an ideal tool to investigate the electrochemical performance of one electrode without the interference from different electrodes [26,44]. Symmetric cells are especially useful for accurate measurement of electrode CE. However, it must be kept in mind that this single-electrode CE may not be representative of the electrode's CE in a full cell, since electrolyte decomposition products of one electrode in a full cell may affect the CE of the other. In order to cycle symmetric cells, at least one of the electrodes needs to be pre-lithiated or pre-delithiated. The electrode configurations of these three categories of coin cells are shown in Figure 1.3.

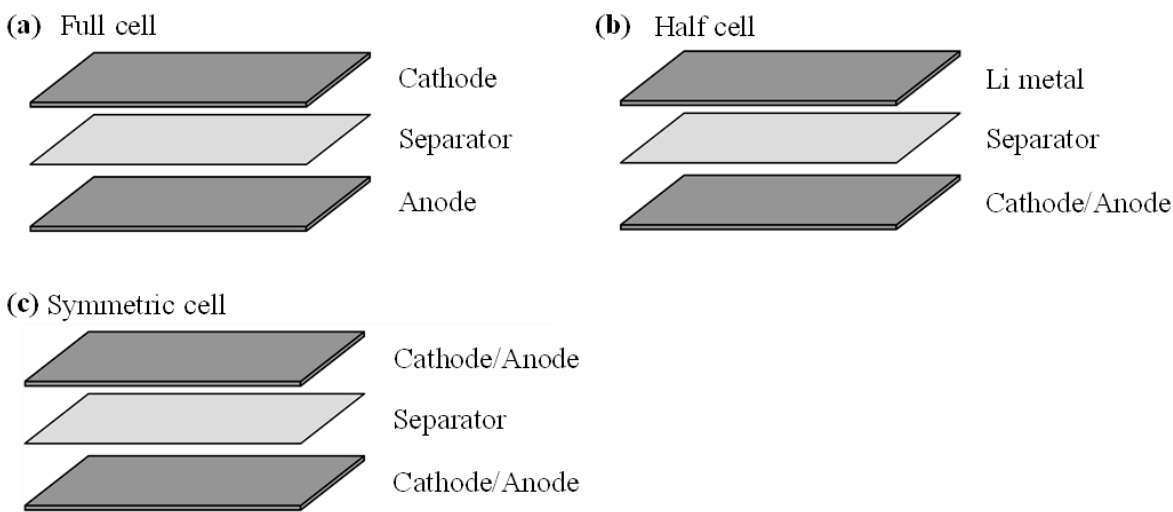


Figure 1.3 Electrode stacking configurations in (a) full cell, (b) half cell, and (c) symmetric cell.

## 1.4 Anode Materials

As aforementioned in Section 1.1, graphite electrodes have been the main anode materials in LIBs for decades. During lithiation, Li ions insert into graphite interlayers, which are bound by van der Waals forces. During delithiation, Li ions are removed from between the graphite layers. This lithiation/delithiation process is highly reversible and the graphite structure can remain unchanged after cycling, leading to excellent cycling capacity retention [45]. At a full electrochemical lithiation,  $\text{LiC}_6$  is formed, which corresponds to a specific/volumetric graphite capacity of  $372 \text{ mAh g}^{-1}/ 719 \text{ Ah L}^{-1}$  [8,46]. This full lithiation expands the spacing between two graphite layers from  $3.36 \text{ \AA}$  to  $3.71 \text{ \AA}$  while the C-C bond length almost remains the same [46]. As a result, graphite electrodes experience a volume expansion of only  $\sim 10\%$  during lithiation, which does not significantly disrupt the SEI layer [24,30,47].

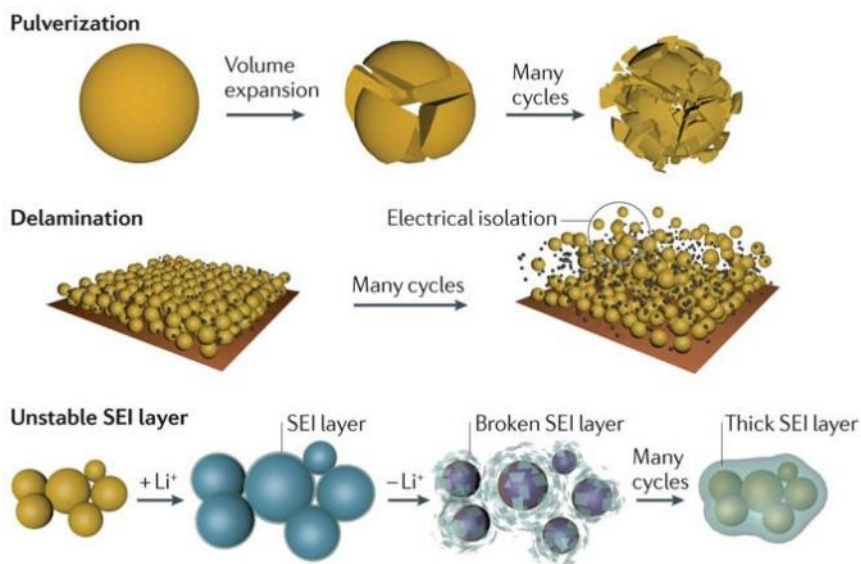


Figure 1.4 The main degradation mechanisms of Si anodes due to their large volume changes during cycling. Reprinted with permission from ref [5]. Copyright 2016 Springer Nature.

Unlike the intercalation process in graphite, crystalline Si first forms amorphous lithiated Si during lithiation [9]. At the end of the first full electrochemical lithiation, the lithiated amorphous Si transforms to a crystalline phase of  $\text{Li}_{15}\text{Si}_4$  [9]. This final product hosts 3.75 Li per Si, corresponding to a theoretical specific capacity of  $3579 \text{ mAh g}^{-1}$  (more than nine times as that of graphite). This high capacity is associated with a huge volume change of 280%. The theoretical volumetric capacity of Si is  $2194 \text{ Ah L}^{-1}$ , three times that of graphite (a more practical metric for evaluating electrode performance than the specific capacity in most applications). The volume changes that occur during the lithiation/delithiation of Si cause multiple issues. Si electrodes can suffer particle pulverization, electrode delamination, and severe disruption of the SEI layer during cycling [48,49]. Consequently, the cycling capacity can drop rapidly, and parasitic reactions can occur excessively. The major degradation mechanisms of Si anodes are illustrated in Figure 1.4.

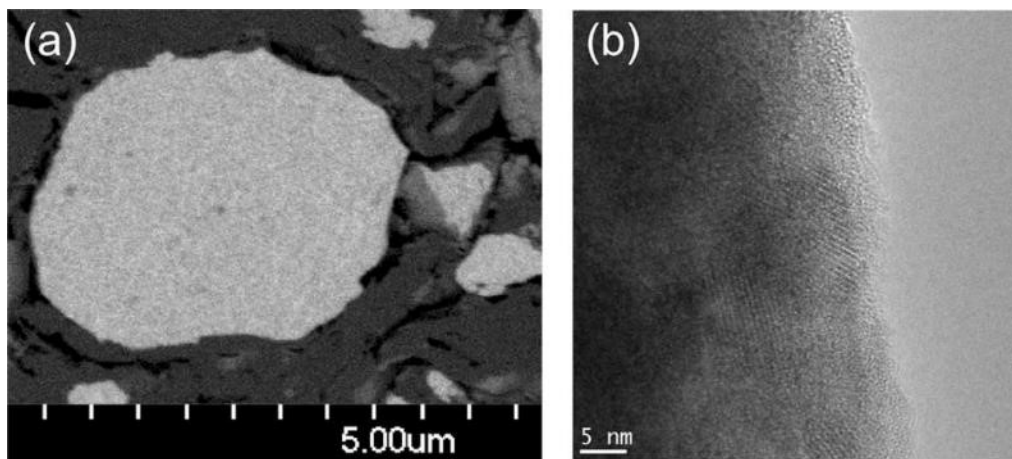


Figure 1.5 (a) Field emission scanning electron microscope image of an ion polished cross section of a 3M L-20772 V6 alloy particle. Surrounding darker regions are graphite. (b) TEM image of particle edge of the alloy particle. Reprinted with permission from ref [50]. Copyright 2014, IOP Publishing.

To utilize Si in LIBs, this huge volume change needs to be suppressed. One practical approach is the use of Si-alloys, which are comprised of Si and inactive element(s) (inert to the

lithiation) [15]. Si-alloy materials are designed to be made of nanosized active Si domains and inactive phase domains, which are evenly distributed throughout micro size particles [8,50]. Figure 1.5(a) shows a scanning electron microscopy (SEM) image of a Si alloy (V6 alloy, 3M Company) particle which contains an active Si phase and inactive phases containing transition metal atoms. The V6 alloy contains active Si domains and inactive domains that contain a metal that has a higher electron density than Si [50]. Due to this difference in electron density, the inactive domains appear darker than Si domains in the SEM image. A uniform contrast is observed, indicating an even distribution of the active and inactive domains in the particle. Figure 1.5(b) shows a transmission electron microscopy (TEM) image of a V6 alloy particle. In this image the active Si and inactive domains can be seen to be less than 15 nm. Inactive phases in Si alloys can dilute silicon's volume expansion significantly (*e.g.* typically to  $\sim 100\%$  volume expansion), with a limited negative impact on energy density, since there is little gain in cell volumetric energy density when Si alloy volume expansion exceeds 100% [8]. As a result, Si-alloy materials have higher cycling capacity retention and lower electrolyte reactivity than Si [50].

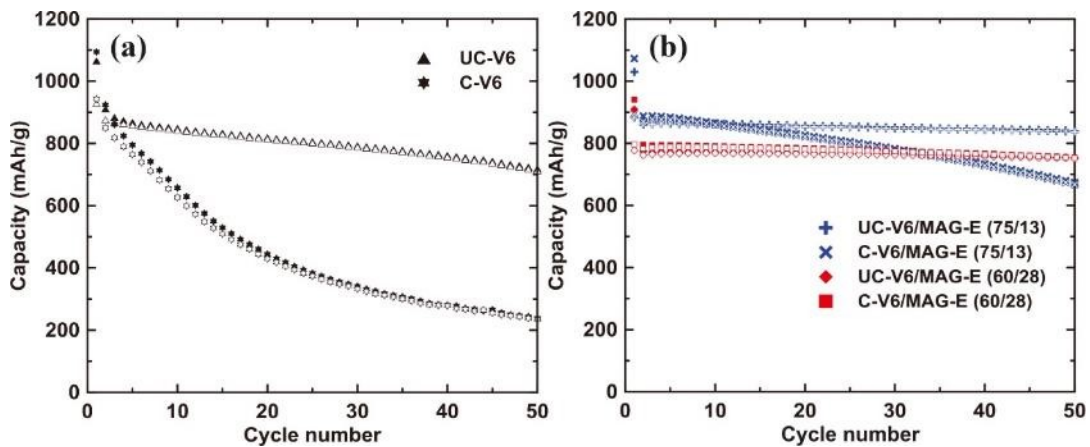


Figure 1.6 (a) Cycling performance of uncalendered and calendered 3M Si-alloy (V6) electrodes. (b) Cycling performance of uncalendered and calendered V6/MAG-E electrodes with different MAG-E contents (by weight ratio). MAG-E is one commonly used graphite for LIBs. Reproduced with permission from ref [51]. Copyright 2014, IOP Publishing.\

A practical and near-term approach for using Si-based materials in commercial LIBs is to utilize them in a blended form with graphite, which additionally buffers the Si volume changes [7,50]. Such composites can have superior performance in capacity retention, compared to electrodes comprising an individual active compound [50,52,53]. Importantly, as-coated electrodes are highly porous (~50-60% porous). To achieve high-volumetric-energy density, commercial electrodes need to be calendered to reduce the porosity to about 25%. This is about the minimum level of porosity that can be used to maximize energy density, while still allowing adequate penetration of electrolyte for ion conduction. Previous studies have shown that the calendering process worsens the cycling performance of Si-containing electrodes [51,54]. As shown in Figure 1.6, calendered V6 Si-alloy electrodes suffer much more severe capacity fade than uncalendered electrodes. After blending with graphite, the cycling performance of calendered electrodes significantly improves.

## **1.5 Cathode Materials**

LiCoO<sub>2</sub> (LCO) is the most commonly used cathode material in LIBs for small portable devices. The merits of LCO include high energy density and easy synthesis [55,56]. However, LCO is usually cycled with a maximum Li extraction of ~0.5 Li per LCO, or the capacity fade is severe. Consequently, the practical capacity of LCO is ~140 mAh g<sup>-1</sup>. Another issue that needs to be addressed for LCO is the toxicity and high cost of cobalt, which makes LCO unsuitable for applications in large-scale energy storage.

The demand for cathode materials with higher energy density and lower cost has shifted academic and industrial interests from LCO to other promising alternatives, such as NMC and NCA [5,57,58]. These low-Co-content cathode materials adopt a similar structure as LCO, with cationic substitution of cobalt by more inexpensive metals. Benefits of these substitutions include

not only significant cost reduction, but also an increase in reversible capacity [38,52,59]. For example, the reported price of Co, Ni, and Mn raw materials are \$32 kg<sup>-1</sup> (CoSO<sub>4</sub>), \$5.5 kg<sup>-1</sup> (NiSO<sub>4</sub>), \$1 kg<sup>-1</sup> (MnSO<sub>4</sub>), respectively [38]. Therefore, the use of LiNi<sub>0.6</sub>Mn<sub>0.2</sub>Co<sub>0.2</sub>O<sub>2</sub> (NMC622) has the potential to reduce the cathode cost by nearly half (please note that there are some other costs needed to produce cathode materials from raw materials, such as manufacturing cost, which has been assumed to be the same for all compositions) [38]. In addition, NMC622 can deliver a reversible capacity of ~200 mAh g<sup>-1</sup> (~0.7 Li per NMC) when cycled with an upper cut-off potential of 4.5 V [60]. Due to these advantages, alternatives, such as NMC, have been used in LIBs for electric vehicles. However, improvements in these alternative cathode materials are still required, in terms of synthesis, cyclability, electrolyte reactivity, and safety [5].

## 1.6 Electrolytes

Electrolytes serve as the medium for the transfer of Li ions between the anode and cathode in a LIB. An ideal LIB electrolyte should have high ionic conductivity, high electrical resistivity, high electrochemical stability, a wide operating temperature range, low cost, and low environmental toxicity [14]. Electrolytes used in commercial LIBs commonly consist of LiPF<sub>6</sub> salt dissolved in organic carbonate solvents with some electrolyte additives [61]. New electrolytes have been intensively explored in the past decades, yet their benefits, if any, are not sufficiently promising to result in adoption by the battery industry [62–65].

Among numerous Li salts, LiPF<sub>6</sub> has been the obvious winner used in commercial LIBs over many decades. Compared to other Li salts, LiPF<sub>6</sub> actually has few outstanding properties, including moderate dissociation constant, ion mobility, chemical stability, and even poor thermal stability [14,66]. The success of LiPF<sub>6</sub> relies on having a well-balanced suite properties that meet all the minimum requirements for LIBs.

In terms of the electrolyte solvent, ethylene carbonate (EC) is widely considered as an indispensable component, since it enables the utilization of graphite anodes in LIBs [67]. As the most important feature, EC can form an effective passivation film (the SEI layer) on graphite, to protect the layered structure from exfoliation during cycling [67]. In addition, EC has a high dielectric constant ( $\epsilon=88.6$  at 40 °C), which can dissolve lithium salts efficiently [68]. However, due to its high melting point (36.4 °C) and high viscosity, EC needs to be mixed with other solvents having low melting points and low viscosities, such as diethylene carbonate (DEC) and ethyl methyl carbonate (EMC) [69,70]. To operate the LIBs at higher potentials, the necessity of EC has been challenged recently because of its relatively poor oxidation stability at high potential ( $> 4.5$  V vs. Li/Li<sup>+</sup>) [61,71].

Commercial electrolytes commonly contain electrolyte additive(s) at a low concentration (typically  $< 10$  wt%) [72,73]. Instead of entirely replacing the electrolyte system, the development of electrolyte additives provides a feasible approach to modify electrolyte performance [34,74,75]. Electrolyte additives generally serve as a sacrificial component, which is preferentially decomposed over other compositions in the electrolyte. This preferential decomposition can form a favorable SEI layer on electrodes, which significantly modifies the further reversibility of battery reactions [76]. For example, Si-containing electrodes cycled in electrolytes with fluoroethylene carbonate (FEC) electrolyte additive have a better capacity retention and a lower parasitic reaction rate with electrolyte than those cycled without FEC [72,77]. This improvement corresponds to the decomposition of FEC forming fluorinated species, such as LiF, in the SEI layer, which more effectively passivates the electrode [78–80].

## 1.7 Solid Electrolyte Interphases

An ideal LIB electrolyte should incur no net chemical changes during repeated battery cycling. However, the chemical and electrochemical stability of electrolytes in commercial LIBs are often challenged by the strong reducing and oxidizing nature of the anode and the cathode, respectively [81–83]. This challenge can become more severe in advanced batteries with higher energy densities [84–86]. Even though most state-of-the-art electrolytes fail to be stable under the typical potential windows used for battery operation (typical 0–4.2 V vs. Li/Li<sup>+</sup>), LIBs can still operate for years [87]. The major contributor to this long service lifetime is the formation of the aforementioned SEI layer, which has a thickness range from 5 to 500 nm [22].

Despite its importance for battery operation having been stressed widely, the SEI layer is still the least understood component in LIBs, due to its complicated composition and sensitive chemical nature [30,88,89]. For example, the main compounds in the SEI layer on graphite electrodes are lithium alkyl carbonates, LiF, Li<sub>2</sub>O, and Li<sub>2</sub>CO<sub>3</sub> in EC-based electrolytes with LiPF<sub>6</sub> salt [89]. Various SEI components are originally from the decomposition of solvents, Li salts, and some impurities [90]. The difficulty in understanding the SEI layer involves not only its complex composition, but also the morphology and arrangement of diverse SEI components [91,92]. A widely used SEI model, introduced in 1997, considers that these SEI components are arranged as a “mosaic” structure, as shown in Figure 1.7 [93]. However, this very indistinct model is incapable of explaining the continuous electrolyte decomposition that occurs after the initial formation of the SEI layer. Moreover, the sensitive chemical nature of the SEI layer hinders available techniques to characterize it. Some SEI components, such as Li<sub>2</sub>O and lithium alkyl carbonates, are sensitive to the water, oxygen, and even nitrogen [89]. If samples are handled improperly (even exposed to air for a few seconds), misleading information may be obtained, such as controversial results about

the presence of  $\text{Li}_2\text{CO}_3$  in the SEI layer [14,94]. In addition, some SEI components may (partially) dissolve in electrolytes [95]. For these reasons, it is more convincing to characterize the SEI layer using *in-situ* and *operando* techniques.

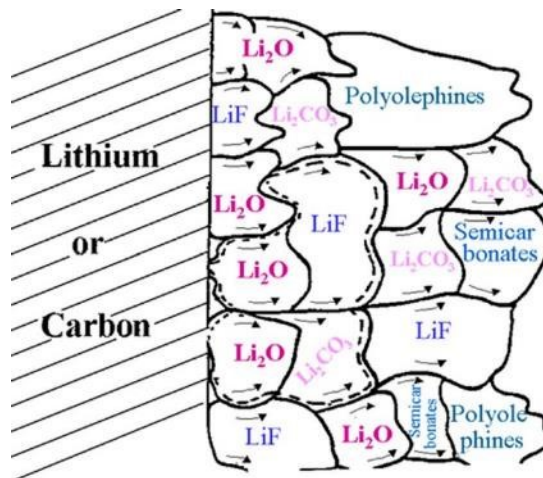


Figure 1.7 Schematic presentation of polyhetero microphase SEI. Reprinted with permission from ref [30]. Copyright 2017, IOP Publishing.

The formation and growth of the SEI layer consumes active Li [24]. The electrochemical reduction of carbonates mainly follows a single-electron mechanism, consuming one Li ion per molecule [96]. For example, EC reacts with  $\text{Li}^+$  and  $e^-$ , mainly generating an organic compound, lithium ethylene decarbonate, at the electrode surface and ethylene gas. The pathway for EC reduction is presented in Figure 1.8. Despite SEI layer formation on the electrode surface, further electrolyte decomposition has not yet been fully prevented, leading to continuous SEI growth and depletion of the lithium ion inventory inside the battery. This results in capacity fade.

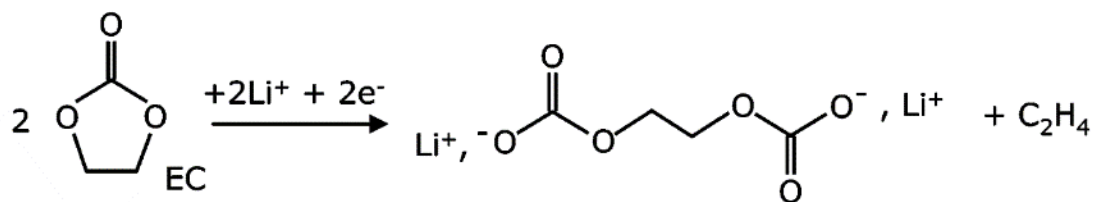


Figure 1.8 One single-electron mechanism for EC reacting with Li<sup>+</sup> and e<sup>-</sup>. Reprinted with permission from ref [97]. Copyright 2005 American Chemical Society

## 1.8 Characterizations of Electrolyte Reactivity

### 1.8.1 The Measurement of Post-first-cycle Irreversible Capacity

Once an initial SEI layer effectively forms during the first cycle, further electrolyte decomposition on the anode should be significantly restricted, gradually reducing to an almost infinitesimal rate, resulting in a long service life (over several years for current commercial LIBs) before the cell failure (where 80% capacity fade is often used as an end of life indicator). When a new electrolyte/electrode system is developed, the effectiveness of the SEI layer at restricting electrolyte decomposition needs to be examined, to reveal the interfacial irreversibility, and to demonstrate the potential service life of this new battery system. The measurement of the irreversible capacity provides a quantitative approach to evaluate the effectiveness of the SEI layer.

CE is commonly used as a measure of the reversibility of a Li-ion battery system. In full LIBs, the CE corresponds to the effectiveness of the SEI layer in restricting electrolyte decomposition in most cases. Among three types of cells, *i.e.* full cells, half cells, and symmetric cells, the definition of the CE is different.

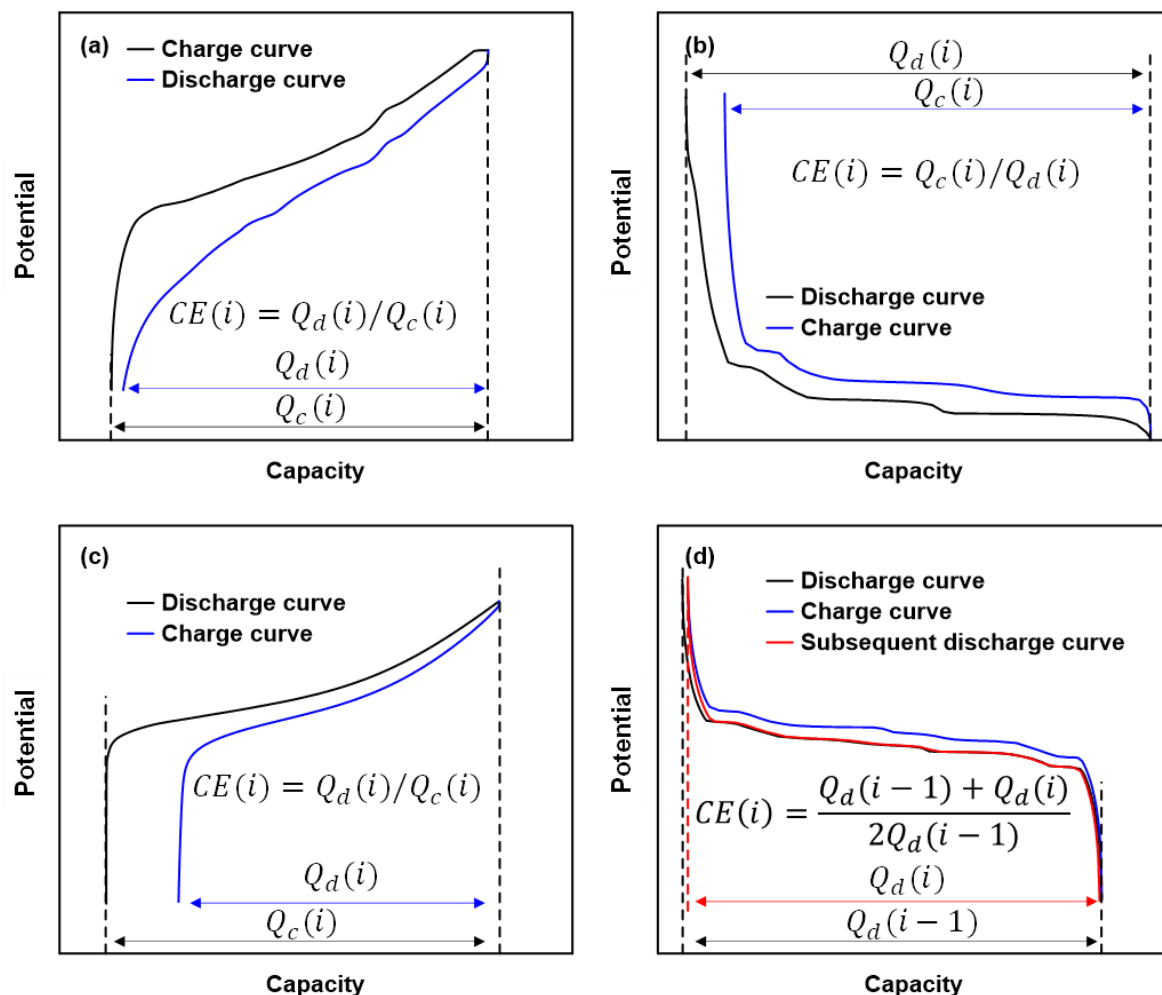


Figure 1.9 Illustrations about the CE calculations at  $i^{\text{th}}$  cycle of (a) full cells, (b) half cells with anode electrodes, (c) half cells with cathode electrodes, (d) symmetric cells.  $Q_d(i)$  and  $Q_c(i)$  are the discharge capacity and the charge capacity at  $i^{\text{th}}$  cycle, respectively.

The calculations of CE in full cell, half cell, and symmetric cell formats are illustrated in Figure 1.9. For full cells, the CE at the  $i^{\text{th}}$  cycle is defined as the discharge capacity,  $Q_d(i)$  divided by the charge capacity,  $Q_c(i)$ . The CE of half cells is defined as the working electrode delithiation capacity divided by the subsequent lithiation capacity. Accordingly, the CE( $i$ ) of half cells with anode electrodes typically is calculated using  $Q_c(i)$  divided by  $Q_d(i)$ , while the corresponding calculation for cathode electrodes is the  $Q_d(i)$  divided by the  $Q_c(i)$ . In order to enable comparisons with the CE obtained from half cells, the CE of symmetric cells is defined in a unique way. The

fade of a symmetric cell is directly related to the CE of the electrode in a half cell. In this report, symmetric cell discharge is defined as the process in which Li ions move from the pre-lithiated electrode to the pre-delithiated one (or the fresh one), while the symmetric cell charge is defined as the reversed process. In most cases, the CE of symmetric cells is calculated on the basis of the discharge capacity at the  $i^{\text{th}}$  cycle and the previous cycle [26], as shown in Figure 1.9(d). However, greater accuracy in CE determination from symmetric cells can be achieved if the CE is calculated from the accumulated fade from many cycles.

Accurate CE determination is actually very challenging. One common approach is to cycle full Li-ion cells where the Li<sup>+</sup>-source is limited. During cycling, full cells are first charged to a certain upper potential limit, then discharged to a certain lower potential limit, and then repeatedly cycled in this manner. The irreversible capacity from the electrolyte decomposition can be obtained through the measured capacity fade during cycling. The capacity fade after each cycle is very tiny (for example, cells, enabling to cycle 1000 times until capacity drops to 80%, have an average capacity fade of only 0.02% at each cycle). This tiny capacity difference is beyond the precision of traditional battery test equipment, such as the commonly used Maccor 4000, which measures capacity with an error of  $> 0.06\%$  [98]. For this reason, a cycling test over hundreds or even thousands of cycles is required, in order to eliminate the charger error. As a result, this method typically requires months or even years to estimate accurate CE (if the test condition is well controlled) when traditional battery test equipment is used.

Table 1.1 Specifications of battery test equipment [23,99].

Manufacturer	Current resolution	Potential resolution	Current accuracy	Potential accuracy	Time between measurements
Maccor 4000 series	16 bit (1 in 65536)	16 bit (15 $\mu\text{V}$ )	0.02-0.05% of full scale	0.02% of full scale	0.01s
Dalhousie HPC	1 in 19,999	10 $\mu\text{V}$	0.005% of full scale	0.0025% of full scale	<1s

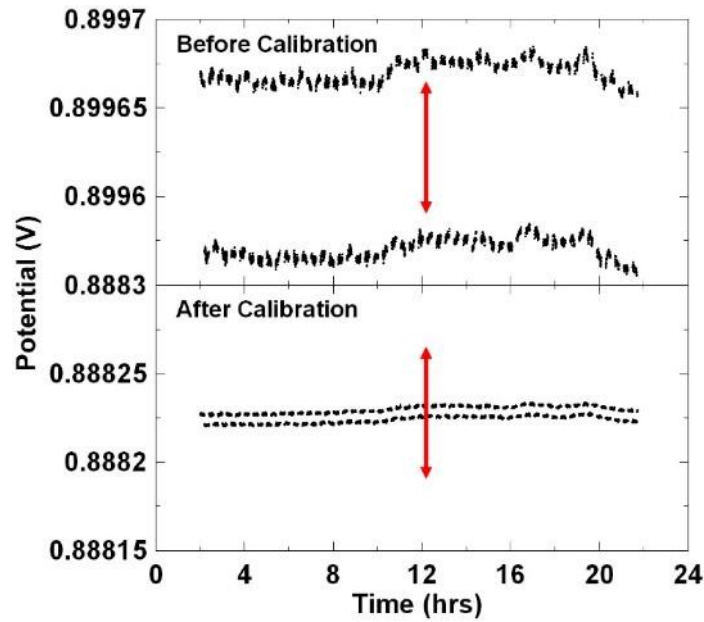


Figure 1.10 The absolute value of the potential across a resistor with a positive and negative current of equal magnitude alternating every six minutes before (top panel) and after (bottom panel) calibration. The red arrows represent an error in current equality of 1 part in 10,000. Reprinted with permission from ref [98]. Copyright 2012, Aaron Smith.

To accelerate this evaluation process (to only weeks), HPCs are used. The specifications of an HPC and a traditional battery charger (Maccor 4000) are summarized in Table 1.1 for comparison. The benefits of HPCs include high potential and current precision and high equality between positive and negative currents. The current equality, as the most important feature of HPC, is carefully controlled, as shown in Figure 1.10. Considering that the CE measurements for full

cells and half cells depend on both charge and discharge capacities, chargers with a high equality of positive and negative current are essential for obtaining CE values with high accuracy [98]. In other words, the measured CE of full cells and half cells using a standard charger might be unreliable. Due to the improved performance in coulombic measurement, HPCs have been successfully applied to evaluate the CE of electrode materials cycled under various conditions, such as at different potential ranges and with different electrolyte compositions [24,73,75,100,101]. This has enabled rational electrode and electrolyte choices towards long battery service lifetime and high energy density [61,102]. However, the high cost of HPCs limits their use.

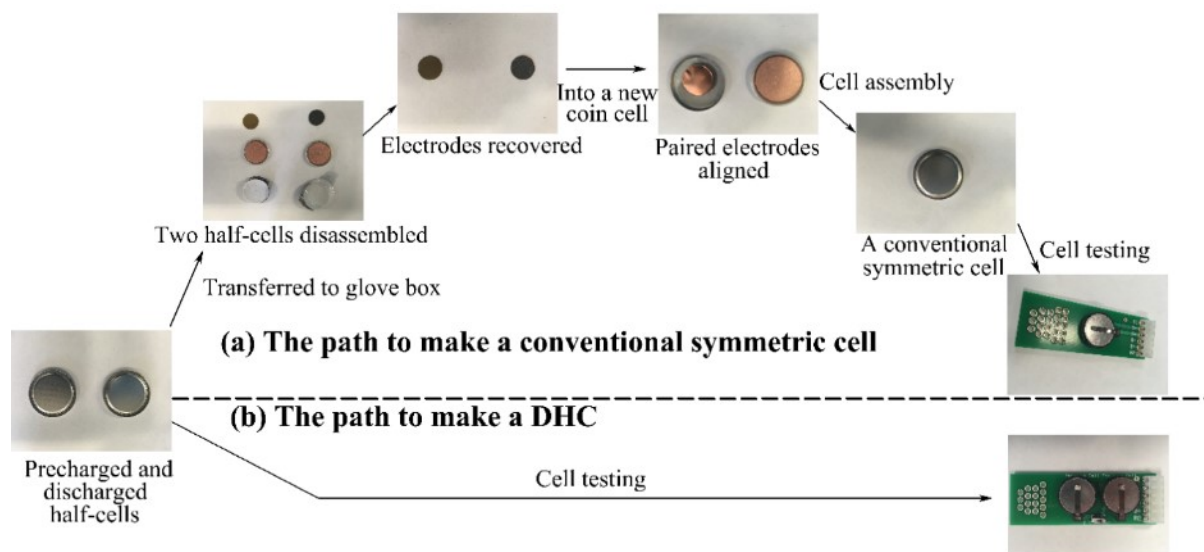


Figure 1.11 An illustration of the construction pathways for making (a) a conventional symmetric cell and (b) a DHC. Reprinted with permission from ref [28]. Copyright 2018, Elsevier.

To efficiently and accurately measure the irreversible capacity using a standard charger, symmetric cells, having two identical working electrodes in each cell, have been introduced. The CE and irreversible capacity of symmetric cells are obtained from either the discharge or charge capacity [26]. The use of symmetric cells avoids the inaccuracy caused by inequalities in positive and negative currents of a standard charger. In addition, the per cycle irreversible capacity

measured in symmetric cells is doubled compared to half cells, due to the presence of two identical working electrodes in each cell. An amplified irreversible capacity leads to a relatively low precision requirement for the charger. However, due to the complex assembly process and electrode alignment issues, conventional symmetric cells can suffer from poor reliability and low CE measurement accuracy [27]. To address these issues, DHCs were designed [27]. As shown in Figure 1.11, the assembly of a DHC is simple and the electrode alignment issue is totally avoided, due to the Li foils used having a larger diameter than the working electrodes. As a result, DHCs have better cycling performance and provide a more accurate CE measurement than conventional symmetric cells.

### 1.8.2 Electrochemical Impedance Spectroscopy

Due to the electrolyte decompositions, the formation and growth of the SEI layer can greatly influence charge transfer kinetics at the electrode-electrolyte interface. EIS provides a non-destructive approach to characterize interfacial charge transfer kinetics, and to monitor SEI layer formation and growth during cycling. EIS is an electrochemical technique which applies, in most cases, small perturbing AC voltage signals at various frequencies to an electrochemical system. The current responses of this system are then recorded. The impedance of this system, as the ratio of the input voltage to the output current, can be acquired, as a function of the frequency. Cell impedance provides abundant information, including internal electrical resistance, electrolyte bulk resistance, ionic resistance in electrode pores, interfacial resistance at the electrode/electrolyte interface, and the solid-state diffusion resistance in electrode materials [103].

To investigate the interfacial impedance growth on working electrodes, EIS measurements have been conducted mainly by two ways: pairing the electrode with a reference electrode (as in a half-cell) [104–107] or pairing with an identical working electrode (as in a conventional symmetric

cell) [44,108]. The use of a reference electrode, such as Li metal, is a conventional approach, in which the impedance can be conveniently measured under a certain potential, state of charge, and cycle number. However, the impedance from the reference electrode is inevitably included, and the removal of this impedance is typically difficult to accomplish [103]. Therefore only changes in working electrode impedance can be measured, if it is assumed that the impedance of the Li electrode is constant (which it often is not). If conventional symmetric cells are used, the acquired impedance only comes from one type of electrode. As a result, the use of conventional symmetric cells totally avoids the interference from a different electrode, and accurate impedance measurement is ensured. However, as a drawback, products of electrolyte reactions at both electrodes in a full cell can contribute to the SEI. Therefore, both half-cell and symmetric cell EIS measurements may not fully represent an electrode's SEI characteristics when used in a full LIB.

The interpretation of EIS spectra is also challenging and sometimes even controversial, mainly due to the complicated nature of electrodes and the electrode/electrolyte interface. In order to interpret the acquired impedance, the related electrochemical processes need to be modeled with an equivalent circuit, and then the interfacial impedance can be extracted on the basis of selected models [35]. Common models consider the working electrode as either a flat and smooth film or a single intercalation particle [35,109,110]. Under this assumption, the following extraction process becomes straightforward. However, these simple models have difficulty simulating electrodes with complicated compositions, such as electrodes containing two different active materials. In addition, these models fail to consider the effect of electrode mass loadings, a basic variable for most lab-made electrodes, on the impedance response [103].

### 1.8.3 Other Characterization Methods

Electrolyte decomposition and the SEI layer have been studied with other analytical tools, both *ex situ* and *in situ*. The electrochemical quartz crystal microbalance (EQCM) provides an *in situ* approach to probe interfacial processes, such as SEI layer growth [90,111]. Acoustic waves are delivered to the sample to measure its resonant frequency, which is related to the sample mass. The change of sample mass, such as from SEI formation and growth, shifts the resonant frequency [112]. Due to its high sensitivity to mass changes, EQCM recently has been applied to quantitatively identify electrolyte decomposition reactions occurring on graphite electrodes at different potentials [90].

Atomic force microscopy (AFM) has been developed as an *in situ* tool to investigate the morphology of the SEI layer [113]. On the basis of the force between its sharp tip and sample surface, AFM can produce topographical images of the sample surface. The samples can be characterized in ambient air or even a liquid environment. For this reason, *in situ* examination of the morphology of SEI formation is possible [114]. However, it is difficult for AFM to provide quantitative insights about the SEI layer [90].

Some *ex situ* characterization methods, such as X-ray photoelectron spectroscopy (XPS) [115,116], SEM [117], TEM [118,119], and gas chromatography [120], have been applied to provide critical chemistry about the electrolyte decomposition and the SEI layer. For example, XPS is a commonly used technique to investigate the composition of the SEI layer. By providing a beam of X-rays to the sample while measuring the kinetic energy of ejected core electrons, the binding energy of the core electrons can be obtained, which is characteristic of the element from which they came. The binding energy shifts when the oxidation state of the element changes. Thus, the composition of the SEI layer can be determined using XPS. The major concerns about the use

of ex situ characterization methods is related to the preparation process, which might alter or contaminate the SEI layer [22].

## **CHAPTER 2 Lifetime as the Key Parameter for Rechargeable Batteries: Potassium-ion Batteries as An Example**

Z. Yan proposed the model and performed the experiments. M.N. Obrovac provided guidance for data interpretation. Z. Yan and M.N. Obrovac prepared manuscript. Figures and text in this chapter are reproduced with permission from Journal of Power Sources 464 (2020) 228228. Copyright 2020, Elsevier.

### **2.1 Introduction**

Remarkable progress has been made to harvest energy from renewable energy sources towards a sustainable energy future with zero carbon and air-pollution emissions [121]. With the rapid innovation of renewable-energy technologies, the need for cost-effective energy storage systems has been growing significantly to convert intermittent renewable energy to electricity on demand [3,122]. Electrochemical energy storage (EES) is considered a promising option for this conversion due to low geographical restrictions, high round-trip efficiency, and fast response time [3,123,124]. Despite many efforts that have been made towards advanced rate capability, superior safety, increased lifetime, and ultrahigh energy density, one fundamental and consensual target for developing practical EES technologies is to reduce their cost [125–128].

Ever since graphite was reported as a host for reversible K de/intercalation, potassium-ion batteries (KIBs) have rapidly attracted intensive interest as a potentially low cost EES technology [123,129–132]. KIBs are commonly considered to have cost advantages over lithium-ion batteries (LIBs) and/or sodium-ion batteries (NIBs), mainly on the basis of three key factors: (1) the cost of K resources, such as  $K_2CO_3$ , is lower than that of Li resources [123]; (2) the replacement of relatively expensive Cu foil with Al foil as the anode current collector can reduce the cost of KIBs

[38]; (3) KIBs potentially have a high operating potential [133], potentially resulting in a higher energy density than NIBs. Unlike these cost benefits, which are frequently stated, key drawbacks of KIBs, which would result in an increase of battery cost, are often understated. For instance, the theoretical capacity for K-intercalation in graphite is only 279 mAh g<sup>-1</sup>, which is 25% less than the theoretical reversible capacity of graphite in LIBs (372 mAh g<sup>-1</sup>) [134]. In addition, K<sup>+</sup> (1.4 Å radius) has a larger ionic radius than Li<sup>+</sup> (0.76 Å) or Na<sup>+</sup> (1.0 Å) [133]. A lower reversible capacity at the anode and a larger ionic size would tend to result in a decrease in the theoretical energy density, potentially resulting in a cost increase from the additional battery materials required to achieve the same level of energy storage [128].

Major efforts on the development of KIBs have been devoted to searching cathode materials with high energy density that are preferably based on inexpensive transition-metal elements (such as Fe, Ti, and Mn) [131,135]. State-of-the-art KIB cathode materials are mainly categorized into three groups [131]: layered oxides (*e.g.* K<sub>0.65</sub>Fe<sub>0.5</sub>Mn<sub>0.5</sub>O<sub>2</sub> [136], K<sub>0.5</sub>MnO<sub>2</sub> [137], KCrO<sub>2</sub> [138], and K<sub>0.6</sub>CoO<sub>2</sub> [139]), hexacyanometalates (*e.g.* K<sub>2</sub>MnFe(CN)<sub>6</sub> [127] and K<sub>1.75</sub>Mn[Fe(CN)<sub>6</sub>]<sub>0.93</sub>·H<sub>2</sub>O [140]), and polyanionic compounds (*e.g.* KVPO<sub>4</sub>F [141]). Some of these materials (*e.g.* K<sub>0.65</sub>Fe<sub>0.5</sub>Mn<sub>0.5</sub>O<sub>2</sub> and K<sub>2</sub>MnFe(CN)<sub>6</sub>) have moderate energy density and are potentially low cost because of the use of inexpensive elements. For example, K<sub>2</sub>MnFe(CN)<sub>6</sub> shows a reversible capacity of ~150 mAh g<sup>-1</sup>, with an average potential of ~3.9 V (at equilibrium) and density of 2.19 g cm<sup>-3</sup>, resulting in a specific/volumetric energy density of ~580 Wh kg<sup>-1</sup>/~1300 Wh L<sup>-1</sup> [127]. However, most of the KIB cathode materials have lower energy density, poorer cycle life, and more severe side reactions with electrolytes than LIB cathodes [127,131,135]. The latter factors can cause a rapid fade in full cells, limiting their practicality.

In this study the cost advantage of KIBs compared to LIBs is examined by undertaking a cost analysis of every step of the battery manufacturing process. As a result of this analysis, battery lifetime was found to be crucial to the economics of KIBs.

## 2.2 Battery Cost Model

The analysis of battery capital cost, expressed as the unit cost of energy capacity, was conducted using the Battery Performance and Cost Model (BatPac, version 3.1) from Argonne National lab [38]. BatPac is a bottom-up cost model, which estimates the battery capital cost by accounting for every step in the battery manufacturing process. In this work, all battery pack models were designed to have an available energy of 50 kWh, which is competitive to four Tesla Powerwall® battery packs having a total usable energy of 54 kWh [142,143]. The maximum electrode coating thickness was 100  $\mu\text{m}$  for each coated side, since electrode coating thicknesses are typically restricted to be below 60  $\mu\text{m}$ , to minimize cracking and electrode delamination [144]. In addition, KIB electrode materials typically have a large volume change during K de/intercalation due to the large  $\text{K}^+$  ionic radius (graphite has a large volume expansion of ~60% upon potassiation, compared to only 10% upon lithiation) [123,133,134]. Thus, an ultra-thick K electrode (>100  $\mu\text{m}$ ) has a high risk of poor capacity retention during cycling. For new batteries, the usable percentage of maximum battery energy was considered 85%. Such restrictions on battery energy usage are commonly used by manufacturers to increase battery lifetime [145,146]. The capacity ratio of anode to cathode, the N/P ratio, was set to 1.1. This is a typical value for commercial Li-ion batteries, where the negative electrode has a designed excess capacity compared to the cathode. This limits the potential safety risk and accelerated aging caused by alkali metal plating at the anode if the cell were to become unbalanced during cycling [147]. It is assumed here that a similar N/P ratio would be required to avoid K plating in K-ion cells.

A model LIB consisting of  $\text{LiNi}_{0.6}\text{Mn}_{0.2}\text{Co}_{0.2}\text{O}_2$  (Li-NMC622) cathode and a graphite anode (on Cu foil) was selected as a reference system. In all KIB models, graphite with a reversible capacity of  $260 \text{ mAh g}^{-1}$  was used as the anode active material and Al was used as the anode current collector. The average potentials of KIB electrode materials were obtained from the literature, on the basis of the equilibrium state measured in half-cells, which was obtained from the mid-point between discharge and charge curves in the second cycle. This represents the best-case scenario, assuming that the potential hysteresis of KIB materials, which is generally larger than that of Li materials now [123], might be greatly narrowed in the future. For the same reason, the internal impedance of KIBs was regarded as the same as that of LIBs, despite KIB materials typically having a much larger impedance than those of LIBs (for example, it was found in this study that graphite electrodes have two orders of magnitude larger interfacial impedance in KIBs than in LIBs, as shown in Figure A.1). The specific capacity of KIB cathodes was also obtained from literature and the density of KIB materials was calculated on the basis of their crystal structures. The initial irreversible capacity of electrode materials, and any volume expansion during lithiation, both of which could reduce the usable battery energy significantly, were ignored, again to give the best-case scenario model for KIBs. More details of the battery parameters used can be found in the APPENDIX B.

One major difficulty in modelling the cost of KIBs is to provide a reasonable price of KIB cathodes and electrolytes. Thus, the price of cathodes was estimated within a range based on an estimated manufacturing cost and the cost of raw materials. The price of raw materials and the calculation of cathode price are detailed in the APPENDIX A. This led to the use of price ranges, to take into account errors in the estimate, rather than quoting exact prices. Where possible, a best-case price scenario was estimated based only on raw material cost. For example, raw material costs

of  $\text{K}_{0.6}\text{CoO}_2$  and  $\text{K}_{0.5}\text{MnO}_2$  (KIB candidate cathodes [137,139]) used in this work are  $\$19.86 \text{ kg}^{-1}$  and  $\$1.68 \text{ kg}^{-1}$ , respectively. An upper price bound was set by assuming a maximum  $\$5 \text{ kg}^{-1}$  manufacturing cost. Here,  $\text{K}_{0.6}\text{CoO}_2$  has a higher price due to the high cost of Co raw material. The price of more common materials could be obtained more accurately, for instance the Li-NMC622 price was set to  $\$17 \text{ kg}^{-1}$  [38]. KIB electrolyte was assumed to be the same price as LIB electrolyte. It is possible that KIB electrolyte may have a lower price than LIB electrolyte. However, the price difference between these two electrolytes would likely be small ( $<1.7\%$ ), if  $\text{Li}^+$  is simply exchanged for  $\text{K}^+$  in the electrolyte [128]. The same approach was used to estimate the costs from purchased items (cell hardware, module hardware, and battery jacket), supporting systems (battery and thermal management systems), and other costs (including direct labor summary, variable overhead, general, sales, administration, research and development, depreciation, profit, and warranty) for Li and K batteries. Although the use of emerging battery technology likely increases these costs, the assumptions used here were intended represent the lowest-cost scenario for KIBs. The currency used in this work is US dollars.

### 2.3 Results and Discussion

To explore whether KIBs have cost advantages over LIBs, a simple approximation is made here by theoretically modelling a fictional “K”-NMC622/graphite (KNMC/G) battery based on a Li-NMC622/graphite (LNMC/G) battery. In this model, elemental Li in the cathode exchanges with elemental K, but the capacity, the potential profile, the density, and even the molar mass of the cathode are assumed to be the same. The element exchange is only assumed to affect the cathode price. The Cu anode current collector is replaced with Al foil. Graphite capacity decreases from  $360 \text{ mAh g}^{-1}$  (*i.e.* the practical capacity of graphite in a Li-ion cell) to  $260 \text{ mAh g}^{-1}$  (*i.e.* the theoretical capacity of graphite potassiation to form  $\text{KC}_8$ ). It is also assumed that the cycling

performance and the safety of K-ion batteries are equivalent to Li-ion, which has not yet been demonstrated. These assumptions represent a best-case scenario model for a K-ion cell, especially since K-ion cells would almost certainly have lower volumetric energy density than Li-ion cells. Therefore, any practical K-ion cell would almost certainly have a lower energy density and higher cost than represented by this model. This method has also been applied to examine the cost benefit of NIBs over LIBs [128].

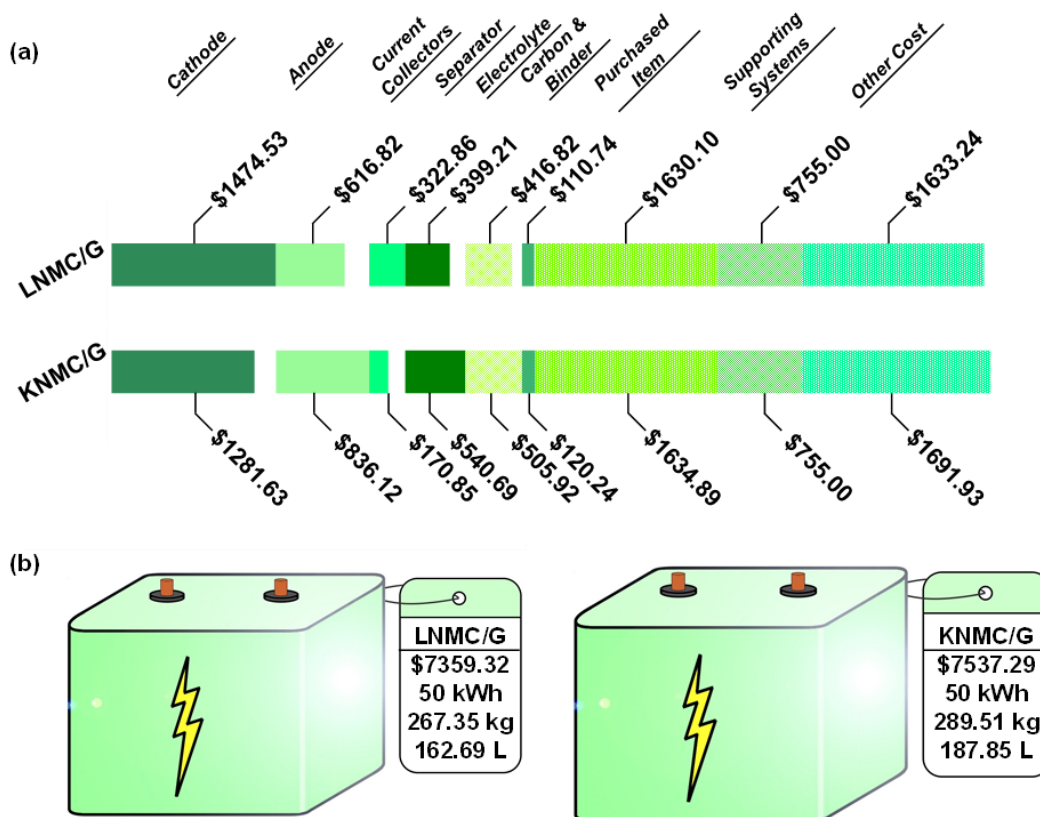


Figure 2.1 (a) Cost breakdown for LNM/G and KNM/G batteries. Purchased items include cell hardware, module hardware, and battery jacket. Supporting systems are battery and thermal management systems. Other costs include direct labor summary, variable overhead, general, sales, administration, research and development, depreciation, profit, and warranty. (b) Total cost, available energy, mass, and volume for the LNM/G and KNM/G batteries.

The cost reduction from exchanging Li for K was estimated on the basis of the cost difference between raw materials. The price of  $\text{Li}_2\text{CO}_3$  and  $\text{K}_2\text{CO}_3$  are  $\$6.5 \text{ kg}^{-1}$  [128] and  $\$0.8 \text{ kg}^{-1}$

<sup>1</sup> [148], respectively. The element exchange results in a price decrease of \$2.2 for 1 kg of K-NMC622 compared to Li-NMC622. To manufacture a 50-kWh LNMC/G battery, a total amount of 85.2 kg Li-NMC622 is required. The use of a corresponding K-NMC622 cathode material results in a cost decrease of \$187.44 per battery pack (as shown in Figure 2.1(a), the final reduction from the cathode is \$192.9 per battery pack; the extra reduction comes from the cost of the cathode production volume variance in the BatPac model, which is based on the difference between the actual and budgeted cathode production). This amount of reduction accounts for almost 2.6% of the cost of the LNMC/G battery (\$7,359.32).

Another cost advantage of KIBs is the use of Al foil for the anode current collector. This is permitted, since, unlike Li, K does not alloy with Al. In the BatPac model, the price of Al and Cu foil were set to \$0.3 m<sup>-2</sup> and \$1.2 m<sup>-2</sup>, respectively [38,128]. According to this model, in the Li-ion battery, 217.68 m<sup>2</sup> of Cu foil (for the anode) and 205.2 m<sup>2</sup> of Al foil (for the cathode) are used, corresponding to a \$322.86 total current collector cost per battery pack. In the K battery, larger current collector areas are needed: 292.32 m<sup>2</sup> and 277.2 m<sup>2</sup> for the anode and the cathode, respectively. This is because the lower volumetric capacity of graphite for K requires that more graphite be used in the K-ion cell to match the energy of the Li-ion cell. As a result, the KNMC/G battery has a cost advantage of only \$152.01 per pack over the LNMC/G battery from the current collectors.

In addition to the larger required amount of current collector, the BatPac model shows that the KNMC/G battery also requires larger amounts of anode, separator, electrolyte, and graphite and binder, compared to the corresponding Li battery. This is due to the lower volumetric capacity of graphite for KIBs [133]. For example, each KNMC/G battery pack requires 66.96 kg of graphite, 491.51 m<sup>2</sup> of separator, and 33.84 L of electrolyte. In comparison, the LNMC/G battery requires

only 48.6 kg, 362.88 m<sup>2</sup>, and 27.84 L, of the same components respectively. Figure 2.1(a) shows the cost of the anode, separator, and electrolyte in these two batteries. Compared to the corresponding Li battery, each KNMC/G battery pack requires an additional \$219.30, \$141.48, and \$89.10 cost for the anode, separator, and electrolyte, respectively. As a result, the KNMC/G battery pack has a total cost of \$7,537.29, which is \$177.97 more than the LNMC/G battery pack (Figure 2.1(b)). In addition, the KNMC/G battery pack is 15% larger in volume and 8% more in weight, compared to the LNMC/G battery pack of the same energy. More details of battery costs can be found in APPENDIX B. According to this analysis, the cost of Li<sub>2</sub>CO<sub>3</sub> would have to reach \$11.5 kg<sup>-1</sup> (*i.e.* almost double the current price), in order for the Li-ion battery to reach cost parity.

A cost analysis of KIBs was also made based on currently known K-ion cathode materials. The widely investigated K-ion cathode materials included in this analysis can be divided into three groups: hexacyanometalates, layered oxides, and polyanionic compounds [123,131]. It is difficult to have the actual cost of these materials, which are not widely available in the market for batteries. Therefore, Figure 2.2 shows the estimated battery capital cost calculated using the BatPac model when these materials are used as the cathode and graphite is the anode plotted as a function of the cathode price. The cost of a Li-NMC622 vs. graphite Li-ion battery is also shown for comparison. Where possible, KIB cathode raw material costs are shown, which represent a best-case KIB cathode price scenario. An upper price bound was set by assuming a maximum \$5 kg<sup>-1</sup> manufacturing cost. The K-ion battery capital cost rises linearly with the cathode price. The type of cathode has a great influence on the total battery cost. Compared to the other cathodes, the K<sub>2</sub>MnFe(CN)<sub>6</sub> cathode results in a relatively lower capital cost. This low capital cost is a result of the high capacity (~150 mAh g<sup>-1</sup>) and the high average potential (~3.9 V) of K<sub>2</sub>MnFe(CN)<sub>6</sub>. Nevertheless, the cost of all these K-ion batteries is higher than the Li-ion reference battery, even

though the K-ion model is based on best case theoretical capacities, while the Li-ion model is based on practical capacities. More details of these models can be found in APPENDIX B and Figure A.2.

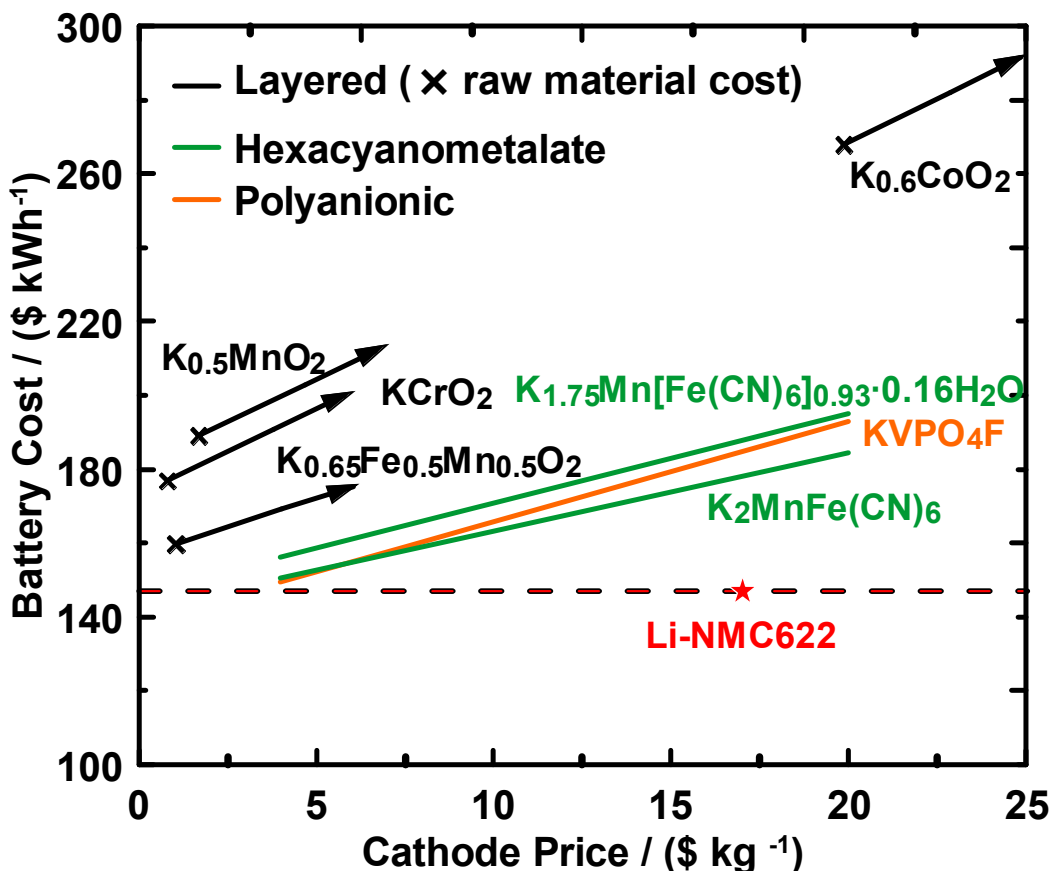


Figure 2.2 A summary of the capital cost of KIBs with selected cathode active materials (coupled with the graphite anode [133]). Cathode prices were estimated with a range. The capital cost of a LIB with Li-NMC622 as cathode (its price was set to \$17 kg<sup>-1</sup>) is presented as reference (red dashed line). Selected K cathodes are divided into three groups: hexacyanometalates (green), *i.e.* K<sub>2</sub>MnFe(CN)<sub>6</sub> [127] and K<sub>1.75</sub>Mn[Fe(CN)<sub>6</sub>]<sub>0.93</sub>·H<sub>2</sub>O [140]; layered oxides (black), *i.e.* K<sub>0.5</sub>MnO<sub>2</sub> [137], KCrO<sub>2</sub> [138], K<sub>0.6</sub>CoO<sub>2</sub> [139], and K<sub>0.65</sub>Fe<sub>0.5</sub>Mn<sub>0.5</sub>O<sub>2</sub>[136]; polyanionic compounds (orange), *i.e.* KVPO<sub>4</sub>F [141]. Where known, raw material costs are shown as a best-case price scenario.

Our results above indicate that all K-ion batteries considered have a higher capital cost than the reference Li-ion battery, due to the use of low energy density electrodes. However, many

researchers have stressed the battery cycle life needs to be considered as one of the most important features for the energy storage [124,128,149–152]. The battery capital cost over cycle life has been recommended as the key factor for cost promise evaluation [3]. This consideration should be true since many strong competitors for energy storage, such as pumped hydro storage and compressed air energy storage, can be operated over decades [3,153]. In addition, LIBs using low-energy-density electrode materials, such as  $\text{Li}_4\text{Ti}_5\text{O}_{12}$  as anode and  $\text{LiFePO}_4$  as cathode, have attracted intensive attentions for energy storage applications, mainly due to their long cycle life [3,154,155].

To illustrate the impact of battery lifetime on cost, the annualized battery capital cost is used, with an expression of the battery capital cost over battery lifetime (unit:  $\text{\$ kWh}^{-1} \text{ year}^{-1}$ ). Details of the calculation can be found in APPENDIX A. This annualized cost is practical for cost evaluation since many energy storage stations, such as the Tesla Powerwall®, have been often designed with a certain service life [143,156,157]. The annualized cost is also convenient for making comparisons with related energy storage and harvest technologies that widely use annualized cost for economic evaluation [158–162].

Up-to-date commercial LIBs can complete 1000 cycles with 80% capacity retention [146,163,164]. Although the battery lifetime is strongly associated with cycling conditions [156,165,166], a simple scenario is assumed here that these LIBs have a service life of 2.74 years, *i.e.* one cycle per day. This magnitude of the longevity has been wide used as a baseline for battery research [23,164], and is more appropriate for commercial applications. Batteries for automotive and grid storage applications have much longer lifetimes. Nevertheless, the main conclusions of this study become even more pronounced as the lifetime is extended. Based on a 2.74 year service life, the annualized capital cost of the Li reference battery is estimated to be  $\text{\$59.69 kWh}^{-1} \text{ year}^{-1}$ . The corresponding values for KIBs with various cycle lives, *i.e.* 200, 750, 1000, and 1500, were

investigated, although commercial KIBs with non-aqueous electrolytes have not yet been reported. Four KIB fictional cathodes, labeled A-D were used, having energy densities as follows: A: a low energy density KIB cathode typical of current prototype materials, B: a moderate energy density KIB cathode, having the theoretically highest energy density that could be achieved with the best prototype KIB cathode materials, C: a high energy density KIB cathode with similar energy density as high-performance LIB cathodes, and D: a ultra-high energy density KIB cathode having superior energy density than high-performance LIB cathodes. Detailed characteristics of these cathodes are described in Table 2.1.

Table 2.1 Cathode materials used to compare current LIB with potential KIB technologies.

Cathode	Description	$V_{avg}$ (V)	Q (mAh g <sup>-1</sup> )	$\rho$ (g cm <sup>-3</sup> )	E (Wh kg <sup>-1</sup> )	E (Wh L <sup>-1</sup> )
Li-NMC622	LIB reference	3.85	180	4.65	693	3222
Cathode A	Low energy density KIB cathode with characteristics typical of current prototype materials.	3	100	2.5	300	750
Cathode B	KIB cathode with specific/volumetric energy density, (slightly) higher than that of the best current prototype materials, such as K <sub>2</sub> MnFe(CN) <sub>6</sub> [127] and KVPO <sub>4</sub> F [141].	4	150	3	600	1800
Cathode C	High energy density KIB cathode with significantly higher characteristics than that of current prototype materials (competitive with advanced LIB cathodes in energy density).	4.5	170	4.5	765	3443
Cathode D	Fictional ultra-high energy density KIB cathode (very difficult to be prototyped even under a long-term development).	5	200	5	1000	5000

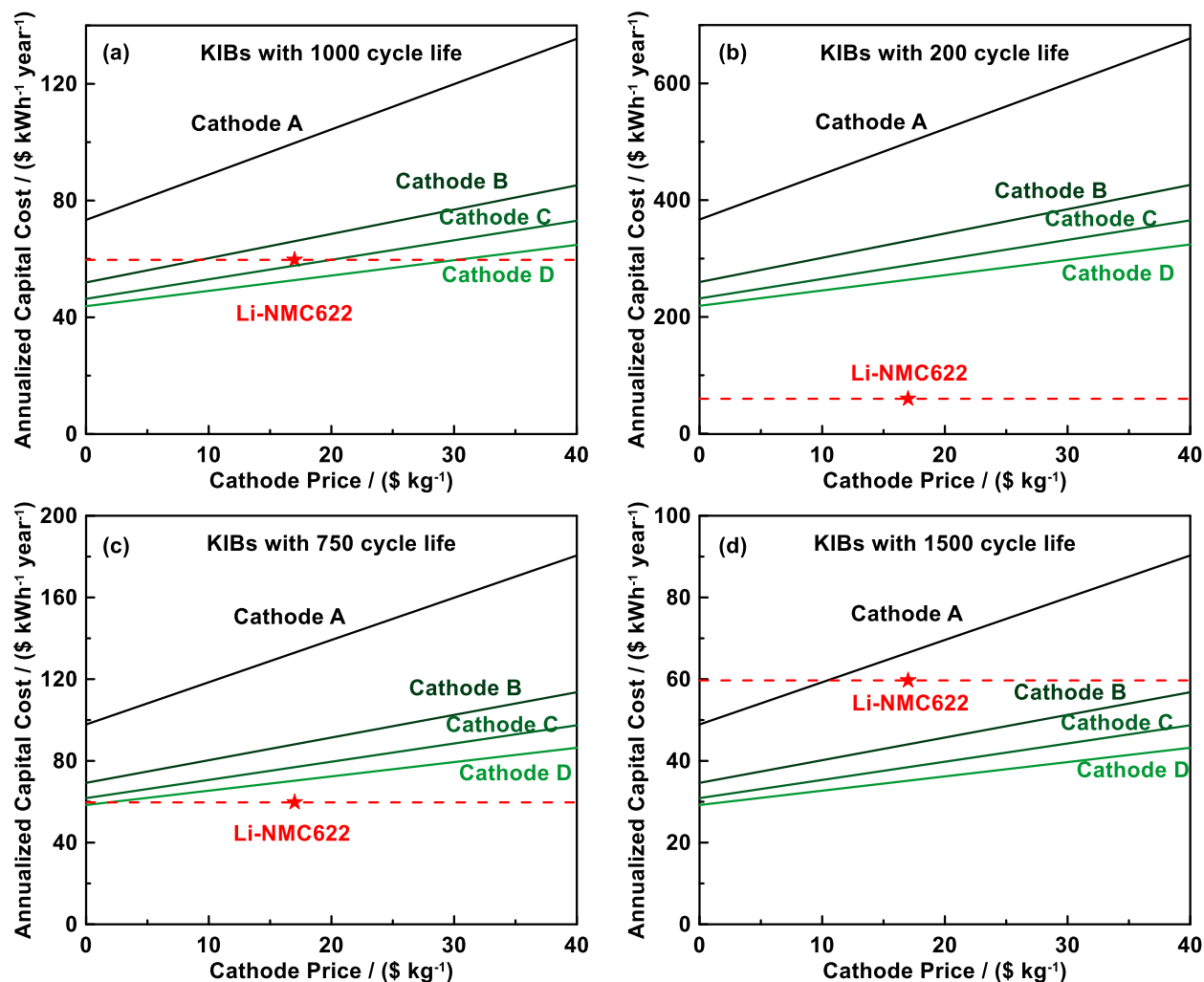


Figure 2.3 Effect of the KIB cycle life on annualized capital cost: (a) 1000 cycles, (b) 200 cycles, (c) 750 cycles, and (d) 1500 cycles. Four fictional cathodes (cycling potential at 50% state of charge, reversible capacity, density) were selected for exploring this effect: Cathode A (3 V, 100  $\text{mAh g}^{-1}$ ,  $2.5 \text{ g cm}^{-3}$ ), Cathode B (4 V, 150  $\text{mAh g}^{-1}$ ,  $3 \text{ g cm}^{-3}$ ), Cathode C (4.5 V, 170  $\text{mAh g}^{-1}$ ,  $4.5 \text{ g cm}^{-3}$ ), and Cathode D (5 V, 200  $\text{mAh g}^{-1}$ ,  $5 \text{ g cm}^{-3}$ ). Cathode prices were given with a range. The LNMC/G battery with a cycle life of 1000 was used as reference.

Figure 2.3 shows the annualized capital cost of KIBs that have the same cycle life as the Li reference battery. The KIB with low-energy-density Cathode A has a higher annualized capital cost than the Li reference battery regardless of cathode price. Using ultra-high-energy-density Cathode D, the KIB can have an annualized cost benefit compared to the Li battery, when the

cathode price is below \$30.26 kg<sup>-1</sup>. This trend agrees with the results above that the use of high-energy-density electrodes can decrease battery cost, if good cycle life is maintained.

After a thorough search of the relevant literature, up-to-date non-aqueous KIBs typically have a poor cycle life (<200 cycles) when examined under proper test conditions, including relatively slow discharge/charge rates ( $\leq 1C$ ) [139,140,167–169]. Among these KIB prototypes, one of the best cyclabilities has been achieved with a graphite/K<sub>2</sub>MnFe(CN)<sub>6</sub> full cell with 7 mol kg<sup>-1</sup> potassium bis(fluorosulfonyl)amide in 1,2-dimethoxyethane as electrolyte [167]. However, this full cell had linear capacity fade at a cycling rate of 1C and only 85% capacity retention after 101 cycles. Figure 2.3(b) shows the annualized capital cost of KIBs that have a cycle life of 85% retention at 200 cycles. The lowest annualized capital cost among these KIBs is \$324.04 kWh<sup>-1</sup> year<sup>-1</sup>, which is more than five times as that of the Li reference battery. Even if the battery cycle life is improved to 750 cycles, these KIBs still have little benefit on the annualized cost, as shown in Figure 2.3(c). Figure 2.3(d) shows that a significant cost benefit could be achieved in KIBs that have a 1500 cycle cycle-life. For example, a KIB even using the low energy density Cathode A can have a lower annualized capital cost than the Li reference battery if its price is below \$10.43 kg<sup>-1</sup>.

A key conclusion of the above analysis is that achieving good cycle life is essential in lowering battery cost. Thus far, cycle life has proven to be a major issue for KIBs. An unavoidable challenge for nonaqueous KIBs is the suppression of continuous irreversible capacity at the graphite anode. This irreversible capacity is mainly caused by electrolyte decomposition [13]. Results of measurements from this study show that the highest steady CE for reversible K-intercalation could be achieved with graphite anodes in different K-electrolytes is 99.2% while 99.8% could be achieved for Li-intercalation, using an electrolyte with no special additives (shown

in Figure A.3). Future KIB research should focus on the development of an optimized electrolyte/graphite system. Such optimized systems will need to exceed the 99.9+% CE achieved in today's commercial LIBs in order for KIBs to reduce battery costs.

Although KIB technology is greatly unexplored and future work is likely to result in improvements in cycle life and energy density, it is well to keep in mind that LIBs are also continually improving. For example, recent research reported that Li-ion cells with  $\text{LiNi}_{0.5}\text{Mn}_{0.3}\text{Co}_{0.2}\text{O}_2$ /artificial graphite could have only ~4% capacity fade after 4000 cycles with a C/3 rate at 20 °C [156]. This advanced LIB prototype provides a promising future for LIBs in the applications of energy storage systems, which pushes the bar even higher for KIBs. The main driver for KIBs is that they may be manufactured using only highly abundant resources, like K, which are likely to remain low cost far into the future, while LIBs are made from less abundant materials. However, such considerations do not affect the outcome of the model in terms of the battery cost. Concerns about LIB costs are mainly related to the potential for cost increases in Li and Co resources. However, much progress has been made in the design of Li cathodes with only a small amount of Co or even without Co [170]. Therefore, the main resource concern for LIBs is the potential price increase in Li resources. However, potential impacts of Li raw material price increases are often overstated, since the amount of active Li in a LIB is small. For instance, if the Li raw material price is doubled the LIB cost estimated by the model would increase by only 3%, which would have no impact on the conclusions of this study. Indeed, a previous study has demonstrated that even more extreme increases in lithium cost (from  $\$7.5 \text{ kg}^{-1}$  to  $\$25 \text{ kg}^{-1}$ ) would result in small increases (<10%) in total battery cost [171]. Moreover, LIB prices have actually followed a decreased trend in recent years, from  $\sim\$1000 \text{ kWh}^{-1}$  in 2010 to  $\sim\$200 \text{ kWh}^{-1}$  in 2016, and to an estimated price of  $\$124 \text{ kWh}^{-1}$  in 2030, mainly driven by manufacturing optimization

[172]. Such considerations make achieving long cycle life in KIB even more necessary for demonstrating their practicality. It should also be mentioned that additional factors, such as safety, that have not been fully explored may also be key to KIB commercialization.

Na-ion batteries have been considered as alternative options for energy storage. Based on the Reference [9], a hard carbon/ $\beta$ -NaMnO<sub>2</sub> sodium-ion battery can cost 20 % more than Li-NMC 622/G LIBs. The KIBs with KVPO<sub>4</sub>F cathode can have a lower capital cost than the sodium-ion battery by 15%. However, prototyped sodium-ion batteries can achieve at least 300 cycles with 80% capacity retention [173]. Therefore, it is even difficult for current KIB prototypes, with the a cycle life of <200, are even difficult to compete the with sodium-ion batteries with regard to theon an annualized capital cost basis.

Many other alternative options for electrochemical energy storage have been proposed, such as Mg-ion, Al-ion, Zn-ion, and Ca-ion rechargeable batteries [174]. These post-LIBs could have some potential benefits to compete with LIBs in the battery capital cost, including higher energy density and lower cost in electrode materials. However, considering the dominance of cycle life in determining cost demonstrated in this study, the same outcome would likely result for these other chemistries: *i.e.* any cost improvement over LIBs must be accompanied by an improvement in battery lifetime.

## 2.4 Conclusions

A cost analysis on KIBs has been conducted on the basis of the BatPac model. A LNMC/G battery, consisting of a Li-NMC622 cathode and a graphite anode, was selected as the reference battery and compared to a fictional high energy density “K”-NMC622/graphite (KNMC/G) battery. Cost reductions in cathode and current collectors could be achieved by utilizing KIBs instead of LIBs. However, due to the relatively low energy density of graphite in KIBs, the total cost of the

KNMC/G battery was found to actually increase by 2.4%, mainly caused by material increases in anode, electrolyte, carbon, binder, and separator. Further analysis with different cathode models shows that achieving superior cycle life to LIBs is essential for KIB technology to have reduced cost. This is true even of the typical low-energy density KIB prototype materials of today: *i.e.* reduced cost can be achieved with these materials, if their cycle life is improved. These results demonstrate that the promise of KIBs as a low-cost alternative to LIBs can be significantly improved if ultra-long cycle life is achieved. This study furthermore demonstrates the importance of cell lifetime in all battery chemistries, including LIBs, in reducing cell cost. A study of battery degradation mechanisms that can reduce lifetime represents the focus of the remainder of this thesis.

## CHAPTER 3 EXPERIMENTAL TECHNIQUES

### 3.1 Cell Construction

#### 3.1.1 Half Cells

Half-cell construction was conducted in an Ar-filled glovebox using standard 2325 coin cell hardware. Half-cells comprised a working electrode and a Li metal counter/reference electrode. The electrodes were separated by microporous polypropylene/polyethylene separator(s), as shown in Figure 3.1(a). Working electrode disks were punched from electrode coatings using a 1.35 cm<sup>2</sup> area circular punch. Lithium metal electrode disks (2.57 cm<sup>2</sup> in area) were punched from Li-metal foil (thickness of 0.38 mm, Aldrich, 99.9%). Two layers of microporous polypropylene (Celgard-2300) with one layer of polyethylene blown microfiber (BMF, 3M Company) were used as cell separators. Electrolyte was added before coin cells were sealed.

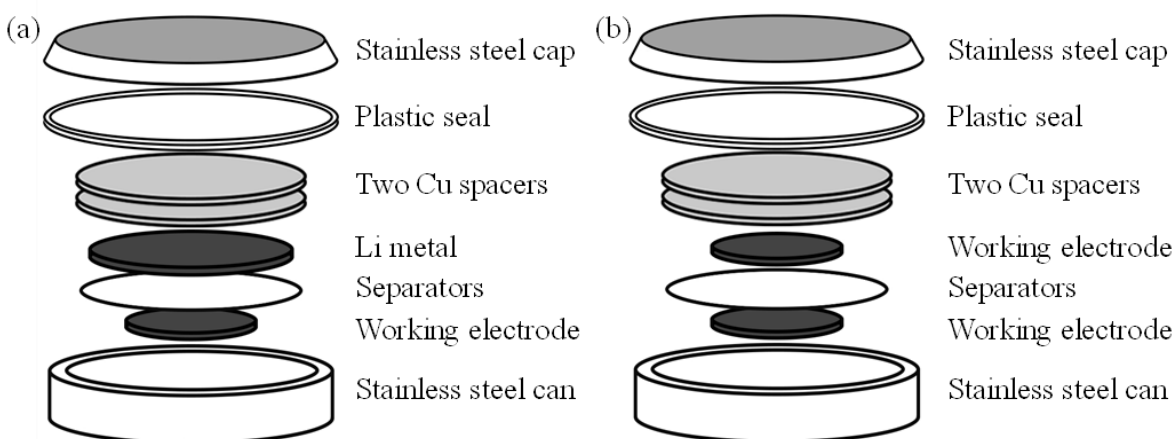


Figure 3.1 Exploded view of (a) a coin-type half cell and (b) a coin-type conventional symmetric cell.

### 3.1.2 Conventional Symmetric Cells

Conventional symmetric cell construction was also conducted in an Ar-filled glovebox using standard 2325 coin cell hardware. For each conventional symmetric cell, two identical working electrodes, one pre-lithiated and the other pre-delithiated (*i.e.* one lithiation and then one delithiation half-cycle) in half cells, were used. To avoid the lithium plating, the mass of the lithiated electrode was always chosen to be slightly less than (~0.02 mg) that of the paired delithiated electrode in each conventional symmetric cell. The two electrodes were carefully aligned to minimize misalignment. Conventional symmetric cells have very similar structure to the half cells, except the use of two working electrodes, as shown in Figure 3.1(b). During symmetric cell cycling, active Li is removed from one working electrode and inserted into the other working electrode during each cycle.

### 3.1.3 Double Half-cells

DHCs were constructed by first constructing two half-cells with identical working electrodes, one pre-lithiated and the other pre-delithiated, as in the case of symmetric cells. The cells were then connected in series via their lithium metal terminals, as shown in Figure 3.2(a). During DHC cycling, active Li is removed from one working electrode while active Li inserts into the other working electrode. Thus, DHCs share a similar working principle to conventional symmetric cells during cycling. For this reason, DHCs are considered as a new type of symmetric cell. Compared to conventional symmetric cells, the use of DHCs avoids the complicated assembly process and electrode alignment issue, which may cause inaccurate measurement in capacity fade. The use of compliant Li foil as the counter electrode also aids in maintaining uniform stack pressure.

### 3.1.4 Quasi-three-electrode Double Half-cells

Quasi-three-electrode double half-cells (QDHCs) were designed to understand the capacity fade of electrodes in symmetric cells. As shown in Figure 3.2(b), QDHCs have the same structure as DHCs, except voltage sense leads are connected to monitor the potential between the Li metal terminals and one working electrode. In this thesis, the pre-delithiated electrodes were chosen to connect the additional voltmeter. Voltage sense leads from Maccor 4000 charger channels (input impedance =  $10^{12} \Omega$ ) were used as these voltmeters. Current leakage through the additional voltage sense leads, though small, was nevertheless large enough to noticeably impact cycle life. Therefore, such cells were principally used for understanding individual electrode behavior in symmetric cells and not for quantitative coulometric studies.

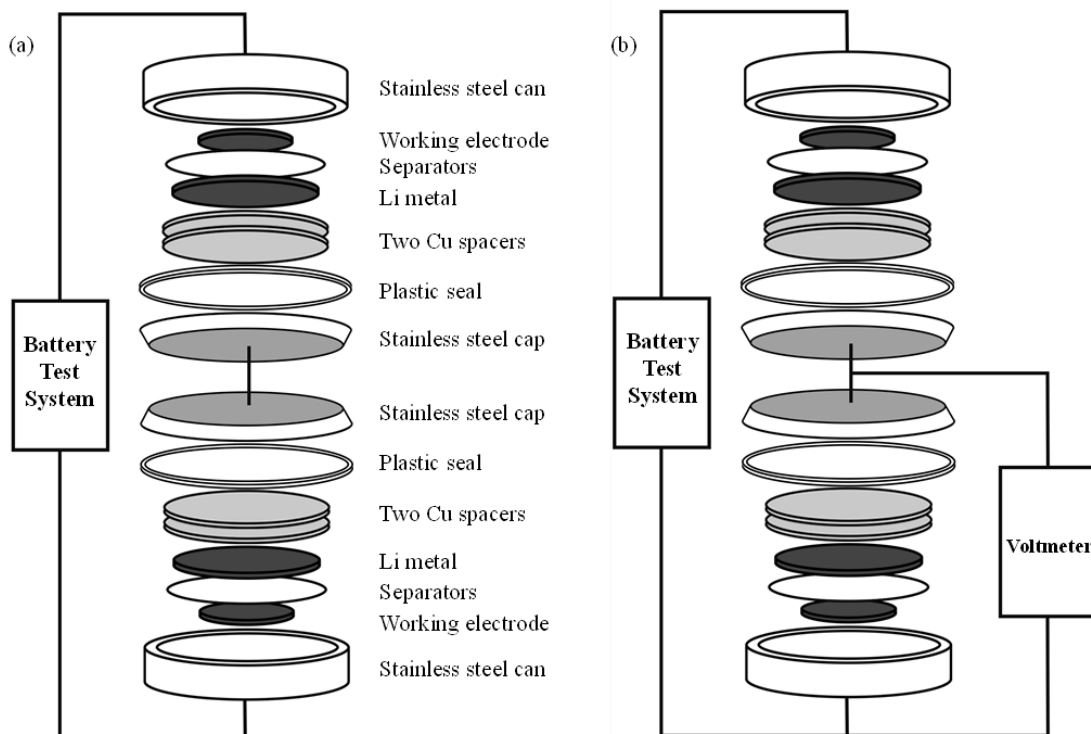


Figure 3.2 Exploded view of (a) a double half-cell with a connection to the battery test system and (b) a quasi-three-electrode double half-cell with a connection to the battery test system and an extra voltmeter.

## 3.2 Electrochemical Measurements

### 3.2.1 Cycling Tests

Cells were tested by charging and discharging with a constant current until the upper cut-off potential or lower cut-off potential was reached. In some cases, a constant potential hold was applied after the cells reached the cut-off potentials, to minimize the impact of increased impedance on measured capacity and to simulate cycling protocols used in practical cells (*i.e.* "CCCV" cycling). During this step, cells were held at the cut-off potential until the applied current dropped below a certain value, which will be specified in each chapter. The term, C rate, refers to the current required to fully charge or discharge a cell in one hour. Accordingly, a C/5 rate refers to the current required to fully charge or discharge a cell in five hours.

### 3.2.2 Electrochemical Impedance Spectroscopy

EIS measurements were conducted by applying a small perturbing alternating voltage signal,  $V(\omega, t)$ , with various frequencies to electrochemical cells and recording the current response,  $I(\omega, t)$ . The impedance of a cell,  $Z(\omega)$ , at each frequency,  $\omega$ , is calculated as the ratio of  $V(\omega, t)$  and  $I(\omega, t)$  [175]:

$$Z(\omega) = \frac{V(\omega, t)}{I(\omega, t)} = \frac{|V| \sin(\omega t)}{|I| \sin(\omega t + \varphi)} \quad (3.1)$$

where  $|V|$  and  $|I|$  are the peak voltage and peak current, respectively,  $\varphi$  is the phase shift between the current response and the alternating voltage, and  $t$  is the time.

For convenience, the impedance is typically expressed in terms of complex numbers. This transformation can be realized using Euler's formula:

$$e^{ix} = \cos x + j \sin x \quad (3.2)$$

where  $j^2 = -1$ .

Three basic circuit elements are widely used to model EIS results: resistors, capacitors, and inductors. These elements have different responses to the input signals. The current response of a resistor to an alternating voltage input is given by:

$$I(\omega, t) = \frac{V(\omega, t)}{R} \quad (3.3)$$

where  $R$  is the resistance of the resistor.

The complex impedance expression of the resistor,  $Z_{Resistor}(\omega)$ , is given by:

$$Z_{Resistor}(\omega) = \frac{V(\omega, t)}{I(\omega, t)} = R \quad (3.4)$$

The current response of pure capacitor to alternating voltage input is given by:

$$I(\omega, t) = \frac{dQ}{dt} = \frac{d(CV)}{dt} = \frac{d}{dt} C|V| \sin(\omega t) = C|V|\omega \cos(\omega t) \quad (3.5)$$

where  $C$  is the capacitance of the capacitor.

The complex impedance expression of the capacitor,  $Z_{Capacitor}(\omega)$ , is given by:

$$Z_{Capacitor}(\omega) = \frac{V(\omega, t)}{I(\omega, t)} = \frac{|V| \cos\left(\omega t - \frac{\pi}{2}\right)}{C|V|\omega \cos(\omega t)} = \frac{|V|e^{i\omega t} e^{-\frac{j\pi}{2}}}{C|V|\omega e^{i\omega t}} = \frac{-j}{C\omega} = \frac{1}{jC\omega} \quad (3.6)$$

The current response of pure inductor to alternating voltage input is given by:

$$I(\omega, t) = \int \frac{V(\omega, t)}{L} dt = \int \frac{|V| \sin(\omega t)}{L} dt = -\frac{|V|}{\omega L} \cos(\omega t) \quad (3.7)$$

where  $L$  is the inductance.

The complex impedance expression of an inductor,  $Z_{Inductor}(\omega)$ , is given by:

$$Z_{Inductor}(\omega) = \frac{V(\omega, t)}{I(\omega, t)} = \frac{|V| \cos\left(\omega t - \frac{\pi}{2}\right)}{-|V| \cos(\omega t)/\omega L} = -\omega L \frac{e^{j\omega t} e^{-\frac{j\pi}{2}}}{e^{j\omega t}} = j\omega L \quad (3.8)$$

In electrical circuits, elements are connected either in series or in parallel. The total impedance,  $Z_{total}$ , of two circuit elements, A and B, in series is:

$$Z_{total} = Z_{e(A)} + Z_{e(B)} \quad (3.9)$$

where  $Z_{e(A)}$  and  $Z_{e(B)}$  are the impedance of the element A and B, respectively.

The total impedance of element A and B in parallel is:

$$Z_{total} = (Z_{e(A)}^{-1} + Z_{e(B)}^{-1})^{-1} \quad (3.10)$$

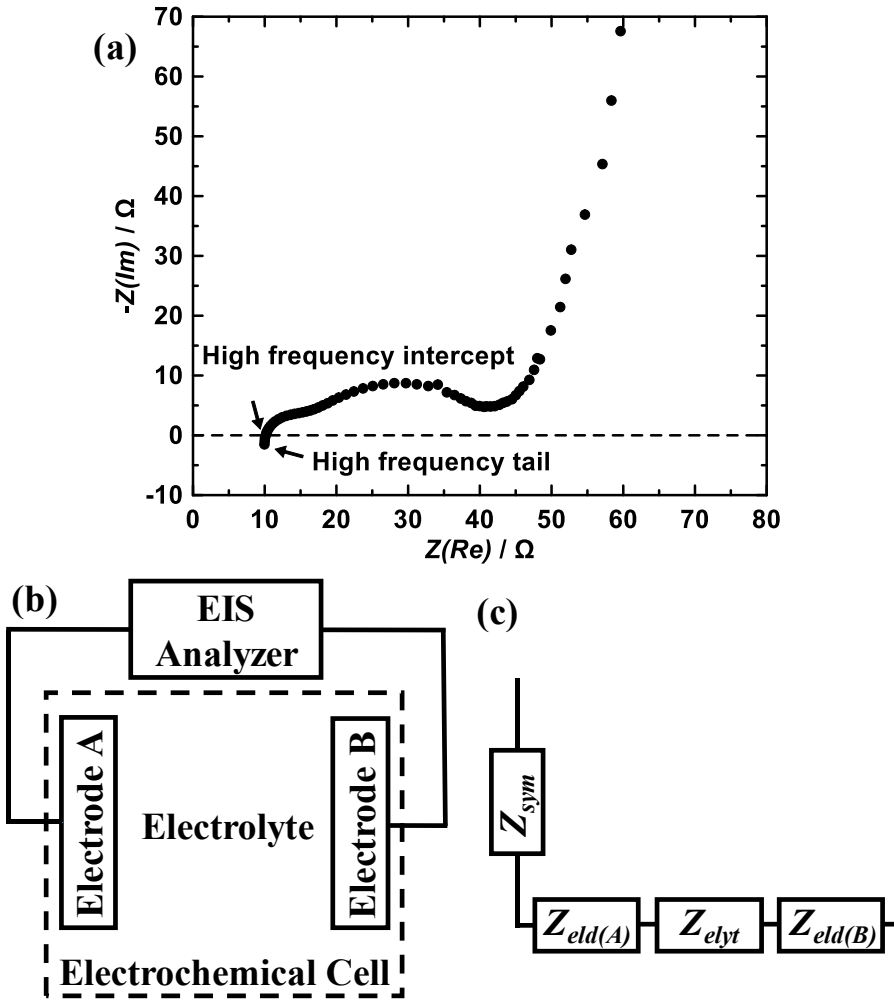


Figure 3.3(a) A representative Nyquist plot, obtained from the EIS. (b) An illustration of the connection between the EIS analyzer and electrochemical cell. (c) An equivalent circuit used to describe (b).

EIS spectra are often represented as Nyquist plots [175,176], sometimes called Cole-Cole plots, in which the negative imaginary part of the impedance is plotted as a function of the real part of the impedance, as shown in Figure 3.3(a). Each data point represents the imaginary part

and the real part of the impedance at one frequency. In Nyquist plots, data points measured at higher frequencies are typically located towards lower values of the real axis.

Figure 3.3(b) illustrates the connection between the EIS analyzer and an electrochemical cell. This connection can be described as the equivalent circuit shown in Figure 3.3(c). The measured impedance of an electrochemical cell described by this equivalent circuit can be expressed as:

$$Z_{total} = Z_{eld(A)} + Z_{elyt} + Z_{eld(B)} + Z_{EIS-sym} \quad (3.11)$$

where  $Z_{eld(A)}$  and  $Z_{eld(B)}$  are the impedance of electrode A and electrode B in the cell, respectively,  $Z_{elyt}$  is the electrolyte impedance, and  $Z_{EIS-sym}$  is the EIS system impedance (*i.e.* cable impedance, the impedance from the EIS analyzer, and the impedance from experimental setup).

Under alternating voltage perturbation, liquid electrolytes are widely recognized as having the behavior of a pure resistor [177]. The system impedance is considered as a combination of resistor(s) and inductor(s). In Nyquist plots,  $Z_{EIS-sym}$  and  $Z_{elyt}$  contribute to the presence of high frequency tail and the shift of the high frequency intercept at the real axis, as shown in Figure 3.3(a). Considering that this research is focused on the electrode impedance, the measured EIS spectra in this report were shifted along with the real axis so that the high frequency intercept is located at  $0 \Omega$  or  $0 \Omega \text{ cm}^2$ . This process excludes the electrolyte impedance and the system impedance (such as the impedance from test leads) from the measured impedance. As a result, this corrected impedance,  $Z_{cor}$ , is expressed as:

$$Z_{cor} = Z_{eld(A)} + Z_{eld(B)} \quad (3.12)$$

If the research focusses on the study of  $Z_{eld(A)}$ , the impedance from electrode B needs to be excluded. However, this exclusion is difficult to achieve, since the  $Z_{eld(B)}$  is typically unknown.

One alternative approach to obtain  $Z_{eld(A)}$  is the use of another identical electrode A to replace electrode B. Under this circumstance, the  $Z_{cor}$  can be expressed as:

$$Z_{cor} = Z_{eld(A)} + Z_{eld(A)} = 2Z_{eld(A)} \quad (3.13)$$

On the basis of Equation 3.12, the use of a conventional symmetric cell for impedance measurement avoids the interference from the counter electrode.

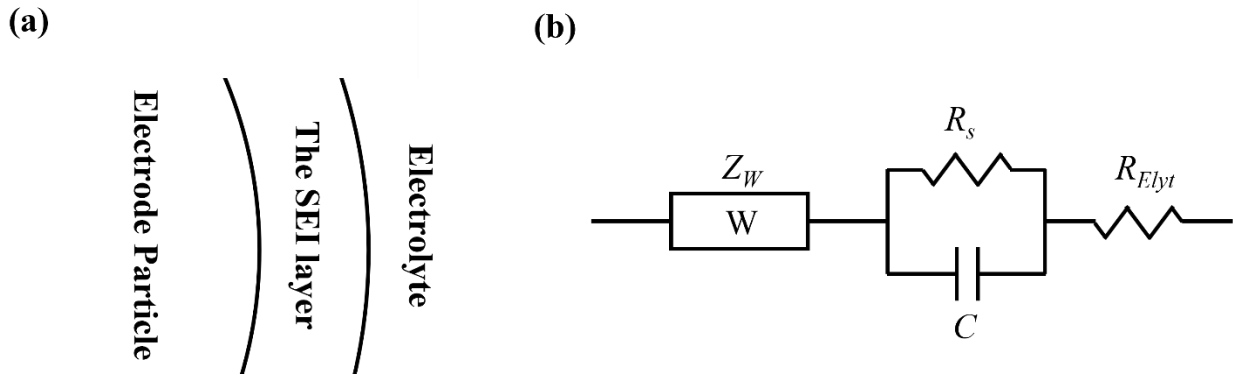


Figure 3.4 (a) A schematic shows an electrode particle, the SEI layer, and the electrolyte. (b) An equivalent circuit used to describe (a).  $Z_w$ ,  $R_s$ ,  $C$ , and  $R_{Elyt}$  represent Warburg impedance, the resistance at the electrode/electrolyte interface, the capacitance at the electrode/electrolyte interface, and the electrolyte resistance, respectively.

To describe an electrochemical system, one simplified consideration is often used, called “one-particle model”. As demonstrated in Figure 3.4, this model involves one single active particle, the SEI layer on the particle surface, and the electrolyte [177]. The impedance of the active particle is generally described as Warburg impedance. Warburg impedance will not be further discussed here since it is beyond the scope of this thesis. The SEI layer is often described as a resistor and a capacitor in parallel. The electrolyte is considered as an ionic resistor. Overall, the equivalent circuit of this model is presented in Figure 3.4(b). However, concerns have been raised regarding the use of this model for EIS analysis because its description of electrochemical systems is

oversimplified [103]. Therefore, more complex models are necessary to interpret real electrochemical systems.

### **3.3 Scanning Electron Microscope**

A SEM produces images of the morphology of samples via focused beams of electrons. SEM can achieve a high resolution below one nanometer, while the resolution of a light microscope is limited to only micrometers. The resolution of SEM depends on the spot size of the electron beam, in which diameters measured in nanometers can be attained.

In SEM, an electron source is required to provide electrons for imaging. A tungsten filament or field-emission tip is generally used as the electron source. An accelerating potential (typically 30 kV) is applied to the generated electron beam. Several strong magnetic fields are used as lenses to refine the electron beam.

When the accelerated electrons are incident upon a sample, two types of interactions between the incident electrons and the atoms of the sample occur: elastic scattering and inelastic scattering. Elastic scattering is related to the interactions between the incident electrons and the atomic nucleus. In the elastic scattering process, almost no energy is transferred to the atom. Inelastic scattering refers to the interaction between the incident electrons and the atomic electrons. In the inelastic scattering process, the incident electrons lose a certain amount of energy, which is transferred to the atom.

Some electrons are emitted from a sample after incident electrons are scattered. The emitted electrons consist of secondary electrons, backscattered electrons, and Auger electrons. In addition, X-rays can be produced during inelastic scattering processes. The emitted X-rays can be detected by an energy dispersive spectrometer and used to analyze the elemental composition of samples.

Secondary electrons are generated from the inelastic scattering process. The outer-shell electrons of atoms are weakly bound to the nucleus. These electrons can be ejected by the incidence of the accelerated electrons. One of the most important features of secondary electrons is their depth penetration which is only less than 2 nm below the sample surface. The generated secondary electrons reveal properties of the surface structure. Thus, secondary-electron images are widely used for the study of the morphology of a specimen.

Some incident electrons are scattered by the interaction with the atomic nucleus, which results from elastic scattering processes. The emitted electrons, called “backscattered electrons”, lose only a small amount of the energy during the interaction. Among all emitted electrons, backscattered electrons can be distinguished by their high kinetic energy. The generation of backscattered electrons is strongly sensitive to the atomic mass of the nucleus. Heavier elements can eject backscattered electrons more efficiently than lighter elements. Therefore, backscattered-electron images can reveal information about the chemical composition of a specimen.

### **3.4 Ion Milling**

Cross-sectioned specimens were prepared via ion milling (JEOL IB-19530CP cross section polisher). The operating principle is shown in Figure 3.5. Generated Ar ions are accelerated from the ion source to the specimen. The part of the specimen under the protection of a shield remains intact while the other part is etched under the exposure of the ion beam. As a result, a cross section of the specimen forms below the edge of the shield.

Each sample for ion milling was processed with a high potential (6.0 kV) for rapid cutting 80 minutes, and then a fine mode (4.0 kV) for 5 minutes in order to obtain high-quality cross-sectioned samples, with an Ar flow rate setting of 5.0 (no unit number) while the operating pressure

was maintained below 0.005 Pa. During ion milling, the ion beam was in a fixed position while the specimen was shifted to adjust the milling position.

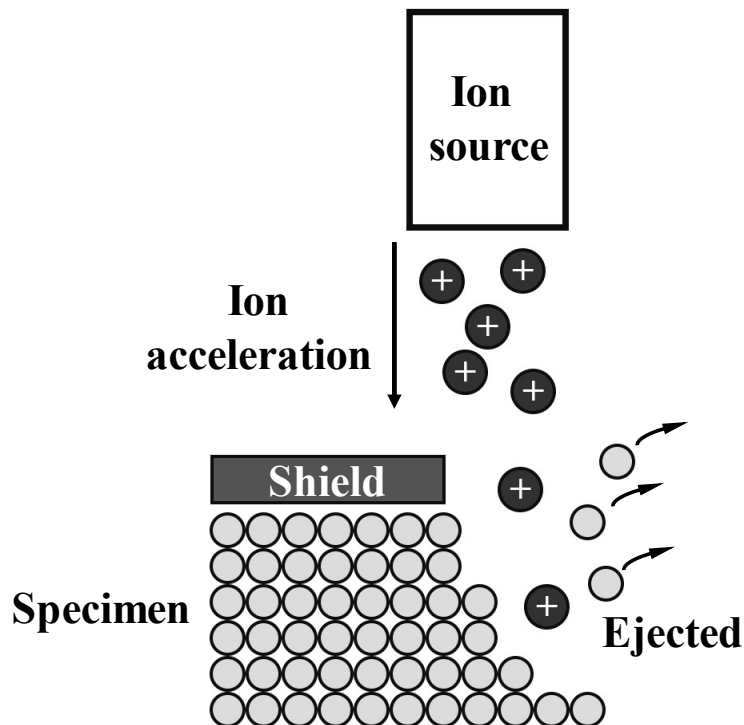


Figure 3.5 A schematic showing the operating principle of ion milling.

### 3.5 X-Ray Diffraction

X-ray diffraction (XRD) is used to examine the crystal structure of materials of interest. X-rays with a wavelength  $\sim 1 \text{ \AA}$  are at the same scale as the distance between lattice planes in a crystal. In the laboratory, X-rays are commonly generated by a vacuum tube via the interaction between high-energy electrons ( $\sim 45 \text{ kV}$  in this thesis) and a heavy metal target (*e.g.*, Cu). The Cu core electrons can be knocked out by the incident electrons, leaving vacancies for Cu electrons with higher energy to fill, resulting in an X-ray emission [178].

X-rays interact with the powder sample and get scattered elastically in all directions by the electrons in the sample. As shown in Figure 3.6, a necessary condition for constructive interference and a peak in intensity to occur is when the X-ray scattering angle,  $\theta$ , and the distance between two lattice planes of the sample ( $d$ ) satisfy Bragg's Law [178]:

$$2d\sin\theta = n\lambda \quad (3.14)$$

where  $\lambda$  is the X-ray wavelength.

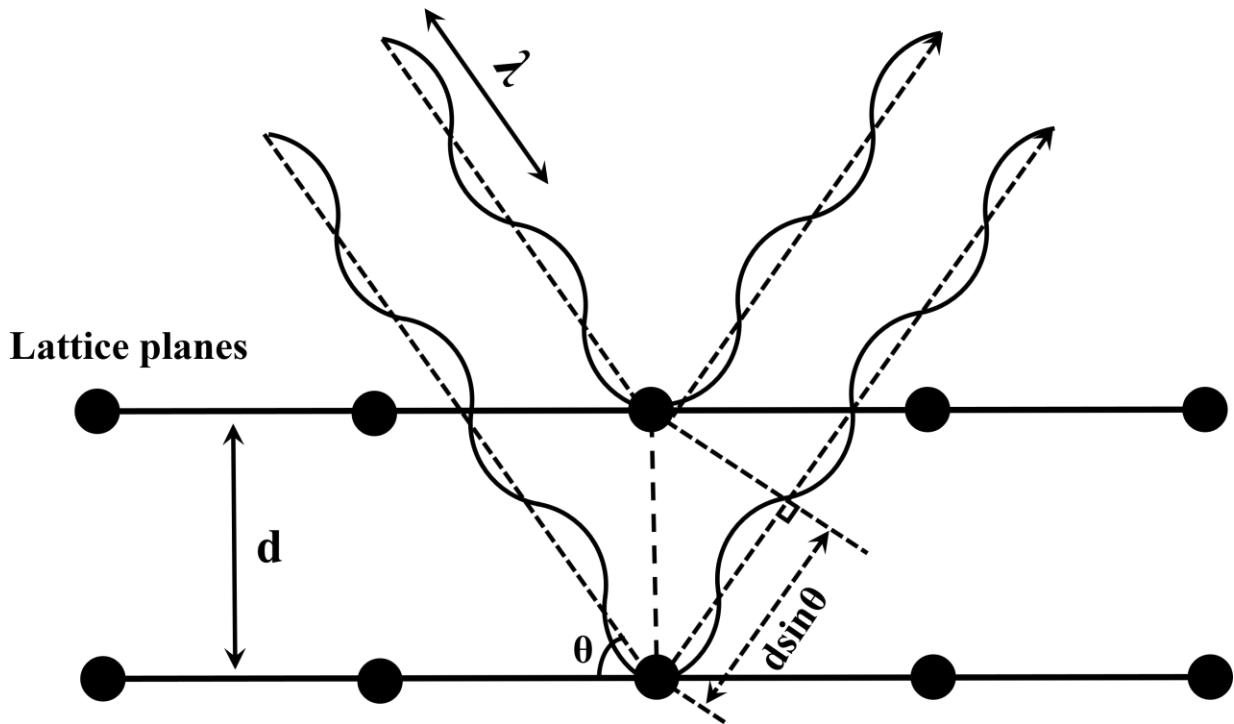


Figure 3.6 Schematic diagram of Bragg scattering from lattice planes in a solid.

As the X-ray source and the detector rotate simultaneously through the same angle, the intensity of diffracted X-ray is recorded. When the diffracted beam is scattered from an odd number of half-wavelengths, there is no XRD peak due to the occurrence of destructive interference. In this thesis, XRD measurements were carried out using a Rigaku Ultima IV diffractometer with Cu  $K\alpha$  X-ray source, a graphite diffracted beam monochromator and a

scintillation counter detector. Powder samples were placed into a sample well with a dimension of 25 mm × 20 mm × 3 mm on a stainless-steel plate. The sample was pressed down by a glass slide to ensure a flat surface, which was even with the top of the sample holder.

## **CHAPTER 4 Understanding Interfacial Impedance Growth in Porous Electrodes Containing Blended Active Materials**

This chapter was reproduced from the following peer-reviewed article:

Z. Yan, C. Wei, and M.N. Obrovac, Understanding Interfacial Impedance Growth in Porous Electrodes Containing Blended Active Materials, *J. Power Sources*, 438 (2019), 226955.

Figures and text in this chapter are reproduced with permission. Copyright 2019, Elsevier.

Z. Yan proposed the impedance model and performed the impedance and SEM experiments. C. Wei prepared cross-sectioned samples and found the difference of impedance growth in Si alloy and graphite. M.N. Obrovac provided guidance and participated in experimental design. Z. Yan and M.N. Obrovac prepared the manuscript for publication.

### **4.1 Introduction**

Lithium ion battery (LIB) active material blended electrodes are comprised of physical mixtures of two or more lithium insertion compounds. Blended electrodes can have superior performance compared to electrodes comprising an individual active compound [52]. For example, the use of Si-alloy/graphite blended electrodes can result in higher cell energy density compared to cells with graphite electrodes and can also have higher capacity retention than cells with pure Si-alloy electrodes [7,50,179]. However, the complexity of blended electrodes makes their properties difficult to understand and predict. Previous studies of blended electrodes are limited, however such studies include the effects of blended active materials on cell potential and rate capability [52,180,181].

During cell cycling, solid-electrolyte interphases (SEI) can be formed on electrodes from electrolyte decomposition reactions. The as-formed SEI layer can subsequently reduce further electrolyte decomposition. The importance of this interphase has been widely recognized for

providing advanced batteries with high service life, safety, and power performance [14,22,182]. Electrochemical impedance spectroscopy (EIS) provides a non-destructive approach to investigate interfacial processes in electrochemical cells [183,184]. However, most circuit models for interpreting EIS spectra consider electrodes either as a flat and smooth film or a single intercalation particle [29,35,108,185,186]. These simple models are insufficient to describe complicated electrochemical systems, in which more than one type of the SEI layer or particle exist. Rational but complex circuit models, such as transmission line models, which may involve a large number (>10 or even >20) circuit components, are needed to fully describe blended electrodes. Recently, a transmission line model involving 25 circuit components (resistors and capacitors) was successfully applied to interpret impedance growth in lithium nickel manganese cobalt oxide (NMC)/graphite cells at high potentials [187].

In this chapter, an inhomogeneous transmission line model (ITLM) is developed to understand the impedance growth in blended electrodes. The results are then successfully applied to describe the impedance growth in Si-alloy/graphite blended electrodes in symmetric cells. This experimental approach ensures high accuracy impedance measurements without interference from counter electrodes [44,108]. Using these methods, a deeper understanding of impedance growth in blended electrodes was gained with suggested strategies for reducing electrode impedance.

## **4.2 Experimental**

Graphite electrodes, Si-alloy electrodes, and Si-alloy/graphite blended electrodes were made to investigate impedance growth. These electrodes were composed of 88 wt% active materials, 2 wt% carbon black (CB) (Super C65, Imery's Graphite and Carbon), and 10 wt% LiPAA (from a 10 wt % aqueous solution of lithium polyacrylate (LiPAA) made by neutralizing a polyacrylic acid solution (average molecular weight ~250,000 g/mol, 35 wt% in H<sub>2</sub>O, Sigma-

Aldrich) with  $\text{LiOH}\cdot\text{H}_2\text{O}$  ( $\geq 98.0\%$ , Sigma-Aldrich) in distilled water). Distilled water (2-3 g per gram of electrode material mixture) was added to this mixture to adjust viscosity. The Si-alloy and graphite powders used were L20772 V6 alloy from 3M Company ( $D_{50} = 2.5 \mu\text{m}$ ) and SFG6L (3  $\mu\text{m}$  average size, Imerys Graphite and Carbon), respectively. Slurry mixing was conducted for one hour using a planetary ball mill (Retsch PM200) with three 13 mm tungsten carbide balls at 100 rpm, unless specified otherwise. Electrodes were cast from distilled water slurries onto copper foil with a 0.10-mm coating bar, then air dried at  $120^\circ\text{C}$  for one hour.

Coin cell construction was conducted in an Ar-filled glovebox using standard 2325 coin cell hardware. 1M  $\text{LiPF}_6$  in ethylene carbonate (EC):diethyl carbonate (DEC):fluoroethylene carbonate (FEC) (3:6:1 v/v/v, all battery grade from BASF) was used as electrolyte. Two layers of Celgard-2300 separator and one layer of polyethylene blown microfiber separator (BMF) (3M Company) were used as cell separators. This multi-layer separator construction provides more uniform stack pressure when hand-coated electrodes are used, resulting in more even current distribution and improved cell consistency and cycling performance. Electrode disks were made using a  $1.35 \text{ cm}^2$  area circular punch. Electrodes were pre-charge/pre-discharged in half-cells, then transferred into symmetric cells, and then cycled in symmetric cells before measuring their impedance. In half-cells, each electrode was paired with a  $2.57 \text{ cm}^2$  circular lithium metal (thickness of 0.38 mm, 99.9%, Sigma-Aldrich) electrode. The procedure for the pre-charge/pre-discharge process, unless specified otherwise, is as follows: one electrode (delithiated electrode) in a half-cell was discharged to 5 mV and then charged to 0.9 V at C/20 rate while the other one (lithiated electrode) was cycled between 5 mV and 0.9 V at C/20 rate once, then discharged to 5 mV at C/5 rate, and then held at 5 mV until the current was less than C/20. All cells were evaluated

with a Maccor Series 4000 Automated Test System at  $30.0 \pm 0.1$  °C. Symmetric cells were cycled at C/5, and held at each potential endpoint until the current was less than C/20.

EIS spectra were measured using a Bio-Logic VMP3 potentiostat/EIS spectrometer. EIS measurements were performed at 10 °C, with a 10 mV amplitude excitation and a frequency range from 100 kHz to 10 mHz. Before EIS measurements, symmetric cells were discharged to 0 V at C/5 rate, then held at 0 V until the current dropped below C/200. After construction, symmetric cells were discharged to 0 V and then impedance spectra were measured, as the first cycle impedance. The experimental setup did not allow an accurate measurement of the high frequency intercept of the EIS spectra due to uncertain cable and connection resistance. For this reason, all impedance spectra were shifted along the real axis (x axis), so that the beginning of the first semicircle in the spectrum is at  $0 \Omega \text{ cm}^2$ . This approach has been commonly used for impedance analysis [33,188]. Error bars were calculated as the range of two samples. Electrode microstructure was examined by first cross sectioning electrodes in a cross section polisher (JEOL IB-19530) and then imaging with a scanning electron microscope (SEM) (TESCAN MIRA3), with an accelerating potential of 20 kV.

### **4.3 Theoretical Model**

Figure 4.1(a) shows a cross-sectional SEM image of a Si-alloy/graphite blended electrode. In the blended electrode, Si-alloy and graphite particles are well dispersed, but considerable void space is left among the particles. A large porosity is typically observed in uncalendared electrodes [51]. The void space will be filled with electrolyte after cell making. During cycling, electrolyte and carbon black provide ionic and electronic conduction paths, respectively [187]. Here, a full-scale description of a porous electrode with blended active materials is developed on the basis of

transmission line model theory, where the transmission line model from reference [187] is adapted with some modifications for blended electrodes.

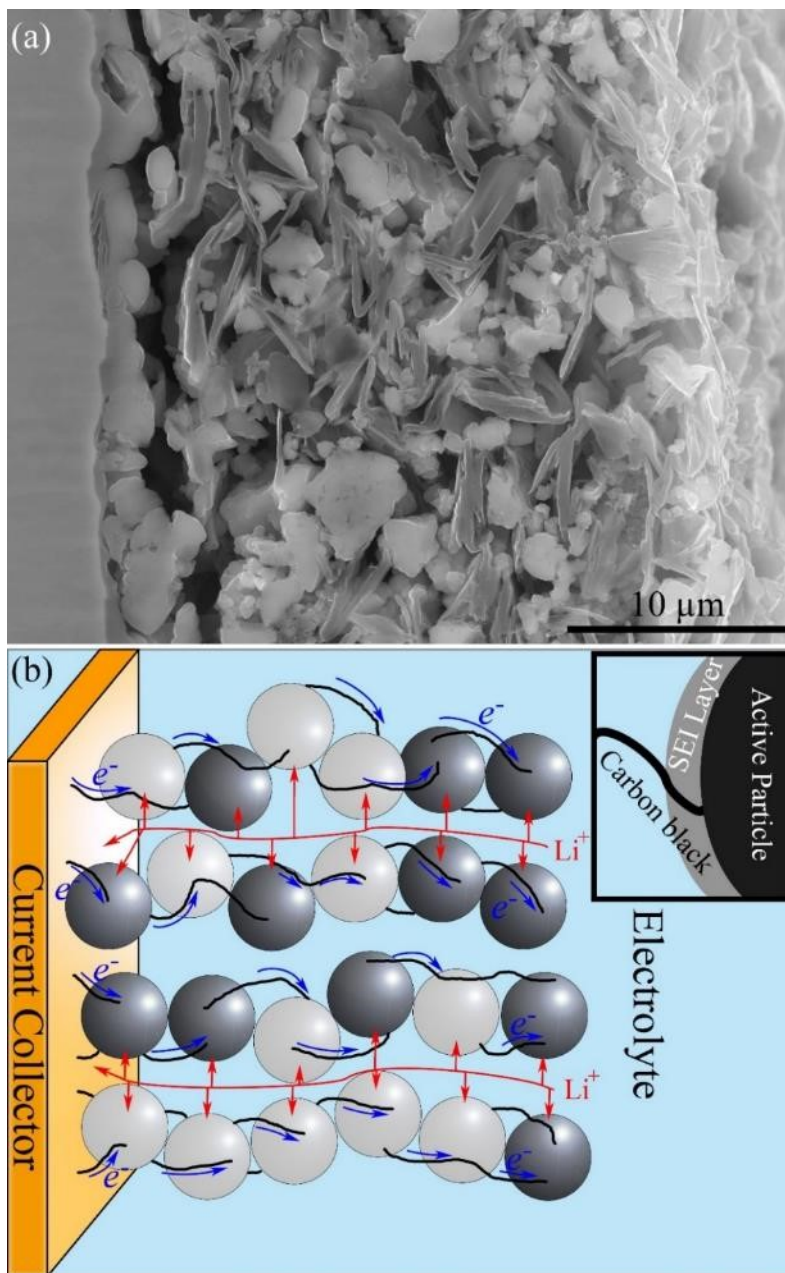


Figure 4.1 (a) Cross-sectional SEM image of Si-alloy/graphite (31.8 wt.% graphite content) blended electrodes. The irregularly shaped particles are Si-alloy. Flake-like particles are graphite. (b) An illustration of a porous electrode containing a blend of active materials (black and grey particles) in electrolyte. The active materials are electronically connected through carbon black (black lines) while the void space among solid materials is filled with electrolyte for  $\text{Li}^+$  ion diffusion. The lithium ion diffusion path and electronic path are represented with red and blue arrows, respectively.

In this model, it is assumed that active materials can be represented as parallel transmission lines aligned perpendicular to the electrode, as shown in Figure 4.1 (b). For electrodes comprised of binary or multinary active material blends, particle arrangement becomes complex. Considering that a single transmission line is insufficient to give a proper description of the particle arrangement, a large transmission line array is needed for modelling.

An equivalent electric circuit for a blended electrode represented as an array of transmission lines is shown in Figure 4.2 (a). This circuit consists of parallel inhomogeneous transmission lines (ITLs). Each ITL can contain circuit components representing the interfacial impedance of two different active particles. The impedance from mass transfer in bulk active materials is not included because mass transfer typically occurs in the low-frequency region of EIS spectra. To obtain the ITLM impedance expression, the problem is divided into two steps (Figure 4.2(b-c)): 1) calculating the impedance expression of a single ITL with a limited number of linked particles and 2) estimating the overall ITLM impedance after considering particle distribution among parallel ITLs.

Here, a simplified ITL with four linked particles is used. A higher number of linked particles than four increases the complexity of impedance expression for ITLM dramatically because each particle in the ITLM is labelled as a unique one. These four particles are labelled as #1, #2, #3, or #4. A Y- $\Delta$  transform was applied to simplify this electrical network.

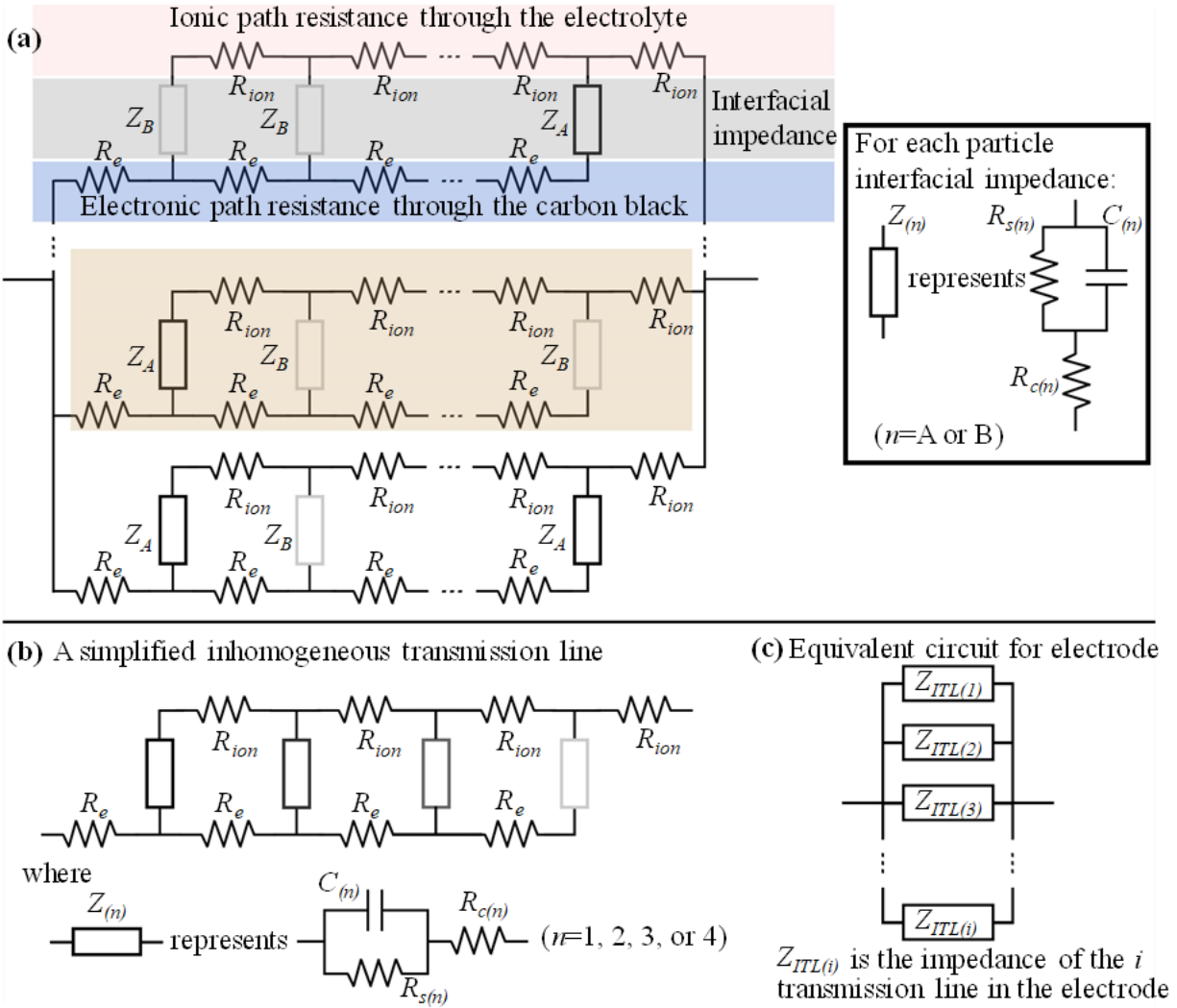


Figure 4.2 (a) An equivalent circuit for porous electrodes containing blended active materials consisting of a mixture of type A and type B active particles.  $R_{ion}$  and  $R_e$  represent the ionic resistance in electrolyte and the electronic resistance in CB, respectively.  $Z_A$  and  $Z_B$  represent the interfacial impedance of two different active materials. The circuits for  $Z_A$  and  $Z_B$  are presented on the right.  $R_{c(n)}$ ,  $R_{s(n)}$ , and  $C_{(n)}$  represent the contact resistances between CB and the  $n^{\text{th}}$  active particle, the  $n^{\text{th}}$ /electrolyte interfacial resistance, and the capacitance of the double layer that is created at the  $n^{\text{th}}$ /electrolyte interface, respectively. (b) A simplified transmission line model circuit with four particle links ( $n = 1-4$ , each particle being either of type A or B). (c) An illustration of the calculation of  $Z_{ITLM}(\omega)$  after considering the electrodes comprised of parallel ITLs on a current collector.

After this simplification, an impedance expression for the ITL was obtained, termed the ITL impedance,  $Z_{ITL}(\omega)$ :

$$Z_{ITL}(\omega) = R_{ion} + R_e + \frac{R_{ion}R_e + R_eZ_1}{R_{ion} + R_e + Z_1 + Z_2} + \frac{R_{ion}R_e + R_{ion}Z_4}{R_{ion} + R_e + Z_3 + Z_4} + \left[ \left( \frac{R_{ion}Z_2 + Z_1Z_2}{R_{ion} + R_e + Z_1 + Z_2} + R_{ion} + \frac{R_{ion}Z_3}{R_{ion} + R_e + Z_3 + Z_4} \right)^{-1} + \left( \frac{Z_2R_e}{R_{ion} + R_e + Z_1 + Z_2} + R_e + \frac{R_eZ_3 + Z_3Z_4}{R_{ion} + R_e + Z_3 + Z_4} \right)^{-1} \right]^{-1} \quad (4.1)$$

where  $Z_{(n)} = \frac{R_{s(n)}}{1 + j\omega R_{s(n)}C(n)} + R_{c(n)}$  ( $n=1, 2, 3, \text{ or } 4$ ),  $j$  and  $\omega$  are the imaginary unit and the input signal frequency, respectively.

Some assumptions were made to obtain the overall ITLM impedance, *i.e.* the number of ITLs in the model and the particle distribution among the ITLs. A particle size of  $\sim 3 \mu\text{m}$ , an electrode area of  $1.35 \text{ cm}^2$ , and an electrode porosity of 50%-70%, would require a set of  $5 \times 10^6$  ITLs. Unless specified, the different particles in an electrode are considered to be randomly arranged in these ITLs. On the basis of these assumptions, the total electrode impedance can be obtained through the following equation:

$$Z_{ITLM}(\omega) = \left[ \sum_{i=1}^N (1/Z_{ITL(i)}(\omega)) \right]^{-1} \quad (4.2)$$

where  $Z_{ITL(i)}(\omega)$  represents the impedance of the  $i^{\text{th}}$  ITL line and  $N$  is the total number of ITLs in the ITLM, which is  $5 \times 10^6$  here. After the values of parameters are inserted in this equation, the impedance was solved using a computer algorithm written in MATLAB [189].

#### 4.4 Results and Discussion

EIS spectra can provide abundant impedance information related to various electrochemical processes occurring at electrodes, including the resistance of electronic transport in conductive additives, the resistance of ionic transport in electrode pores and bulk electrolytes, the impedance of charge transfer and transport through electrode/electrolyte interfaces, and the impedance of ion diffusion in active materials [103,187]. As shown in Figure 4.3(a), a typical EIS spectrum (Nyquist plot) of the lithiated anode electrodes made here is composed of semicircular

components in the middle-frequency region and a spike in the low-frequency region. Typically, no information about the high frequency intercept of the spectrum is provided, as is the case here, as explained in the experimental section. Among the electrochemical processes mentioned above, the process of charge transfer and transport through the electrode/electrolyte interface is generally considered as the major contribution to the presence of the semicircle(s) in EIS spectra [29,44,186,190].

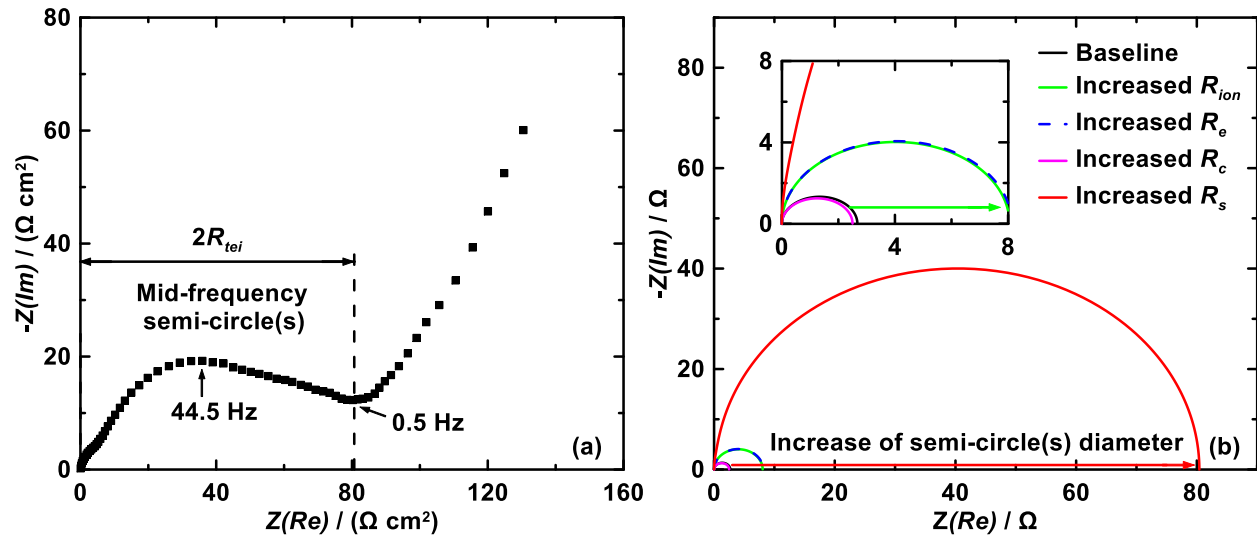


Figure 4.3 (a) A typical EIS spectrum of lithiated anode electrodes in the symmetric cells made here (a graphite electrode is used here as an example). (b) EIS spectra generated from ITLM simulation results. The  $Z_{ITLM}(\omega)$  changes when  $R_{ion}$ ,  $R_e$ ,  $R_c$ , or  $R_s$  increase by 32 times. The parameter values for the baseline are presented in Table 4.1. The inset in (b) shows an expanded view of (b).

Table 4.1 The baseline value for inhomogeneous transmission line.

Parameters	$R_e$	$R_{ion}$	$R_{s(n)}$	$R_{c(n)}$	$C_{(n)}$
Value	26 MΩ	25 MΩ	50 MΩ	50 MΩ	1 F

Figure 4.3(b) shows ITLM simulation results using the baseline parameter values listed in Table 1. EIS spectra are also shown resulting from changing different parameters in the simulation, as indicated. The simulation results also show that an increase in the particle/electrolyte interfacial

resistance,  $R_s$ , results in a significantly larger contribution to the semicircle growth in EIS spectra compared to the other circuit elements, *i.e.* the ionic path resistance through electrolyte ( $R_{ion}$ ), the electronic path resistance through carbon black or other conductive additives ( $R_c$ ), and the contact resistance between carbon black and active particles ( $R_e$ ). This strong correlation of the semicircle diameter and  $R_s$  is also observed in ITLM Monte Carlo simulations of binary active particle systems (Figure C.1). The electrode impedance,  $Z_{el}$ , is equal to the half of impedance in symmetric cells,  $Z_{sym}$  [44,108,184]. Thus, the measured total electrode/electrolyte interfacial resistance,  $R_{tei}$ , can be obtained from measured semicircle resistance(s) from symmetric cells,  $R_{semi}$ , based on the following equation:

$$R_{tei} = R_{semi}/2 \quad (4.3)$$

Here, the diameter of calculated semicircle(s) for ITL and for ITLM represent the calculated ITL interfacial resistance,  $R_{ITL}$ , and the estimated overall ITLM interfacial resistance,  $R_{ITLM}$ , respectively.

As discussed above,  $R_{tei}$  can be extracted from EIS spectra. However,  $R_{tei}$  varies even when electrode composition is constant. Figure 4.4(a) shows measured impedance of graphite electrodes with various mass loadings,  $m_{areal}$ . Even though all of these electrodes have the same electrode composition and porosity (these coatings were obtained from the same slurry), their  $R_{tei}$  values are significantly different. The electrodes with  $0.50 \text{ mg cm}^{-2}$  mass loading have a  $R_{tei}$  of  $70 \text{ } \Omega \text{ cm}^2$ , which is almost twice as large as the electrodes with a mass loading of  $0.95 \text{ mg cm}^{-2}$ . For these electrodes with the same composition, the correlation between measured  $R_{tei}$  and  $m_{areal}$ , follows:

$$R_{tei} \propto m_{areal}^{-1} \quad (4.4)$$

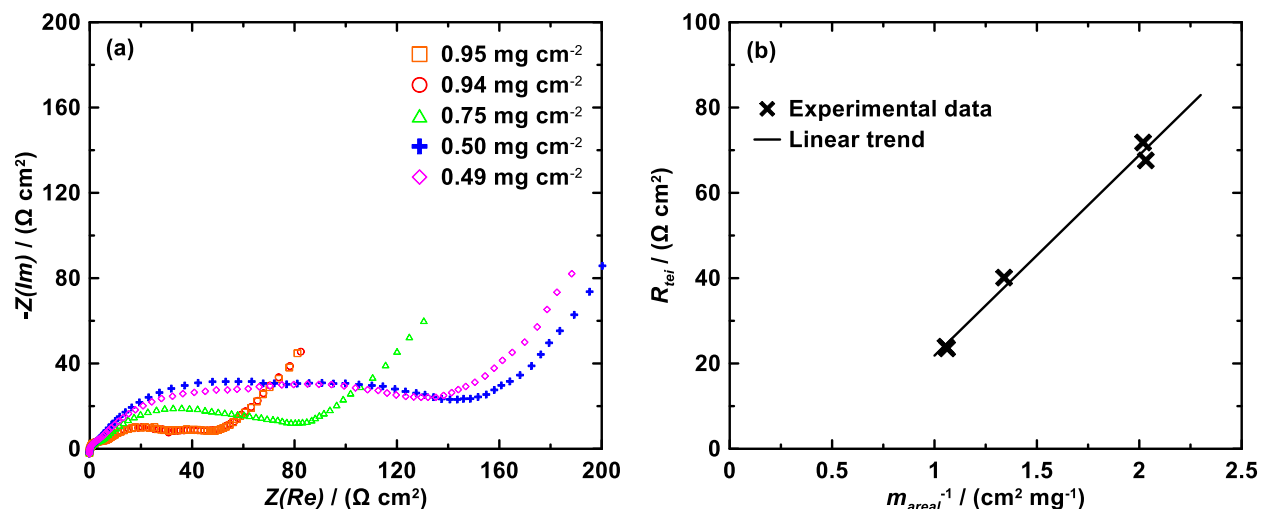


Figure 4.4 (a) Nyquist plots of graphite electrodes with various loading masses, measured at the 1<sup>st</sup> cycle in symmetric cells. (b) Plots of  $R_{tei}$  versus  $m_{areal}^{-1}$ . A linear fit was used to show the trend between  $R_{tei}$  and  $m_{areal}^{-1}$ .

This dependence is shown in Figure 4.4(b). Electrodes with a larger mass loading have a higher surface area, which results in a lower interfacial impedance. A similar trend has been observed previously [103]. This trend can also be explained by the transmission line model, in which the increased amount of transmission line in parallel can decrease the electrode impedance. Therefore, to compare the impedance growth in different electrodes properly, impedances must first be normalized by the first cycle impedance. In this way, any the variations from  $m_{areal}$  are excluded.

Figure 4.5(a-c) show EIS spectra of graphite, Si-alloy, and Si-alloy/graphite (31.8 wt.% graphite content) blended electrodes measured at different cycles. The interfacial impedance among these three electrodes are different, owing to differences in mass loading (as discussed above), packing density and surface area. Therefore, relative changes in interfacial resistance were used to understand the impedance growth among electrodes of different compositions. The relative interfacial resistances from Figure 4.5(a-c), are summarized in Figure 4.5(d).

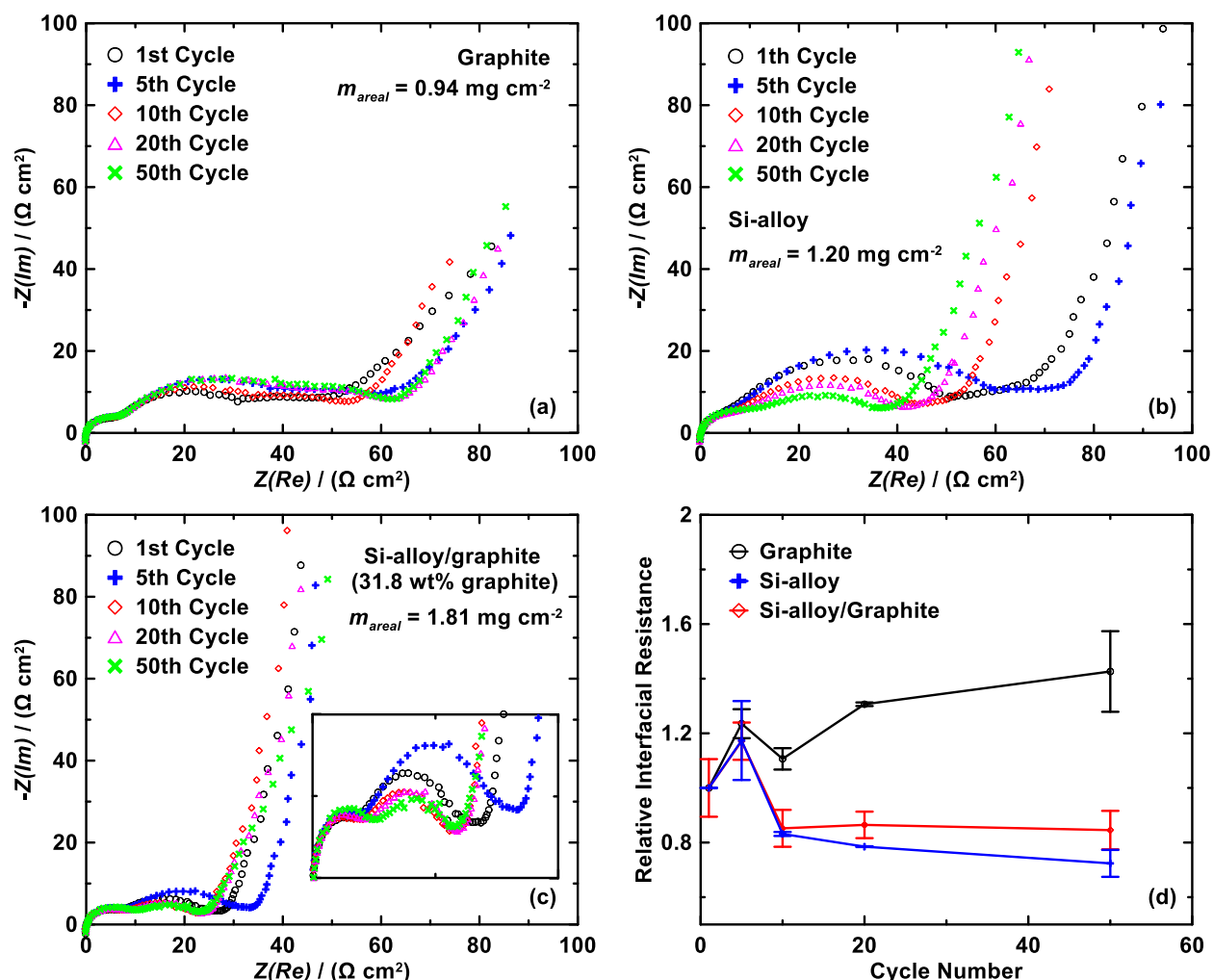


Figure 4.5 Nyquist plots for (a) graphite, (b) Si-alloy, and (c) Si-alloy/graphite (31.8 wt.% graphite content) blended electrodes measured at different cycles. The inset in (c) shows an expanded view. (d) The relative interfacial resistance vs. cycle number of these three electrodes. The relative interfacial resistances were calculated on the basis of  $R_{\text{tei}}$  values at different cycles, after normalizing by the first cycle  $R_{\text{tei}}$ .

Differences in the resistance growth of these three electrodes are observed, starting at the 10<sup>th</sup> cycle. The impedance changes during the initial cycles among all electrodes may be related to the changes in SEI compositions [88]. Graphite electrodes have an increased relative interfacial resistance, mainly caused by continuous SEI growth [44]. The interfacial impedance of the Si-alloy reduces quickly during the first few cycles, as has been observed previously for Si-based electrodes [191] and then becomes constant. A possible explanation for the constant interfacial

impedance of Si-alloy and Si-alloy containing electrodes is related to the use of FEC as an electrolyte additive, which has been found to reduce SEI growth drastically [192]. It has also been observed that the high volume expansion of Si-alloy particles during cycling (shown in Figure C.5), severely disrupts the SEI layer on the Si-alloy, exposing fresh alloy surfaces to the electrolyte and resulting in the formation of a new low-impedance SEI layer on the Si-alloy and constant interfacial impedance during cycling [193]. A more plausible explanation of the reduced impedance of the Si-alloy containing electrodes is that it is due to the continual increase in surface area of the Si-alloy during cycling, due to particle fracture [72]. This would tend to increase the interfacial area between Si-alloy and electrolyte during cycling, reducing interfacial impedance. The relative impedance growth of the Si-alloy/graphite electrodes is similar to that of the Si-alloy electrodes after 10 cycles.

In order to explain why the relative impedance growth of the Si-alloy/graphite electrode is similar to that of a pure Si-alloy electrode, a more comprehensive study of the impedance growth in blended electrodes is presented in Figure 4.6. Figure 4.6(a) shows the interfacial resistance relative to the first cycle of Si-alloy/graphite blended electrodes with different graphite contents. There is a nonlinear increase in the relative resistance with increasing graphite content. The related Nyquist plots are shown in Figure C.6. Impedance growth is suppressed when the alloy content is about 40 wt. % or higher.

To model this behavior using ITLM, the electrode is assumed to be comprised of particles A whose interfacial impedance remains constant during cycling (*i.e.* Si-alloy) and particles B whose impedance increases during cycling (*i.e.* graphite). Figure 4.6(b) shows the interfacial resistance growth in ITLs with blended particles, compared to the impedance change in a four-particle-B ITL, BBBB line, where  $R_{sA} = 800 \text{ M}\Omega$  and  $R_{sB}$  is increased from  $50 \text{ M}\Omega$  to  $1000 \text{ M}\Omega$ .

Both a higher proportion and a higher interfacial resistance of particle B result in a higher  $R_{ITL}$ . For each particle ratio, the particle arrangement in an ITL has a little effect on the  $R_{ITL}$ . However, the growth of  $R_{ITL}$  in blended ITLs are significantly smaller than the BBBB line. The reason for this impedance suppression is related to low impedance interface paths for lithium ion diffusion provided by particle A. Details of impedance spectra of ITLs with different particle arrangements can be found in Figure C.2-C.4.

Figure 4.6(c) shows simulated distributions of A and B particles in ITLs electrodes with different A:B ratios, where A and B are randomly dispersed throughout the electrode ITLs. Generally, electrodes with a high particle B content have a high proportion of “particle-B-rich” ITLs. The results also show that electrodes with a low particle B content still contain some BBBB lines. The simulation scale and complexity described by the ITLM is much larger than most circuit models, in which electrodes can be only considered as either a flat and smooth film or a single intercalation particle [185].

Overall interfacial electrode resistances,  $Z_{ITLM}(\omega)$ , were calculated on the basis of  $Z_{ITL}(\omega)$  and ITL distributions. Figure 4.6(d) shows normalized ITLM interfacial impedance growth in blended electrodes. The interfacial impedance of electrodes only containing particle A and particle B were considered as the lower reference limit and the upper reference limit, respectively. The result shows that an increased amount of the particle with high interfacial impedance can increase the overall electrode interfacial impedance. However, this impedance growth is not linear. With a small amount of low interfacial impedance particles, the overall interfacial impedance is significantly suppressed. This trend becomes more evident when the impedance difference between the two particles increases. These theoretical results explain the trend in the experimental data shown in Figure 4.6(a).

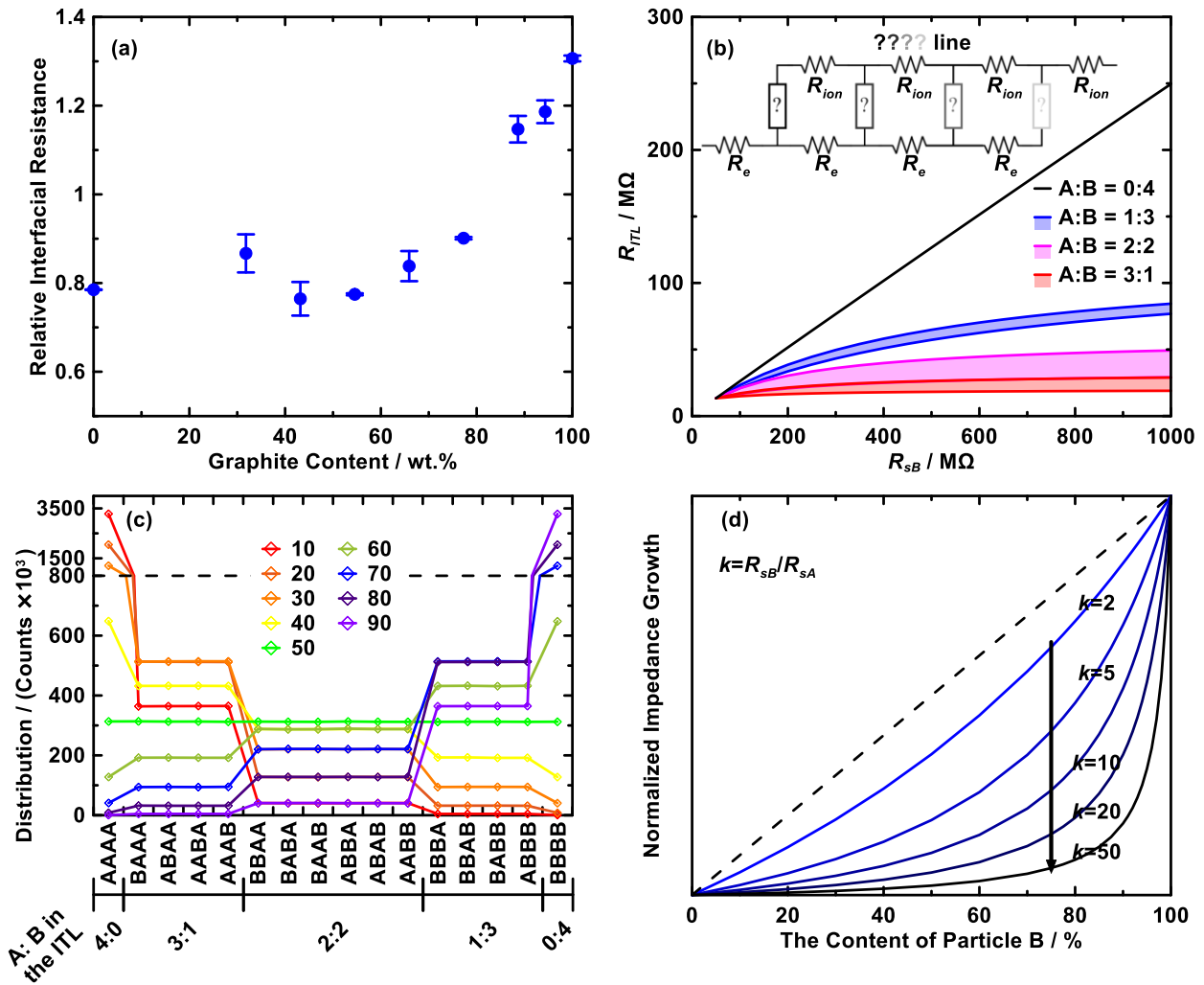


Figure 4.6 (a) A summary of the relative interfacial resistance growth of graphite, Si-alloy, and graphite/Si-alloy blended electrodes with different graphite contents at 20<sup>th</sup> cycle. (b) Plots of  $R_{ITL}$  versus  $R_{sB}$  with different ratios of the two particle types. Particle A has a constant interfacial impedance and particle B has a larger interfacial impedance. The value for all parameters, except  $R_{sB}$ , is presented in Table 4.1. The solid bands for each particle ratio reveal the range in  $R_{ITL}$  values caused by the different particle arrangements. Question marks can be either A or B of the particle interfacial impedance, including two resistors and a capacitor as shown on the right of Figure 4.2(a). (c) The distribution of ITLs in simulated electrodes with different particle B content, which varies from 10% to 90%. (d) Normalized ITLM interfacial impedance growth with increasing particle B content.  $k$  represents the ratio of  $R_{sB} / R_{sA}$ , and ranges from 2 to 50. The value of all parameters, except  $R_{sA}$  and  $R_{sB}$ , is presented in Table 4.1. The value of  $R_{sA}$  was set as 800 M $\Omega$ , which is close to the measured data of  $R_{ITLM} = 40 \Omega$ .

The effect of particle dispersion on interfacial impedance growth was also investigated.

Figure C.7 shows a cross-sectional SEM image of a Si-alloy/graphite electrode intentionally made

with a poor dispersion. The SEM image indicates the presence of Si-alloy and graphite aggregated regions in the electrode. As shown in Figure C.8 and Figure C.9, blended electrodes with a poor particle dispersion have a similar interfacial impedance to those with a good dispersion, both from experiment and theoretical calculation. For these electrodes, the low interfacial impedance particles still provide a feasible ionic pathway to suppress interfacial impedance growth. Therefore, particle dispersion does not have a major effect on interfacial impedance growth in blended electrodes. This implies that a feasible approach to suppress high impedance growth in electrodes is to include low impedance particles in the electrode formulation.

#### **4.5 Conclusions**

In this chapter, the interfacial impedance growth in electrodes comprising a blend of different active materials is comprehensively studied both in experiment and theory. Experimental data shows that the measured interfacial impedance is strongly related to the electrode mass loading. After excluding this variation, the effect of one of the active materials having high impedance was considered. It was found that blended electrodes show a nonlinear interfacial impedance growth with increasing amounts of high interfacial impedance particles. An inhomogeneous transmission line model (ITLM) was developed to understand the impedance growth in this complicated electrochemical system. The ITLM includes a large number of parallel inhomogeneous transmission lines (ITLs), which are able to simulate systems with multiple active materials. Theoretical calculations also show that a small proportion of low interfacial impedance particles can suppress the electrode interfacial impedance in blended electrodes, which agrees with the experimental result. This study provides a feasible approach to suppress the high impedance growth in electrodes, simply by adding to the electrode formulation a small amount of active material that have a low interfacial impedance.

## CHAPTER 5 Understanding Degradation Patterns in Li Cells with Si-Alloy Negative Electrodes

Figure 5.1 and 5.8(d) in this chapter were reproduced/adapted from the following meeting abstract:

Zilai Yan, Yijia Liu, Timothy Hatchard, Ben Scott, Yidan Cao, Simeng Cao, Mark N. Obrovac, Understanding Anode Capacity Fade in Symmetric Cells, *ECS Meeting Abstracts*, MA2020-02 826. The figures are reproduced/adapted with permission. Copyright 2020, IOP Publishing.

Z. Yan proposed the model and performed the experiments. Yijia Liu, Benjamin Scott, Yidan Cao, and Simeng Cao provided guidance for the synthesis of Si alloys and discussions about Si alloy electrochemical performance. Yijia Liu performed the density measurement. T.D. Hatchard provided discussion about Si alloy degradation behaviors in symmetric cells. M.N. Obrovac provided guidance for data interpretation. Z. Yan and M.N. Obrovac prepared manuscript.

### 5.1 Introduction

With the ever-increasing demand for higher energy density and lower cost rechargeable Li-ion batteries, thousands of novel electrode materials have been synthesized and examined [1,5,59,194]. Most are evaluated electrochemically in half cells, where Li metal is used as the reference/counter electrode [195–198]. Such cell format can provide basic testing of materials of interest, such as the potential profile, specific capacity, and cycling capacity retention [39]. Yet half cells often fail to predict how electrode materials perform in actual Li-ion cells, partially due to the presence of the Li metal, which provides an essentially infinite supply of Li during cell cycling. The excess Li can mask problems with side reactions at the working electrode, such as solid electrolyte interphase (SEI) growth [40,41].

Symmetric cells are a cell format with two identical electrodes, initially at different states of charge. The use of identical electrodes allows the investigation of electrochemical behavior, including electrode impedance and parasitic reactivity, without the interference from utilizing a counter electrode [26,44]. For cycling studies, prior to symmetric cell assembly, one electrode needs to be in a lithiated state, while the other is in a delithiated state [26]. This arrangement also limits the amount of active Li in cells. Side reactions at electrodes that consume active Li can be measured quantitatively using symmetric cell cycling capacity fade data. This is one of only a few methods to measure parasitic reactivity precisely only using traditional battery chargers, such as the Maccor 4000 used here [26,27,199]. The benefits of symmetric cells for precise parasitic reactivity measurements have been well discussed in References [26,27].

Symmetric cells were initially developed to investigate electrode materials that have no fade during cycling in half-cells, such as graphite,  $\text{Li}_4\text{Ti}_5\text{O}_{12}$ , and inactive materials [26,28]. Under this circumstance, any capacity fade in a symmetric cell is directly related to parasitic surface reactions at the electrodes. However, many promising electrode materials, such as Si alloys, have multiple degradation mechanisms, in addition to parasitic surface reactions, including electrode mechanical failure (including the mechanical failure of the coating and due to alloy particle fracture) [50,170]. The capacity fade of these materials in symmetric cells is related to some combination of mechanical electrode fade and parasitic reactions. The contribution from parasitic reactions is difficult to obtain in these instances, since deconvolution of the two contributions to fade is impossible. Moreover, the lower and upper cutoff potentials of working electrodes are poorly controlled in symmetric cells. In half-cell experiments, cell potentials are measured vs. a reference/counter electrode to determine the discharge/charge endpoint. In symmetric cells, the cell potential corresponds to the potential difference between two working electrodes. Side

reactions occurring at working electrodes can change the Li inventory in symmetric cells, which may perturb the electrode endpoint potentials during cycling. This could cause cycling capacity fluctuations when the electrode capacity is dependent on the cutoff potential [200].

Herein, the capacity fade of Si alloy electrodes and Si-alloy/graphite blended electrodes undergoing multiple degradation mechanisms has been investigated in symmetric and half-cells. Si-alloys are anode materials that can increase the energy density of Li-ion cells by up to 20%. Si-alloys, however, suffer not only severe SEI growth and repair but also mechanical failure, mainly due to large volume changes during cycling [8,16,201–203]. In addition, Si-alloys have been generally cycled with limited upper cutoff potential of  $\sim 0.9$  V in half cells, to approach a test condition relevant to commercial cells [50]. Many Si alloys are not fully delithiated at this cutoff potential, potentially resulting in an extra capacity reserve in symmetric cells above the intended electrode cutoff potential [50,204]. A Li accounting model was developed to describe the relationship between symmetric cell capacity fade and multiple degradation mechanisms. Quasi-three-electrode double half cells (QDHCs) and double half cells (DHCs, details in Ref. [27]) were used experimentally to understand the related anode degradation behavior and to measure the symmetric cell capacity fade, respectively.

## 5.2 Experimental

$\text{Si}_{80}\text{W}_{20}$  and  $\text{Si}_{75}\text{W}_{15}$  alloy were prepared as described in Reference [205]. A total of 0.5 mL (based on true density) of silicon powder (Sigma-Aldrich, -325 mesh, 99%) and a stoichiometric amount of tungsten powder (12  $\mu\text{m}$ , 99.9%, Aldrich) were sealed in a 65 mL stainless steel milling vial under an argon atmosphere with 180 g of 1.6 mm 440C stainless steel balls. The precursors were milled for 8 hours in a SPEX 8000 mill under the optimal conditions as described in Reference [206]. After milling, the powder was recovered from the vial by milling in

ethanol (99.89%, containing 0.10% H<sub>2</sub>O, Commercial Alcohols) and then dried in a solvent oven at 120 °C in air. The resulting powder is a homogeneous Si<sub>80</sub>W<sub>20</sub> alloy consisting of amorphous Si and nanocrystalline Si<sub>2</sub>W and W. The XRD pattern and SEM images with EDS compositional mappings of Si<sub>80</sub>W<sub>20</sub> are shown in Figure D.1. The true density of the Si<sub>80</sub>W<sub>20</sub> and Si<sub>75</sub>W<sub>15</sub> alloy was determined to be 5.8717 g/cm<sup>3</sup> and 7.2820 g/cm<sup>3</sup> by helium pycnometry (Micromeritics AccuPyc II 1340 gas pycnometer), respectively.

Graphite electrodes, Si<sub>80</sub>W<sub>20</sub> electrodes, and Si<sub>80</sub>W<sub>20</sub>/graphite (Si<sub>80</sub>W<sub>20</sub>/G) blended electrodes were made to understand symmetric cell capacity fade. These electrodes were composed of active materials, carbon black (CB) (Super C65, Imery's Graphite and Carbon), and lithium polyacrylate (LiPAA) (from a 10 wt % LiPAA aqueous solution, made by neutralizing a polyacrylic acid solution (average molecular weight ~250,000 g/mol, 35 wt% in H<sub>2</sub>O, Sigma-Aldrich) with LiOH·H<sub>2</sub>O (≥98.0%, Sigma-Aldrich) in distilled water) in a volumetric ratio of 70/5/25. Distilled water was added to this mixture to adjust viscosity. Unless otherwise specified, MAG-E (20 μm average size, Hitachi) was used as active graphite. Where indicated, another type of graphite (3 μm average size, Imerys Graphite and Carbon) was used. Si-based materials and graphite electrode coatings were formulated on a volumetric basis. For example, Si<sub>80</sub>W<sub>20</sub>/G 20/50 electrodes have Si<sub>80</sub>W<sub>20</sub> and graphite with a volume ratio of 20/50, based on true densities. SiO (Sigma Aldrich, -325 mesh, 99%) and Si<sub>75</sub>W<sub>15</sub> were also blended with graphite, following the same procedure above. Slurry mixing was conducted for one hour using a planetary ball mill (Retsch PM200) with three 13 mm tungsten carbide balls at 100 rpm. Electrodes were cast from distilled water slurries onto copper foil with a 0.004-inch coating bar, then air dried at 120 °C for 1 hour, cut into 1.3 cm disks, then heated under vacuum for 1 hour at 120 °C and assembled into cells with no further air exposure.

Coin cell construction was conducted in an Ar-filled glovebox using standard 2325 coin cell hardware. 1M LiPF<sub>6</sub> in ethylene carbonate (EC):diethyl carbonate (DEC):fluoroethylene carbonate (FEC) (3:6:1 v/v/v, all battery grade from BASF) was used as electrolyte. Two layers of Celgard-2300 separator and one layer of polyethylene blown microfiber separator (BMF) (3M Company) were used as cell separators. This multi-layer separator construction provides more uniform stack pressure when hand-coated electrodes are used, resulting in more even current distribution and improved cell consistency and cycling performance.[27] Electrode disks were cut using a 1.35 cm<sup>2</sup> area circular punch. In half-cells, each electrode was paired with a 2.57 cm<sup>2</sup> circular lithium metal (thickness of 0.38 mm, 99.9%, Sigma-Aldrich) electrode. For higher accuracy, the active material mass in each electrode was evaluated from its first charge (delithiation) capacity and the average specific capacity (obtained from at least four samples) [27,207].

DHC [27] or QDHC cells include two half cells with the nominally identical electrodes, in the configurations shown in Figure D.2(a,b). QDHCs are identical to DHCs, excepting that an extra potential probe lead is connected to a high-impedance potential terminal of a battery charger, to monitor the potential difference between the Li metal electrode terminals and one of the electrodes. The Li metal electrode terminals are used as a reference electrode (RE) in a quasi-3-electrode cell configuration. In this work, the potential of the pre-delithiated electrode was measured versus the Li metal electrodes. To avoid lithium plating, the mass of the pre-lithiated electrode was always chosen to be slightly less than that of the pre-delithiated electrode.

To prepare a DHC or QDHC, one half cell was discharged to 5 mV and then charged to the target cutoff potential at C/20 rate. The other cell was first discharged and charged the same way, then discharged to 5 mV at C/5 rate, and then trickle discharged until the current fell below

C/20 rate. Unless otherwise specified, the cutoff potential was 0.9 V. DHCs and QDHCs were cycled at C/5 rate and then trickled to C/20 between the positive/negative of the cutoff potential. DHCs for SEI growth measurements were cycled under a current-corrected cycling protocol, in which the cycling rate was well controlled to the designed rate regardless the capacity fade. This constant C-rate protocol is achieved through correcting the current of each cycle on the basis of the capacity from the previous cycle (charge capacity), except the initial cycle which is determined from the theoretical capacity. As a result, the DHCs were cycled at a true C/5 rate before the trickle process, even though the DHCs only had about 50% remaining capacity after 50 cycles. Cells were evaluated using a Maccor Series 4000 Automated Test System and thermostatically controlled at  $30.0 \pm 0.1$  °C. Cycling under other temperatures will be specified. The specific capacity of both DHCs and QDHCs was calculated with respect to the active material mass in the pre-lithiated electrode. Error bars were calculated as the range of four samples, unless specified.

X-ray diffraction (XRD) measurements were carried out using a Rigaku Ultima IV diffractometer with Cu K $\alpha$  X-ray source, a graphite diffracted beam monochromator and a scintillation counter detector. XRD patterns were collected at 0.05° intervals with a dwell time of 3 s.

Images of sample morphology and elemental distribution maps of samples were obtained using a field emission scanning electron microscope (FESEM) (TESCAN MIRA3) with an accelerating voltage of 20 kV. Sample cross sections were prepared using a cross-section polisher (JEOL IB-19530).

### **5.3 A Li Inventory Model**

A Li inventory model, inspired by Reference [150], was developed to interpret anode capacity fade in symmetric cells. In past studies, the term symmetric cell commonly refers to single

cells with identical electrodes, however, in this work the DHC and QDHC formats are included in this category. To distinguish the symmetric cell types, traditional symmetric cells will be referred to as TSCs, double half cells as DHCs, and quasi double half cells as QDHCs. The term symmetric cell or SC will be used to refer generally to all three of these symmetric cell types. The Li inventory model attempts to establish a mathematical relationship between multiple anode degradation processes and measured experimental data, such as cycling charge/discharge capacity. To describe the cycling process, here the symmetric cell electrodes having the initial states of lithiation and delithiation are called electrode A and B, respectively. Symmetric cell discharge is considered as the process where electrode A undergoes delithiation, while symmetric cell charge is considered as the reversed process. Figure 5.1(a) illustrates the notation, showing the initial discharge potential profiles of a symmetric cell and each of its individual electrodes A and B. In this study, three categories of mechanisms that can change the Li inventory at both electrodes are included:

1. Electrode mechanical failure irreversibly trapping active Li within the electrode.
2. Li loss due to electrochemical or chemical decomposition of electrolyte.
3. Reversible capacity fluctuation associated with electrode upper endpoint potential change.

Furthermore, it is assumed that most of the Li loss associated with Category 2 can be attributed to SEI growth and repair on active negative electrode material surfaces [24].

Electrodes are typically cycled in symmetric cells up to upper cutoff potentials that both reflect their potential range when used in practical applications (e.g.  $\sim 0$  V - 0.9 V for negative electrodes) and at which the active materials are fully delithiated. However, Si-based negative electrode materials can have significant capacity above 0.9 V, as shown in Figure 5.1(b). In addition, if symmetric cell capacity continuously fades during cycling, this results in a decreased active Li inventory. As a result, the electrodes can only be partially lithiated at the endpoint of the

symmetric discharge/charge process, leading to an increased electrode endpoint potential at the end of lithiation: *i.e.* the delithiation of the paired electrode will have an endpoint above the intended upper cutoff potential, which may result in this electrode providing additional capacity (here termed "excess capacity").

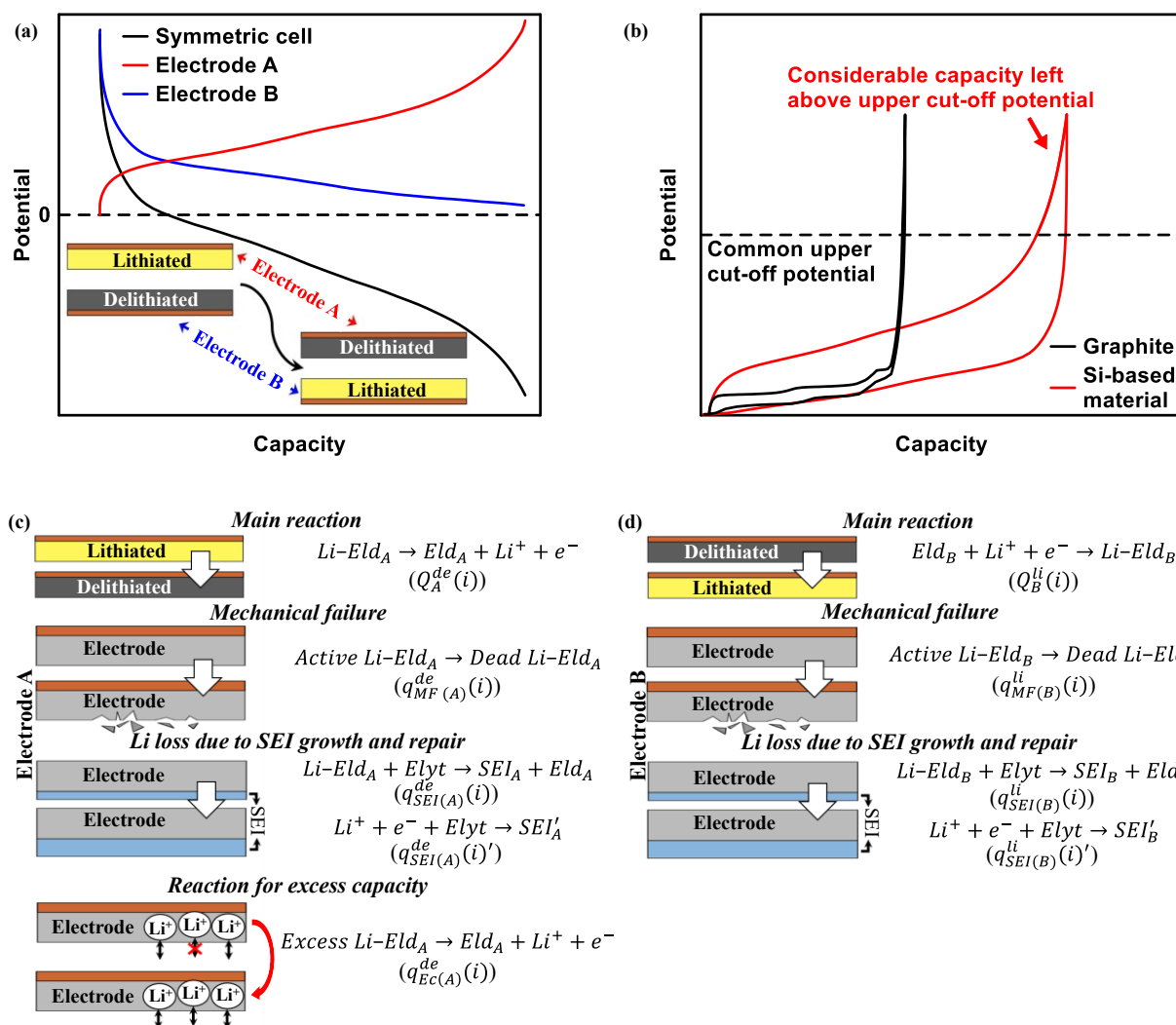


Figure 5.1 (a) An example of potential curves of a symmetric cell during discharge and individual contributions from electrode A and electrode B. (b) An example of potential curves of a Si-based anode material and graphite in half cell. As shown, unlike graphite, Si-based anode materials often have considerable capacity above typical upper cut-off potentials. Illustrations of the main reaction, side reactions, and the reaction for excess capacity at (c) electrode A and (d) electrode B that occur during the  $i^{th}$  symmetric cell discharge. The capacities for each reaction during a single symmetric cell discharge/charge process are labelled in brackets.  $Li-Eld$ ,  $Eld$ , and  $Elyt$  stand for lithiated electrode, delithiated electrode, and electrolyte, respectively.

To keep track of symmetric cell capacity according to the above assumptions, each capacity component is defined as follows. Prior to symmetric cell cycling, electrode A and B have undergone conditioning cycles to put them in their initial state of charge for symmetric cell cycling and to remove initial irreversible capacity. For electrode A this consists of one lithiation and, for electrode B, one lithiation and one delithiation. Therefore, prior to symmetric cell cycling, electrode A is assumed to be fully lithiated with reversible capacity  $Q_0$  and electrode B is assumed to be delithiated to the intended upper cutoff potential. Side reaction capacity occurring at electrode A and B during the formation cycling are initialized with values of  $q_A$  and  $q_B$ , respectively.

The lithium inventory in electrodes A and B may then be quantified during cycling as shown in Figure 5.1(c) and (d), respectively. When a symmetric cell is discharged, most of the active Li is transferred from electrode A to electrode B. The capacity delivered through the reversible Li delithiation process in electrode A and reversible Li lithiation process in electrode B are as  $Q_A^{de}(1)$  and  $Q_B^{li}(1)$ , respectively. Simultaneously, three possible types of degradation mechanisms are considered to occur at both electrodes during each symmetric cell discharge/charge: electrode mechanical failure, SEI growth and repair via chemical reactions, and SEI growth and repair via electrochemical reactions, which are given as  $q_{MF}(1)$ ,  $q_{SEI}(1)$ , and  $q_{SEI}(1)'$ , respectively. Even at low potentials, parasitic oxidation reactions may occur, as observed recently in graphite electrodes during the delithiation process [90]. Such behavior, however, is not included in this paper, since it has not investigated in Si-based materials and its contribution is likely small. If any, the capacity of other side reactions, particularly during the delithiation process, will be underestimated to some extent. In addition, excess capacity due to the upper endpoint potential change (triggered by side reactions and considered occurring only at electrode delithiation process) is given as  $q_{Ec}(1)$ .

Figure 5.1(c) and (d) illustrate the various capacity contributing mechanisms that occur during symmetric cell discharge on electrodes A and B, respectively. During the first symmetric cell discharge, all reversible capacity in electrode A is released, thus at the end of discharge there is no active reversible capacity left in electrode A and  $Q_A^{de}(1)$  is equal to  $Q_0$ . Side reactions at electrode A can consume active Li, *i.e.* from electrode mechanical failure or SEI growth and repair, but this capacity can be partially reimbursed by the excess capacity. The amount of capacity delivered from electrode A to electrode B, *i.e.* the measured cycling capacity, can be calculated by subtracting the total capacity due to degradation mechanisms and excess capacities,  $q_A^{de}(1)$  (or inventory-change capacity), from  $Q_A^{de}(1)$ . Similarly,  $Q_B^{li}(1)$  is equal to the inventory-change capacity at electrode B,  $q_B^{li}(1)$ , subtracted from the cycling capacity.

Table 5.1 Li inventory of a hypothetical symmetric cell for its first cycle.\*

	Initial state	First discharge	First charge
Reversible capacity in electrode A	$Q_0$	0	$Q_0 - q_A^{de}(1) - q_A^{li}(1) - q_B^{li}(1) - q_B^{de}(1)$
Side reaction capacity at electrode A	$q_A$	$q_A + q_A^{de}(1)$	$q_A + q_A^{de}(1) + q_A^{li}(1)$
Reversible capacity in electrode B	0	$Q_0 - q_A^{de}(1) - q_B^{li}(1)$	0
Side reaction capacity at electrode B	$q_B$	$q_B + q_B^{li}(1)$	$q_B + q_B^{li}(1) + q_B^{de}(1)$
Cycling capacity	0	$Q_0 - q_A^{de}(1)$	$Q_0 - q_A^{de}(1) - q_B^{li}(1) - q_B^{de}(1)$

\*  $q_M^{de}(1) = q_{MF(M)}^{de}(1) + q_{SEI(M)}^{de}(1) + q_{SEI(M)}^{de}(1)' - q_{Ec(M)}^{de}(1)$  and

$q_M^{li}(1) = q_{MF(M)}^{li}(1) + q_{SEI(M)}^{li}(1) + q_{SEI(M)}^{li}(1)'$  ( $M=A$  or  $B$ )

Based on this Li inventory tracking process, the relations between the inventory-change capacity and cycling capacity, which are measurable, can be established. The first cycle Li inventory of the hypothetical symmetric cell shown in Figure 5.1 is summarized in Table 5.1. The symmetric cell Li inventory of the following cycles can be further obtained, as shown in Table 5.2. On the basis of this Li inventory analysis, the capacity from degradation mechanisms and the excess capacity, leading to the symmetric cell capacity change (*i.e.* the inventory-change capacity), can be measured throughout the cycling test.

Table 5.2 Li inventory of a hypothetical symmetric cell for its post-first cycle.\*

	$i^{\text{th}}$ discharge ( $i \geq 2$ )	$i^{\text{th}}$ charge ( $i \geq 2$ )
Reversible capacity in electrode A	0	$Q_0 - \sum_{n=1}^i [q_A^{de}(n) + q_A^{li}(n) + q_B^{li}(n) + q_B^{de}(n)]$
Side reaction capacity at electrode A	$q_A + \sum_{n=1}^{i-1} [q_A^{de}(n) + q_A^{li}(n)] + q_A^{de}(i)$	$q_A + \sum_{n=1}^i [q_A^{de}(n) + q_A^{li}(n)]$
Reversible capacity in electrode B	$Q_0 - \sum_{n=1}^{i-1} [q_A^{de}(n) + q_A^{li}(n) + q_B^{li}(n) + q_B^{de}(n)] - q_A^{de}(i) - q_B^{li}(i)$	0
Side reaction capacity at electrode B	$q_B + \sum_{n=1}^{i-1} [q_B^{li}(n) + q_B^{de}(n)] + q_B^{li}(i)$	$q_B + \sum_{n=1}^i [q_B^{li}(n) + q_B^{de}(n)]$
Cycling capacity	$Q_0 - \sum_{n=1}^{i-1} [q_A^{de}(n) + q_A^{li}(n) + q_B^{li}(n) + q_B^{de}(n)] - q_A^{de}(i)$	$Q_0 - \sum_{n=1}^{i-1} [q_A^{de}(n) + q_A^{li}(n)] - q_A^{de}(i) - \sum_{n=1}^i [q_B^{li}(n) + q_B^{de}(n)]$

\*  $q_M^{de}(i) = q_{MF(M)}^{de}(i) + q_{SEI(M)}^{de}(i) + q_{SEI(M)}^{de}(i)' - q_{Ec(M)}^{de}(i)$  and

$q_M^{li}(i) = q_{MF(M)}^{li}(i) + q_{SEI(M)}^{li}(i) + q_{SEI(M)}^{li}(i)'$  ( $M=A$  or  $B$ )

Although it is convenient to obtain the inventory-change capacity occurring at each electrode from the capacity difference between charge and adjacent discharge, standard chargers fail to provide the required high accuracy for this measurement, due to positive and negative current imbalance [98]. To avoid this issue, cell capacity fade, which can be measured accurately

even by standard chargers, is utilized. Here, discharge capacity fade per cycle,  $\Delta D(i)$ , and charge capacity fade per cycle,  $\Delta C(i)$ , are used, which are the fade between the  $i^{\text{th}}$  cycle and the previous cycle. The differential of electrode inventory-change capacity during cycling ( $i \geq 2$ ) is:

$$q_A^{de}(i) + q_A^{li}(i-1) - q_A^{de}(i+1) - q_A^{li}(i) = \Delta C(i) - \Delta D(i+1) \quad (5.1)$$

$$q_B^{li}(i-1) + q_B^{de}(i-1) - q_B^{li}(i) - q_B^{de}(i) = \Delta D(i) - \Delta C(i) \quad (5.2)$$

To acquire the electrode inventory-change rate at each cycle, it is assumed that electrode A and electrode B have the same specific inventory-change rate at the steady state. Thus,

$$\frac{q_A^{de}(i+1) + q_A^{li}(i)}{q_B^{li}(i) + q_B^{de}(i)} = \frac{m_A}{m_B} \quad (\text{at the steady state}) \quad (5.3)$$

where  $m_A$  and  $m_B$  are the electrode material mass of electrode A and B, respectively.  $m_A$  and  $m_B$  can be measured experimentally. In addition,

$$q_A^{de}(2) + q_A^{li}(1) + q_B^{li}(1) + q_B^{de}(1) = \Delta D(2) \quad (5.4)$$

where  $\Delta D(2)$  can be measured experimentally. On the basis of equations (3.1-3.4), the inventory-change capacities of electrodes A and B in symmetric cells can be calculated.

To demonstrate the usefulness of the Li-inventory model, Figure 5.2(a) shows the capacity fade of  $\text{Si}_{80}\text{W}_{20}$  electrodes cycled in a DHC. Here, the capacity fade measurement was conducted in the DHC cell format. The pros and cons of different symmetric cell formats will be discussed later. The capacity fade in Figure 5.2(a) shows that there is a loss of Li-inventory in the cell. The capacity fade of a symmetric cell can further be translated into cell CE, as discussed in Reference [26]. In the present notation the CE of the  $i^{\text{th}}$  cycle can be expressed as:

$$CE(i) = \begin{cases} 1 - \frac{q_A^{de}(2) + q_A^{li}(1) + q_B^{li}(1) + q_B^{de}(1)}{2[Q_0 - q_A^{de}(1)]} & (i = 2) \\ 1 - \frac{[q_A^{de}(i) + q_A^{li}(i-1) + q_B^{li}(i-1) + q_B^{de}(i-1)]}{2\{Q_0 - \sum_{n=1}^{i-2} [q_A^{de}(n) + q_A^{li}(n) + q_B^{li}(n) + q_B^{de}(n)] - q_A^{de}(i-1)\}} & (i \geq 3) \end{cases} \quad (5.5)$$

This is the typical information derived from symmetric cells. Utilizing the Li-inventory model, it is possible to derive the inventory-change capacity occurring at each individual electrode that is responsible for the overall capacity fade of the cell, as shown in Figure 5.2(b). Here, electrode A shows a slightly smaller specific inventory-change capacity compared to electrode B, showing that the two electrodes are not exactly identical. These differences can be due to the different preparation conditions of electrodes A and B in half cells prior to their assembly into the symmetric cell. The inventory-change capacity at each individual electrode is the sum of many degradation mechanisms, as mentioned above. Quantifying the contribution of each degradation mechanism to capacity fade, is more difficult to achieve and is the goal of the rest of this study. To do this, the contributions of SEI growth, mechanical failure, and excess capacity need to be further considered.

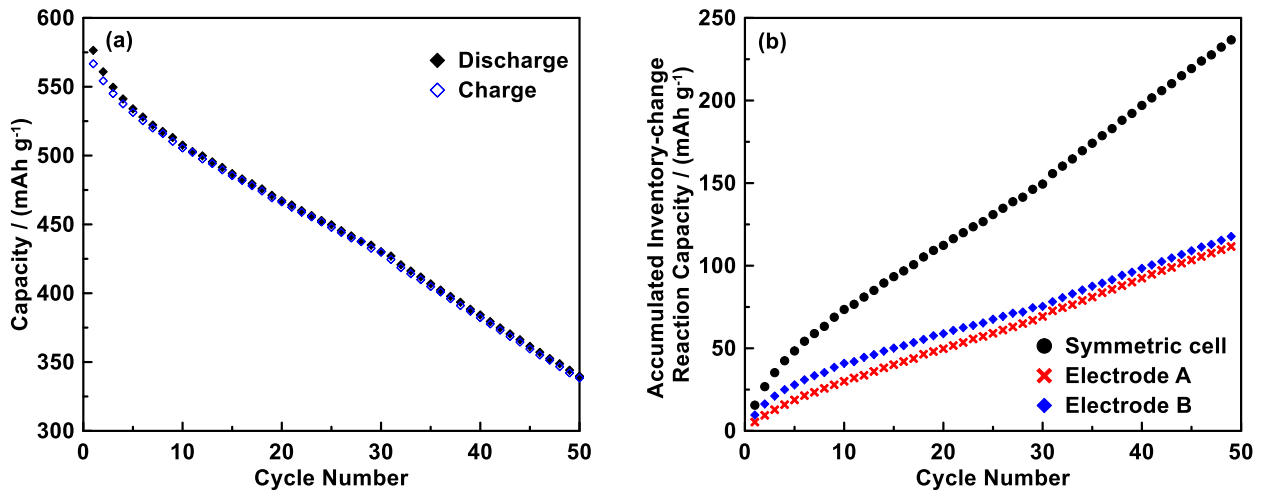


Figure 5.2 Si<sub>80</sub>W<sub>20</sub> DHC (a) Charge and discharge capacity and (b) accumulated inventory-change reaction capacity versus cycle number of the pre-lithiated electrode (electrode A), and pre-delithiated electrode (electrode B). The specific capacity of electrode A and B were calculated with respect to their corresponding active material mass. To acquire the electrode inventory-change rate for each cycle, it was assumed that electrode A and B have achieved the same average specific steady state reaction rate during these cycles, as applied in equation (5.3).

## 5.4 Anode Degradation Behavior in Symmetric Cells

The appropriate choice of cell format is crucial to measure and understand anode capacity fade in symmetric cells. Although capacity fade measurement has been commonly conducted in conventional symmetric cells [26,208,209], some concerns remain about the result accuracy because of the complex cell assembly process and electrode alignment issues. As a new type of symmetric cells, DHCs (Figure D.2(a)) have been designed to overcome these issues, providing improved measurement accuracy and reliability [27]. To understand anode degradation behavior in symmetric cells in-depth, DHCs were modified to QDHCs (Figure D.2(b)), where the Li terminals serve as quasi-reference electrodes to monitor the potential of each WE. It needs to be pointed out that the use of the extra connection between the Li terminals and one of the WEs could continuously induce a tiny amount of unwanted capacity into the WE, since the impedance of these potential sense leads is not infinite. This is as shown in Figure D.2(c-d), which illustrates that the measured capacity fade of a graphite QDHC is lower than in a DHC, due to leakage current ( $\sim 0.005 \text{ mA g}^{-1}$ ) between the Li-counter electrode and a graphite WE via the quasi-reference electrode connection to the charger. Because of this reason, results from QDHCs are only used here to illustrate the potential behavior of individual electrodes, while DHCs are used for qualitative analysis.

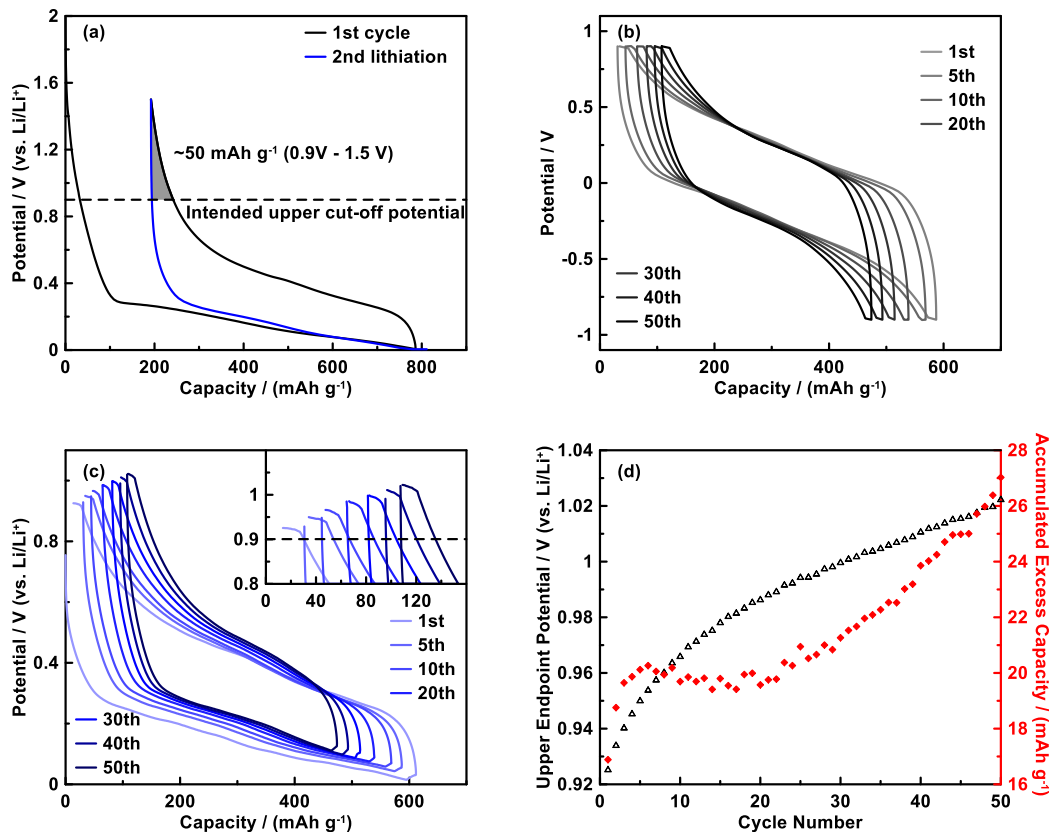


Figure 5.3 (a) Potential curves of a  $\text{Si}_{80}\text{W}_{20}$  half cell. The grey area represents the excess capacity above 0.9 V. Potential curves of (b) a  $\text{Si}_{80}\text{W}_{20}$  QDHC and (c) the pre-delithiated  $\text{Si}_{80}\text{W}_{20}$  electrode in the QDHC. The inset in (c) shows an expanded view of potential curves above 0.8 V. The dashed line represents the intended upper cut-off potential. (d) The upper endpoint potential and released accumulated excess capacity of the prelithiated  $\text{Si}_{80}\text{W}_{20}$  electrode during cycling.

To approach test conditions relevant to commercial cells, Si-alloy anodes are commonly cycled in half cells with an upper cutoff potential of 0.9 V, where the anodes may be only partially delithiated [50]. As shown in Figure 5.3(a), the  $\text{Si}_{80}\text{W}_{20}$  electrode (here cycled in a half-cell) releases an excess capacity of  $\sim 50 \text{ mAh g}^{-1}$  when delithiated from 0.9 V to 1.5 V. The presence of additional capacity above 0.9 V is typical for Si-based anodes and makes such electrodes unsuitable for study using traditional symmetric cell methods. To see how this electrode cycles in symmetric cells, QDHCs were constructed with  $\text{Si}_{80}\text{W}_{20}$  WEs. These QDHCs were cycled as symmetric cells between  $\pm 0.9 \text{ V}$ , as shown in Figure 5.3(b), while individual electrode potential was measured using the Li-quasi REs, shown in Figure 5.3(c). During symmetric cell cycling, the

Si<sub>80</sub>W<sub>20</sub> electrode experienced varying endpoint potentials, as observed from the shifting upper and lower endpoint potentials during cycling. The shift of the upper endpoint potential can cause some of the excess capacity to be accessed during symmetric cell cycling, as shown in the inset of Figure 5.3(c). Both SEI growth and mechanical failure, which cause irreversible loss of active Li can be attributed to the observed increase in the upper potential endpoint. The excess capacity from one electrode can be approximately evaluated based on the capacity above the intended cut-off potential.

The upper endpoint potential and the amount of accumulated excess capacity of one Si<sub>80</sub>W<sub>20</sub> electrode during cycling are summarized in Figure 5.3(d). A significant increase in the Si<sub>80</sub>W<sub>20</sub> excess capacity was observed after just 20 cycles (~20 mAh/g or 3% of the total electrode capacity). The Si<sub>80</sub>W<sub>20</sub> electrode upper endpoint consecutively shifted to a higher potential, due to the Li inventory loss in the symmetric cell. Such anode endpoint potential shifts have also been observed in Si/ LiNi<sub>0.8</sub>Co<sub>0.15</sub>Al<sub>0.05</sub>O<sub>2</sub> full cells [200]. This implies that symmetric cells might more realistically emulate full cell cycling than half cells. The Si<sub>80</sub>W<sub>20</sub> symmetric cell shown in Figure 5.2 experiences a capacity loss of 245 mAh g<sup>-1</sup> after 50 cycles. Roughly, the capacity reimbursed by the excess capacity is about 44 mAh g<sup>-1</sup> (the initial excess capacity of electrode A is not included), or about 18% of the measured capacity loss. Accordingly, the total capacity loss from SEI growth and mechanical failure should be corrected to be ~245 mAh g<sup>-1</sup> + 44 mAh g<sup>-1</sup> = 289 mAh g<sup>-1</sup>. In other words, the capacity loss analysis of Si-alloy symmetric cells without considering the excess capacity would result in an inaccurate determination of the capacity loss contributions from SEI growth and mechanical failure that traps active Li.

Electrode mechanical failure in QDHCs was also investigated using Si<sub>80</sub>W<sub>20</sub>/G 20/50 electrodes with an intended cutoff potential of 2.5 V as an example. This increased upper cutoff

potential was used to minimize the excess capacity effect and cause a more severe mechanical failure for alloys, due to higher volume contraction at a more complete state of delithiation. Graphite was utilized to improve electrical contact to the alloy particles. Without graphite, pure  $\text{Si}_{80}\text{W}_{20}$  electrodes suffered dramatic capacity fade in QDHCs and in half cells when cycled to this high upper cutoff potential, as shown in Figure D.3.

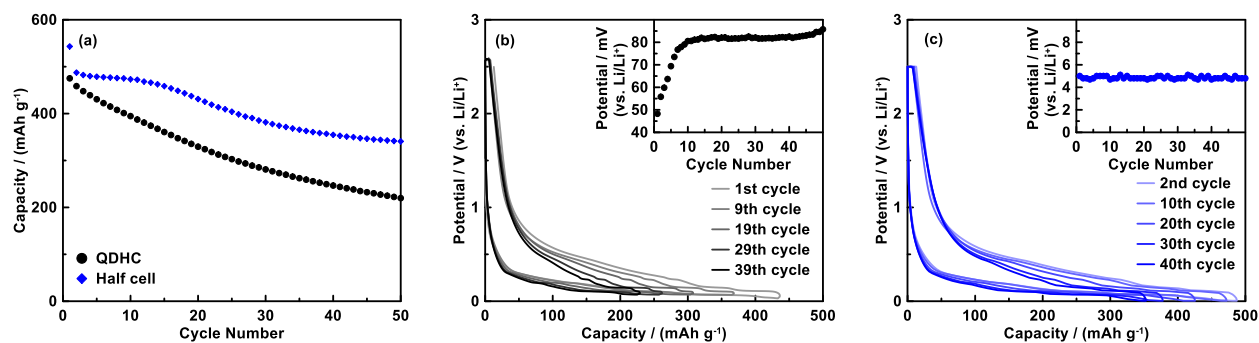


Figure 5.4 (a) Capacity versus cycle number of  $\text{Si}_{80}\text{W}_{20}/\text{G}$  20/50 electrodes cycled in a QDHC and a half cell. Potential curves of the  $\text{Si}_{80}\text{W}_{20}/\text{G}$  20/50 (b) QDHC and (c) half cell. The insets in (b) and (c) show the corresponding lower endpoint potential versus cycle number. Only in this experiment, SFG6L was used as the graphite material.

As shown in Figure 5.4(a), the  $\text{Si}_{80}\text{W}_{20}/\text{G}$  20/50 electrode in half cell has good capacity retention during the first ten cycles and then suffers severe capacity fade, resulting in a poor capacity retention of 70% after 50 cycles. The severe capacity fade may be related to the applied high potential endpoint, which could oxidize the Si-alloy SEI layer. This capacity fade is mainly caused by electrode mechanical failure, since any Li loss due to side reactions with electrolyte can be compensated with lithium from the Li counter electrode. In the QDHC, no sudden capacity fade behavior is observed. In addition, it was found that the QDHC is seen to have a capacity fade of 54% after 50 cycles, which is even less half of the half-cell capacity fade, indicating that anode degradation resulting from electrode mechanical failure can behave differently in symmetric cells and half cells. Figure 5.4(b) and (c) show the potential profiles of the  $\text{Si}_{80}\text{W}_{20}/\text{G}$  20/50 electrode

in QDHCs and half cells, respectively. The endpoint potential of the Si<sub>80</sub>W<sub>20</sub>/G 20/50 electrode in the half cell is fixed at 5 mV during cycling. In contrast, the Si<sub>80</sub>W<sub>20</sub>/G 20/50 electrode in the QDHC has a lower endpoint potential of 48 mV at the first cycle. The lower endpoint potential then shifts up to 80 mV after 10 cycles. This increasing endpoint potential is likely responsible for the greater cell fade experienced by the symmetric cell compared to the half-cell.

The above result also reveals that the Si<sub>80</sub>W<sub>20</sub>/G 20/50 electrode has a lower lithiation depth in symmetric cells than in half cells, indicating that the anode volume change in symmetric cells is smaller. Therefore, the alloy should have experienced less mechanical failure in the symmetric cell compared to the half cell. To see if this is the case, after cycling for 50 cycles, the QDHCs were separated and cycled as individual half cells. These cells had substantially greater capacity than the Si<sub>80</sub>W<sub>20</sub>/G 20/50 electrode half cells after 50 cycles. The amount of capacity loss as measured by half-cells is equated with mechanical failure. This indicates that the Si<sub>80</sub>W<sub>20</sub>/G 20/50 electrodes suffer less mechanical failure when cycled in symmetric cells than in half cells. The amount of mechanical failure encountered by the Si<sub>80</sub>W<sub>20</sub>/G 20/50 electrode during cycling in the QDHC and half-cell formats are compared in Figure D.4. This effect must be kept in mind when comparing full cell and symmetric cell alloy cycling performance with half-cell cycling.

A lithium inventory and associated SEI growth for Si-alloy materials are difficult to quantify in the cases above. The main challenge is related to the presence of multiple degradation mechanisms and excess capacity. In the next part of this work, a method to measure the capacity fade specifically from SEI growth for Si-alloy electrodes will be proposed and the SEI growth behavior on Si-alloys will be studied.

## 5.5 The Measurement of SEI Growth and Repair

SEI growth, considered as a major source of cell capacity fade, needs to be carefully investigated. However, SEI growth on Si-alloys, often masked by other simultaneous degradation processes, is difficult to quantify. Considering that graphite is commonly blended with Si-based anode materials to improve electrode stability, this strategy is also used here in the measurement of the SEI growth capacity. Benefits of this method are:

1. Graphite can act as an internal reference to stabilize the electrode endpoint potentials during cycling.
2. Electrode mechanical failure may be suppressed.
3. Si-based materials have been used in commercial LIBs by blending them into graphite electrodes [210]. It is practical to evaluate the SEI growth on Si-alloy materials in the same environment in which they will be utilized.

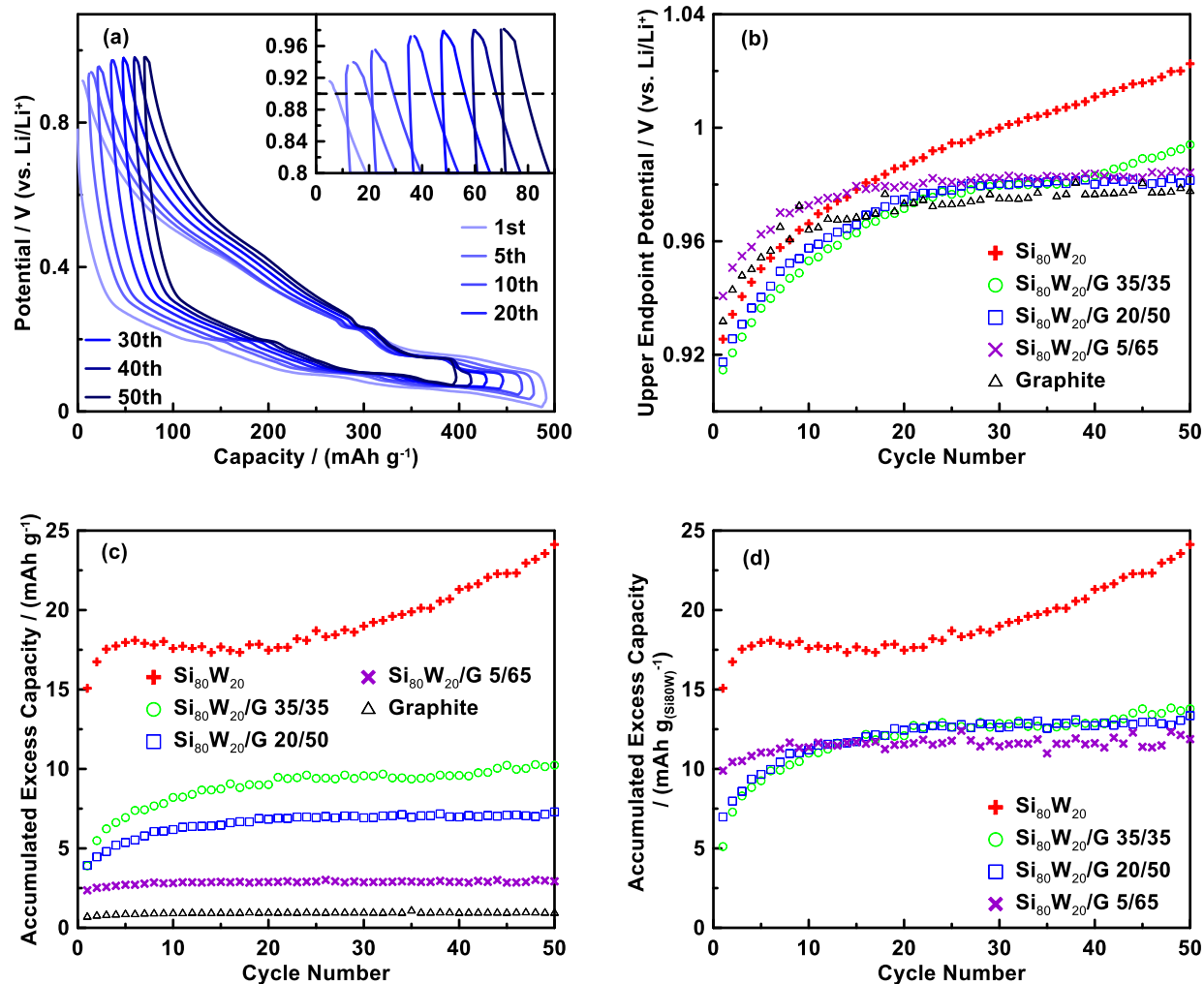


Figure 5.5 (a) Potential curves of a  $\text{Si}_{80}\text{W}_{20}/\text{G}$  20/50 QDHC at various cycles. The inset in (a) shows an expanded view of potential curves above 0.8 V. A summary of (b) upper endpoint potential and (c) accumulated excess capacity versus cycle number of  $\text{Si}_{80}\text{W}_{20}$ , graphite, and various  $\text{Si}_{80}\text{W}_{20}/\text{G}$  electrodes in QDHCs. (d) Accumulated excess capacity of  $\text{Si}_{80}\text{W}_{20}$  in various  $\text{Si}_{80}\text{W}_{20}/\text{G}$  blended electrodes when cycled in QDHCs, with a comparison to a neat  $\text{Si}_{80}\text{W}_{20}$  electrode.

Figure 5.5(a) shows the potential profiles of a  $\text{Si}_{80}\text{W}_{20}/\text{G}$  20/50 electrode cycled in a QDHC at various cycles with a practical cut-off potential of  $\pm 0.9$  V. The inset in the figure clearly shows that the increase of the upper endpoint potential has been suppressed after 20 cycles. Figure 5.5(b) shows a comparison of the endpoint potential trends for Si-alloy, Si-alloy/graphite, and graphite electrodes in QDHCs. While endpoint potential for the Si-alloy electrode QDHC continuously

increases, the Si-alloy/graphite blended electrode QDHC endpoint potentials behave the same as the pure graphite QDHC; where the endpoint potentials become stabilized after about 20 cycles. When the alloy content is high, as in the Si<sub>80</sub>W<sub>20</sub>/G 35/35 electrode, the upper endpoint potential again begins to increase after 35 cycles. The suppression of the increase in upper endpoint potential in the alloy/graphite blended electrode coatings is due to the presence of graphite, which has a relatively flat potential curve near the lithiation endpoint. This has the desirable effect of limiting the lower potential cutoff shift, which, in turn, also keeps the upper potential endpoint of the paired electrode from shifting in the symmetric cell. In other words, the lower potential plateau of graphite effectively provides the symmetric cell with a built-in lower potential reference.

The effectiveness of different graphite contents on suppressing the upper potential endpoints of the symmetric cell electrodes from shifting can be more clearly seen in their differential capacity. Figure D.5(a) shows the 2<sup>nd</sup>, 30<sup>th</sup>, and 50<sup>th</sup> delithiation differential capacity curves of a graphite electrode cycled in a QDHC. Peaks corresponding to the delithiation of the 1<sup>st</sup> (~0.11 V), 2<sup>nd</sup> (~0.15 V), and 3<sup>rd</sup> (~0.23 V) stages of graphite are clearly visible. These peaks are also visible for the alloy/graphite blended electrodes cycled in QDHCs (Figure D.5(b-d)), however, as the graphite content decreases, the graphite staging peaks become broader and shift to higher potentials, especially for the Si<sub>80</sub>W<sub>20</sub>/G 35/35 electrode. This is indicative of an increase in polarization on the graphite component of the electrode when the alloy content is increased, which may be due to poorer electrical connection within the electrode. This polarization decreases during cycling, which might be attributed to the alloy electrode continually expanding during cycling, resulting in internal compressive forces and improved electrical contact. In addition to the polarization effect, lithium loss during cycling results in the disappearance of the stage-1 delithiation peak during cycling when the amount of graphite in the electrode is insufficiently high.

This occurs for the  $\text{Si}_{80}\text{W}_{20}/\text{G}$  35/35 and 20/50 electrode blends, shown in Figure D.5(c and d), after about 40 cycles and 48 cycles, respectively. When this plateau is not active, the graphite no longer acts as an internal potential limit in the QDHC and, as a result, the upper cutoff potential will begin to increase, as shown in Figure 5.5(b). In contrast, when sufficient graphite is added graphite polarization remains low and the stage 1 delithiation plateau can be maintained ( $\text{Si}_{80}\text{W}_{20}/\text{G}$  5/65 electrode blend and the  $\text{Si}_{80}\text{W}_{20}/\text{G}$  20/50 electrode blend between cycles ~20-50). As a result, the excess capacity can be effectively suppressed when sufficient graphite was added and, as a consequence, the excess capacity of the blended electrodes is much less than that of the alloy electrode. Furthermore, blended electrodes with higher graphite content have lower amounts the excess capacity, as shown in Figure 5.5(c).

To further understand the origin of the excess capacity, the accumulated excess capacity per  $\text{Si}_{80}\text{W}_{20}$  mass in blended electrodes is shown in Figure 5.5(d). This figure shows that the accumulated excess capacity of the  $\text{Si}_{80}\text{W}_{20}/\text{graphite}$  electrode becomes constant after 20 cycles. In contrast, when graphite is not present the excess capacity is higher and increases during cycling. Therefore, the use of Si-alloy/graphite composited electrodes can significantly suppress the excess capacity increase. Of course, there is a limit to this strategy, since if the alloy content in the electrode becomes too low, error in its contribution to the electrode capacity will become large.

Although half-cells have been often used to evaluate alloy electrode mechanical failure [48,211], Figure D.4 demonstrates that electrodes can have a different severity of mechanical failure when cycled in half cells and symmetric cells. Considering that one major difference between electrodes cycled in these two cell formats is the endpoint potentials,  $\text{Si}_{80}\text{W}_{20}/\text{G}$  blended electrodes with  $\text{Si}_{80}\text{W}_{20}/\text{G}$  ratios ranging from 100/0 to 5/65 were cycled in half-cells with several lower cutoff potentials, as shown in Figure D.6. The pure  $\text{Si}_{80}\text{W}_{20}$  electrodes suffered from some

initial capacity fade during the first 20 cycles. Such capacity fade phenomenon is due to mechanical failure. In contrast, the blended electrodes do not show this initial fade and generally exhibit less capacity fade as the graphite content is increased.

From Figure D.6, it is easy to conclude that the addition of graphite in the blended electrodes has reduced the capacity fade of the alloy. However, the good cycling of the graphite component could be masking fade in the alloy component of the electrode, especially when the alloy component becomes small. To deconvolute the alloy capacity from the graphite capacity, a simple assumption was made that the graphite component of the electrode has no capacity fade. This assumption is supported by the differential capacity plots of the QDHCs, shown in Figure D.5. From cycle 1-20, the graphite differential capacity staging peaks sharpen and polarization is reduced. After this, there is little change in the differential capacity excepting a reduction (or complete disappearance) in the stage 1 delithiation peak. For instance, even though the stage 1 differential capacity peak has disappeared after 30 cycles for the  $\text{Si}_{80}\text{W}_{20}/\text{G}$  35/35 electrode cycled in a QDHC, as shown in Figure D.5(d), the remaining staging peaks remain unaffected. This shows that the graphite active mass remains constant during cycling in these electrode blends and that the majority of the fade can be attributed to the alloy content.

According to the above analysis, the alloy contribution to the capacity fade can be deconvoluted from the total capacity of these blended electrodes by subtracting the graphite capacity. This is shown in Figure D.7 for half-cells of the different electrode blends cycled to a 5 mV lower potential limit, where the graphite capacity ( $336 \text{ mAh g}^{-1}$ ) was determined from a pure graphite half-cell. The alloy capacity and fade are roughly the same in the  $\text{Si}_{80}\text{W}_{20}/\text{G}$  20/50 and 10/60 electrodes. However, the alloy capacity is significantly lower and a higher capacity fade rate is observed for the  $\text{Si}_{80}\text{W}_{20}/\text{G}$  5/65 electrode. This effect is due to excessive polarization during

cycling on the alloy component, when the alloy content becomes low. At potentials below 0.4 V the cell current is carried by both the alloy and graphite active components of the electrodes. However, at potentials above 0.4 V only the anode component is active and must carry all of the current. At the lowest anode content of Si<sub>80</sub>W<sub>20</sub>/G 5/65 the alloy component only accounts for about 10% of the total electrode capacity. Therefore, at potentials above 0.4 V and for the C/5 rates used here the alloy component is cycling at a 1.8C effective rate. This causes increased polarization, leading to reduced capacity and increased fade. It should be kept in mind, however, that the alloy fade will be less in the symmetric cells than the half cells shown here, as discussed above in relation to Figure D.4. A further evaluation of the electrode mechanical failure can be done by measuring the electrode reversible capacity (in half cells) before and after cycling in symmetric cells.

According to the discussion above, Si<sub>80</sub>W<sub>20</sub>/G blended electrodes in symmetric cells have low excess capacity. Such cells are also expected to have very little fade. This is demonstrated in Figure D.8 for Si<sub>80</sub>W<sub>20</sub>/G 20/50 electrodes cycled in a DHC at 60°C. Before and after cycling 100 times in the DHC format, the individual cells of the DHC were cycled as half cells. The difference in half cell capacity during delithiation at C/20 rate before and after DHC cycling was used to measure the extent of fade from mechanical failure. No fade was detected by this method. Therefore, it was assumed that fade from mechanical failure was insignificant and capacity fade is primarily related to SEI growth on Si<sub>80</sub>W<sub>20</sub> and carbonaceous materials. Assuming that SEI growth on an electrode is equal to the sum of that on each electrode constituent [27], the expressions of side reaction capacity at  $i^{\text{th}}$  cycle can be presented as below:

$$q_M^{de}(i) \approx q_{SEI(M(C))}^{de}(i) + q_{SEI(M(C))}^{de}(i)' + q_{SEI(M(Si))}^{de}(i) + q_{SEI(M(Si))}^{de}(i)' \quad (M = A \text{ or } B) \quad (5.6)$$

$$q_M^{li}(i) \approx q_{SEI(M(C))}^{li}(i) + q_{SEI(M(C))}^{li}(i)' + q_{SEI(M(Si))}^{li}(i) + q_{SEI(M(Si))}^{li}(i)' \quad (M = A \text{ or } B) \quad (5.7)$$

where C and Si represent carbonaceous and Si-alloy materials, respectively. Future measurements should be conducted to also confirm the extent of fade from mechanical failure at the 30 °C and 45 °C temperature used for symmetric cell cycling and for all of the electrode blends. If fade from mechanical failure is present, then it can be easily measured and incorporated in the model by adding additional terms for this fade component in Equations (5.6) and (5.7).

To easily deconvolute the SEI growth on  $\text{Si}_{80}\text{W}_{20}$  from blended electrodes, it was assumed that the graphite component's SEI growth is independent of the alloy component, as observed for the graphite component capacity fade. In addition, DHCs were cycled with a constant C-rate cycling protocol. With this protocol, symmetric cells have an almost identical C-rate during each cycle, regardless of capacity fade. This cycling protocol enables the SEI growth on carbonaceous materials to be obtained as a function of cycle number (equivalent to a function of time in constant C-rate cycling) from DHCs containing graphite electrodes (Figure D.10). The amount of SEI growth capacity for these constant C-rate cycled graphite DHCs can then be used to estimate the graphite SEI growth capacity of the graphite component of alloy/graphite blended DHCs, also cycled at constant C-rate.

Figure D.9(a) compares the capacity fade of  $\text{Si}_{80}\text{W}_{20}$  electrodes cycled in DHCs with a constant current constant voltage (CCCV) cycling protocol and a constant C-rate CCCV cycling protocol to illustrate the difference between the two cycling methods. In this example, a pure alloy electrode is used, since irreversible Li loss will be greatest in this electrode and differences between the two cycling methods is most apparent. As shown in Figure D.9(b), the time per cycle of the symmetric cell cycled using a conventional CCCV cycling protocol decreases by about 40% after 50 cycles due to capacity fade, while the time per cycle of the cell cycled with constant C-rate cycling increases by only about 8%, which is primarily due to the error in estimating the initial

cycle capacity. The slow increase in cycle time of the h constant C-rate cycled cell is due to a longer CCCV step as cycling proceeds, presumably due to changes in cell impedance. The shorter cycling time of the conventional CCCV cycled cell means that there is less time for SEI growth per cycle and therefore, less lithium loss per cycle. As a result the fade is less for the conventional CCCV cycled cell, as shown in Figure D.9(a). Such a situation would not allow the SEI capacity from graphite to be deconvoluted by simple subtraction. In contrast, since constant C-rate cycled alloy/graphite blended cells and graphite cells will have spent about the same amount time per cycle at any given cycle number, this enables the graphite SEI component to be deconvoluted by simple subtraction. It should be noted, however, that in alloy/graphite blended electrodes, the graphite component will experience a larger proportion of time per cycle above 0.4 V (*i.e.* fully delithiated) than in a pure graphite cell. Therefore, graphite could potentially have decreased SEI growth per cycle in blended electrodes, especially with high alloy content. To gauge the potential impact of this effect, multiple alloy graphite blends were evaluated in this study. As will be shown below, the calculated SEI alloy growth is the same for all cells, showing that this effect is insignificant for the different electrode blends used in this study.

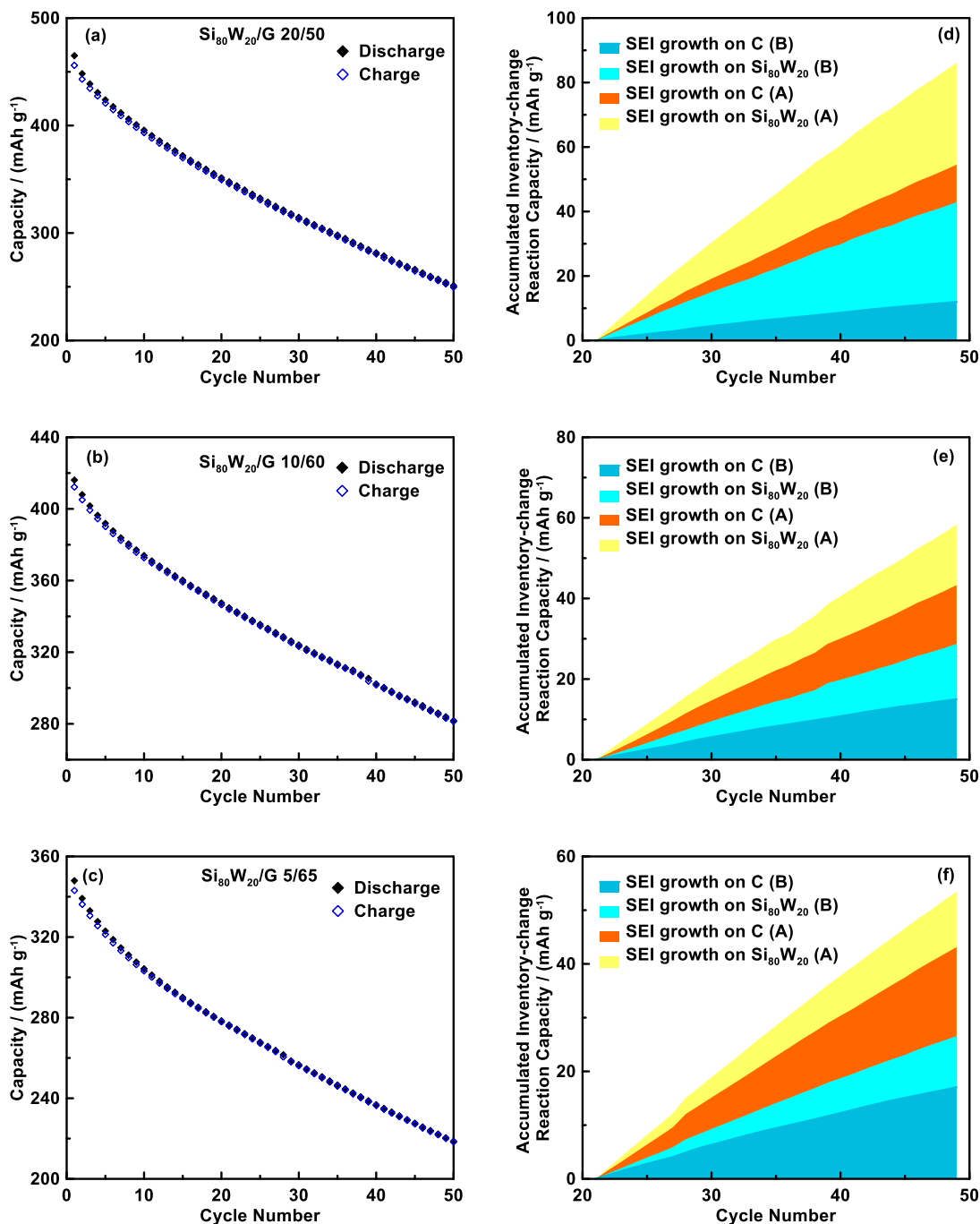


Figure 5.6 (a-c) Capacity and (d-f) corresponding accumulated inventory-change reaction capacity versus cycle number of Si<sub>80</sub>W<sub>20</sub>/G 20/50, Si<sub>80</sub>W<sub>20</sub>/G 10/60, and Si<sub>80</sub>W<sub>20</sub>/G 5/65 electrodes in DHCs, respectively. The DHCs were cycled with a constant C-rate protocol. In the legends, C represents carbonaceous materials, including graphite and carbon black. A and B represent electrode A and B, respectively. The inventory-change reaction capacity is analyzed only from cycle 21 to 50, since during these cycles the blended electrodes have negligible excess capacity increase and mechanical failure.

Figure 5.6(a), (b), and (c) show the capacity of Si<sub>80</sub>W<sub>20</sub>/G 20/50, Si<sub>80</sub>W<sub>20</sub>/G 10/60, Si<sub>80</sub>W<sub>20</sub>/G 5/65 electrodes cycled at a constant C-rate in DHCs, respectively. These three types of blended electrodes have different capacity fade rates. For example, the capacity of the Si<sub>80</sub>W<sub>20</sub>/G 20/50 DHC drops by 215 mAh g<sup>-1</sup> after 50 cycles while the corresponding fade of the Si<sub>80</sub>W<sub>20</sub>/G 5/65 DHC is 130 mAh g<sup>-1</sup>. During these cycles, the blended electrodes have negligible increase in excess capacity. Assuming mechanical failure is insignificant, as discussed above, the capacity fade will only be related to SEI growth. Utilizing Equations (5.6) and (5.7), this fade was deconvoluted and presented as the SEI growth on the graphite and Si<sub>80</sub>W<sub>20</sub> electrode components for electrode A and B individually, as shown in Figure 5.6(d) and (e), and (f). Results show that the accumulated capacity caused by SEI growth has a roughly linear trend with cycle number (nearly identical to time for constant C-rate cycling), both on graphite and Si<sub>80</sub>W<sub>20</sub>. This is consistent with previously reported linear SEI growth rates with time on graphite electrodes [47]. In addition, from Figure 5.6(d) and (e), and (f) it can be observed that the proportion of SEI growth on Si<sub>80</sub>W<sub>20</sub> increases with an increased amount of Si<sub>80</sub>W<sub>20</sub> in electrodes.

Figure 5.7 shows the accumulated SEI growth capacity on Si<sub>80</sub>W<sub>20</sub> per unit Si<sub>80</sub>W<sub>20</sub> mass in Si<sub>80</sub>W<sub>20</sub>/G 20/50, Si<sub>80</sub>W<sub>20</sub>/G 10/60, and Si<sub>80</sub>W<sub>20</sub>/G 5/65 electrodes. In these three electrodes, the accumulated specific SEI growth capacities on Si<sub>80</sub>W<sub>20</sub> are almost equivalent. The average specific SEI growth capacity per cycle on Si<sub>80</sub>W<sub>20</sub> in these three types of blended electrodes is about 2.0 mAh g<sup>-1</sup>, as shown in Figure 5.7(b). This result was achieved even with the low alloy content Si<sub>80</sub>W<sub>20</sub>/G 5/65 electrode, showing the robustness of the method. However, measurement error and increased polarization on the alloy will eventually cause measurement issues when the alloy content becomes too small (*e.g.*, the alloy content is below 1% by volume).

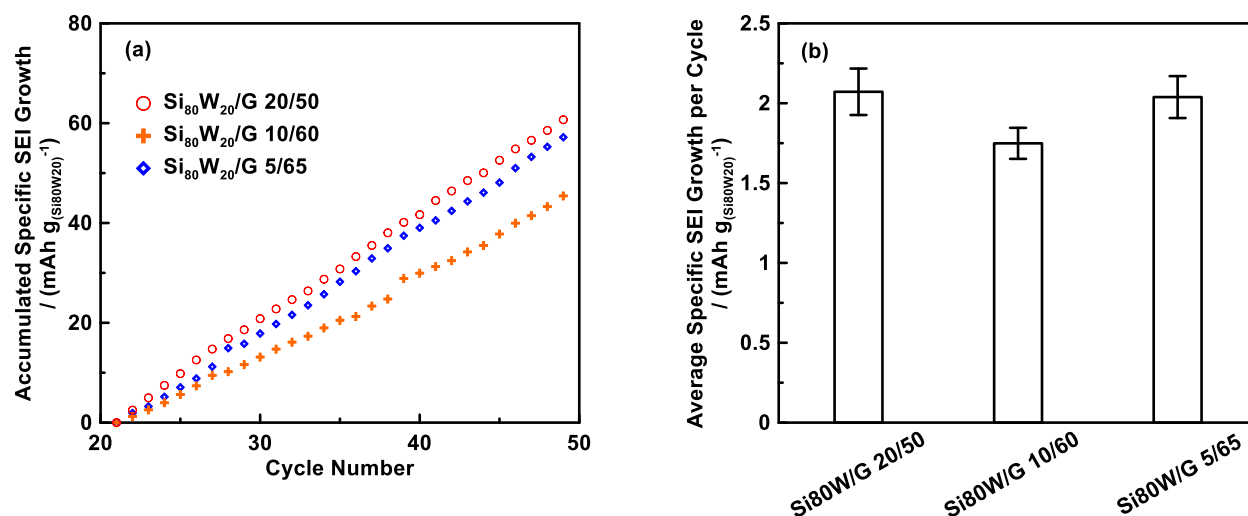


Figure 5.7 Accumulated specific SEI growth on Si<sub>80</sub>W<sub>20</sub> per Si<sub>80</sub>W<sub>20</sub> mass, versus cycle number of Si<sub>80</sub>W<sub>20</sub>/G 20/50, Si<sub>80</sub>W<sub>20</sub>/G 10/60, and Si<sub>80</sub>W<sub>20</sub>/G 5/65 DHCs cycled with a constant C-rate protocol. (b) A summary of the average SEI growth on Si<sub>80</sub>W<sub>20</sub> per cycle per Si<sub>80</sub>W<sub>20</sub> mass in these electrodes (between the 21<sup>st</sup> and 50<sup>th</sup> cycle).

To demonstrate the usefulness of the method for deconvoluting SEI growth, it was applied to different cycling conditions and electrode materials. To see if the effect of temperature on SEI growth, DHCs were constructed with Si<sub>80</sub>W<sub>20</sub>/G 20/50 electrodes and cycled at 45°C and 60°C. Figure 5.8(a) and (b) show the capacity vs. cycle number of the Si<sub>80</sub>W<sub>20</sub>/G 20/50 electrode DHCs at 45°C and 60°C, respectively. To ensure stable upper cut-off potentials throughout the measurements at these elevated temperatures only 40 charge/discharge constant C-rate cycles were conducted. The DHC of the Si<sub>80</sub>W<sub>20</sub>/G 20/50 electrode cycled at 45°C has a similar initial capacity, but a slightly higher capacity fade than the DHC of the Si<sub>80</sub>W<sub>20</sub>/G 20/50 electrode cycled at 30°C (Figure 5.6(a)). The DHC of the Si<sub>80</sub>W<sub>20</sub>/G 20/50 electrode cycled at 60°C has a significantly greater initial capacity, which is likely attributed to reduced polarization at this temperature. This cell also had an increased fade rate. The individual cells from the 60°C DHC were cycled as half cells before and after DHC cycling. These results (shown in Figure D.8) show that no fade from electrode mechanical failure occurred during the 60°C cycling. Since no fade from mechanical

was observed at this extreme temperature, no mechanical failure was also assumed for the cells cycled at lower temperatures.

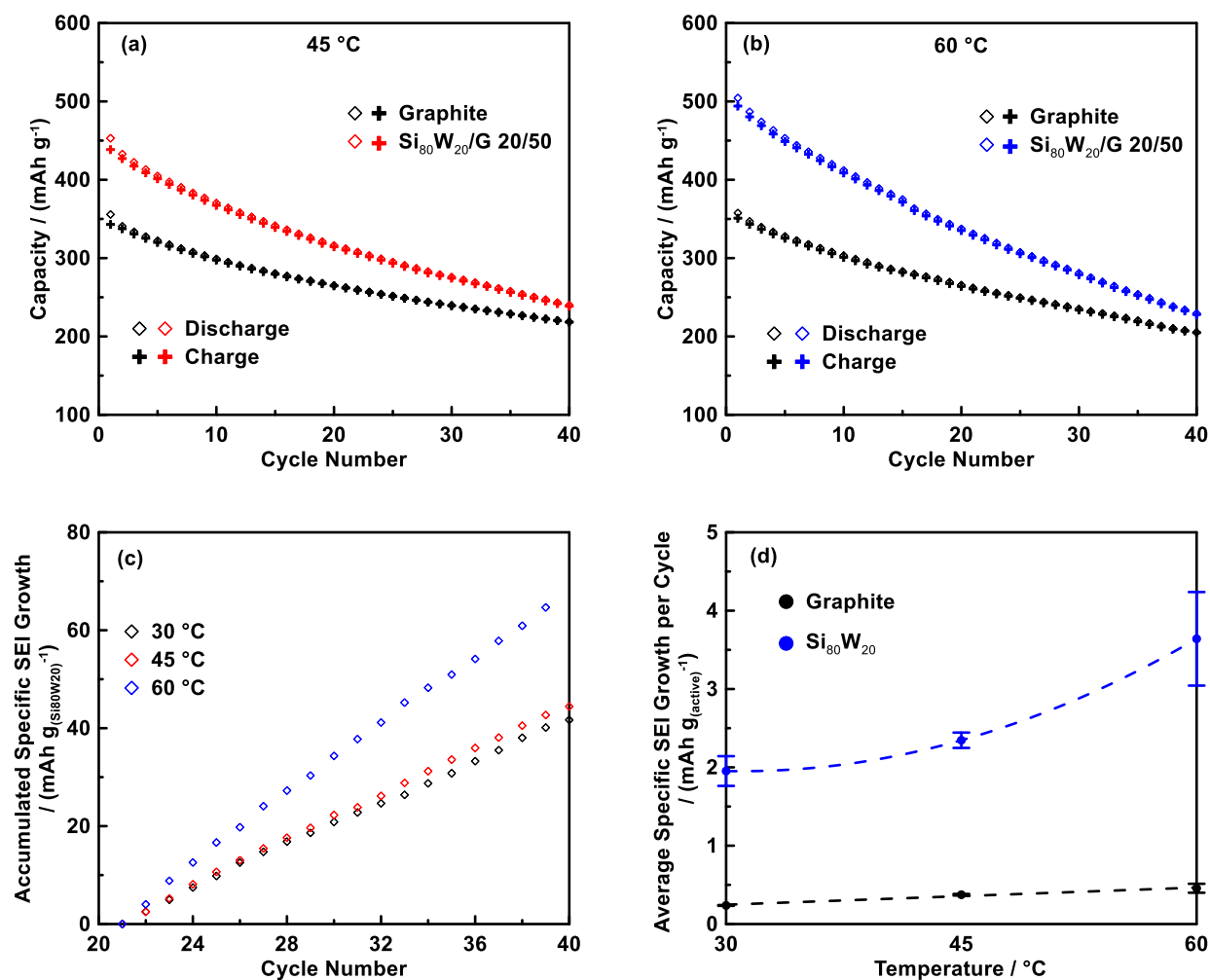


Figure 5.8 Capacity versus cycle number of graphite and Si<sub>80</sub>W<sub>20</sub>/G 20/50 electrodes in DHCs at (a) 45 °C and (b) 60 °C. The DHCs were cycled with a constant C-rate protocol. (c) The accumulated specific SEI growth on Si<sub>80</sub>W<sub>20</sub> per Si<sub>80</sub>W<sub>20</sub> mass versus cycle number for Si<sub>80</sub>W<sub>20</sub>/G 20/50 electrodes at 30 °C, 45 °C and 60 °C. (d) A summary of the average specific SEI growth on carbonaceous materials and on Si<sub>80</sub>W<sub>20</sub> per cycle at different temperatures. The average fade at 60 °C was evaluated between cycles 21 and 30. Error bars for Si<sub>80</sub>W<sub>20</sub> at 60 °C were calculated as the range of six samples. The other error bars were calculated as the range of four samples.

Figure 5.8(c) shows the specific accumulated SEI growth capacity on Si<sub>80</sub>W<sub>20</sub> at 30 °C, 45 °C and 60 °C. The average specific accumulated SEI growth capacity per cycle for the graphite and alloy components of the Si<sub>80</sub>W<sub>20</sub>/G 20/50 electrode are shown in Figure 5.8(d). The

accumulated specific SEI growth capacity per cycle is relatively low for graphite at all temperatures. As temperature increases from 30 °C to 60 °C, the specific accumulated SEI growth capacity on graphite increases roughly linearly from about 0.2 mAh/g·cycle to 0.4 mAh/g·cycle. This increase in SEI growth on graphite with temperature is consistent with previous reports [24]. In contrast, accumulated specific SEI growth capacity per cycle on Si<sub>80</sub>W<sub>20</sub> is much higher than graphite, increasing from about 2 mAh/g·cycle to 3.6 mAh/g·cycle over the same temperature range. This increase is nonlinear, indicating that the rate of electrolyte reaction on the alloy component becomes accelerated with increasing temperature. These results indicate that the severe SEI growth on Si-alloy materials could be a challenge to overcome, particularly at elevated temperatures.

Such measurements can be used to compare the electrolyte reactivity on different Si-alloy compositions, such as Si<sub>75</sub>W<sub>25</sub> and Si<sub>80</sub>W<sub>20</sub>. Figure D.11(a) shows the capacity vs. cycle number of a Si<sub>75</sub>W<sub>25</sub>/G 20/50 DHC. Because of its higher W-content Si<sub>75</sub>W<sub>25</sub> has a lower capacity and volume expansion compared to Si<sub>80</sub>W<sub>20</sub>. As a result, the fade rate of the DHC is also less. As shown in Figure D.11(b) this results in less accumulated SEI growth per cycle as measured per gram of active material or as a percent of its reversible capacity. Therefore, as expected, less SEI growth occurs when alloy expansion is less. By this method a balance between SEI growth and reversible capacity might be determined for new alloy materials.

Finally, such measurements can additionally be applied to establish an effective comparison of electrolyte reactivity between completely different Si-based active material chemistries. For example, SiO is now a commonly used commercial anode material. Figure D.12(a) and (b) show the capacity of SiO/G 20/50 and 10/60 blended electrode half cells before and after cycling as DHC format. No mechanical failure could be detected in these cells during the DHC

cycling. Therefore, as with the Si<sub>80</sub>W<sub>20</sub>/G cells, all of the fade measured during DHC cycling could be attributed to SEI growth. Figure D.13(a) and (b) show the capacity vs. cycle number of the DHCs prepared using SiO/G 20/50 and 10/60 blended electrodes. The accumulated capacity from SEI growth for these cells was determined in the same manner as described above for the Si<sub>80</sub>W<sub>20</sub>/G blended electrodes. Figure D.13(c) and (d) shows the accumulated capacity from SEI growth for each component in these cells. As with the Si<sub>80</sub>W<sub>20</sub>/G blended electrodes, the SEI growth increases linearly with cycle number for all active electrode components. Figure D.13(e) compares the average accumulated specific SEI growth capacity per cycle on SiO with that of Si<sub>80</sub>W<sub>20</sub>. This is plotted as a percent of the reversible capacity in Figure D.13(f). SiO has an average SEI growth capacity per cycle of 1.5 mAh g<sup>-1</sup> (0.13% of its reversible capacity), which is much lower than the average SEI growth capacity on Si<sub>80</sub>W<sub>20</sub> (2.0 mAh g<sup>-1</sup> or 0.34% of its reversible capacity).

## 5.6 Conclusions

A Li inventory model has been proposed to describe and interpret the anode capacity fade in symmetric cells containing Si-alloy materials. Multiple anode degradation mechanisms, *i.e.* electrode mechanical failure and SEI growth and repair have been included in the model, as well as the excess capacity, affected by the electrode upper endpoint potential shift. On the basis of this model, a correlation between the symmetric cell capacity fade and undergoing multiple mechanisms to change the amount of active Li has been established. Furthermore, it was found that blending graphite with Si-alloy materials is an effective way to eliminate the effects of the upper endpoint potential shift. Moreover, DHCs were found to be an effective symmetric cell format that can be used to quantitatively determine capacity contributions from SEI growth and mechanical failure, which is not possible to do in conventional symmetric cells. Using these

techniques the SEI growth on Si-alloys have been quantitatively determined in Si-alloy/graphite blends. This includes a comparison of SEI growth on Si-alloy vs. graphite, the temperature dependence of SEI growth on Si-alloy, a comparison of SEI growth on Si-alloys with different degrees of volume expansion, and finally, a comparison of SEI growth on Si-alloy materials with different material chemistries. It is believed that this method will be highly useful for the measurement of capacity degradation in Si-alloy and other materials and therefore could be an extremely useful tool for future battery materials development.

## CHAPTER 6 Current-corrected Cycling Strategies for True Electrode Performance

### Measurement and Prolonged Cell Cycle Life

This chapter was reproduced from the following peer-reviewed article:

Zilai Yan, Benjamin Scott, Stephen L. Glazier, Mark N. Obrovac, Current-Corrected Cycling Strategies for True Electrode Performance Measurement, *Batteries & Supercaps*, doi.org/10.1002/batt.202100345. Figures and text in this chapter are reproduced with permission. Copyright 2021, Wiley-VCH GmbH.

Z. Yan and M.N. Obrovac proposed the research plan. Z. Yan performed experiments. Benjamin Scott provided help to establish the current-corrected cycling tests on Maccor. Stephen Glazier provided pouch cells. M.N. Obrovac provided guidance and participated in experimental design. Z. Yan and M.N. Obrovac prepared the manuscript.

#### 6.1 Introduction

Towards a modern society with zero CO<sub>2</sub> emissions, rechargeable batteries have been identified as a key technology, enabling electric vehicles and emerging as a strong candidate for grid energy storage [3,212,213]. Challenges remain, for the development of batteries with higher energy density, longer service lifetime, improved safety, faster rate, and lower cost [214,215]. To improve battery performance, extensive research in new electrodes has taken place via their synthesis, and evaluation for their electrochemical performance [216,217].

One of the most common strategies to investigate electrode performance is the utilization of galvanostatic cycling [218–220]. In each charge/discharge step, a constant current is applied until a designed potential is reached. The C-rate is widely used to describe the discharge/charge rate and is defined as the current at which a cell can be fully charged or discharged in one hour. A cell's cycling rate is commonly expressed in terms of the C-rate as C/#, where # is the number of

hours desired to reach the end of discharge or charge [221]. This key parameter is often presented along with measured capacity since the cell/electrode capacity is a strong function of the cycling rate.

For traditional galvanostatic cycling (TGC), the current value is generally set according to the predicted cell/electrode capacity and remains unchanged throughout the test. To test electrode performance under different rates (*e.g.* in a rate cycling test), a universal current value (in most cases obtained from the theoretical capacity at low rates) is unfortunately used, due to the difficulty in predicting the capacity under these rates [222,223]. In reality, high-rate performance is likely measured at a much higher rate than the designed rate because of significantly declined cell capacity due to polarization/diffusion effects. Available data at designed cycling rates is challenging to gather, seriously hindering high-rate battery development [224]. In addition, electrodes suffer degradation and capacity loss. This also results in accelerated actual cycling rates [55]. For example, if an electrode is initially evaluated at a designed rate of  $C/5$  but suffers 50% capacity loss during cycling, this means that during cycling the actual cycling rate continuously increases from  $C/5$  to  $C/2.5$ . Figure E.1 illustrates the relationship between capacity retention and the actual cycling rate. As the cell capacity becomes reduced, then the actual cycling rate increases. If the electrode loses its capacity significantly, the cycling rate can rise to extremely high values. Since cell polarization (caused by high-rate cycling) also reduces capacity, the observed performance of an electrode during TGC at high rates has little to do with its ability to operate under a fixed discharge/charge time.

In this study, a current-corrected galvanostatic cycling (CCGC) strategy is proposed, to ensure that electrodes and related electrochemical cells of interest are evaluated at designed cycling rates, while the TGC results are presented as a comparison. This advanced cycling strategy is

successfully implemented to evaluate electrode performance in long-term cycling and rate performance tests. The CCGC method is also investigated to examine its impact on the cycle life of commercial cells.

## 6.2 Experimental

Graphite electrodes (NOVONIX Battery Technology Solutions Ltd., Bedford NS, Canada) had a mass loading of  $7.35 \text{ mg cm}^{-2}$  and a press density of  $1.55 \text{ g cm}^{-3}$ . LiNiO<sub>2</sub> electrodes comprised LiNiO<sub>2</sub> (lab-made in this study), carbon black (Super C65), and PVDF (grade 301F, KYNAR) with a weight ratio of 96:2:2. The details of LiNiO<sub>2</sub> synthesis can be found in the APPENDIX E. An XRD pattern and SEM images of the synthesized LiNiO<sub>2</sub> is shown in Figure E.2. Lattice parameters and site occupations derived from Rietveld refinement are listed in Table S1. The synthesized LiNiO<sub>2</sub> is single-phase ( $\alpha$ -NaFeO<sub>2</sub> structure) with ~2% Ni present in the Li sites. Si electrodes comprised Si (99%, 325 mesh, Sigma-Aldrich), CB (Super C65), and LiPAA (from a 10 wt % LiPAA aqueous solution, with LiOH·H<sub>2</sub>O ( $\geq 98.0\%$ , Sigma-Aldrich) in distilled water) in a volumetric ratio of 70/5/25. An appropriate amount of N-methyl-2-pyrrolidone (NMP) or distilled water was added to the PVDF and LiPAA-based electrode mixtures, respectively, to adjust viscosity. Slurry mixing was conducted for one hour using a planetary ball mill (Retsch PM200) with three 13 mm tungsten carbide balls at 100 rpm. Electrode slurries were cast onto Al foil (for LiNiO<sub>2</sub> electrodes) or Cu foil (for Si electrodes) with a 0.004-inch coating bar. The coatings were air dried at 120 °C for 1 hour and then cut into  $1.35 \text{ cm}^2$  disks. All electrodes were heated under vacuum for 1 hour at 120 °C and assembled into cells with no further air exposure.

Coin cell construction was conducted in an Ar-filled glovebox using standard 2325 coin cell hardware. For cells with graphite or Si electrodes, 1M LiPF<sub>6</sub> in ethylene carbonate (EC):diethyl carbonate (DEC):fluoroethylene carbonate (FEC) (3:6:1 v/v/v, all battery grade from

BASF) was used as electrolyte. For cells with LiNiO<sub>2</sub> electrodes, 1M LiPF<sub>6</sub> in EC:DEC (1:2 v/v) was used as electrolyte. Two layers of Celgard-2300 separator and one layer of polyethylene blown microfiber nonwoven fabric (BMF) (3M Company) were used as cell separators. Each electrode was paired with a 2.57 cm<sup>2</sup> circular lithium metal (thickness of 0.38 mm, 99.9%, Sigma-Aldrich) electrode.

402040-size pouch-type Li-ion cells (capacity of ~275 mAh) used in this study used an artificial graphite negative electrode with a 12.4 mg cm<sup>-2</sup> loading mass, and a NMC622 positive electrode with a 19.4 mg cm<sup>-2</sup> loading mass. After vacuum drying overnight, 1.2 g of electrolyte (1.2 M LiPF<sub>6</sub> in EC: ethyl methyl carbonate (EMC): dimethyl carbonate (DMC)) 25:5:70 by weight with 2% wt. vinylene carbonate (VC)) was added into the dry pouch cells in a dry room with an operating dew point of -50 °C, then vacuum sealed. Formation cycles were conducted by holding cells at 1.5 V for 24 hours at 40 °C, then charging to 4.2 V at a rate of C/20, and then discharge to 3.8 V at C/20 rate.

Cells were evaluated using a Maccor Series 4000 Automated Test System and thermostatically controlled at 30.0 ± 0.1 °C, unless otherwise specified. Pouch cells were cycled between 2.8 V- 4.2 V.

### 6.3 Results and Discussion

In most cases, CCGC can be accomplished by setting the current of each cycle based on the capacity of the previous cycle, except the initial cycle which was determined from the theoretical capacity. However, it was found that this method failed to achieve convergent cycling results in the cases where the cycling capacity was highly sensitive to the current density (*e.g.*, graphite electrodes cycled at high rates (>1C) during the rate cycling in this work). Therefore, this

was resolved by setting the current according to the average capacity from the previous four cycles (starting from the 5<sup>th</sup> cycle) for cycling rate testing. Despite this, small oscillations in current were still observed. In this case, the initial-cycle current was also determined from the theoretical capacity. From the second to the fourth cycle, the current was determined by the average capacity of previous cycles. Ideally, common optimization algorithms, such as gradient descent, should be used if enabled by the charger's software, in order to efficiently find an optimized current to measure electrode performance at the designed rate.

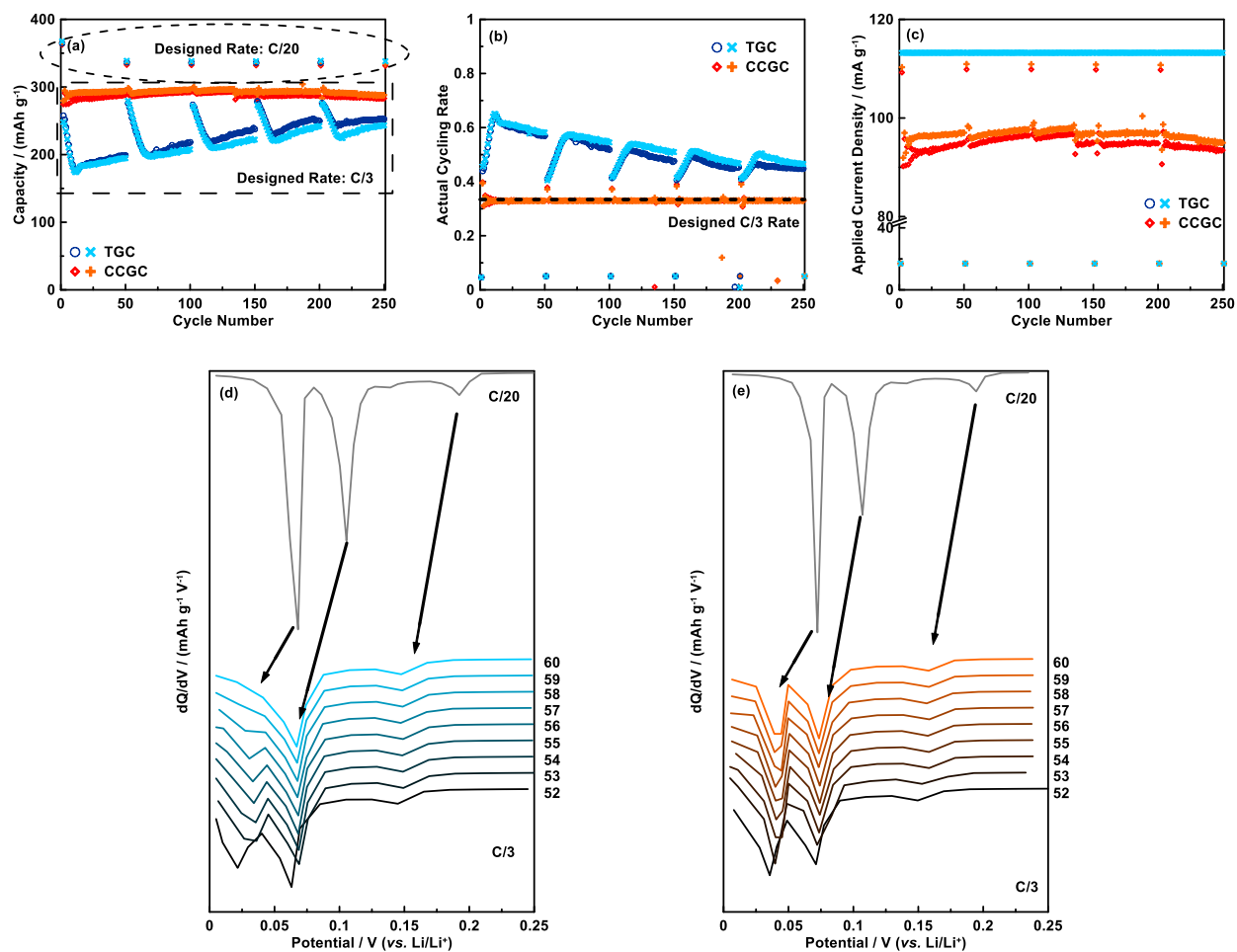


Figure 6.1 (a) Lithiation capacity, (b) the actual cycling rate, and (c) the applied current density of graphite electrodes in half cells cycled with CCGC and TGC protocols. In each 50 cycles, the graphite electrodes were first cycled at the rate of C/20, followed by 49 cycles at the rate of C/3 between 5 mV and 0.9 V. The dQ/dV curves of the graphite electrodes at indicated cycle number, cycled with (d) TGC and (e) CCGC protocols. Arrows indicate how the differential capacity peaks of graphite are shifted between C/20 and C/3 cycling rates.

Figure 6.1(a) shows the capacity vs. cycle number of graphite electrodes cycled under CCGC and TGC conditions. When graphite electrodes were cycled at a slow C/20 rate, the graphite capacity remained constant and is nearly identical for both cycling methods, even after 250 cycles. This result indicates that the graphite electrodes remained highly reversible throughout this test. Differences in capacities become apparent for electrodes cycled at a C/3 rate. For each 50-cycle loop, graphite electrodes cycled under TGC conditions showed rapid initial capacity fade during the first 10 cycles and then slightly recovered their capacity (the reasons for this behavior are explained below). Correspondingly, during TGC the actual cycling rate increased during the initial capacity fade of each 50-cycle loop to almost as twice the designed rate (as shown in Figure 6.1(b)) since the applied current density during the TGC test remained unchanged, as shown in Figure 6.1(c). In contrast, the applied current density at each cycle was actively modified in the CCGC method. For example, as shown in Figure 6.1(c), during CCGC a relatively high current density ( $\sim 110 \text{ mA g}^{-1}$ ) was applied during the initial C/3 cycle in each 50-cycle loop, since this rate was based on the previous cycle's capacity, which was conducted at a lower C/20 rate and consequently had a high reversible capacity of  $\sim 330 \text{ mAh g}^{-1}$ . According to the CCGC protocol, the current density was quickly modified to  $\sim 96 \text{ mA g}^{-1}$ , due to the relatively smaller reversible capacity measured at the C/3 cycling rate. As a result, the graphite capacity remained stable at  $\sim 290 \text{ mAh g}^{-1}$  during CCGC cycling (Figure 6.1(a)) and the actual cycling rates were well controlled, staying at the designed C/3 rate (Figure 6.1(b)). Moreover, as shown in Figure 6.1(c), despite the continual adjustments in current, the applied current density remained relatively stable at about 90 - 95 mA/h/g during C/3 cycling. Nevertheless, the CCGC method could be improved further to limit small current oscillations at high rates if the simple method of averaging the capacities of previous cycles to determine the cycling rate of the next cycle was modified, *e.g.* by utilizing the gradient

descent method, as mentioned above, (which could not be accommodated with the utilized charger's software) or at least by only including those previous cycles measured at the same rate in the averaging.

Figure 6.1(d) and (e) show differential capacity curves of graphite cycled under C/3 TGC and CCGC conditions, respectively, during cycles 52-60. This cycling range corresponds to the region of severe fade in the TGC cycled cell during the first 10 cycles of the second 50-cycle loop. Also shown in each figure is the differential capacity curve of graphite cycled at C/20 rate for reference. Graphite has three major dQ/dV peaks at  $\sim 0.2$  V,  $\sim 0.1$  V, and  $\sim 0.07$  V during slow lithiation. These three peaks correspond to staging phenomenon, due to the formation of  $\text{LiC}_{24}$ ,  $\text{LiC}_{12}$ , and  $\text{LiC}_6$ , respectively [225]. During fast charging (at the C/3 rate), the dQ/dV curves become broader and are shifted towards low potentials for both the TGC and CCGC methods, as shown in Figure 6.1(d) and (e). The peaks corresponding to  $\text{LiC}_6$  formation shift from  $\sim 0.07$  V at C/20 to  $\sim 0.03$  V at C/3. This peak is heavily affected by the induced polarization using TGC, resulting in capacity loss and poor cycling performance. A slight recovery in the capacity after the initial 10 cycles is also related to a partially improved kinetics during  $\text{LiC}_6$  formation. Figure E.3 shows dQ/dV curves of the graphite electrode between cycles 60-100 for the TGC method. The  $\text{LiC}_6$  formation peak appears after cycle 65 lithiation endpoint. The intensity of this peak keeps growing during these cycles. In contrast, since the cell cycled utilizing CCGC is charged and discharged at a lower and more constant rate, its differential capacity peaks are sharper and show less variability between cycles. In addition, the narrower  $\text{LiC}_6$  formation peak does not become truncated by the lower cutoff potential and retains its capacity due to the stabilized cycling rate.

Figure E.4 shows the average overpotential (calculated by the area between charge and discharge curves divided by the capacity) of the graphite electrodes cycled with TGC and CCGC.

The average overpotential can be considered as the sum of inherent zero-current potential hysteresis and cell-resistance induced polarization [226]. At a C/20 rate, graphite electrodes have a similar overpotential of  $\sim 0.04$  V under these two cycling methods. At a C/3 rate, CCGC results have an average overpotential of  $\sim 0.085$  V at initial cycles, that gradually increases up to  $\sim 0.12$  V after 250 cycles. At the same rate, TGC results have a higher overpotential of 0.02-0.03 V during cycling.

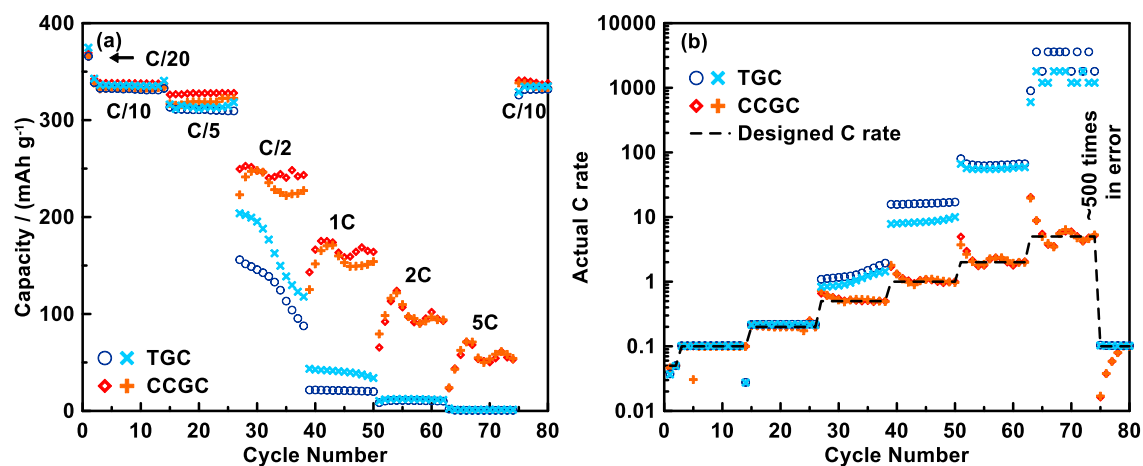


Figure 6.2 (a) Lithiation capacity and (b) the actual cycling rate of graphite electrodes cycled at different rates using CCGC and TGC.

Figure 6.2(a) shows the capacity vs cycle number of graphite electrodes cycled at different rates ranging from C/20 to 5C using TGC and CCGC methods. For TGC, the capacity decreases quickly at rates higher than C/5 and becomes negligible when the rate is  $\geq 2C$ . This is because the actual cycling rates are much higher than the designed rates when the capacity becomes lower due to polarization, as shown in Figure 6.2(b). For instance, at a designed 5C rate, the observed actual cycling rate for TGC is 1200C – 3600C, about 500 times in error. In addition to the low

capacities at high rates, at C/2 the capacity is not stable, due to the increasing overpotential, which causes staging plateaus to be truncated by the lower potential cutoff.

In contrast, the actual cycling rates are well managed with the CCGC method. Since the cycling current is based on the average cell capacity of the previous four cycles (CCGC results based on the average cell capacity of less than previous four cycles were not convergent in this case), the first cycle of each rate step has a low capacity (Figure 6.2(a)) and an actual cycling rate that is higher than the designed rate (Figure 6.2(b)). As shown in Figure 6.2(b), as cycling proceeds, the current then corrects itself so that the actual current approaches the designed current after a few cycles. For subsequent cycles, there are small oscillations in the actual rate around the designed rate. This is due to overcorrection of the cell current. Again, some common optimization methods, such as gradient descent, should be adapted in future work as an efficient strategy for this current adjustment. Nevertheless, for the simple averaging method used here, the oscillations become small as cycling proceeds at the same rate. Here, the level of accuracy from these small oscillations ( $\pm < 10.6\%$  of the designed rate during the last five cycles) was deemed acceptable.

The differences between the TGC and CCGC results in Figure 6.2(b) are remarkable. Even at 5C cycling, the graphite electrode still can deliver a capacity of  $\sim 50 \text{ mAh g}^{-1}$  utilizing CCGC. Moreover, the impact of increasing polarization on capacity is significantly reduced for CCGC, so that there is no observable capacity fade in each rate step (contrasted to the rapid fade of the same electrode at C/2 for TGC cycling). It is believed that the CCGC rate test results shown in Figure 6.2(a) provide significant additional information to the TGC results and even may be superior for gaining practical knowledge about materials rate performance. For instance, if a device requires a cell to charge and discharge in 2 hours, it can be easily seen from the CCGC results that, when designing such a cell, graphite should be assumed to have a capacity of about 250 mAh/g. In

contrast, the TGC results provide no useful information on how such a cell should be designed (the actual charge and discharge time by TGC method should be 1.3 hours, based on the theoretical capacity of graphite,  $372 \text{ mAh g}^{-1}$ ). The CCGC method can provide much needed information on electrode performance, especially at high rates, and will therefore likely be highly beneficial for researchers in designing high-rate batteries.

The use of CCGC as a method to investigate the degradation of electrode materials was also explored. Here materials degradation refers to processes that cause the loss of active lithium and/or the loss of sites available for lithium insertion, resulting in capacity fade. Most often, degradation processes are accompanied by an increase in electrode overpotential, either as true hysteresis or increased polarization, which can also cause capacity fade. When TGC is used, the actual cycling rate increases as material degradation occurs, further increasing impedance, and further inducing capacity fade. This makes it difficult to understand how much capacity fade is coming from increased impedance/increased actual cycling rate and how much fade is attributable to materials degradation.

$\text{LiNiO}_2$  is well known to suffer from capacity fade due to cation mixing and structural degradation associated with the oxidation of  $\text{Ni}^{2+}$  in  $\text{Li}^+$  sites during delithiation [55,227]. This causes both increased impedance and trapped  $\text{Li}^+$  and empty  $\text{Li}^+$  sites that are inaccessible towards lithiation. Figure 6.3 shows the cycling performance of  $\text{LiNiO}_2$  cycled under CCGC and TGC conditions. Differential capacity plots of the same cells are shown in Figure 6.3(c) and (d). Under these two methods, the  $\text{LiNiO}_2$  electrodes have the almost capacity fade behavior during the first 70 cycles. During this time, overpotential in both cells increases in the same manner, as shown in Figure 6.3(b). CCGC cycling has no impact on this increased polarization, which may indicate a true electrode performance. The increased polarization results in the 4.2 V delithiation differential

capacity peak becoming truncated by the upper cutoff potential, resulting in the observed capacity fade. Differences between the TGC and CCGC methods become observable after 70 cycles, where the capacity retention of CCGC cycled  $\text{LiNiO}_2$  becomes higher than  $\text{LiNiO}_2$  cycled utilizing TGC.

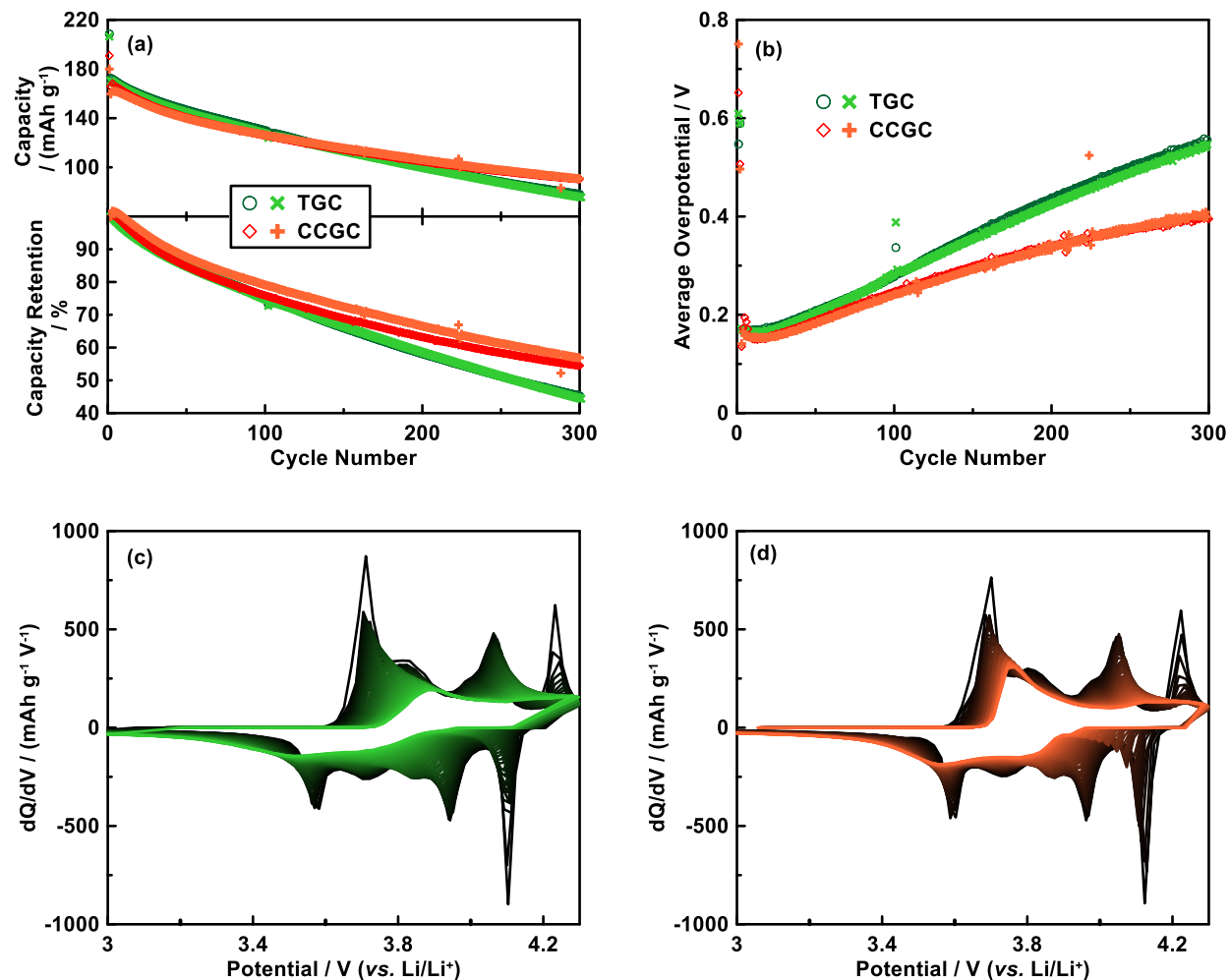


Figure 6.3 (a) Delithiation capacity (top panel) and capacity retention (bottom panel) of  $\text{LiNiO}_2$  electrodes cycled on the basis of TGC and CCGC. The initial cycle was set at the rate of C/20, followed by the cycling at C/2 rate. The actual cycling rate for  $\text{LiNiO}_2$  electrodes under TGC at the second delithiation is C/1.4. (b) Average overpotential of the  $\text{LiNiO}_2$  electrodes cycled by TGC and CCGC. The  $dQ/dV$  curves between 2<sup>th</sup> and 300<sup>th</sup> cycle of the  $\text{LiNiO}_2$  electrodes (c) TGC and (d) CCGC. Later cycles are towards either green or orange.

After 300 cycles, the capacity retentions of  $\text{LiNiO}_2$  electrodes evaluated by CCGC and TGC are  $\sim 56\%$  and  $\sim 45\%$ , respectively (Figure 6.3(a), bottom panel). As shown in Figure 6.3(b)

after cycle 70, cell polarization increases much faster under TGC than that under CCGC. This result indicates that the TGC can induce additional polarization during electrode degradation, resulting in excessive capacity fade. This effect is reduced in CCGC cycling, which is less susceptible to polarization induced capacity fade.

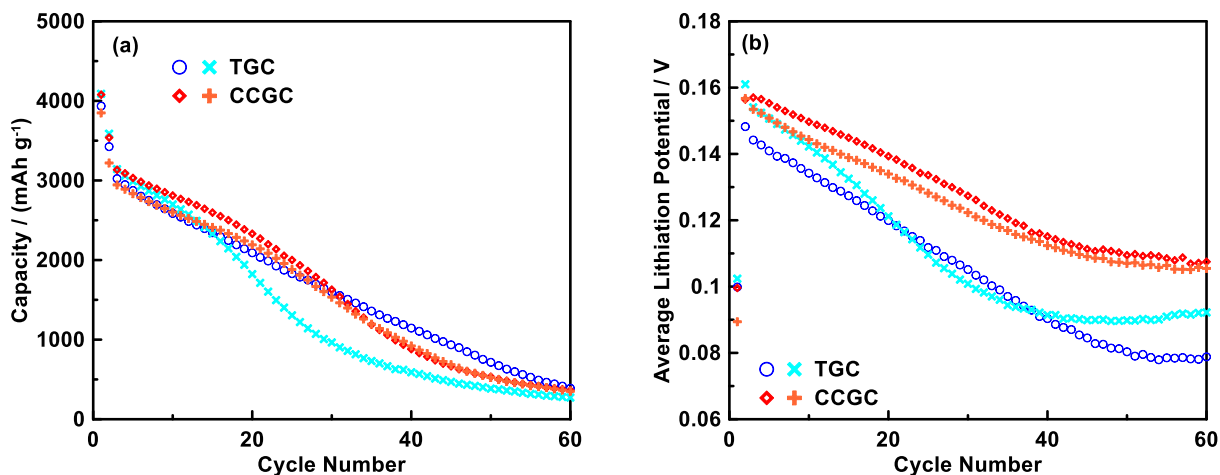


Figure 6.4 (a) Lithiation capacity of Si electrodes cycled with TGC and CCGC. The initial cycle was set at the rate of  $C/20$  between 5 mV-1.5 V. The following cycles were set at  $C/4$  between 5 mV-0.9 V. The actual cycling rate for Si electrodes under TGC at the second lithiation is  $C/3.9$ . (b) Average lithiation potential of the Si electrodes cycled by TGC and CCGC.

Si is another electrode material that suffers from severe degradation during cycling. During lithiation and delithiation, Si undergoes a large volume expansion and contraction. This results in SEI growth which causes increased impedance polarization. In addition, the volume expansion and formation of  $\text{Li}_{15}\text{Si}_4$  during cycling can induce electrode fracture, resulting in capacity fade from the disconnection of active material. The Si potential curves of the initial cycle (at  $C/20$  rate) of the Si cells tested with TGC and CCGC are identical, as shown in Figure E.4. Figure 6.4(a) shows the capacity vs. cycle number of Si electrodes cycled with TGC and CCGC methods. There are inconsistent results in the capacity fade of the two TGC cells. One cell showed linear fade over

the entire 60 cycles, while the other TGC cell had the same behavior over the first 15 cycles, but then suffered from severe capacity fade. Figure E.5(a-d) show the  $dQ/dV$  curves of the two TGC cells at the 2<sup>nd</sup>, 12<sup>th</sup>, 20<sup>th</sup>, and 40<sup>th</sup> cycles, respectively. The cell exhibiting severe nonlinear capacity fade has a single delithiation peak at  $\sim 0.45$  V, corresponding to  $Li_{15}Si_4$  delithiation. This indicates that  $Li_{15}Si_4$  was formed during the previous lithiation half-cycle. The  $dQ/dV$  curve of the cell with linear fade, also comprises a sharp peak due to  $Li_{15}Si_4$  delithiation, but also has a significant component due to the delithiation of lithiated amorphous Si ( $a-Li_xSi$ ), which consists of two broad differential capacity peaks at about 0.3 and 0.5 V. As cycling proceeds, the  $Li_{15}Si_4$  delithiation peak area becomes reduced, and by cycle 40 (Figure E.5(e)) the  $dQ/dV$  curve of this cell can almost be completely assigned to the delithiation of  $a-Li_xSi$ . This behavior is characteristic of increasing impedance polarization, resulting in  $Li_{15}Si_4$  formation suppression [50]. The  $Li_{15}Si_4$  formation is heavily affected by the lithiation rate [50]. This is reflected in Figure 6.4(b), which shows the average lithiation potentials of the Si electrodes. Due to the poor cycling-rate management by the TGC method, the overpotentials of the TGC cells are inconsistent.

In contrast, there is high consistency in the capacity fade and average lithiation potential of the CCGC results. As shown in Figure 6.4(b), the overpotential of the CCGC cells was reduced compared to the TGC cells. As a result,  $Li_{15}Si_4$  formed in both CCGC cycled cells (as shown by the  $Li_{15}Si_4$  delithiation peak in the  $dQ/dV$  curve in Figure E.5(e)). As with the TGC cell that showed severe  $Li_{15}Si_4$  formation, the CCGC cells both had severe nonlinear fade. This is consistent with  $Li_{15}Si_4$  formation being associated with alloy fracturing. In summary, for Si electrodes which are highly sensitive to overpotential, CCGC cycling resulted in greater consistency in cycling results due to its use of a consistent cycling rate.

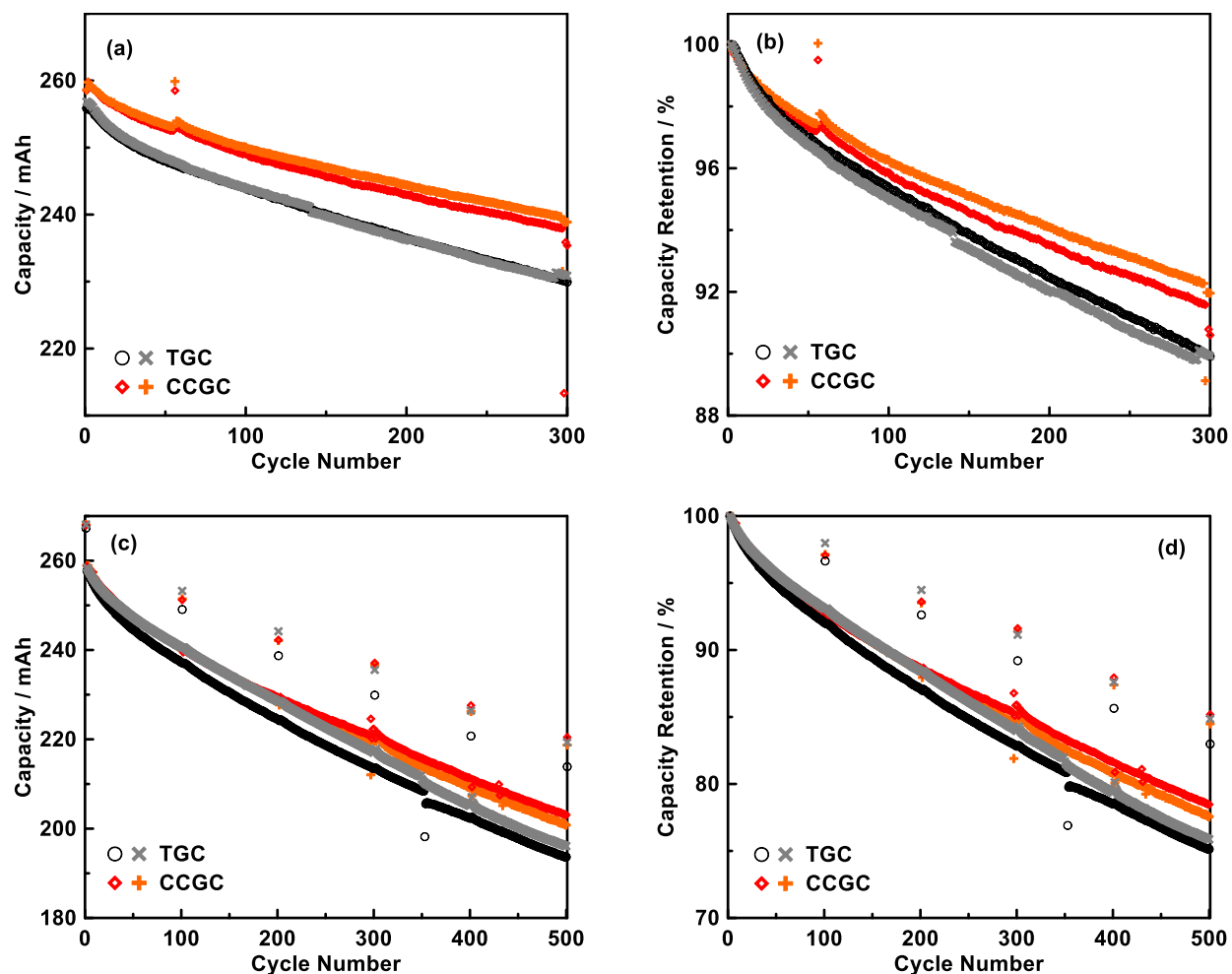


Figure 6.5 (a) Capacity and (b) capacity retention of the Li-ion pouch cells cycled at 30 °C on the basis of TGC and CCGC. Cells were charged at the rate of 1C, trickled until the current below  $C/5$ , then discharged at  $C/2$  rate. A power outage occurred near the  $\sim 300^{\text{th}}$  cycle. (c) Capacity and (d) capacity retention of the Li-ion pouch cells cycled at 45 °C on the basis of TGC and CCGC. For these cells, in every 100 cycles, cells were initially charged and discharged at  $C/5$  rate, then charged at 2C rate, held at the upper potential limit until the current dropped below  $C/2$ , and then discharged at  $C/2$  rate for the following 99 cycles.

Figure 6.5 shows the impact of the CCGC method on the cycle life of pouch-type Li-ion cells at a  $C/2$  rate. To reflect real-world charging conditions, the constant-current-constant-voltage charging protocol (CCCV) is adapted here: during each charge process, the constant current step is followed by a constant potential step, holding the cell at high potentials until the current drops below a designed value. At a 1C rate at 30 °C (Figure 6.5(a)), the Li-ion cells cycled with the

CCGC method delivered a capacity of ~256 mAh during the first few cycles, 5 mAh higher than the cells cycled by the TGC method. The difference in the delivered capacity further increases during cycling. Approaching the 300<sup>th</sup> cycle, the capacity difference is about 10 mAh. As shown in Figure 6.5(b) Li-ion cells cycled with CCGC have a 2% lower capacity fade than cells cycled under TGC conditions. Figure 6.5(c) and (d) show the capacity and capacity retention, respectively, of Li-ion cells cycled at 45°C at a 2C rate under TGC and CCGC conditions. At every 100<sup>th</sup> cycle, a slow C/5 charging step applied. Initially, the Li-ion cells delivered a similar amount of capacity under both cycling methods about 267 mAh for the slow charging rate and 258 mAh for the fast charging rate, as shown in Figure 6.5(c). Capacity differences became greater after 200 cycles. In contrast, there is little difference between the C/5 capacity of cells cycled by both methods, since during slow cycling increases in cell impedance have less effect on capacity. For this reason, the capacity fade during the lower rate C/5 cycling provides a measure of the amount of capacity lost from electrode degradation. The cells cycled with TGC have a higher fade rate at 2C than at C/5, indicating that cell impedance growth is impacting its capacity in a significant way. In this case the fade rate is a combination of electrode degradation and increasing cell impedance. Interestingly, the capacity fade rate of the CCGC cells at 2C becomes nearly the same as the fade rate of the C/5 cycles, indicating that cell impedance increase also has little effect on CCGC cycling capacity. This means that the CCGC fade rate can approximate the rate of growth of electrode degradation reactions, even if high cycling rates are used. Therefore, CCGC represents a valuable method for researchers to evaluate the impact of electrode degradation during cycling while reducing interference from impedance effects.

Although CCGC is introduced here as a cycling method for cell characterization, it may also have practical uses in extended in the life of Li-ion cells. Practical Li-ion cells are rarely

cycled between their fully-discharged and fully-charged states. Therefore, the direct use of previous cycle capacity is difficult to achieve for the practical applications, especially during discharge. Luckily, many promising techniques have been developed to estimate the remaining capacity of a Li-ion cell, such as empirical methods and impedance-based methods [228]. For practical cells, it may be possible to utilize the CCGC method, at least during charging, with the assistance of these capacity estimation techniques. Full cells commonly suffer two types of degradation behavior: time-dependent capacity fade and cycle-dependent capacity fade. The CCGC method generally utilizes lower current values than the TGC method. From this aspect, the CCGC method might result in a worse cycle life if cell degradation is dominated by time-dependent capacity fade. However, for fast-charging applications, cell degradation is likely dominated by cycle-dependent capacity fade due to the presence of Li plating [229]. The use of the CCGC method during charging is likely to reduce the risk of Li plating, resulting in increased capacity retention, without users noticing any difference in the charging time even if cell fade occurs.

## **6.4 Conclusions**

An advanced galvanostatic cycling method, termed current-corrected galvanostatic cycling (CCGC), has been developed to evaluate the electrode performance under designed cycling rates. With traditional galvanostatic cycling (TGC), actual cycling rates can deviate significantly than the designed cycling rate. For instance, it was observed here that when using TGC to cycle graphite electrodes at a designed 5C rate, the actual cycling rate was ~500 times larger. As a result, TGC cycling is a poor indication of a cell's ability to cycle at a designed rate. Furthermore, under such conditions, a positive feedback exists where capacity fade results in increased actual rate, leading to increased overpotential and further capacity fade. This makes fade from cell degradation very

difficult or impossible to deconvolute from accelerating increases in overpotential induced by the TGC method.

In contrast, it was found that the use of CCGC can totally avoid such errors, providing the electrode performance exactly under designed cycling rates. On the basis of this new cycling strategy, the electrode electrochemical properties without induced polarization can be obtained, as exemplified with  $\text{LiNiO}_2$  and Si electrodes. Therefore, this method is highly useful in electrode/battery performance evaluation for practical cell design, and may have application in improving cycle life of practical cells, particularly in fast-charging applications (such as the use of an adjusted and lowered applied current, which may reduce the chance of Li plating).

## CHAPTER 7 Conclusions and Future Work

### 7.1 Conclusions

In this thesis, strategies to evaluate degradation processes of next-generation electrode materials were proposed, mainly relying on electrochemical measurements. First, the importance of battery lifetime was addressed in Chapter 2, using potassium-ion batteries as an example. By implementing new electrode materials, potassium-ion batteries have been claimed to have cost benefits, and therefore are proposed as strong candidates to replace lithium-ion batteries in some applications. In this thesis it was shown that this cost benefit needs to take into account battery lifetime, termed here as annualized battery cost. With poor lifetimes, the annualized battery cost increases dramatically, and any cost advantage can disappear. This study also emphasizes that degradation processes occurring at electrode materials need to be evaluated carefully because the irreversibility is often less than 0.5% of the reversible capacity per cycle.

In Chapter 4, the interfacial impedance growth in electrodes comprising a blend of different active materials were comprehensively studied both in experiment and theory. The interfacial impedance growth is strongly correlated to the electrolyte decomposition on the electrode surface. In experiments, the measured interfacial impedance was found to be strongly related to the electrode mass loading. Therefore, a mass loading correction is needed to allow further analysis. A theoretical inhomogeneous transmission line model was developed to understand the impedance growth in this complicated electrochemical system. Both experiment and theory show that a small proportion of low interfacial impedance particles can suppress electrode interfacial impedance in blended electrodes. This study also provides a fundamental approach to examine interfacial impedance growth in electrodes.

In Chapter 5, a Li inventory model was proposed to describe and interpret anode capacity fade in symmetric cells. Multiple anode degradation mechanisms, *i.e.* electrode mechanical failure, SEI growth and repair, and excess capacity, were included in the model. In addition, the model took into account the excess capacity, which results from shifts in the electrode upper endpoint potential. On the basis of this model, a correlation between the symmetric cell capacity fade and multiple degradation mechanisms that change the amount of active Li was established. Results show that the accumulated excess capacity of each Si<sub>80</sub>W<sub>20</sub> electrode in symmetric cells can reimburse over 25 mAh g<sup>-1</sup> or about 18% of the reversible capacity consumed by the SEI growth and electrode mechanical failure after 50 cycles.

In addition, the measurement of the SEI growth capacity on Si-alloy materials was established. The strategy is based on blended electrodes with a graphite material. After cycling, the degradation capacity from alloy material was deconvoluted. Results show high consistency in blended electrodes with different alloy/graphite ratios. This approach can be applied to aid battery researchers to develop Si-alloys with lower SEI growth rates.

In Chapter 6, an advanced galvanostatic cycling method, termed current-corrected galvanostatic cycling (CCGC), was developed to evaluate electrode performance at a designed cycling rate. Under traditional galvanostatic cycling (TGC), large differences develop between the actual and designed rates, especially as the designed rate is increased. For example, when TGC was used to cycle graphite electrodes at a designed 5C rate, the actual cycling rate was observed to be ~500 times greater. The use of current-corrected galvanostatic cycling can avoid such differences, allowing electrode performance to be evaluated under actual cycling rates that are consistent with the designed rates. In addition, commercial cells with longer cycle life were achieved by adapting this cycling method.

## 7.2 Future Work

### 7.2.1 Mechanical Failure Analysis of Alloy/graphite Blended Electrodes

As mentioned in Chapter 5, additional data are necessary to further confirm the mechanical failure of alloy/graphite blended electrodes after cycling in symmetric cells. In this thesis, it was assumed that the mechanical failure was negligible, based on the measured mechanical failure of the same electrodes cycled under similar, but not exactly the same conditions. To obtain a more exact value of the mechanical failure, the capacity of the blended electrodes should be measured in half cells before and after cycling as DHCs. This would enable mechanical failure to be included in the SEI growth calculation. As demonstrated in Chapter 5, SEI growth and Li-consuming mechanical failure, can cause symmetric-cell capacity fade, while the growth of excess capacity of blended electrodes is well restricted. If any mechanical failure can be measured based on this additional test, a deconvolution between the SEI growth capacity and the mechanical failure can be achieved. Such a deconvolution could be conducted by assuming a constant capacity fade per cycle caused by the mechanical failure because the half-cell cycling data has shown that the capacity of the blended electrodes decreased slightly with a linear trend. These data include the Si<sub>80</sub>W<sub>20</sub>/graphite electrodes with ratios of 20/50, 10/60, and 5/65, cycled at 30 °C. As a result of this refinement, a more accurate value of SEI growth could be obtained. Directly measuring the mechanical failure in DHC experiments would be especially important in systems where mechanical failure is more severe than in the electrodes studied here.

### 7.2.2 Optimization of Alloy Material and Electrolyte towards Slow SEI Growth

Chapter 5 describes the investigation of alloy materials degradation behavior utilizing symmetric cells. Such a strategy can be adapted to optimize alloy materials and electrolytes to reduce SEI growth. This includes optimization of alloy material morphology and electrolyte

compositions, both of which can impact SEI growth. In the case of material morphology, it may have contradicting impacts on the SEI growth. On one hand, alloy materials with a larger particle size have a smaller surface area to react with the electrolyte, resulting in a decreased SEI growth. On the other hand, the larger particle size may be more vulnerable to fracture during cycling, causing the formation of fresh electrode/electrode interfaces for accelerated SEI growth. Measuring SEI growth and mechanical failure independently utilizing DHCs as described in Chapter 5 could enable optimization of material morphology to reduce the SEI growth rate. In the case of electrolytes, the electrolyte composition can have a significant impact on the SEI growth as well as the mechanical failure. Utilizing the methods developed in Chapter 5 for measuring the SEI growth, future work can adapt this strategy to separate the capacity fade from the SEI growth and the mechanical failure in symmetric cells and to obtain valuable information about the electrolyte compositions on the alloy material degradation. Thus, such work can accelerate the implementation of alloy materials into practical batteries with long cycle life. Many advanced electrolytes, such as CO<sub>2</sub> containing electrolytes [230], are poorly understood and should be further investigated by this method. In addition, electrode formulations should be further optimized using this symmetric-cell method.

### 7.2.3 Decoding Capacity Fade and Coulombic Efficiency in Li Cells

Ambitious goals have been set worldwide towards reaching higher energy and lower cost batteries, primarily stemming from the emergence of new electrode chemistries [5]. Various promising candidates, particularly for Li cells, have been highlighted, including near-term strategies, *e.g.*, Ni-rich layered oxide positive electrodes and Si-based negative electrode materials; and long-term strategies, *e.g.*, Li metal as the negative electrode or the “so-called” anode-free cell format [231,232].

Despite their high-energy and cost promise, significant progress is often needed to further improve the performance of these emerging electrode chemistries, especially their electrochemical reversibility, which is strongly associated to cell lifetime [179,233]. Galvanostatic-based cycling strategies are almost universally applied, to investigate this critical performance parameter in all types of cell configurations [234]. To examine cell reversibility, two key metrics are used, *i.e.*, capacity retention and coulombic efficiency (CE). Mostly, CE serves as the gold-standard indicator to quantify the cycling stability of electrode/cell chemistries of interest [218,235]. However, the true meaning of CE may differ depending on cell configuration, and the origin of imperfect CE is not well interpreted, particularly for cells that undergo multiple degradation mechanisms. Consequently, concerns about the misinterpretation of CE have been raised recently [218].

Characteristic patterns in the cell capacity and CE that are unique to different degradation mechanisms have been noticed. This includes including oscillations in the cell capacity that, when coupled with information from the CE can be used to uniquely identify different degradation mechanisms, including loss of active material, electrolyte oxidation, and electrolyte reduction. This has the potential to provide important information about cell degradation mechanisms while utilizing only simple measurements. In future work, the impact of common degradation mechanisms (electrolyte decomposition and the loss of active material) on the capacity fade and CE of representative Li cells (ranging from basic configurations, *i.e.*, Li//Li symmetric cells and Cu//Li cells, to Li metal cells, *e.g.*, LiNi<sub>1-x-y</sub>Mn<sub>x</sub>Co<sub>y</sub>O<sub>2</sub> (NMC)//Li cells and NMC//Li cells, and to next-generation Li-ion cells (NMC//Si cells) should be explored.

Such future work could provide a fundamental understanding of the capacity fade of the above cell configurations. This could provide an effective way to examine degradation behavior, utilizing only simple electrochemical measurements. Experimental data utilizing many different

cell configurations should be included to test the effectiveness of such a capacity fade interpretation.

#### 7.2.4 Kinetics Analysis of Electrode Materials at High Rates

Electrode materials suffer declined electrochemical performance at high rates, such as decreased reversible capacity and worsened overpotential. Chapter 6 has indicated that the true electrochemical performance of electrode materials at high rates can be measured using current-corrected galvanostatic cycling (CCGC). Further studies are needed to conduct in-depth analyses on the (de)lithiation mechanisms of typical electrode materials (such as graphite) at high rates where the (de)lithiation is kinetically limited. There are many questions to be answered: using the graphite electrode as an example: what are the key factors limiting the lithiation process at high rates? Does any inhomogeneous lithiation behavior among graphite particles (particularly across the electrode) occur during a fast lithiation? Can an atomic-scale understanding of the lithiation process based on the measured electrochemical performance be established? In Chapter 6, it shows the graphite electrode has a decreased capacity when cycled at a higher rate. However, there are many factors that could have an impact on the lithiation kinetics, such as the Li mobility in the electrolyte, the Li transportation across the electrode/electrolyte interface, and the Li diffusion in bulk graphite particle. In addition, the graphite lithiation behavior may be significantly different across the electrode. For example, the graphite near the electrolyte can have a much higher lithiation degree than the graphite near the current collector if the lithiation rate is high. Therefore, many other studies, such as impedance analysis and kinetic modeling, are needed to further interpret graphite lithiation behavior at different cycling rates. Combining CCGC results and the proposed analysis above, it is expected that the impact of increased cycling rate on the electrode

capacity fade could be further understood. This understanding would provide useful guidance to design batteries with better fast-charging performance.

## BIBIOGRAPHY

- [1] J.B. Goodenough, K.-S.S. Park, The Li-ion Rechargeable Battery: A Perspective, *J. Am. Chem. Soc.* 135 (2013) 1167–1176.
- [2] J.-M. Tarascon, M. Armand, Issues and Challenges Facing Rechargeable Lithium Batteries, *Nature*. 414 (2001) 359–367.
- [3] Z. Yang, J. Zhang, M.C.W. Kintner-Meyer, X. Lu, D. Choi, J.P. Lemmon, J. Liu, Electrochemical Energy Storage for Green Grid, *Chem. Rev.* 111 (2011) 3577–3613.
- [4] J. Liu, Z. Bao, Y. Cui, E.J. Dufek, J.B. Goodenough, P. Khalifah, Q. Li, B.Y. Liaw, P. Liu, A. Manthiram, Y.S. Meng, V.R. Subramanian, M.F. Toney, V. V Viswanathan, M.S. Whittingham, J. Xiao, W. Xu, J. Yang, X.-Q. Yang, J.-G. Zhang, Pathways for Practical High-energy Long-cycling Lithium Metal Batteries, *Nat. Energy*. 4 (2019) 180–186.
- [5] J.W. Choi, D. Aurbach, Promise and Reality of Post-lithium-ion Batteries with High Energy Densities, *Nat. Rev. Mater.* 1 (2016) 16013.
- [6] B. Xu, D. Qian, Z. Wang, Y.S. Meng, Recent progress in cathode materials research for advanced lithium ion batteries, *Mater. Sci. Eng. R Reports*. 73 (2012) 51–65.
- [7] S. Chae, S.-H. Choi, N. Kim, J. Sung, J. Cho, Integration of Graphite and Silicon Anodes for the Commercialization of High-Energy Lithium-Ion Batteries, *Angew. Chemie Int. Ed.* (2019) 2–28.
- [8] M.N. Obrovac, V.L. Chevrier, Alloy Negative Electrodes for Li-Ion Batteries, *Chem. Rev.* 114 (2014) 11444–11502.
- [9] M.N. Obrovac, L. Christensen, Structural Changes in Silicon Anodes during Lithium Insertion/Extraction, *Electrochem. Solid-State Lett.* 7 (2004) A93.
- [10] J.N. Reimers, J.R. Dahn, Electrochemical and In Situ X-Ray Diffraction Studies of Lithium Intercalation in  $\text{Li}_x\text{CoO}_2$ , *J. Electrochem. Soc.* 139 (1992) 2091–2097.
- [11] J. Kim, H. Lee, H. Cha, M. Yoon, M. Park, J. Cho, Prospect and Reality of Ni-Rich Cathode for Commercialization, *Adv. Energy Mater.* 8 (2018) 1702028.
- [12] J.-H. Kim, K.-J. Park, S.J. Kim, C.S. Yoon, Y.-K. Sun, A method of increasing the energy density of layered Ni-rich  $\text{Li}[\text{Ni}_{1-2x}\text{Co}_x\text{Mn}_x]\text{O}_2$  cathodes ( $x = 0.05, 0.1, 0.2$ ), *J. Mater. Chem. A*. 7 (2019) 2694–2701.
- [13] C.R. Birkl, M.R. Roberts, E. McTurk, P.G. Bruce, D.A. Howey, Degradation diagnostics for lithium ion cells, *J. Power Sources*. 341 (2017) 373–386.
- [14] K. Xu, Nonaqueous Liquid Electrolytes for Lithium-Based Rechargeable Batteries, *Chem. Rev.* 104 (2004) 4303–4418.
- [15] M.N. Obrovac, L. Christensen, D.B. Le, J.R. Dahn, Alloy Design for Lithium-Ion Battery Anodes, *J. Electrochem. Soc.* 154 (2007) A849–A855.

- [16] M.N. Obrovac, Si-alloy Negative Electrodes for Li-ion Batteries, *Curr. Opin. Electrochem.* 9 (2018) 8–17.
- [17] M. Gauthier, D. Mazouzi, D. Reyter, B. Lestriez, P. Moreau, D. Guyomard, L. Roué, A Low-cost and High Performance Ball-milled Si-based Negative Electrode for High-energy Li-ion Batteries, *Energy Environ. Sci.* 6 (2013) 2145–2155.
- [18] A. Manthiram, J.C. Knight, S.-T. Myung, S.-M. Oh, Y.-K. Sun, Nickel-Rich and Lithium-Rich Layered Oxide Cathodes: Progress and Perspectives, *Adv. Energy Mater.* 6 (2016) 1501010.
- [19] S.P. V Nadimpalli, V.A. Sethuraman, S. Dalavi, B. Lucht, M.J. Chon, V.B. Shenoy, P.R. Guduru, Quantifying Capacity Loss Due to Solid-electrolyte-interphase Layer Formation on Silicon Negative Electrodes in Lithium-ion Batteries, *J. Power Sources.* 215 (2012) 145–151.
- [20] Y. Oumellal, N. Delpuech, D. Mazouzi, N. Dupre, J. Gaubicher, P. Moreau, P. Soudan, B. Lestriez, D. Guyomard, The Failure Mechanism of Nano-sized Si-based Negative Electrodes for Lithium Ion Batteries, *J. Mater. Chem.* 21 (2011) 6201–6208.
- [21] M. Nie, D.P. Abraham, Y. Chen, A. Bose, B.L. Lucht, Silicon Solid Electrolyte Interphase (SEI) of Lithium Ion Battery Characterized by Microscopy and Spectroscopy, *J. Phys. Chem. C.* 117 (2013) 13403–13412.
- [22] K. Xu, Electrolytes and Interphases in Li-Ion Batteries and Beyond, *Chem. Rev.* 114 (2014) 11503–11618.
- [23] A.J. Smith, J.C. Burns, S. Trussler, J.R. Dahn, Precision Measurements of the Coulombic Efficiency of Lithium-Ion Batteries and of Electrode Materials for Lithium-Ion Batteries, *J. Electrochem. Soc.* 157 (2010) A196–A202.
- [24] A.J. Smith, J.C. Burns, X. Zhao, D. Xiong, J.R. Dahn, A High Precision Coulometry Study of the SEI Growth in Li/Graphite Cells, *J. Electrochem. Soc.* 158 (2011) A447.
- [25] J. Li, L.E. Downie, L. Ma, W. Qiu, J.R. Dahn, Study of the Failure Mechanisms of LiNi<sub>0.8</sub>Mn<sub>0.1</sub>Co<sub>0.1</sub>O<sub>2</sub> Cathode Material for Lithium Ion Batteries, *J. Electrochem. Soc.* 162 (2015) A1401–A1408.
- [26] J.C. Burns, L.J. Krause, D.-B. Le, L.D. Jensen, A.J. Smith, D. Xiong, J.R. Dahn, Introducing Symmetric Li-Ion Cells as a Tool to Study Cell Degradation Mechanisms, *J. Electrochem. Soc.* 158 (2011) A1417–A1422.
- [27] Z. Yan, M.N. Obrovac, Electrolyte Reactivity on Graphite and Copper as Measured in Lithium Double Half Cells, *J. Electrochem. Soc.* 164 (2017) A2977–A2986.
- [28] Z. Yan, M.N. Obrovac, Selecting Inactive Materials with Low Electrolyte Reactivity for Lithium-ion Cells, *J. Power Sources.* 397 (2018) 374–381.
- [29] S.S. Zhang, K. Xu, T.R. Jow, EIS Study on the Formation of Solid Electrolyte Interface in Li-ion Battery, *Electrochim. Acta.* 51 (2006) 1636–1640.
- [30] E. Peled, S. Menkin, Review—SEI: Past, Present and Future, *J. Electrochem. Soc.* . 164

- (2017) A1703–A1719.
- [31] W. Waag, S. Käbitz, D.U. Sauer, Experimental Investigation of the Lithium-ion Battery Impedance Characteristic at Various Conditions and Aging States and Its Influence on the Application, *Appl. Energy*. 102 (2013) 885–897.
- [32] P. Lu, C. Li, E.W. Schneider, S.J. Harris, Chemistry, Impedance, and Morphology Evolution in Solid Electrolyte Interphase Films during Formation in Lithium Ion Batteries, *J. Phys. Chem. C*. 118 (2014) 896–903.
- [33] D.J. Xiong, R. Petibon, M. Nie, L. Ma, J. Xia, J.R. Dahn, Interactions between Positive and Negative Electrodes in Li-Ion Cells Operated at High Temperature and High Voltage, *J. Electrochem. Soc.* 163 (2016) A546–A551.
- [34] L. Madec, L. Ma, K.J. Nelson, R. Petibon, J.-P. Sun, I.G. Hill, J.R. Dahn, The Effects of a Ternary Electrolyte Additive System on the Electrode/Electrolyte Interfaces in High Voltage Li-Ion Cells, *J. Electrochem. Soc.* 163 (2016) A1001–A1009.
- [35] J.P. Meyers, M. Doyle, R.M. Darling, J. Newman, The Impedance Response of a Porous Electrode Composed of Intercalation Particles, *J. Electrochem. Soc.* 147 (2000) 2930.
- [36] J. Guo, A. Sun, X. Chen, C. Wang, A. Manivannan, Cyclability Study of Silicon-carbon Composite Anodes for Lithium-ion Batteries Using Electrochemical Impedance Spectroscopy, *Electrochim. Acta*. 56 (2011) 3981–3987.
- [37] A. Yoshino, K. Sanechika, T. Nakajima, Secondary Battery, (1987).
- [38] P.A. Nelson, K.G. Gallagher, I. Bloom, D.W. Dees, Modeling the Performance and Cost of Lithium-ion Batteries for Electric-drive Vehicles - SECOND EDITION, (2012).
- [39] T. Marks, S. Trussler, A.J. Smith, D. Xiong, J.R. Dahn, A Guide to Li-Ion Coin-Cell Electrode Making for Academic Researchers, *J. Electrochem. Soc.* 158 (2011) A51–A57.
- [40] S. Chen, C. Niu, H. Lee, Q. Li, L. Yu, W. Xu, J.-G.G. Zhang, E.J. Dufek, M.S. Whittingham, S. Meng, J. Xiao, J. Liu, Critical Parameters for Evaluating Coin Cells and Pouch Cells of Rechargeable Li-Metal Batteries, *Joule*. 3 (2019) 1094–1105.
- [41] V. Murray, D.S. Hall, J.R. Dahn, A Guide to Full Coin Cell Making for Academic Researchers, *J. Electrochem. Soc.* 166 (2019) A329–A333.
- [42] S. Choi, T. Kwon, A. Coskun, J.W. Choi, Highly Elastic Binders Integrating Polyrotaxanes for Silicon Microparticle Anodes in Lithium Ion Batteries, *Science*. 357 (2017) 279–283.
- [43] N. Kim, S. Chae, J. Ma, M. Ko, J. Cho, Fast-charging High-energy Lithium-ion Batteries via Implantation of Amorphous Silicon Nanolayer in Edge-plane Activated Graphite Anodes, *Nat. Commun.* 8 (2017) 812.
- [44] C.H. Chen, J. Liu, K. Amine, Symmetric Cell Approach and Impedance Spectroscopy of High Power Lithium-ion Batteries, *J. Power Sources*. 96 (2001) 321–328.
- [45] H. Buqa, M. Holzapfel, F. Krumeich, C. Veit, P. Novák, Study of Styrene Butadiene Rubber and Sodium Methyl Cellulose as Binder for Negative Electrodes in Lithium-ion Batteries, *J. Power Sources*. 161 (2006) 617–622.

- [46] J.R. Dahn, R. Fong, M.J. Spoon, Suppression of Staging in Lithium-intercalated Carbon by Disorder in the Host, *Phys. Rev. B.* 42 (1990) 6424–6432.
- [47] M.B. Pinson, M.Z. Bazant, Theory of SEI Formation in Rechargeable Batteries: Capacity Fade, Accelerated Aging and Lifetime Prediction, *J. Electrochem. Soc.* 160 (2013) A243–A250.
- [48] M.N. Obrovac, L.J. Krause, Reversible Cycling of Crystalline Silicon Powder, *J. Electrochem. Soc.* 154 (2007) A103–A108.
- [49] V.A. Sethuraman, A. Nguyen, M.J. Chon, S.P. V Nadimpalli, H. Wang, D.P. Abraham, A.F. Bower, V.B. Shenoy, P.R. Guduru, Stress Evolution in Composite Silicon Electrodes during Lithiation/Delithiation, *J. Electrochem. Soc.* 160 (2013) A739–A746.
- [50] V.L. Chevrier, L. Liu, D.B.B. Le, J. Lund, B. Molla, K. Reimer, L.J. Krause, L.D. Jensen, E. Figgemeier, K.W. Eberman, Evaluating Si-Based Materials for Li-Ion Batteries in Commercially Relevant Negative Electrodes, *J. Electrochem. Soc.* 161 (2014) A783–A791.
- [51] Z. Du, R.A. Dunlap, M.N. Obrovac, High Energy Density Calendered Si Alloy/Graphite Anodes, *J. Electrochem. Soc.* 161 (2014) A1698–A1705.
- [52] S.B. Chikkannanavar, D.M. Bernardi, L. Liu, A Review of Blended Cathode Materials for Use in Li-ion Batteries, *J. Power Sources.* 248 (2014) 91–100.
- [53] M. Ko, S. Chae, J. Ma, N. Kim, H.-W. Lee, Y. Cui, J. Cho, Scalable synthesis of silicon-nanolayer-embedded graphite for high-energy lithium-ion batteries, *Nat. Energy.* 1 (2016) 16113.
- [54] G. Jeong, S.M. Lee, N.S. Choi, Y.-U. Kim, C.K. Lee, Stabilizing Dimensional Changes in Si-based Composite Electrodes by Controlling the Electrode Porosity: An In Situ Electrochemical Dilatometric Study, *Electrochim. Acta.* 56 (2011) 5095–5101.
- [55] H. Li, N. Zhang, J. Li, J.R. Dahn, Updating the Structure and Electrochemistry of  $\text{Li}_x\text{NiO}_2$  for  $0 \leq x \leq 1$ , *J. Electrochem. Soc.* 165 (2018) A2985–A2993.
- [56] M.S. Whittingham, Lithium Batteries and Cathode Materials, *Chem. Rev.* 104 (2004) 4271–4302.
- [57] B.L. Ellis, K.T. Lee, L.F. Nazar, Positive Electrode Materials for Li-Ion and Li-Batteries, *Chem. Mater.* 22 (2010) 691–714.
- [58] P. Rozier, J.M. Tarascon, Review—Li-Rich Layered Oxide Cathodes for Next-Generation Li-Ion Batteries: Chances and Challenges, *J. Electrochem. Soc.* 162 (2015) A2490–A2499.
- [59] M.S. Whittingham, Ultimate Limits to Intercalation Reactions for Lithium Batteries, *Chem. Rev.* 114 (2014) 11414–11443.
- [60] Y. Ruan, X. Song, Y. Fu, C. Song, V. Battaglia, Structural Evolution and Capacity Degradation Mechanism of  $\text{LiNi}_{0.6}\text{Mn}_{0.2}\text{Co}_{0.2}\text{O}_2$  Cathode Materials, *J. Power Sources.* 400 (2018) 539–548.
- [61] R. Petibon, J. Xia, L. Ma, M.K.G. Bauer, K.J. Nelson, J.R. Dahn, Electrolyte System for High Voltage Li-Ion Cells, *J. Electrochem. Soc.* 163 (2016) A2571–A2578.

- [62] C.S. Rustomji, Y. Yang, T.K. Kim, J. Mac, Y.J. Kim, E. Caldwell, H. Chung, Y.S. Meng, Liquefied Gas Electrolytes for Electrochemical Energy Storage Devices, *Science*. 356 (2017) eaal4263.
- [63] L. Xue, K. Ueno, S.-Y. Lee, C.A. Angell, Enhanced Performance of Sulfone-based Electrolytes at Lithium Ion Battery Electrodes, Including the  $\text{LiNi}_0.5\text{Mn}_1.5\text{O}_4$  High Voltage Cathode, *J. Power Sources*. 262 (2014) 123–128.
- [64] Y. Abu-Lebdeh, I. Davidson, New Electrolytes Based on Glutaronitrile for High Energy/Power Li-ion Batteries, *J. Power Sources*. 189 (2009) 576–579.
- [65] S. Dalavi, M. Xu, B. Ravdel, L. Zhou, B.L. Lucht, Nonflammable Electrolytes for Lithium-Ion Batteries Containing Dimethyl Methylphosphonate, *J. Electrochem. Soc.* 157 (2010) A1113–A1120.
- [66] M. Ue, M. Takeda, M. Takehara, S. Mori, Electrochemical Properties of Quaternary Ammonium Salts for Electrochemical Capacitors, *J. Electrochem. Soc.* 144 (1997) 2684–2688.
- [67] R. Fong, U. von Sacken, J.R. Dahn, Studies of Lithium Intercalation into Carbons Using Nonaqueous Electrochemical Cells, *J. Electrochem. Soc.* 137 (1990) 2009–2013.
- [68] M.S. Ding, Liquid Phase Boundaries, Dielectric Constant, and Viscosity of PC-DEC and PC-EC Binary Carbonates, *J. Electrochem. Soc.* 150 (2003) A455–A462.
- [69] J.M. Tarascon, D. Guyomard, New Electrolyte Compositions Stable over the 0 to 5 V Voltage Range and Compatible with the  $\text{Li}_{1+x}\text{Mn}_2\text{O}_4$ /Carbon Li-ion Cells, *Solid State Ionics*. 69 (1994) 293–305.
- [70] D. Guyomard, J.M. Tarascon, Rechargeable  $\text{Li}_{1+x}\text{Mn}_2\text{O}_4$ /Carbon Cells with a New Electrolyte Composition: Potentiostatic Studies and Application to Practical Cells, *J. Electrochem. Soc.* 140 (1993) 3071–3081.
- [71] L. Ma, S.L. Glazier, R. Petibon, J. Xia, J.M. Peters, Q. Liu, J. Allen, R.N.C. Doig, J.R. Dahn, A Guide to Ethylene Carbonate-Free Electrolyte Making for Li-Ion Cells, *J. Electrochem. Soc.* 164 (2017) A5008–A5018.
- [72] L.J. Krause, T. Brandt, V.L. Chevrier, L.D. Jensen, Surface Area Increase of Silicon Alloys in Li-Ion Full Cells Measured by Isothermal Heat Flow Calorimetry, *J. Electrochem. Soc.* 164 (2017) A2277–A2282.
- [73] R. Fathi, J.C. Burns, D.A. Stevens, H. Ye, C. Hu, G. Jain, E. Scott, C. Schmidt, J.R. Dahn, Ultra High-Precision Studies of Degradation Mechanisms in Aged  $\text{LiCoO}_2$ /Graphite Li-Ion Cells, *J. Electrochem. Soc.* 161 (2014) A1572–A1579.
- [74] S.S. Zhang, A Review on Electrolyte Additives for Lithium-ion Batteries, *J. Power Sources*. 162 (2006) 1379–1394.
- [75] L. Madec, J. Xia, R. Petibon, K.J. Nelson, J.-P. Sun, I.G. Hill, J. Dahn, Effect of Sulfate Electrolyte Additives on  $\text{LiNi}_{1/3}\text{Mn}_{1/3}\text{Co}_{1/3}\text{O}_2$ /Graphite Pouch Cell Lifetime: Correlation between XPS Surface Studies and Electrochemical Test Results, *J. Phys. Chem. C*. 118 (2014) 29608–29622.

- [76] A.M. Haregewoin, A.S. Wotango, B.-J. Hwang, Electrolyte Additives for Lithium Ion Battery Electrodes: Progress and Perspectives, *Energy Environ. Sci.* 9 (2016) 1955–1988.
- [77] N.-S. Choi, K.H. Yew, K.Y. Lee, M. Sung, H. Kim, S.-S. Kim, Effect of Fluoroethylene Carbonate Additive on Interfacial Properties of Silicon Thin-film Electrode, *J. Power Sources.* 161 (2006) 1254–1259.
- [78] Y. Okuno, K. Ushirogata, K. Sodeyama, Y. Tateyama, Decomposition of the Fluoroethylene Carbonate Additive and the Glue Effect of Lithium Fluoride Products for the Solid Electrolyte Interphase: an ab Initio Study, *Phys. Chem. Chem. Phys.* 18 (2016) 8643–8653.
- [79] E. Markevich, G. Salitra, D. Aurbach, Fluoroethylene Carbonate as an Important Component for the Formation of an Effective Solid Electrolyte Interphase on Anodes and Cathodes for Advanced Li-Ion Batteries, *ACS Energy Lett.* 2 (2017) 1337–1345.
- [80] K. Leung, S.B. Rempe, M.E. Foster, Y. Ma, J.M. Martinez del la Hoz, N. Sai, P.B. Balbuena, Modeling Electrochemical Decomposition of Fluoroethylene Carbonate on Silicon Anode Surfaces in Lithium Ion Batteries, *J. Electrochem. Soc.* 161 (2014) A213–A221.
- [81] M.D. Tikekar, S. Choudhury, Z. Tu, L.A. Archer, Design Principles for Electrolytes and Interfaces for Stable Lithium-metal Batteries, *Nat. Energy.* 1 (2016) 16114.
- [82] A. Lewandowski, A. Świdorska-Mocek, Ionic Liquids as Electrolytes for Li-ion Batteries—An Overview of Electrochemical Studies, *J. Power Sources.* 194 (2009) 601–609.
- [83] D. Aurbach, Y. Talyosef, B. Markovsky, E. Markevich, E. Zinigrad, L. Asraf, J.S. Gnanaraj, H.-J. Kim, Design of Electrolyte Solutions for Li and Li-ion Batteries: a Review, *Electrochim. Acta.* 50 (2004) 247–254.
- [84] L. Ma, J. Xia, J.R. Dahn, Improving the High Voltage Cycling of Li[Ni<sub>0.42</sub>Mn<sub>0.42</sub>Co<sub>0.16</sub>]O<sub>2</sub> (NMC442)/Graphite Pouch Cells Using Electrolyte Additives, *J. Electrochem. Soc.* 161 (2014) A2250–A2254.
- [85] K.J. Nelson, G.L. d'Eon, A.T.B. Wright, L. Ma, J. Xia, J.R. Dahn, Studies of the Effect of High Voltage on the Impedance and Cycling Performance of Li[Ni<sub>0.4</sub>Mn<sub>0.4</sub>Co<sub>0.2</sub>]O<sub>2</sub>/Graphite Lithium-Ion Pouch Cells, *J. Electrochem. Soc.* 162 (2015) A1046–A1054.
- [86] J.-S. Bridel, T. Azais, M. Morcrette, J.-M. Tarascon, D. Larcher, In Situ Observation and Long-Term Reactivity of Si/C/CMC Composites Electrodes for Li-Ion Batteries, *J. Electrochem. Soc.* 158 (2011) A750–A759.
- [87] J.C. Burns, A. Kassam, N.N. Sinha, L.E. Downie, L. Solnickova, B.M. Way, J.R. Dahn, Predicting and Extending the Lifetime of Li-Ion Batteries, *J. Electrochem. Soc.* 160 (2013) A1451–A1456.
- [88] M. Gauthier, T.J. Carney, A. Grimaud, L. Giordano, N. Pour, H.-H. Chang, D.P. Fenning, S.F. Lux, O. Paschos, C. Bauer, F. Maglia, S. Lupart, P. Lamp, Y. Shao-Horn, Electrode–Electrolyte Interface in Li-Ion Batteries: Current Understanding and New Insights, *J. Phys. Chem. Lett.* 6 (2015) 4653–4672.

- [89] P. Verma, P. Maire, P. Novák, A Review of the Features and Analyses of the solid Electrolyte Interphase in Li-ion Batteries, *Electrochim. Acta.* 55 (2010) 6332–6341.
- [90] T. Liu, L. Lin, X. Bi, L. Tian, K. Yang, J. Liu, M. Li, Z. Chen, J. Lu, K. Amine, K. Xu, F. Pan, In situ Quantification of Interphasial Chemistry in Li-ion Battery, *Nat. Nanotechnol.* 14 (2019) 50–56.
- [91] Z.L. Brown, S. Jurng, C.C. Nguyen, B.L. Lucht, Effect of Fluoroethylene Carbonate Electrolytes on the Nanostructure of the Solid Electrolyte Interphase and Performance of Lithium Metal Anodes, *ACS Appl. Energy Mater.* 1 (2018) 3057–3062.
- [92] C. Wang, Y.S. Meng, K. Xu, Perspective—Fluorinating Interphases, *J. Electrochem. Soc.* 166 (2019) A5184–A5186.
- [93] E. Peled, D. Golodnitsky, G. Ardel, Advanced Model for Solid Electrolyte Interphase Electrodes in Liquid and Polymer Electrolytes, *J. Electrochem. Soc.* 144 (1997) L208–L210.
- [94] S.H. Kang, D.P. Abraham, A. Xiao, B.L. Lucht, Investigating the Solid Electrolyte Interphase Using Binder-free Graphite Electrodes, *J. Power Sources.* 175 (2008) 526–532.
- [95] C. Stetson, Y. Yin, C.-S. Jiang, S.C. DeCaluwe, M. Al-Jassim, N.R. Neale, C. Ban, A. Burrell, Temperature-Dependent Solubility of Solid Electrolyte Interphase on Silicon Electrodes, *ACS Energy Lett.* 4 (2019) 2770–2775.
- [96] K. Xu, G. V Zhuang, J.L. Allen, U. Lee, S.S. Zhang, P.N. Ross, T.R. Jow, Syntheses and Characterization of Lithium Alkyl Mono- and Dicarbonates as Components of Surface Films in Li-Ion Batteries, *J. Phys. Chem. B.* 110 (2006) 7708–7719.
- [97] R. Dedryvère, L. Gireaud, S. Grugeon, S. Laruelle, J.-M. Tarascon, D. Gonbeau, Characterization of Lithium Alkyl Carbonates by X-ray Photoelectron Spectroscopy: Experimental and Theoretical Study, *J. Phys. Chem. B.* 109 (2005) 15868–15875.
- [98] A.J. Smith, A High Precision Study of Li-ion Batteries, Dalhousie University, (2012).
- [99] T.M. Bond, J.C. Burns, D.A. Stevens, H.M. Dahn, J.R. Dahn, Improving Precision and Accuracy in Coulombic Efficiency Measurements of Li-Ion Batteries, *J. Electrochem. Soc.* 160 (2013) A521–A527.
- [100] J. Xia, J. Self, L. Ma, J.R. Dahn, Sulfolane-Based Electrolyte for High Voltage Li(Ni<sub>0.42</sub>Mn<sub>0.42</sub>Co<sub>0.16</sub>)O<sub>2</sub> (NMC442)/Graphite Pouch Cells, *J. Electrochem. Soc.* 162 (2015) A1424–A1431.
- [101] D. Xiong, J.C. Burns, A.J. Smith, N. Sinha, J.R. Dahn, A High Precision Study of the Effect of Vinylene Carbonate (VC) Additive in Li/Graphite Cells, *J. Electrochem. Soc.* 158 (2011) A1431–A1435.
- [102] J. Li, H. Li, W. Stone, S. Glazier, J.R. Dahn, Development of Electrolytes for Single Crystal NMC532/Artificial Graphite Cells with Long Lifetime, *J. Electrochem. Soc.* 165 (2018) A626–A635.
- [103] N. Ogihara, Y. Ito, T. Sasaki, Y. Takeuchi, Impedance spectroscopy characterization of porous electrodes under different electrode thickness using a symmetric cell for high-

- performance lithium-ion batteries, *J. Phys. Chem. C*. 119 (2015) 4612–4619.
- [104] P. Karayaylali, R. Tatar, Y. Zhang, K.-L. Chan, Y. Yu, L. Giordano, F. Maglia, R. Jung, I. Lund, Y. Shao-Horn, Editors' Choice—Coating-Dependent Electrode-Electrolyte Interface for Ni-Rich Positive Electrodes in Li-Ion Batteries, *J. Electrochem. Soc.* 166 (2019) A1022–A1030.
- [105] S. Solchenbach, D. Pritzl, E.J.Y. Kong, J. Landesfeind, H.A. Gasteiger, A Gold Micro-Reference Electrode for Impedance and Potential Measurements in Lithium Ion Batteries, *J. Electrochem. Soc.* 163 (2016) A2265–A2272.
- [106] S.S. Zhang, K. Xu, T.R. Jow, The low temperature performance of Li-ion batteries, *J. Power Sources*. 115 (2003) 137–140.
- [107] Q. Wu, W. Lu, J. Prakash, Characterization of a commercial size cylindrical Li-ion cell with a reference electrode, *J. Power Sources*. 88 (2000) 237–242.
- [108] R. Petibon, C.P. Aiken, N.N. Sinha, J.C. Burns, H. Ye, C.M. VanElzen, G. Jain, S. Trussler, J.R. Dahn, Study of Electrolyte Additives Using Electrochemical Impedance Spectroscopy on Symmetric Cells, *J. Electrochem. Soc.* 160 (2013) A117–A124.
- [109] M. Haruta, T. Okubo, Y. Masuo, S. Yoshida, A. Tomita, T. Takenaka, T. Doi, M. Inaba, Temperature effects on SEI formation and cyclability of Si nanoflake powder anode in the presence of SEI-forming additives, *Electrochim. Acta*. 224 (2017) 186–193.
- [110] S. Zhang, P. Shi, Electrochemical impedance study of lithium intercalation into MCMB electrode in a gel electrolyte, *Electrochim. Acta*. 49 (2004) 1475–1482.
- [111] J.M. Griffin, A.C. Forse, W.-Y. Tsai, P.-L. Taberna, P. Simon, C.P. Grey, In situ NMR and electrochemical quartz crystal microbalance techniques reveal the structure of the electrical double layer in supercapacitors, *Nat. Mater.* 14 (2015) 812.
- [112] K. Jensen, K. Kim, A. Zettl, An atomic-resolution nanomechanical mass sensor, *Nat. Nanotechnol.* 3 (2008) 533.
- [113] A. v. Cresce, S.M. Russell, D.R. Baker, K.J. Gaskell, K. Xu, In Situ and Quantitative Characterization of Solid Electrolyte Interphases, *Nano Lett.* 14 (2014) 1405–1412.
- [114] F.J. Giessibl, Advances in atomic force microscopy, *Rev. Mod. Phys.* 75 (2003) 949–983.
- [115] V. Eshkenazi, E. Peled, L. Burstein, D. Golodnitsky, XPS analysis of the SEI formed on carbonaceous materials, *Solid State Ionics*. 170 (2004) 83–91.
- [116] R.I.R. Blyth, H. Buqa, F.P. Netzer, M.G. Ramsey, J.O. Besenhard, P. Golob, M. Winter, XPS studies of graphite electrode materials for lithium ion batteries, *Appl. Surf. Sci.* 167 (2000) 99–106.
- [117] M. Lu, H. Cheng, Y. Yang, A comparison of solid electrolyte interphase (SEI) on the artificial graphite anode of the aged and cycled commercial lithium ion cells, *Electrochim. Acta*. 53 (2008) 3539–3546.
- [118] M. Nie, B.L. Lucht, Role of Lithium Salt on Solid Electrolyte Interface (SEI) Formation and Structure in Lithium Ion Batteries, *J. Electrochem. Soc.* 161 (2014) A1001–A1006.

- [119] Y. Li, Y. Li, A. Pei, K. Yan, Y. Sun, C.-L. Wu, L.-M. Joubert, R. Chin, A.L. Koh, Y. Yu, J. Perrino, B. Butz, S. Chu, Y. Cui, Atomic structure of sensitive battery materials and interfaces revealed by cryo-electron microscopy, *Science*. 358 (2017) 506 LP – 510.
- [120] J. Self, C.P. Aiken, R. Petibon, J.R. Dahn, Survey of Gas Expansion in Li-Ion NMC Pouch Cells, *J. Electrochem. Soc.* 162 (2015) A796–A802.
- [121] J.E. Trancik, Back the Renewables Boom, *Nature*. 507 (2014) 300–302.
- [122] W.A. Braff, J.M. Mueller, J.E. Trancik, Value of Storage Technologies for Wind and Solar Energy, *Nat. Clim. Chang.* 6 (2016) 964.
- [123] H. Kim, J.C. Kim, M. Bianchini, D.H. Seo, J. Rodriguez-Garcia, G. Ceder, Recent Progress and Perspective in Electrode Materials for K-ion Batteries, *Adv. Energy Mater.* 8 (2018) 1702384.
- [124] B. Dunn, H. Kamath, J.-M. Tarascon, Electrical energy storage for the grid: a battery of choices, *Science*. 334 (2011) 928–935.
- [125] J.D. Milshtein, R.M. Darling, J. Drake, M.L. Perry, F.R. Brushett, The Critical Role of Supporting Electrolyte Selection on Flow Battery Cost, *J. Electrochem. Soc.* 164 (2017) A3883–A3895.
- [126] Z. Li, M.S. Pan, L. Su, P.C. Tsai, A.F. Badel, J.M. Valle, S.L. Eiler, K. Xiang, F.R. Brushett, Y.M. Chiang, Air-breathing Aqueous Sulfur Flow Battery for Ultralow-cost Long-duration Electrical Storage, *Joule*. 1 (2017) 306–327.
- [127] L. Xue, Y. Li, H. Gao, W. Zhou, X. Lü, W. Kaveevivitchai, A. Manthiram, J.B. Goodenough, Low-cost High-energy Potassium Cathode, *J. Am. Chem. Soc.* 139 (2017) 2164–2167.
- [128] C. Vaalma, D. Buchholz, M. Weil, S. Passerini, A Cost and Resource Analysis of Sodium-ion Batteries, *Nat. Rev. Mater.* 3 (2018) 18013.
- [129] A. Eftekhari, Z. Jian, X. Ji, Potassium Secondary Batteries, *ACS Appl. Mater. Interfaces*. 9 (2017) 4404–4419.
- [130] K. Kubota, M. Dahbi, T. Hosaka, S. Kumakura, S. Komaba, Towards K-Ion and Na-Ion Batteries as “Beyond Li-Ion,” *Chem. Rec.* 18 (2018) 459–479.
- [131] C. Vaalma, D. Buchholz, S. Passerini, Non-aqueous Potassium-ion Batteries: a Review, *Curr. Opin. Electrochem.* 9 (2018) 41–48.
- [132] T. Hosaka, K. Kubota, A.S. Hameed, S. Komaba, Research Development on K-Ion Batteries, *Chem. Rev.* (2020).
- [133] S. Komaba, T. Hasegawa, M. Dahbi, K. Kubota, Potassium Intercalation into Graphite to Realize High-voltage/High-power Potassium-ion Batteries and Potassium-ion Capacitors, *Electrochem. Commun.* 60 (2015) 172–175.
- [134] Z. Jian, W. Luo, X. Ji, Carbon Electrodes for K-Ion Batteries, *J. Am. Chem. Soc.* 137 (2015) 11566–11569.

- [135] H. Kim, H. Ji, J. Wang, G. Ceder, Next-Generation Cathode Materials for Non-aqueous Potassium-Ion Batteries, *Trends Chem.* 1 (2019) 682–692.
- [136] T. Deng, X. Fan, J. Chen, L. Chen, C. Luo, X. Zhou, J. Yang, S. Zheng, C. Wang, Layered P2-Type  $K_{0.65}Fe_{0.5}Mn_{0.5}O_2$  Microspheres as Superior Cathode for High-Energy Potassium-Ion Batteries, *Adv. Funct. Mater.* 28 (2018) 1800219.
- [137] H. Kim, D.-H. Seo, J.C. Kim, S.-H. Bo, L. Liu, T. Shi, G. Ceder, Investigation of Potassium Storage in Layered P3-Type  $K_{0.5}MnO_2$  Cathode, *Adv. Mater.* 29 (2017) 1702480.
- [138] H. Kim, D.-H. Seo, A. Urban, J. Lee, D.-H. Kwon, S.-H. Bo, T. Shi, J.K. Papp, B.D. McCloskey, G. Ceder, Stoichiometric Layered Potassium Transition Metal Oxide for Rechargeable Potassium Batteries, *Chem. Mater.* 30 (2018) 6532–6539.
- [139] H. Kim, J.C. Kim, S.-H. Bo, T. Shi, D.-H. Kwon, G. Ceder, K-Ion Batteries Based on a P2-Type  $K_{0.6}CoO_2$  Cathode, *Adv. Energy Mater.* 7 (2017) 1700098.
- [140] X. Bie, K. Kubota, T. Hosaka, K. Chihara, S. Komaba, A novel K-ion battery: hexacyanoferrate(ii)/graphite cell, *J. Mater. Chem. A.* 5 (2017) 4325–4330.
- [141] H. Kim, D.-H. Seo, M. Bianchini, R.J. Clément, H. Kim, J.C. Kim, Y. Tian, T. Shi, W.-S. Yoon, G. Ceder, A New Strategy for High-Voltage Cathodes for K-Ion Batteries: Stoichiometric  $KVPO_4F$ , *Adv. Energy Mater.* 8 (2018) 1801591.
- [142] D. Aelenei, R.A. Lopes, L. Aelenei, H. Gonçalves, Investigating the potential for energy flexibility in an office building with a vertical BIPV and a PV roof system, *Renew. Energy.* 137 (2019) 189–197.
- [143] [https://www.tesla.com/en\\_CA/powerwall](https://www.tesla.com/en_CA/powerwall). (Accessed 18 September 2019). Last accessed.
- [144] H. Zheng, J. Li, X. Song, G. Liu, V.S. Battaglia, A comprehensive understanding of electrode thickness effects on the electrochemical performances of Li-ion battery cathodes, *Electrochim. Acta.* 71 (2012) 258–265.
- [145] A. Millner, Modeling Lithium Ion Battery Degradation in Electric Vehicles, in: 2010 IEEE Conf. Innov. Technol. an Effic. Reliab. Electr. Supply, CITRES 2010, (2010): pp. 349–356.
- [146] M. Ecker, N. Nieto, S. Käbitz, J. Schmalstieg, H. Blanke, A. Warnecke, D.U. Sauer, Calendar and cycle life study of  $Li(NiMnCo)O_2$ -based 18650 lithium-ion batteries, *J. Power Sources.* 248 (2014) 839–851.
- [147] Q. Liu, C. Du, B. Shen, P. Zuo, X. Cheng, Y. Ma, G. Yin, Y. Gao, Understanding undesirable anode lithium plating issues in lithium-ion batteries, *RSC Adv.* 6 (2016) 88683–88700.
- [148] J.A. Ober, Mineral Commodity Summaries 2018, <http://pubs.er.usgs.gov/publication/70194932>, n.d.
- [149] R. Schmich, R. Wagner, G. Hörpel, T. Placke, M. Winter, Performance and cost of materials for lithium-based rechargeable automotive batteries, *Nat. Energy.* 3 (2018) 267–278.

- [150] A.J. Smith, J.C. Burns, D. Xiong, J.R. Dahn, Interpreting High Precision Coulometry Results on Li-ion Cells, *J. Electrochem. Soc.* 158 (2011) A1136–A1142.
- [151] C.P. Grey, J.M. Tarascon, Sustainability and in situ monitoring in battery development, *Nat. Mater.* 16 (2016) 45–56.
- [152] S. Chu, Y. Cui, N. Liu, The path towards sustainable energy, *Nat. Mater.* 16 (2016) 16–22.
- [153] A. Castillo, D.F. Gayme, Grid-scale energy storage applications in renewable energy integration: A survey, *Energy Convers. Manag.* 87 (2014) 885–894.
- [154] N. Takami, H. Inagaki, Y. Tatebayashi, H. Saruwatari, K. Honda, S. Egusa, High-power and long-life lithium-ion batteries using lithium titanium oxide anode for automotive and stationary power applications, *J. Power Sources.* 244 (2013) 469–475.
- [155] K. Zaghib, M. Dontigny, A. Guerfi, P. Charest, I. Rodrigues, A. Mauger, C.M. Julien, Safe and fast-charging Li-ion battery with long shelf life for power applications, *J. Power Sources.* 196 (2011) 3949–3954.
- [156] J.E. Harlow, X. Ma, J. Li, E. Logan, Y. Liu, N. Zhang, L. Ma, S.L. Glazier, M.M.E. Cormier, M. Genovese, S. Buteau, A. Cameron, J.E. Stark, J.R. Dahn, A Wide Range of Testing Results on an Excellent Lithium-Ion Cell Chemistry to be used as Benchmarks for New Battery Technologies, *J. Electrochem. Soc.* 166 (2019) A3031–A3044.
- [157] S.Y. Wang, J.L. Yu, Optimal sizing of the CAES system in a power system with high wind power penetration, *Int. J. Electr. Power Energy Syst.* 37 (2012) 117–125.
- [158] Y. Yang, H. Li, A. Aichhorn, J. Zheng, M. Greenleaf, Sizing Strategy of Distributed Battery Storage System With High Penetration of Photovoltaic for Voltage Regulation and Peak Load Shaving, *IEEE Trans. Smart Grid.* 5 (2014) 982–991.
- [159] M. Naumann, R.C. Karl, C.N. Truong, A. Jossen, H.C. Hesse, Lithium-ion Battery Cost Analysis in PV-household Application, *Energy Procedia.* 73 (2015) 37–47.
- [160] D.B. Nelson, M.H. Nehrir, C. Wang, Unit sizing and cost analysis of stand-alone hybrid wind/PV/fuel cell power generation systems, *Renew. Energy.* 31 (2006) 1641–1656.
- [161] W.D. Kellogg, M.H. Nehrir, G. Venkataramanan, V. Gerez, Generation unit sizing and cost analysis for stand-alone wind, photovoltaic, and hybrid wind/PV systems, *IEEE Trans. Energy Convers.* 13 (1998) 70–75.
- [162] B. Ould Bilal, V. Sambou, P.A. Ndiaye, C.M.F. Kébé, M. Ndong, Optimal design of a hybrid solar–wind–battery system using the minimization of the annualized cost system and the minimization of the loss of power supply probability (LPSP), *Renew. Energy.* 35 (2010) 2388–2390.
- [163] <https://www.apple.com/batteries/service-and-recycling/> (Last accessed September 18, 2019).
- [164] M. Broussely, P. Biensan, F. Bonhomme, P. Blanchard, S. Herreyre, K. Nechev, R.J. Staniewicz, Main aging mechanisms in Li ion batteries, *J. Power Sources.* 146 (2005) 90–96.

- [165] L. Ma, J. Xia, J.R. Dahn, Ternary Electrolyte Additive Mixtures for Li-Ion Cells that Promote Long Lifetime and Less Reactivity with Charged Electrodes at Elevated Temperatures, *J. Electrochem. Soc.* 162 (2015) A1170–A1174.
- [166] S.S. Zhang, The effect of the charging protocol on the cycle life of a Li-ion battery, *J. Power Sources.* 161 (2006) 1385–1391.
- [167] T. Hosaka, K. Kubota, H. Kojima, S. Komaba, Highly concentrated electrolyte solutions for 4 V class potassium-ion batteries, *Chem. Commun.* 54 (2018) 8387–8390.
- [168] X. Lin, J. Huang, H. Tan, J. Huang, B. Zhang, K<sub>3</sub>V<sub>2</sub>(PO<sub>4</sub>)<sub>2</sub>F<sub>3</sub> as a robust cathode for potassium-ion batteries, *Energy Storage Mater.* 16 (2019) 97–101.
- [169] D. Li, W. Tang, C. Wang, C. Fan, A polyanionic organic cathode for highly efficient K-ion full batteries, *Electrochem. Commun.* 105 (2019) 106509.
- [170] J. Lee, D.A. Kitchaev, D.-H. Kwon, C.-W. Lee, J.K. Papp, Y.-S. Liu, Z. Lun, R.J. Clément, T. Shi, B.D. McCloskey, J. Guo, M. Balasubramanian, G. Ceder, Reversible Mn<sup>2+</sup>/Mn<sup>4+</sup> double redox in lithium-excess cathode materials, *Nature.* 556 (2018) 185–190.
- [171] R.E. Ciez, J.F. Whitacre, The cost of lithium is unlikely to upend the price of Li-ion storage systems, *J. Power Sources.* 320 (2016) 310–313.
- [172] I.-Y.L. Hsieh, M.S. Pan, Y.-M. Chiang, W.H. Green, Learning only buys you so much: Practical limits on battery price reduction, *Appl. Energy.* 239 (2019) 218–224.
- [173] J.-Y. Hwang, S.-M. Oh, S.-T. Myung, K.Y. Chung, I. Belharouak, Y.-K. Sun, Radially aligned hierarchical columnar structure as a cathode material for high energy density sodium-ion batteries, *Nat. Commun.* 6 (2015) 6865.
- [174] A. Ponrouch, J. Bitenc, R. Dominko, N. Lindahl, P. Johansson, M.R. Palacin, Multivalent rechargeable batteries, *Energy Storage Mater.* 20 (2019) 253–262.
- [175] J.R. Macdonald, W.B. Johnson, Fundamentals of Impedance Spectroscopy, Wiley, (2005).
- [176] H.-K. Song, Y.-H. Jung, K.-H. Lee, L.H. Dao, Electrochemical impedance spectroscopy of porous electrodes: the effect of pore size distribution, *Electrochim. Acta.* 44 (1999) 3513–3519.
- [177] S. Zhang, M.S. Ding, K. Xu, J. Allen, T.R. Jow, Understanding Solid Electrolyte Interface Film Formation on Graphite Electrodes, *Electrochem. Solid-State Lett.* 4 (2001) A206–A208.
- [178] J. Epp, 4 - X-ray diffraction (XRD) techniques for materials characterization, in: G. Hübschen, I. Altpeter, R. Tschuncky, H.-G.B.T.-M.C.U.N.E. (NDE) M. Herrmann (Eds.), Woodhead Publishing, (2016): pp. 81–124.
- [179] R. Petibon, V.L. Chevrier, C.P. Aiken, D.S. Hall, S.R. Hyatt, R. Shunmugasundaram, J.R. Dahn, Studies of the Capacity Fade Mechanisms of LiCoO<sub>2</sub>/Si-Alloy: Graphite Cells, *J. Electrochem. Soc.* 163 (2016) A1146–A1156.
- [180] H. Kitao, T. Fujihara, K. Takeda, N. Nakanishi, T. Nohma, High-Temperature Storage Performance of Li-Ion Batteries Using a Mixture of Li-Mn Spinel and Li-Ni-Co-Mn Oxide

- as a Positive Electrode Material, *Electrochem. Solid-State Lett.* 8 (2005) A87.
- [181] S. Jung, Mathematical model of lithium-ion batteries with blended-electrode system, *J. Power Sources.* 264 (2014) 184.
- [182] C. Sun, S. Rajasekhara, J.B. Goodenough, F. Zhou, Monodisperse porous LiFePO<sub>4</sub> microspheres for a high power Li-ion battery cathode, *J. Am. Chem. Soc.* 133 (2011) 2132.
- [183] M. Galeotti, L. Cinà, C. Giammanco, S. Cordiner, A. Di Carlo, Performance Analysis and SOH (State of Health) Evaluation of Lithium Polymer Batteries through Electrochemical Impedance Spectroscopy, *Energy.* 89 (2015) 678–686.
- [184] I.J. Gordon, S. Genies, G. Si Larbi, A. Boulineau, L. Daniel, M. Alias, Original Implementation of Electrochemical Impedance Spectroscopy (EIS) in Symmetric Cells: Evaluation of Post-mortem Protocols Applied to Characterize Electrode Materials for Li-ion Batteries, *J. Power Sources.* 307 (2016) 788–795.
- [185] J.-M. Atebamba, J. Moskon, S. Pejovnik, M. Gaberscek, On the Interpretation of Measured Impedance Spectra of Insertion Cathodes for Lithium-Ion Batteries, *J. Electrochem. Soc.* 157 (2010) A1218–A1228.
- [186] T. Swamy, Y.-M. Chiang, Electrochemical Charge Transfer Reaction Kinetics at the Silicon-Liquid Electrolyte Interface, *J. Electrochem. Soc.* 162 (2015) A7129–A7134.
- [187] D.W. Abarbanel, K.J. Nelson, J.R. Dahn, Exploring Impedance Growth in High Voltage NMC/Graphite Li-Ion Cells Using a Transmission Line Model, *J. Electrochem. Soc.* 163 (2016) A522–A529.
- [188] A.S. Keefe, S. Buteau, I.G. Hill, J.R. Dahn, Temperature Dependent EIS Studies Separating Charge Transfer Impedance from Contact Impedance in Lithium-Ion Symmetric Cells, *J. Electrochem. Soc.* 166 (2019) A3272–A3279.
- [189] MATLAB, MATLAB, The MathWorks Inc., n.d.
- [190] U. Tröltzsch, O. Kanoun, H.R. Tränkler, Characterizing aging effects of lithium ion batteries by impedance spectroscopy, in: *Electrochim. Acta*, (2006): pp. 1664–1672.
- [191] R. Ruffo, S.S. Hong, C.K. Chan, R.A. Huggins, Y. Cui, Impedance Analysis of Silicon Nanowire Lithium Ion Battery Anodes, *J. Phys. Chem. C.* 113 (2009) 11390–11398.
- [192] H. Nakai, T. Kubota, A. Kita, A. Kawashima, Investigation of the Solid Electrolyte Interphase Formed by Fluoroethylene Carbonate on Si Electrodes, *J. Electrochem. Soc.* 158 (2011) A798–A801.
- [193] R. Yuge, A. Toda, K. Fukatsu, N. Tamura, T. Manako, K. Nakahara, K. Nakano, Effect of Volume Expansion on SEI Covering Carbon-Coated Nano-Si/SiO Composite, *J. Electrochem. Soc.* 160 (2013) A1789–A1793.
- [194] D.A. Kitchaev, Z. Lun, W.D. Richards, H. Ji, R.J. Clément, M. Balasubramanian, D.-H. Kwon, K. Dai, J.K. Papp, T. Lei, B.D. McCloskey, W. Yang, J. Lee, G. Ceder, Design principles for high transition metal capacity in disordered rocksalt Li-ion cathodes, *Energy Environ. Sci.* 11 (2018) 2159–2171.

- [195] J. Hong, W.E. Gent, P. Xiao, K. Lim, D.-H. Seo, J. Wu, P.M. Csernica, C.J. Takacs, D. Nordlund, C.-J. Sun, K.H. Stone, D. Passarello, W. Yang, D. Prendergast, G. Ceder, M.F. Toney, W.C. Chueh, Metal–oxygen decoordination stabilizes anion redox in Li-rich oxides, *Nat. Mater.* 18 (2019) 256–265.
- [196] H. Li, M. Cormier, N. Zhang, J. Inglis, J. Li, J.R. Dahn, Is Cobalt Needed in Ni-Rich Positive Electrode Materials for Lithium Ion Batteries?, *J. Electrochem. Soc.* 166 (2019) A429–A439.
- [197] L. Zheng, T.D. Hatchard, M.N. Obrovac, A high-quality mechanofusion coating for enhancing lithium-ion battery cathode material performance, *MRS Commun.* 9 (2019) 245–250.
- [198] K.J. Griffith, K.M. Wiaderek, G. Cibin, L.E. Marbella, C.P. Grey, Niobium tungsten oxides for high-rate lithium-ion energy storage, *Nature.* 559 (2018) 556–563.
- [199] P.M. Attia, S. Das, S.J. Harris, M.Z. Bazant, W.C. Chueh, Electrochemical kinetics of sei growth on Carbon Black: Part I. experiments, *J. Electrochem. Soc.* 166 (2019) E97–E106.
- [200] N.P. Wagner, K. Asheim, F. Vullum-Bruer, A.M. Svensson, Performance and failure analysis of full cell lithium ion battery with  $\text{LiNi}_{0.8}\text{Co}_{0.15}\text{Al}_{0.05}\text{O}_2$  and silicon electrodes, *J. Power Sources.* 437 (2019) 226884.
- [201] X. Zhao, M.T. Schreiber, L. MacEachern, R.J. Sanderson, R.A. Dunlap, M.N. Obrovac, Combinatorial Study of the Si-Sn-O System as Negative Electrode Materials in Li-Ion Cells, *J. Electrochem. Soc.* 163 (2016) A203–A209.
- [202] S. Chae, M. Ko, S. Park, N. Kim, J. Ma, J. Cho, Micron-sized Fe–Cu–Si ternary composite anodes for high energy Li-ion batteries, *Energy Environ. Sci.* 9 (2016) 1251–1257.
- [203] X. Zhao, R.A. Dunlap, M.N. Obrovac, Low Surface Area Si Alloy/Ionomer Composite Anodes for Lithium-Ion Batteries, *J. Electrochem. Soc.* 161 (2014) A1976–A1980.
- [204] X. Zhao, R.J. Sanderson, M.A. Al-Maghrabi, R.A. Dunlap, M.N. Obrovac, Electrochemistry of Sputtered and Ball Milled Si-Fe-O Alloys in Li Cells, *J. Electrochem. Soc.* 164 (2017) A1165–A1172.
- [205] Y. Liu, B. Scott, M.N. Obrovac, Ball Milled Si-W Alloys: Part I. Microstructural and Phase Evolution during Ball Milling, *J. Electrochem. Soc.* 166 (2019) A1170–A1175.
- [206] T.D. Hatchard, A. Genkin, M.N. Obrovac, Rapid mechanochemical synthesis of amorphous alloys, *AIP Adv.* 7 (2017) 45201.
- [207] J. Moškon, M. Pivko, R. Dominko, M. Gaberšček, Accurate Determination of Battery Electrode Loading (Mass) from Electrochemical Impedance Spectroscopy, *ECS Electrochem. Lett.* 4 (2015) A4–A6.
- [208] T.D. Hatchard, M.N. Obrovac, Evaluation of Electrolyte Salts and Solvents for Na-Ion Batteries in Symmetric Cells, *J. Electrochem. Soc.* 161 (2014) A1748–A1752.
- [209] C. Shen, D. Xiong, L.D. Ellis, K.L. Gering, L. Huang, J.R. Dahn, Using the Charge-Discharge Cycling of Positive Electrode Symmetric Cells to Find Electrolyte/Electrode

- Combinations with Minimum Reactivity, *J. Electrochem. Soc.* 164 (2017) A3349–A3356.
- [210] R. Petibon, V.L. Chevrier, C.P. Aiken, D.S. Hall, S.R. Hyatt, R. Shunmugasundaram, J.R. Dahn, Studies of the Capacity Fade Mechanisms of LiCoO<sub>2</sub>/Si-Alloy: Graphite Cells, *J. Electrochem. Soc.* 163 (2016) A1146–A1156.
- [211] J. Li, L. Christensen, M.N. Obrovac, K.C. Hewitt, J.R. Dahn, Effect of Heat Treatment on Si Electrodes Using Polyvinylidene Fluoride Binder, *J. Electrochem. Soc.* 155 (2008) A234–A238.
- [212] S. Chu, A. Majumdar, Opportunities and challenges for a sustainable energy future, *Nature*. 488 (2012) 294–303.
- [213] H.-H. Ryu, H.H. Sun, S.-T. Myung, C.S. Yoon, Y.-K. Sun, Reducing cobalt from lithium-ion batteries for the electric vehicle era, *Energy Environ. Sci.* 14 (2021) 844–852.
- [214] M. Ue, K. Sakaushi, K. Uosaki, Basic knowledge in battery research bridging the gap between academia and industry, *Mater. Horizons*. 7 (2020) 1937–1954.
- [215] J.B. Goodenough, Rechargeable batteries: challenges old and new, *J. Solid State Electrochem.* 16 (2012) 2019–2029.
- [216] J. Huang, P. Zhong, Y. Ha, D.-H. Kwon, M.J. Crafton, Y. Tian, M. Balasubramanian, B.D. McCloskey, W. Yang, G. Ceder, Non-topotactic reactions enable high rate capability in Li-rich cathode materials, *Nat. Energy*. 6 (2021) 706–714.
- [217] Z.-J. Han, N. Yabuuchi, K. Shimomura, M. Murase, H. Yui, S. Komaba, High-capacity Si-graphite composite electrodes with a self-formed porous structure by a partially neutralized polyacrylate for Li-ion batteries, *Energy Environ. Sci.* 5 (2012) 9014–9020.
- [218] J. Xiao, Q. Li, Y. Bi, M. Cai, B. Dunn, T. Glossmann, J. Liu, T. Osaka, R. Sugiura, B. Wu, J. Yang, J.-G. Zhang, M.S. Whittingham, Understanding and applying coulombic efficiency in lithium metal batteries, *Nat. Energy*. 5 (2020) 561–568.
- [219] Y. Son, T. Lee, B. Wen, J. Ma, C. Jo, Y.-G. Cho, A. Boies, J. Cho, M. De Volder, High energy density anodes using hybrid Li intercalation and plating mechanisms on natural graphite, *Energy Environ. Sci.* 13 (2020) 3723–3731.
- [220] A.J. Merryweather, C. Schnedermann, Q. Jacquet, C.P. Grey, A. Rao, Operando optical tracking of single-particle ion dynamics in batteries, *Nature*. 594 (2021) 522–528.
- [221] C. Heubner, M. Schneider, A. Michaelis, Diffusion-Limited C-Rate: A Fundamental Principle Quantifying the Intrinsic Limits of Li-Ion Batteries, *Adv. Energy Mater.* 10 (2020) 1902523.
- [222] A.S. Hameed, A. Katogi, K. Kubota, S. Komaba, A Layered Inorganic–Organic Open Framework Material as a 4 V Positive Electrode with High-Rate Performance for K-Ion Batteries, *Adv. Energy Mater.* 9 (2019) 1902528.
- [223] Y. Cao, T.D. Hatchard, R.A. Dunlap, M.N. Obrovac, Mechanofusion-derived Si-alloy/graphite composite electrode materials for Li-ion batteries, *J. Mater. Chem. A*. 7 (2019) 8335–8343.

- [224] X.-G. Yang, T. Liu, Y. Gao, S. Ge, Y. Leng, D. Wang, C.-Y. Wang, Asymmetric Temperature Modulation for Extreme Fast Charging of Lithium-Ion Batteries, *Joule*. 3 (2019) 3002–3019.
- [225] Q. Liu, S. Li, S. Wang, X. Zhang, S. Zhou, Y. Bai, J. Zheng, X. Lu, Kinetically Determined Phase Transition from Stage II (LiC<sub>12</sub>) to Stage I (LiC<sub>6</sub>) in a Graphite Anode for Li-Ion Batteries, *J. Phys. Chem. Lett.* 9 (2018) 5567–5573.
- [226] S.L. Glazier, K.J. Nelson, J.P. Allen, J. Li, J.R. Dahn, The Effect of Different Li(Ni<sub>1-x</sub>-yMn<sub>x</sub>Coy)O<sub>2</sub> Positive Electrode Materials and Coatings on Parasitic Heat Flow as Measured by Isothermal Microcalorimetry, Ultra-High Precision Coulometry and Long Term Cycling, *J. Electrochem. Soc.* 164 (2017) A1203–A1212.
- [227] H.-H. Ryu, G.-T. Park, C.S. Yoon, Y.-K. Sun, Suppressing detrimental phase transitions via tungsten doping of LiNiO<sub>2</sub> cathode for next-generation lithium-ion batteries, *J. Mater. Chem. A*. 7 (2019) 18580–18588.
- [228] R. Xiong, L. Li, J. Tian, Towards a smarter battery management system: A critical review on battery state of health monitoring methods, *J. Power Sources*. 405 (2018) 18–29.
- [229] J.C. Burns, D.A. Stevens, J.R. Dahn, In-Situ Detection of Lithium Plating Using High Precision Coulometry, *J. Electrochem. Soc.* 162 (2015) A959–A964.
- [230] L.J. Krause, V.L. Chevrier, L.D. Jensen, T. Brandt, The Effect of Carbon Dioxide on the Cycle Life and Electrolyte Stability of Li-Ion Full Cells Containing Silicon Alloy, *J. Electrochem. Soc.* 164 (2017) A2527–A2533.
- [231] X. Wang, Y.-L. Ding, Y.-P. Deng, Z. Chen, Ni-Rich/Co-Poor Layered Cathode for Automotive Li-Ion Batteries: Promises and Challenges, *Adv. Energy Mater.* 10 (2020) 1903864.
- [232] R. Weber, M. Genovese, A.J. Louli, S. Hames, C. Martin, I.G. Hill, J.R. Dahn, Long cycle life and dendrite-free lithium morphology in anode-free lithium pouch cells enabled by a dual-salt liquid electrolyte, *Nat. Energy*. 4 (2019) 683–689.
- [233] I. Abe, T. Horiba, Y. Abe, K. Hida, T. Matsuyama, S. Yasuno, S. Komaba, Investigation and Improvement of Metallic Aluminum as Alloying Electrode in Non-Aqueous Li Cells, *J. Electrochem. Soc.* 167 (2020) 110513.
- [234] J. Chen, X. Fan, Q. Li, H. Yang, M.R. Khoshi, Y. Xu, S. Hwang, L. Chen, X. Ji, C. Yang, H. He, C. Wang, E. Garfunkel, D. Su, O. Borodin, C. Wang, Electrolyte design for LiF-rich solid–electrolyte interfaces to enable high-performance micro-sized alloy anodes for batteries, *Nat. Energy*. 5 (2020) 386–397.
- [235] C.-J. Huang, B. Thirumalraj, H.-C. Tao, K.N. Shitaw, H. Sutiono, T.T. Hagos, T.T. Beyene, L.-M. Kuo, C.-C. Wang, S.-H. Wu, W.-N. Su, B.J. Hwang, Decoupling the origins of irreversible coulombic efficiency in anode-free lithium metal batteries, *Nat. Commun.* 12 (2021) 1452.

## A- APPENDIX A Supplementary Information for Chapter 2

### ***Contents:***

Electrode Preparation and Cell Construction

Electrochemical Impedance Spectroscopy

Cathode Price Estimation

Estimation of Annualized Capital Cost

Figure A.1 Nyquist plots for aged MAG-E electrodes in (a) 1M LiPF<sub>6</sub>/EC:DEC and (b) 0.5M KPF<sub>6</sub>/EC:DEC.

Figure A.2 Cost breakdown of KIBs with selected cathodes with the LNMC/G as reference.

Figure A.3 Cycling performance of graphite anodes in DHCs with selected electrolytes.

## Electrode Preparation and Cell Construction

Electrode slurries were prepared by mixing graphite and sodium carboxymethyl cellulose (Na-CMC) (degree of substitution (DS) =0.7, average Mw ~ 90000, Sigma-Aldrich) in a weight ratio of 90/10 in distilled water. This electrode composition was adapted from Reference [133]. The slurries were spread onto either Cu foil or Al foil with a 0.006-inch coating bar. The coatings were dried in air at 120 °C for 1 h. Three different types of graphite were used in this work: MAG-E (Hitachi), KS6L (Timcal), and natural graphite (230U, Asbury). Electrode disks were obtained from electrode coatings using a 1.35 cm<sup>2</sup> area circular punch. Half-cells were constructed from standard 2325 coin cell hardware. Electrodes were assembled into coin cells with a Li foil (99.5%, Sigma-Aldrich) or K foil (98%, Sigma-Aldrich) counter/reference electrode. Two layers of Celgard-2300 separator and one interleaving layer of BMF separator (3M Company) were used as cell separators. K electrolytes used in this work were 0.5 M KPF<sub>6</sub> (99.5%, Sigma-Aldrich) in ethylene carbonate (EC): diethyl carbonate (DEC) (1:2 v/v), 0.5 M KPF<sub>6</sub> in propylene carbonate (PC): EC (1:1 wt/wt), and 1 M potassium bis(trifluoromethanesulfonyl)imide (KTFSI) (98%, Sigma-Aldrich) in EC: DEC (1:2 v/v). Li electrolyte was 1M LiPF<sub>6</sub> (Gotion) in EC: DEC (1:2 v/v). All electrolyte solvents are from BASF. Cell assembly was conducted in an Ar-filled glovebox.

Double half-cells (DHCs) were constructed simply by connecting the Li or K terminals of two nominally identical half-cells [27]. Before this construction, one half-cell was discharged and then charged. The other half-cell was discharged, charged, then discharged with a trickle until C/40. The lower and upper cut-off voltages for these half-cells were 5 mV and 0.9 V (Li cells) or 2 V (K cells), respectively. DHCs were discharged/charged between ±0.9 V (Li cells) or ±2 V (K cells). The rate of discharge/charge was set to C/20. All cells were evaluated with a Maccor Series 4000 Automated Test System at 30.0 ± 0.1 °C.

## Electrochemical Impedance Spectroscopy

Impedance measurements were conducted by electrochemical impedance spectroscopy (EIS). AC impedance spectra were collected using Bio-Logic VMP3 with a 10 mV amplitude excitation and a frequency range from 100 kHz to 0.5mHz. Conventional symmetric cells, in which electrodes were recovered from cycled DHCs (20 cycles), were used for impedance measurements. Before impedance measurements, these conventional symmetric cells were discharged to 0 V at C/20 rate, then trickled until the current dropped down below C/200. EIS measurements were performed at 10 °C.

## Cathode Price Estimation

Price of K layered oxides,  $P$  / (\$ kg<sup>-1</sup>), was estimated using the following equation [38]:

$$P = C_0 + \frac{1}{M_w} \sum_i (P_i M_{w(i)} x_i / y_i) \quad (\text{A. 1})$$

where  $C_0$  is the manufacturing cost of layered oxides from raw materials;  $M_w$  is the molecular weight of layered oxides;  $P_i$  and  $M_{w(i)}$  are the price and the molecular weight of alkali or transition metal raw materials, respectively.  $x_i$  and  $y_i$  are the molar stoichiometry of alkali or transition metal in layered oxides and raw materials, respectively. It is assumed that no raw material is wasted for manufacturing cathode materials.

$C_0$  was set to a range of 0-5 \$ kg<sup>-1</sup>. All raw materials and their prices used in this work are listed below:

Raw material	Li <sub>2</sub> CO <sub>3</sub>	K <sub>2</sub> CO <sub>3</sub>	CoSO <sub>4</sub>	NiSO <sub>4</sub>	Cr <sub>2</sub> O <sub>3</sub>	MnSO <sub>4</sub>	Fe <sub>2</sub> O <sub>3</sub>
Price / (\$ kg <sup>-1</sup> )	6.5 [128]	0.8 [148]	32 [38]	5.5 [38]	0.6 [148]	1 [38]	~0.14 [148]

After a thorough search of the relevant literature, no detailed price information of battery-grade K hexacyanometallates and polyanionic compounds could be found. For this reason, a price range between 4-20 \$ kg<sup>-1</sup> was used for these compounds.

### Estimation of Annualized Capital Cost

The annualized capital cost,  $C_{ann}$ , was calculated on the basis of battery capital cost,  $C_{cap}$ , service lifetime,  $T_{life}$ , and average available energy factor,  $f_{aae}$ :

$$C_{ann} = \frac{C_{cap}}{T_{life}} f_{aae} \quad (A.2)$$

The  $f_{aae}$  was applied to describe the effect of continuous capacity fade on available battery energy. It is assumed that batteries have a linear capacity fade, which has been observed in long-term cycling results [47,156,158]. It is assumed that the battery has no impedance growth. Then, the  $f_{aae}$  is 0.9 if the battery is considered to be failed if its capacity is below 80%.

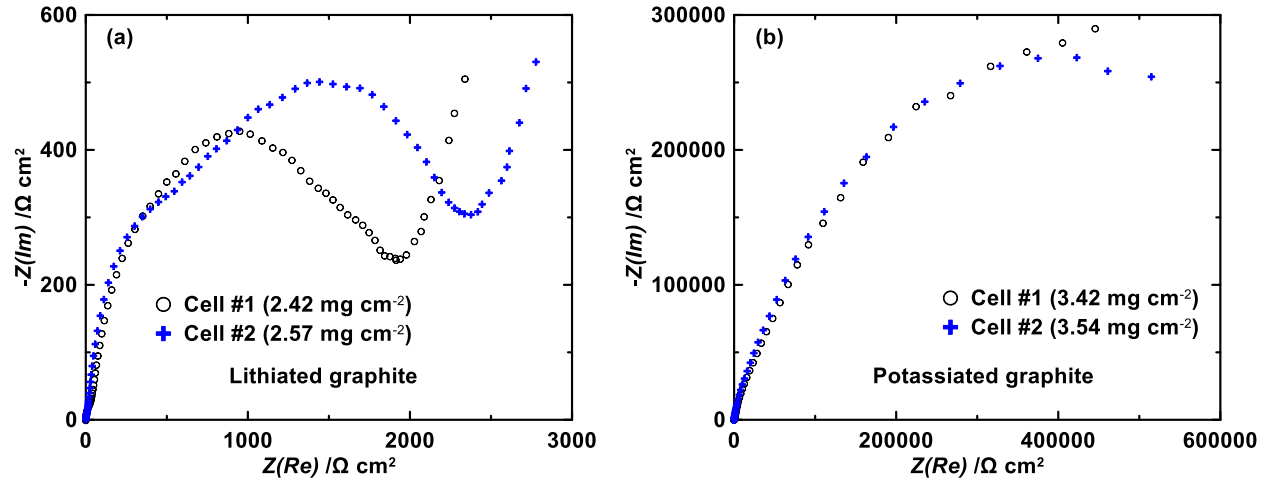


Figure A.1 Nyquist plots for aged MAG-E electrodes in (a) 1M LiPF<sub>6</sub>/EC:DEC and (b) 0.5M KPF<sub>6</sub>/EC:DEC. The electrode mass loadings of each cell have been presented in the figures.

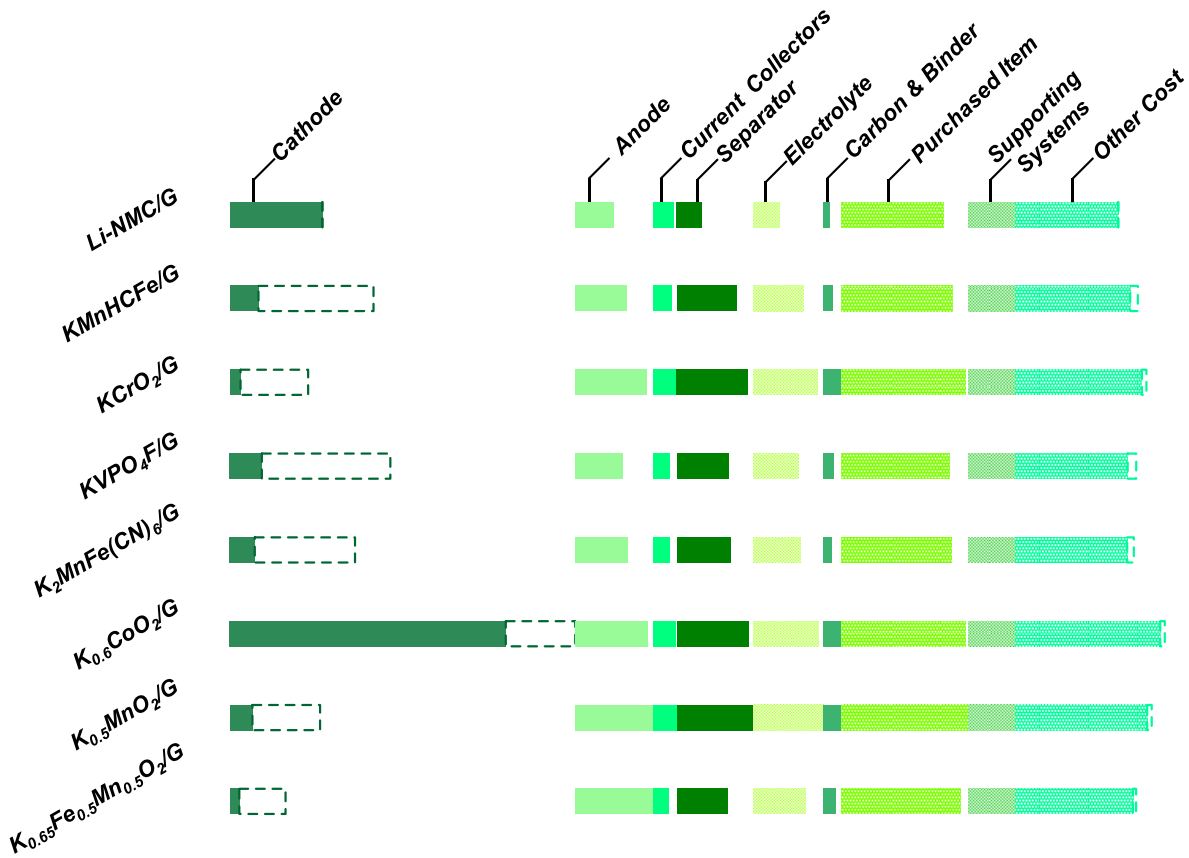


Figure A.2 Cost breakdown of KIBs with selected cathodes with the LNMC/G as reference. The dash bars represent the cost increases due to the price increase of K cathodes from their lower to their upper price limits.

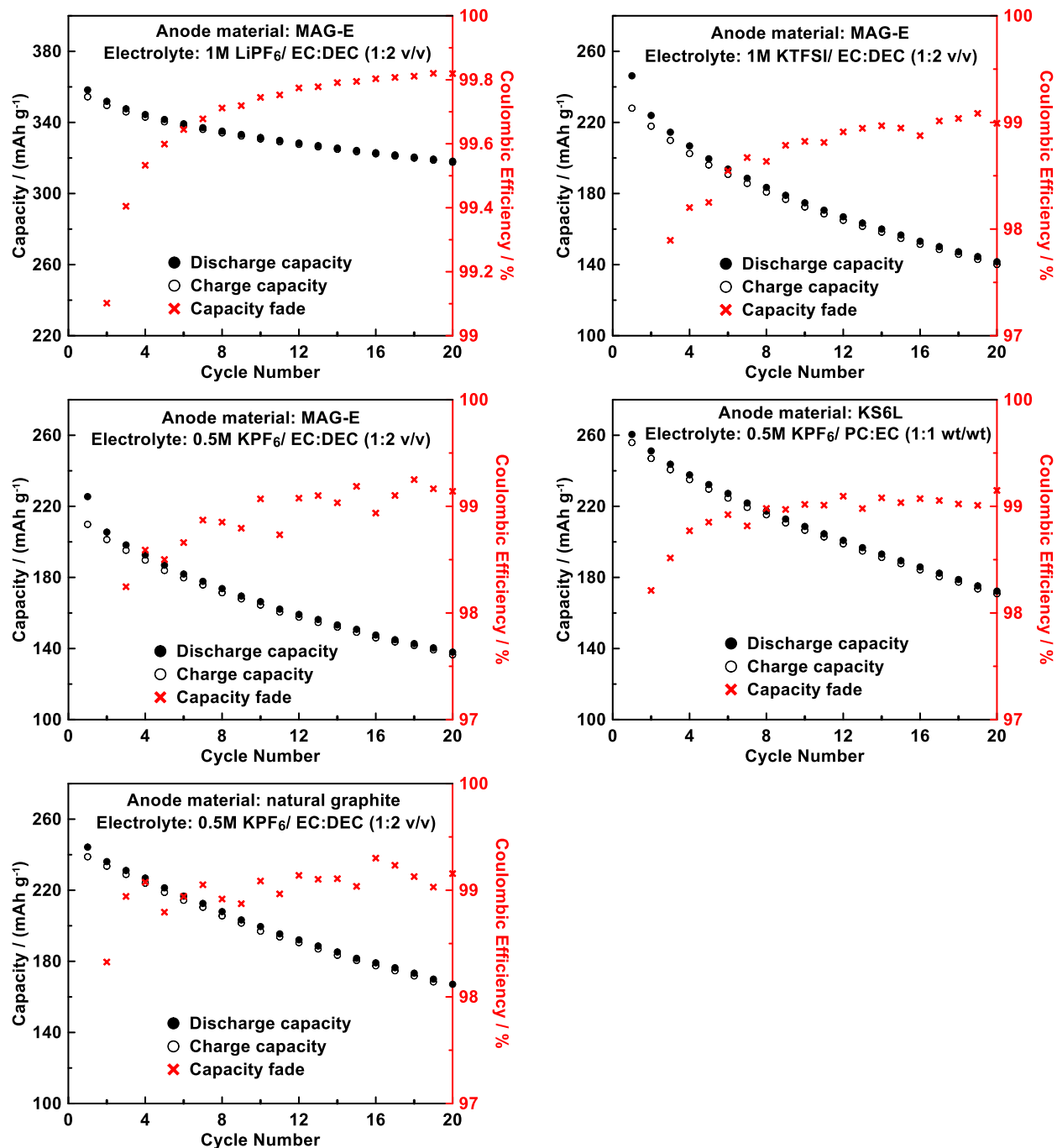


Figure A.3 Cycling performance of graphite anodes in DHCs with selected electrolytes. The specific capacity of DHCs was calculated with respect to the active material mass in the pre-lithiated electrode.

**B- APPENDIX B Details of the Cost Models**

Table B.1 The battery systems used in the Chapter 3.

	<b>Cathode</b>	<b>Anode</b>	<b>Cathode price:</b>
LNMC/G	Li-NMC622	Graphite	17.00
KNMC/G	"K"-NMC622	Graphite	14.80
KMnHCFe/G (Low price)	$K_{1.75}Mn[Fe(CN)_6]_{0.93} \cdot H_2O$	Graphite	4.00
KMnHCFe/G (High price)	$K_{1.75}Mn[Fe(CN)_6]_{0.93} \cdot H_2O$	Graphite	20.00
KCrO2/G (Low Price)	KCrO2	Graphite	0.80
KCrO2/G (high Price)	KCrO2	Graphite	5.80
KVPO4F/G (Low Price)	KVPO4F	Graphite	4.00
KVPO4F/G (High Price)	KVPO4F	Graphite	20.00
K2MnFeCN6/G (low Price)	$K_2MnFe(CN)_6$	Graphite	4.00
K2MnFeCN6/G (High Price)	$K_2MnFe(CN)_6$	Graphite	20.00
K0.6CoO2/G (Low Price)	K0.6CoO2	Graphite	19.86
K0.6CoO2/G (High Price)	K0.6CoO2	Graphite	24.87
K0.5MnO2/G (Low Price)	K0.5MnO2	Graphite	1.68
K0.5MnO2/G (High Price)	K0.5MnO2	Graphite	6.68
K0.65Fe0.5Mn0.5O2/G (Low price)	K0.65Fe0.5Mn0.5O2	Graphite	1.04
K0.65Fe0.5Mn0.5O2/G (High price)	K0.65Fe0.5Mn0.5O2	Graphite	6.04

Table B.2 Modifications of different battery systems in BatPac model (part one).

Sheet	File Id	Description	LN MC/G	KN MC/G	KMnHCF e/G(Low price)	KMnHCF e/G(High price)	KCrO2/G(Low Price)	KCrO2/G(high Price)	KVPO4F /G(Low Price)	KVPO4F /G(High Price)
Chem	E4	Selected system	NM C62 2-G	NM C62 2-G	NMC622-G	NMC622-G	NMC622-G	NMC622-G	NMC622-G	NMC622-G
Chem	N7	Cathode: active material capacity, mAh/g:	180	180	130	130	92	92	105	105
Chem	N9	Cathode: active material, %	89	89	89	89	89	89	89	89
Chem	N10	Cathode: carbon, %	6	6	6	6	6	6	6	6
Chem	N11	Cathode: binder, %	5	5	5	5	5	5	5	5
Chem	N15	Cathode: density, g/cm3	4.65	4.65	2.30	2.30	4.29	4.29	3.13	3.13
Chem	N18	Maximum thickness limit, $\mu\text{m}$	100	100	100	100	100	100	100	100
Chem	N21	N/P capacity ratio after formation	1.1	1.1	1.1	1.1	1.1	1.1	1.1	1.1
Chem	N22	Anode: active material capacity, mAh/g:	360	260	260	260	260	260	260	260
Chem	N24	Anode: active material, %	95	95	95	95	95	95	95	95

Sheet	Field	Description	LN MC/G	KN MC/G	KMnHCF e/G(Low price)	KMnHCF e/G(High price)	KCrO2/G(Low Price)	KCrO2/G(high Price)	KVPO4F /G(Low Price)	KVPO4F /G(High Price)
Chem	N25	Anode: carbon, %	0	0	0	0	0	0	0	0
Chem	N26	Anode: binder, %	5	5	5	5	5	5	5	5
Chem	N30	Anode: density, g/cm <sup>3</sup>	2.24	2.24	2.24	2.24	2.24	2.24	2.24	2.24
Chem	N37	Material of negative Foil	Cu	Al	Al	Al	Al	Al	Al	Al
Chem	N38	Thickness of negative Foil, $\mu\text{m}$	10.00	15.00	15.00	15.00	15.00	15.00	15.00	15.00
Chem	N45	Open circuit voltage at 20% SOC, V	3.57	3.57	3.57	3.57	1.75	1.75	3.70	3.70
Chem	N46	Open circuit voltage at 50% SOC, V	3.75	3.75	3.80	3.80	2.67	2.67	4.16	4.16
Chem	N47	Open circuit voltage at 80% SOC (mid SOC-HP), V	4.00	4.00	3.89	3.89	3.33	3.33	4.59	4.59
Chem	N48	Open circuit voltage at 100% SOC, V	4.20	4.20	4.26	4.26	3.72	3.72	4.72	4.72
Chem	N64	Maximum charging current density, mA/cm <sup>2</sup>	15.53	11.36	9.00	9.00	9.00	9.00	9.00	9.00

Sheet	Field	Description	LN MC/G	KN MC/G	KMnHCF e/G(Low price)	KMnHCF e/G(High price)	KCrO2/G(Low Price)	KCrO2/G(high Price)	KVPO4F /G(Low Price)	KVPO4F /G(High Price)
Chem	N81	Cathode: active materials price, \$/kg	17.00	14.80	4.00	20.00	0.80	5.80	4.00	20.00
Chem	N86	Anode: active materials price, \$/kg	12.50	12.50	12.50	12.50	12.50	12.50	12.50	12.50
Chem	N91	Negative current collector foil, \$/m2	1.20	0.30	0.30	0.30	0.30	0.30	0.30	0.30
Battery design: only the "F" column changed										
Battery Design	F59	Vehicle type (microHEV, HEV-HP, PHEV, EV)	EV	EV	EV	EV	EV	EV	EV	EV
Battery Design	F60	Pack heat transfer fluid (EG-W, CA, CoolA )	EG-W	EG-W	EG-W	EG-W	EG-W	EG-W	EG-W	EG-W
Battery Design	F65	Number of cells per module	12	12	12	12	12	12	12	12
Battery Design	F66	Number of cells in parallel	1	1	1	1	1	1	1	1
Battery	F67	Number of modules in row	5	5	5	5	5	5	5	5

Design										
Sheet	Field	Description	LN MC/G	KN MC/G	KMnHCF e/G(Low price)	KMnHCF e/G(High price)	KCrO2/G(Low Price)	KCrO2/G(high Price)	KVPO4F /G(Low Price)	KVPO4F /G(High Price)
Battery Design	F68	Number of rows of modules per pack	4	4	4	4	4	4	4	4
Battery Design	F102	Override: maximum pack required sustained C-rate on discharge, A/Ah	0.3	0.7	0.7	0.7	0.7	0.7	0.7	0.7
Battery Design	F203	Pack energy, kWh	50	50	50	50	50	50	50	50

Table B.3 Modifications of different battery systems in BatPac model (part two).

Sheet	Field	Description	K <sub>2</sub> MnFeC N <sub>6</sub> /G(low Price)	K <sub>2</sub> MnFeC N <sub>6</sub> /G(High Price)	K <sub>0.6</sub> C oO <sub>2</sub> /G( Low Price)	K <sub>0.6</sub> Co O <sub>2</sub> /G( High Price)	K <sub>0.5</sub> MnO 2/G (Low Price )	K <sub>0.5</sub> MnO 2/G (High Price )	K <sub>0.65</sub> Fe 0.5Mn0.5 O <sub>2</sub> /G (Low price)	K <sub>0.65</sub> Fe 0.5Mn0.5 O <sub>2</sub> /G (High price)
Chem	E4	Selected system	NMC622-G	NMC622-G	NMC622-G	NMC622-G	NMC622-G	NMC622-G	NMC622-G	NMC622-G
Chem	N7	Cathode: active material capacity, mAh/g:	156	156	90	90	100	100	151	151
Chem	N9	Cathode: active material, %	89	89	89	89	89	89	89	89
Chem	N10	Cathode: carbon, %	6	6	6	6	6	6	6	6
Chem	N11	Cathode: binder, %	5	5	5	5	5	5	5	5
Chem	N15	Cathode: density, g/cm <sup>3</sup>	2.19	2.19	4.39	4.39	3.88	3.88	4.56	4.56
Chem	N18	Maximum thickness limit, μm	100	100	100	100	100	100	100	100
Chem	N21	N/P capacity ratio after formation	1.1	1.1	1.1	1.1	1.1	1.1	1.1	1.1

Sheet	Field	Description	K <sub>2</sub> MnFeC N <sub>6</sub> /G(low Price)	K <sub>2</sub> MnFeC N <sub>6</sub> /G(High Price)	K <sub>0.6</sub> C oO <sub>2</sub> /G( Low Price)	K <sub>0.6</sub> Co O <sub>2</sub> /G( High Price)	K <sub>0.5</sub> MnO 2/G (Low Price )	K <sub>0.5</sub> MnO 2/G (High Price )	K <sub>0.65</sub> Fe 0.5Mn0.5 O <sub>2</sub> /G (Low price)	K <sub>0.65</sub> Fe 0.5Mn0.5 O <sub>2</sub> /G (High price)
Chem	N 2 2	Anode: active material capacity, mAh/g:	260	260	260	260	260	260	260	260
Chem	N 2 4	Anode: active material, %	95	95	95	95	95	95	95	95
Chem	N 2 5	Anode: carbon, %	0	0	0	0	0	0	0	0
Chem	N 2 6	Anode: binder, %	5	5	5	5	5	5	5	5
Chem	N 3 0	Anode: density, g/cm <sup>3</sup>	2.24	2.24	2.24	2.24	2.24	2.24	2.24	2.24
Chem	N 3 7	Material of negative Foil	Aluminum	Aluminum	Aluminum	Aluminum	Aluminum	Aluminum	Aluminum	Aluminum
Chem	N 3 8	Thickness of negative Foil, μm	15.00	15.00	15.00	15.00	15.00	15.00	15.00	15.00
Chem	N 4 5	Open circuit voltage at 20% SOC, V	3.50	3.50	1.87	1.87	1.80	1.80	1.83	1.83

Sheet	Field	Description	K2MnFeCN6/G(low Price)	K2MnFeCN6/G(High Price)	K0.6CoO2/G(Low Price)	K0.6CoO2/G(High Price)	K0.5MnO2/G(Low Price)	K0.5MnO2/G(High Price)	K0.65Fe0.5Mn0.5O2/G(Low price)	K0.65Fe0.5Mn0.5O2/G(High price)
Chem	N46	Open circuit voltage at 50% SOC, V	3.69	3.69	2.65	2.65	2.46	2.46	2.49	2.49
Chem	N47	Open circuit voltage at 80% SOC (mid SOC-HP), V	3.79	3.79	3.43	3.43	3.18	3.18	3.16	3.16
Chem	N48	Open circuit voltage at 100% SOC, V	4.08	4.08	3.66	3.66	3.64	3.64	3.77	3.77
Chem	N64	Maximum charging current density, mA/cm2	9.00	9.00	9.00	9.00	9	9	11.36	11.36
Chem	N81	Cathode: active materials price, \$/kg	4.00	20.00	19.86	24.87	1.68	6.68	1.04	6.04
Chem	N86	Anode: active materials price, \$/kg	12.50	12.50	12.50	12.50	12.50	12.50	12.50	12.50
Chem	N91	Negative current collector foil, \$/m2	0.30	0.30	0.30	0.30	0.30	0.30	0.30	0.30
Battery design: only the "F" column changed										
Battery	F59	Vehicle type (microHEV, HEV-HP, PHEV, EV)	EV	EV	EV	EV	EV	EV	EV	EV

Design										
Sheet	Field	Description	K <sub>2</sub> MnFeC N <sub>6</sub> /G(low Price)	K <sub>2</sub> MnFeC N <sub>6</sub> /G(High Price)	K <sub>0.6</sub> C oO <sub>2</sub> /G( Low Price)	K <sub>0.6</sub> Co O <sub>2</sub> /G( High Price)	K <sub>0.5</sub> MnO 2/G (Low Price )	K <sub>0.5</sub> MnO 2/G (High Price )	K <sub>0.65</sub> Fe 0.5Mn0.5 O <sub>2</sub> /G (Low price)	K <sub>0.65</sub> Fe 0.5Mn0.5 O <sub>2</sub> /G (High price)
Battery Design	F60	Pack heat transfer fluid (EG-W, CA, CoolA )	EG-W	EG-W	EG-W	EG-W	EG-W	EG-W	EG-W	EG-W
Battery Design	F65	Number of cells per module	12	12	12	12	12	12	12	12
Battery Design	F66	Number of cells in parallel	1	1	1	1	1	1	1	1
Battery Design	F67	Number of modules in row	5	5	5	5	5	5	5	5
Battery Design	F68	Number of rows of modules per pack	4	4	4	4	4	4	4	4
Battery Design	F102	Override: maximum pack required sustained C-rate on discharge, A/Ah	0.7	0.7	0.7	0.7	0.7	0.7	0.6	0.6

Sheet	Field	Description	$K_2MnFeC_6$ /G(low Price)	$K_2MnFeC_6$ /G(High Price)	$K_{0.6}CoO_2$ /G(Low Price)	$K_{0.6}CoO_2$ /G(High Price)	$K_{0.5}MnO_2$ /G (Low Price)	$K_{0.5}MnO_2$ /G (High Price)	$K_{0.65}Fe_{0.5}Mn_{0.5}O_2$ /G (Low price)	$K_{0.65}Fe_{0.5}Mn_{0.5}O_2$ /G (High price)
Battery Design	F203	Pack energy, kWh	50	50	50	50	50	50	50	50

Table B.4 Cost details for different battery systems in BatPac model (part one).

Sheet	Field	Description								
System			LN MC/ G	KN MC/ G	KMnHCFE/ G(Low price)	KMnHCFE/ G(High price)	KCrO2/G (Low Price)	KCrO2/G (high Price)	KVPO4F/ G(Low Price)	KVPO4F/ G(High Price)
Materials										
Cost Breakdown	F 21	Positive Active Material, \$/Pack	147 4.53	1281 .63	457.50	2287.50	172.08	1247.61	511.10	2555.48
Cost Breakdown	F 22	Negative Active Material, \$/Pack	616. 82	836. 12	817.70	817.70	1143.77	1143.77	751.67	751.67
Cost Breakdown	F 23	Carbon and Binders, \$/Pack	110. 74	120. 24	150.22	150.22	282.62	282.62	162.47	162.47
Cost Breakdown	F 24	Positive Current Collector, \$/Pack	61.5 7	83.1 4	143.68	143.68	172.30	172.30	125.92	125.92
Cost Breakdown	F 25	Negative Current Collector, \$/Pack	261. 29	87.7 1	150.29	150.29	179.88	179.88	131.95	131.95
Cost Breakdown	F 26	Separators, \$/Pack	399. 22	540. 69	941.70	941.70	1131.80	1131.80	822.98	822.98
Cost Breakdown	F 27	Electrolyte, \$/Pack	416. 82	505. 92	798.66	798.66	1020.86	1020.86	707.08	707.08

<b><i>Purchased Items</i></b>										
Cost Breakdown	F 28	Cell Hardware, \$/Pack	230.60	202.29	215.15	215.15	223.44	223.44	211.32	211.32
Cost Breakdown	F 29	Module Hardware, \$/Pack	872.42	878.95	898.64	898.64	975.34	975.34	880.26	880.26
Cost Breakdown	F 30	Battery Jacket, \$/Pack	527.07	553.66	651.90	651.90	779.46	779.46	629.67	629.67
<b><i>Supporting System</i></b>										
Cost Breakdown	F 32	Battery Management System, \$/Pack	715.00	715.00	715.00	715.00	715.00	715.00	715.00	715.00
Cost Breakdown	F 33	Thermal Management System, \$/Pack	40.00	40.00	40.00	40.00	40.00	40.00	40.00	40.00
<b><i>Other cost</i></b>										
Summary of Results	F 62	Direct Labor Summary, \$/pack	157.90	164.25	178.68	178.68	187.63	187.63	175.21	175.21
Summary of Results	F 63	Variable Overhead, \$/pack	147.57	153.35	167.07	167.07	180.15	180.15	164.50	164.50
Summary of Results	F 64	General, Sales, Administration, \$/pack	181.87	188.96	205.93	205.93	223.32	223.32	202.95	202.95
Summary of Results	F 65	Research and Development, \$/pack	168.81	175.30	191.19	191.19	210.20	210.20	188.83	188.83

Summary of Results	F66	Depreciation, \$/pack	422.03	438.25	477.98	477.98	525.50	525.50	472.08	472.08
Summary of Results	F67	Profit, \$/pack	204.83	212.16	228.46	246.76	253.49	264.25	223.08	243.52
Summary of Results	F68	Warranty, \$/pack	350.23	359.67	373.79	477.29	429.06	489.90	356.22	471.85
		<b>Materials</b>	334.098	3455.46	3459.74	5289.74	4103.31	5178.83	3213.16	5257.55
		<b>Purchased Items</b>	163.010	1634.89	1765.69	1765.69	1978.24	1978.24	1721.25	1721.25
		<b>Supporting Systems</b>	755.00	755.00	755.00	755.00	755.00	755.00	755.00	755.00
		<b>Other cost</b>	163.324	1691.93	1823.10	1944.91	2009.36	2080.95	1782.87	1918.95
		Total cost to OEM for complete system, \$	735.932	7537.29	7803.54	9755.34	8845.91	9993.02	7472.28	9652.75
<b>Material Details</b>										
Chem	E7	Cathode: active material capacity, mAh/g:	180.00	180.00	130.00	130.00	92.00	92.00	105.00	105.00
Chem	D81	Cathode: active material cost, \$/kg	17.00	14.80	4.00	20.00	3.80	20.80	4.00	20.00
Chem	E15	Cathode: active material density, g/cm <sup>3</sup>	4.65	4.65	2.24	2.24	4.29	4.29	3.13	3.13
Chem	E22	Anode: active material capacity, mAh/g:	360.00	260.00	260.00	260.00	260.00	260.00	260.00	260.00

Chem	D86	Anode: active material cost, \$/kg	12.50	12.50	12.50	12.50	12.50	12.50	12.50	12.50
Chem	E37	Anode: current collector	Copper	Aluminum						
Chem	D91	Anode: current collector cost, \$/m2	1.20	0.3	0.3	0.3	0.3	0.3	0.3	0.3
Chem	E21	N/P capacity ratio	1.10	1.10	1.10	1.10	1.10	1.10	1.10	1.10
<b>Cell Details</b>										
Battery Design	F111	Positive electrode thickness, $\mu\text{m}$	100.00	73.15	100.00	100.00	100	100	100	100
Battery Design	F112	Negative electrode thickness, $\mu\text{m}$	98.72	99.98	55.59	55.59	65.63	65.63	58.35	58.35
Battery Design	F118	Cell Area, $\text{cm}^2$	12973.52	17704.06	31326.72	31326.72	37886.98	37886.98	27265.05	27265.05
Battery Design	F120	Number of bicell layers	42	47	51	51	49	49	51	51
Battery Design	F83	Cell capacity	55.97	55.87	54.96	54.96	78.47	78.47	50.21	50.21
Chem	E46	Open circuit voltage at 50% SOC, V	3.75	3.75	3.80	3.80	2.67	2.67	4.16	4.16
<b>Battery Details</b>										
Battery Design	F65	Number of cells per module	12	12	12	12	12	12	12	12

Battery Design	F 66	Number of cells in parallel	1	1	1	1	1	1	1	1
Battery Design	F 67	Number of modules in row	5	5	5	5	5	5	5	5
Battery Design	F 68	Number of rows of modules per pack	4	4	4	4	4	4	4	4
Battery Design	F 70	Number of modules in parallel	1	1	1	1	1	1	1	1
Battery Design	F 60	Cooling fluid	EG-W							
<b>Battery Performance</b>										
Chem	E 66	Available battery energy, % of total	85.00	85.00	85.00	85.00	85.00	85.00	85.00	85.00
Battery Design	F 219	Energy, kWh	50.00	50.00	50.00	50.00	50.00	50.00	50.00	50.00
Battery Design	F 220	Mass, kg	267.35	289.51	378.91	378.91	562.10	562.10	370.79	370.79
Battery Design	F 221	Volume, L	162.69	187.85	270.12	270.12	327.91	327.91	245.86	245.86
		<b>Total battery cost, \$/kWh</b>	<b>147.19</b>	<b>150.75</b>	<b>156.07</b>	<b>195.11</b>	<b>176.92</b>	<b>199.86</b>	<b>149.45</b>	<b>193.05</b>

Table B.5 Cost details for different battery systems in BatPac model (part two).

Sheet	Field	Description								
<b>System</b>			K2MnFeCN6/G(lowPrice)	K2MnFeCN6/G(HighPrice)	K0.6CoO2/G(Low Price)	K0.6CoO2/G(High Price)	K0.5MnO2/G (Low Price)	K0.5MnO2/G (High Price)	K0.65Fe0.5Mn0.5O2/G (Low price)	K0.65Fe0.5Mn0.5O2/G (High price)
<b>Materials</b>										
Cost Breakdown	F21	Positive Active Material, \$/Pack	398.70	1993.48	4392.04	5497.79	361.13	1437.48	152.57	888.17
Cost Breakdown	F22	Negative Active Material, \$/Pack	841.64	841.64	1153.25	1153.25	1238.02	1238.02	1229.81	1229.81
Cost Breakdown	F23	Carbon and Binders, \$/Pack	134.87	134.87	290.35	290.35	287.08	287.08	206.07	206.07
Cost Breakdown	F24	Positive Current Collector, \$/Pack	129.20	129.20	174.18	174.18	185.72	185.72	122.90	122.90
Cost Breakdown	F25	Negative Current Collector, \$/Pack	135.38	135.38	181.82	181.82	193.73	193.73	128.97	128.97
Cost Breakdown	F26	Separators, \$/Pack	845.84	845.84	1144.39	1144.39	1220.99	1220.99	804.70	804.70
Cost Breakdown	F27	Electrolyte, \$/Pack	751.00	751.00	1031.48	1031.48	1105.44	1105.44	817.22	817.22

<b>Purchased Items</b>										
Cost Breakdown	F 28	Cell Hardware, \$/Pack	213.10	213.10	223.85	223.85	226.53	226.53	215.23	215.23
Cost Breakdown	F 29	Module Hardware, \$/Pack	899.08	899.08	976.85	976.85	996.93	996.93	975.04	975.04
Cost Breakdown	F 30	Battery Jacket, \$/Pack	641.06	641.06	772.20	772.20	793.65	793.65	709.77	709.77
<b>Supporting System</b>										
Cost Breakdown	F 32	Battery Management System, \$/Pack	715.00	715.00	715.00	715.00	715.00	715.00	715.00	715.00
Cost Breakdown	F 33	Thermal Management System, \$/Pack	40.00	40.00	40.00	40.00	40.00	40.00	40.00	40.00
<b>Other cost</b>										
Summary of Results	F 62	Direct Labor Summary, \$/pack	175.33	175.33	188.14	188.14	190.29	190.29	176.37	176.37
Summary of Results	F 63	Variable Overhead, \$/pack	163.49	163.49	180.87	180.87	184.95	184.95	169.62	169.62
Summary of Results	F 64	General, Sales, Administration, \$/pack	201.41	201.41	224.27	224.27	229.86	229.86	210.33	210.33
Summary of Results	F 65	Research and Development, \$/pack	186.72	186.72	211.23	211.23	217.68	217.68	198.13	198.13

Summary of Results	F66	Depreciation, \$/pack	466.80	466.80	528.08	528.08	544.20	544.20	495.34	495.34
Summary of Results	F67	Profit, \$/pack	222.01	237.95	296.98	308.03	264.99	275.75	234.72	242.08
Summary of Results	F68	Warranty, \$/pack	358.71	448.92	670.32	732.86	461.51	522.38	383.42	425.03
		<b>Materials</b>	3236.61	4831.40	8367.51	9473.26	4592.11	5668.45	3462.24	4197.84
		<b>Purchased Items</b>	1753.23	1753.23	1972.90	1972.90	2017.10	2017.10	1900.04	1900.04
		<b>Supporting Systems</b>	755.00	755.00	755.00	755.00	755.00	755.00	755.00	755.00
		<b>Other cost</b>	1774.47	1880.62	2299.88	2373.48	2093.47	2165.12	1867.94	1916.90
		Total cost to OEM for complete system, \$	7519.32	9220.26	13395.29	14574.64	9457.69	10605.67	7985.22	8769.78
<b>Material Details</b>										
Chem	E7	Cathode: active material capacity, mAh/g:	156	156	90	90	100	100	151	151
Chem	D81	Cathode: active material cost, \$/kg	4.00	20.00	22.86	39.87	4.68	21.68	4.04	21.04
Chem	E15	Cathode: active material density, g/cm <sup>3</sup>	2.19	2.19	4.39	4.39	3.88	3.88	4.56	4.56
Chem	E22	Anode: active material capacity, mAh/g:	260.00	260.00	260.00	260.00	260.00	260.00	260.00	260.00

Chem	D 86	Anode: active material cost, \$/kg	12.50	12.50	12.50	12.50	12.50	12.50	12.50	12.50
Chem	E 37	Anode: current collector	Aluminum							
Chem	D 91	Anode: current collector cost, \$/m <sup>2</sup>	0.3	0.3	0.3	0.3	0.3	0.3	0.3	0.3
Chem	E 21	N/P capacity ratio	1.10	1.10	1.10	1.10	1.10	1.10	1.10	1.10
<b>Cell Details</b>										
Battery Design	F 11 1	Positive electrode thickness, $\mu\text{m}$	100	100	100	100	100	100	89	89
Battery Design	F 11 2	Negative electrode thickness, $\mu\text{m}$	63.87	63.87	65.46	65.46	66.05	66.05	99.98	99.98
Battery Design	F 11 8	Cell Area, cm <sup>2</sup>	28081.02	28081.02	38319.39	38319.39	40952.85	40952.85	26761.91	26761.91
Battery Design	F 12 0	Number of bicell layers	49	49	49	49	49	49	44	44
Battery Design	F 83	Cell capacity	56.61	56.61	79.17	79.17	85.37	85.37	84.45	84.45
Chem	E 46	Open circuit voltage at 50% SOC, V	3.69	3.69	2.65	2.65	2.46	2.46	2.49	2.49
<b>Battery Details</b>										
Battery Design	F 65	Number of cells per module	12	12	12	12	12	12	12	12

Battery Design	F 66	Number of cells in parallel	1	1	1	1	1	1	1	1
Battery Design	F 67	Number of modules in row	5	5	5	5	5	5	5	5
Battery Design	F 68	Number of rows of modules per pack	4	4	4	4	4	4	4	4
Battery Design	F 70	Number of modules in parallel	1	1	1	1	1	1	1	1
Battery Design	F 60	Cooling fluid	EG-W							
<b>Battery Performance</b>										
Chem	E 66	Available battery energy, % of total	85.00	85.00	85.00	85.00	85.00	85.00	85.00	85.00
Battery Design	F 21 9	Energy, kWh	50.00	50.00	50.00	50.00	50.00	50.00	50.00	50.00
Battery Design	F 22 0	Mass, kg	353.74	353.74	571.58	571.58	584.72	584.72	447.69	447.69
Battery Design	F 22 1	Volume, L	256.78	256.78	330.64	330.64	349.78	349.78	272.58	272.58
		<b>Total battery cost, \$/kWh</b>	<b>150.39</b>	<b>184.41</b>	<b>267.91</b>	<b>291.49</b>	<b>189.15</b>	<b>212.11</b>	<b>159.70</b>	<b>175.40</b>

## **C- APPENDIX C Supplementary Information for Chapter 4**

This document includes:

- Experimental procedure for cycled electrode samples prepared for SEM characterization
- Supplementary Figures C.1-C.9

### **Experimental Procedure for Cycled Electrode Samples Prepared for SEM Characterization**

Cycled electrodes were recovered in an Ar-filled glove box, rinsed in dimethyl carbonate (battery grade from BASF) to remove residual electrolyte salt, and then vacuum dried. To minimize air exposure, a desiccator was used to transfer the cycled electrode samples between the Ar-filled glove box and the cross-section polisher. After ion milling, the electrodes were stored in an Ar-filled glove box until being transferred to the SEM using an Ar-filled plastic bag. A stream of argon gas was flowed over the air-sensitive electrodes during the sample loading procedure for the cross-section polisher and SEM.

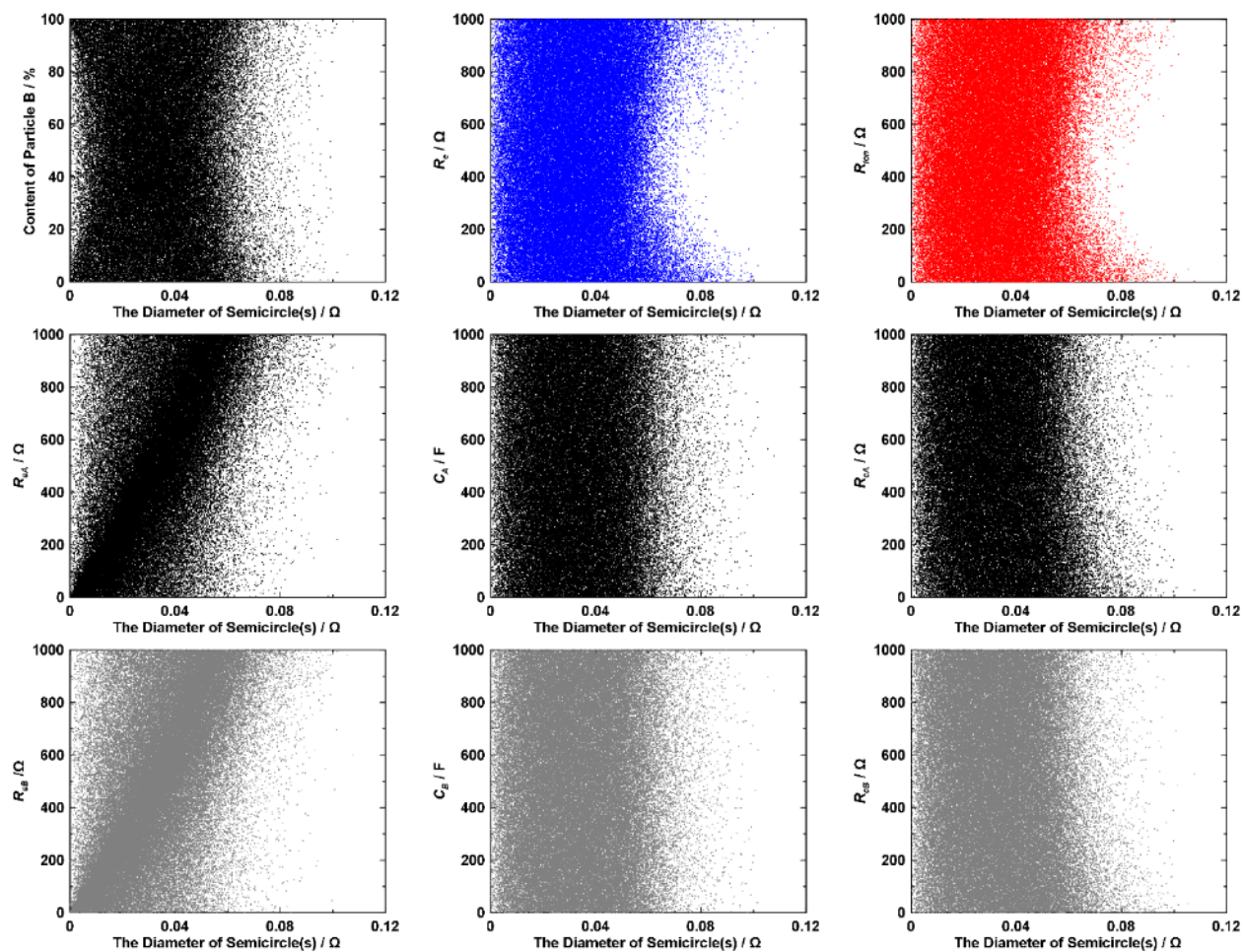


Figure C.1 Monte Carlo simulation to investigate the effect of parameters on the IES spectra of blended electrodes. All parameters were randomized between 0-1000  $\Omega$  or 0-1000 F, except the content of the two different particles, which was randomized between 0-100%. 100,000 trials were made to explore the major contribution to the overall interfacial resistance growth. 5000 ITLs were used for the simulation of  $Z_{ITLM}$ . These results show that  $R_{SA}$  and  $R_{SB}$ , related to the interfacial resistance of particle A and B, have a strong correlation to the semicircle(s) growth.

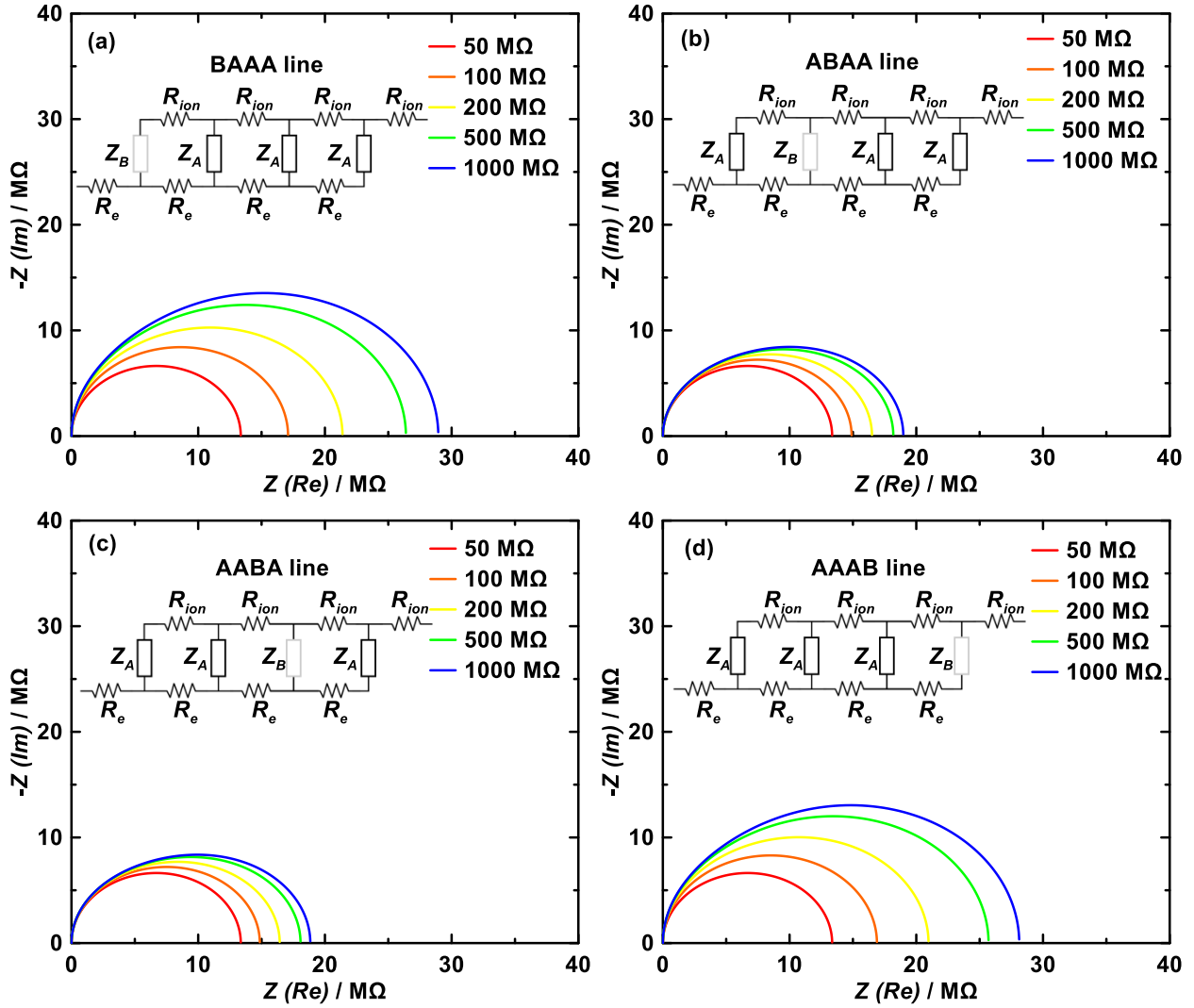


Figure C.2 The impedance growth in the four-particle-linked ITL containing one particle B, which can have an increased interfacial resistance ( $R_{sB}$ ). Four possible transmission lines have been presented in (a-d) along with the increase of  $R_{sB}$  in particle B.

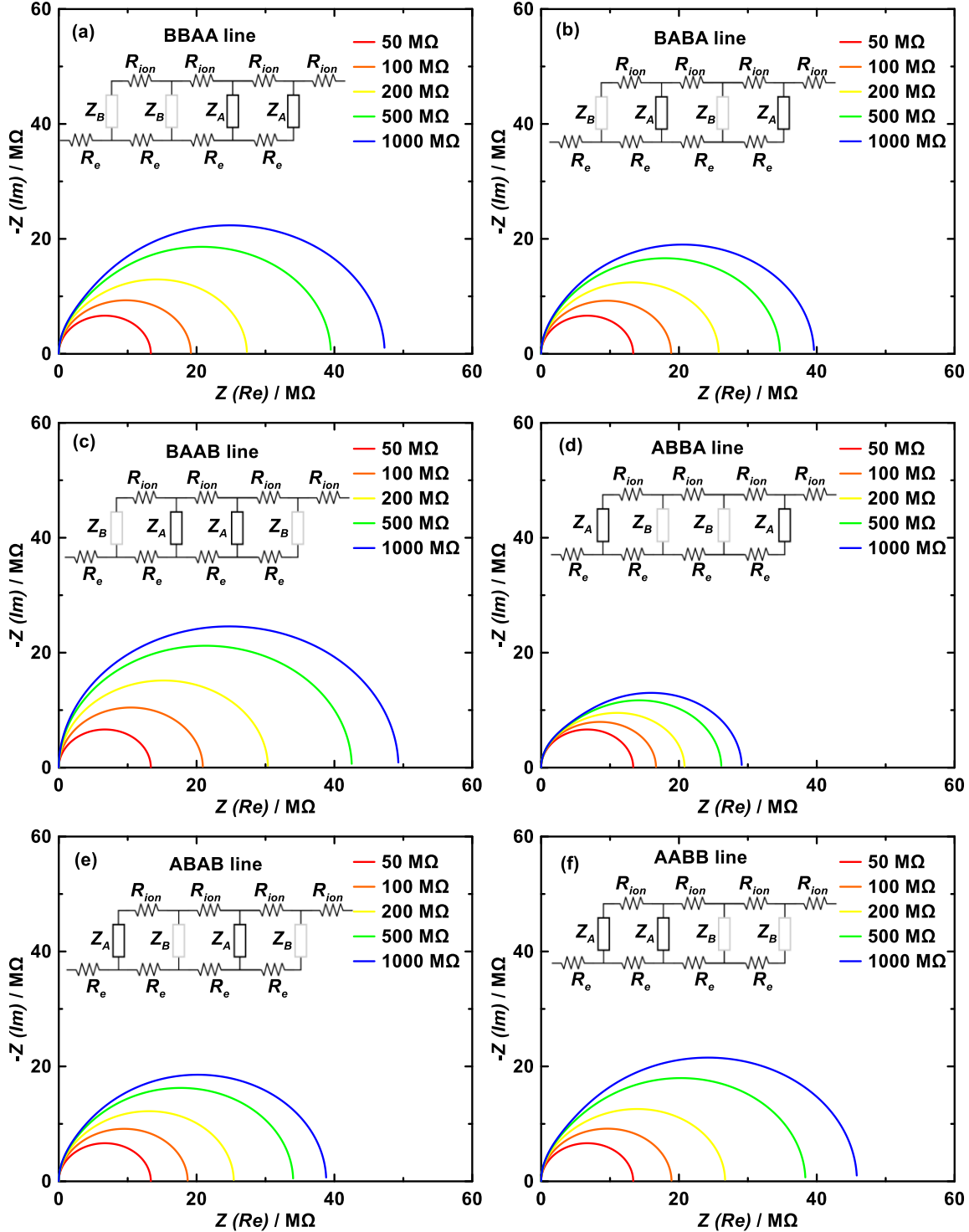


Figure C.3 The impedance growth in the four-particle-linked ITL containing two B particles, which can have an increased interfacial resistance ( $R_{sB}$ ). Six possible transmission lines have been presented in (a-f) along with the increase of  $R_{sB}$  in particle B.

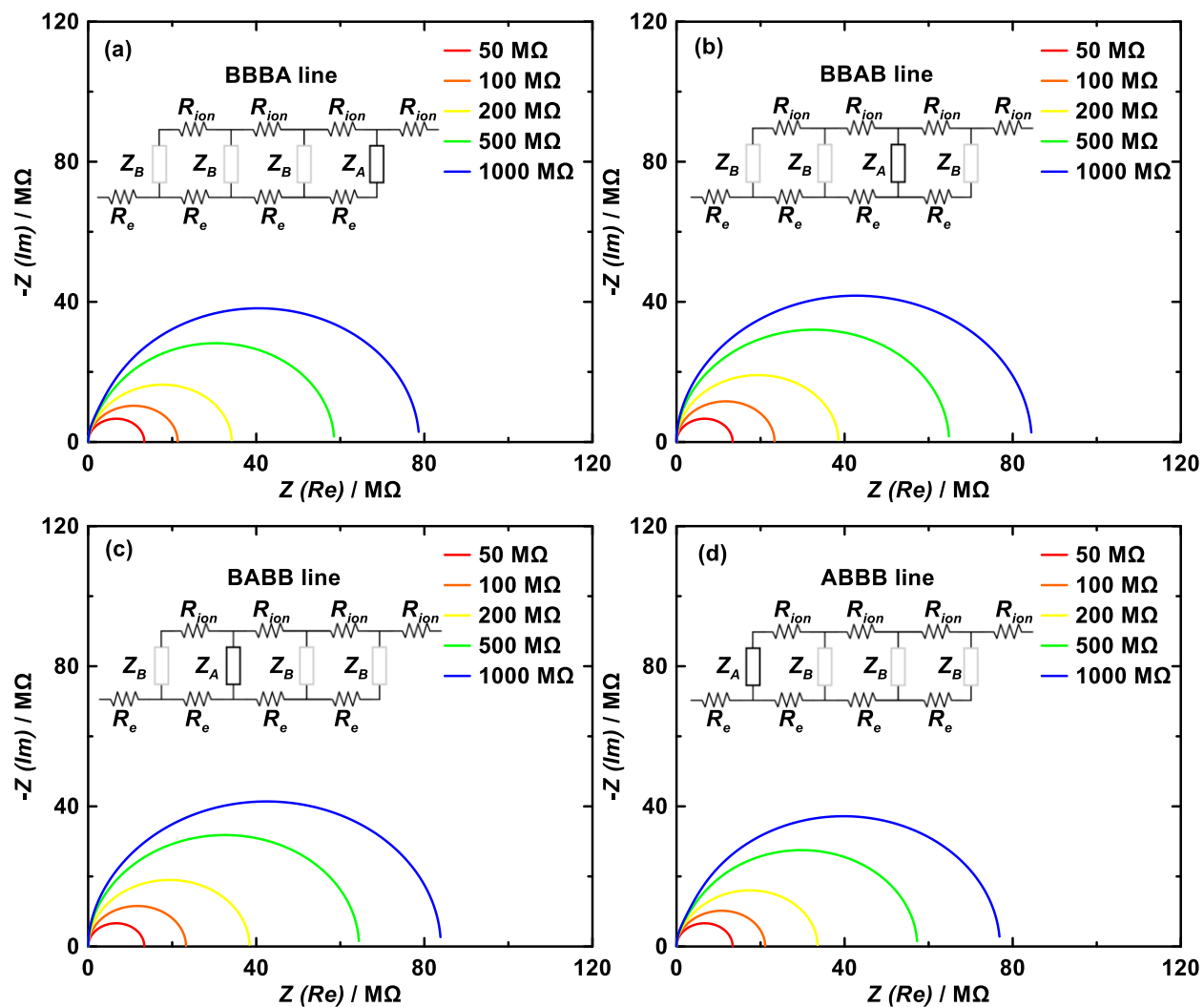


Figure C.4 The impedance growth in the four-particle-linked ITL containing three B particles, which can have an increased interfacial resistance ( $R_{SB}$ ). Four possible transmission lines have been presented in (a-f) along with the increase of  $R_{SB}$  in particle B.

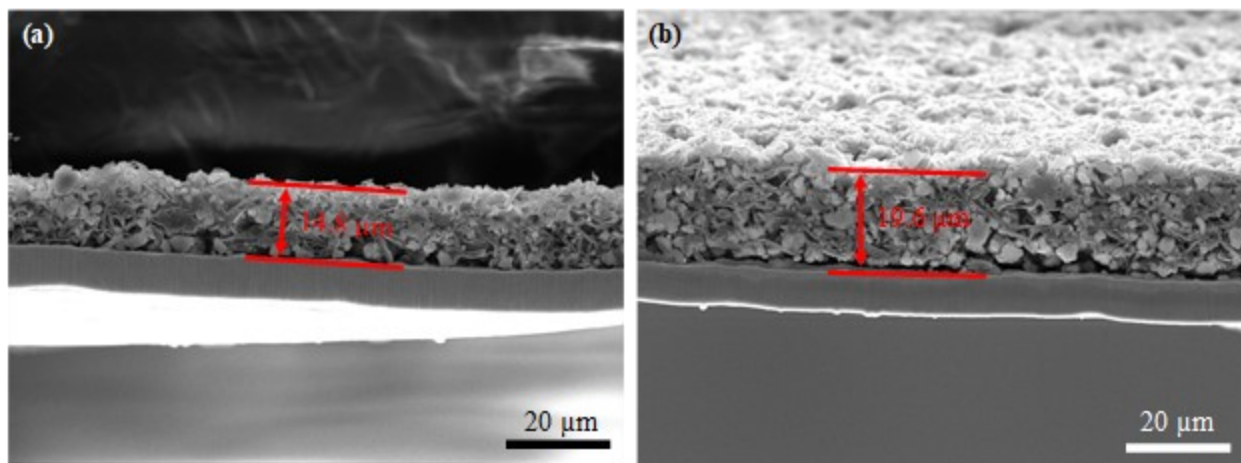


Figure C.5 Cross-sectional SEM images of Si-alloy/graphite (31.8 wt.% graphite content) blended electrodes, (a) pristine and (b) electrochemically lithiated to the state of charge of ~50% after 20 cycles. These two electrodes in pristine condition have a similar thickness. The volume expansion of the Si-alloy/graphite blended electrode at the state of charge of ~50% is ~30%. This result agrees within 19% of a direct measurement of the volume expansion as measured with a micrometer.

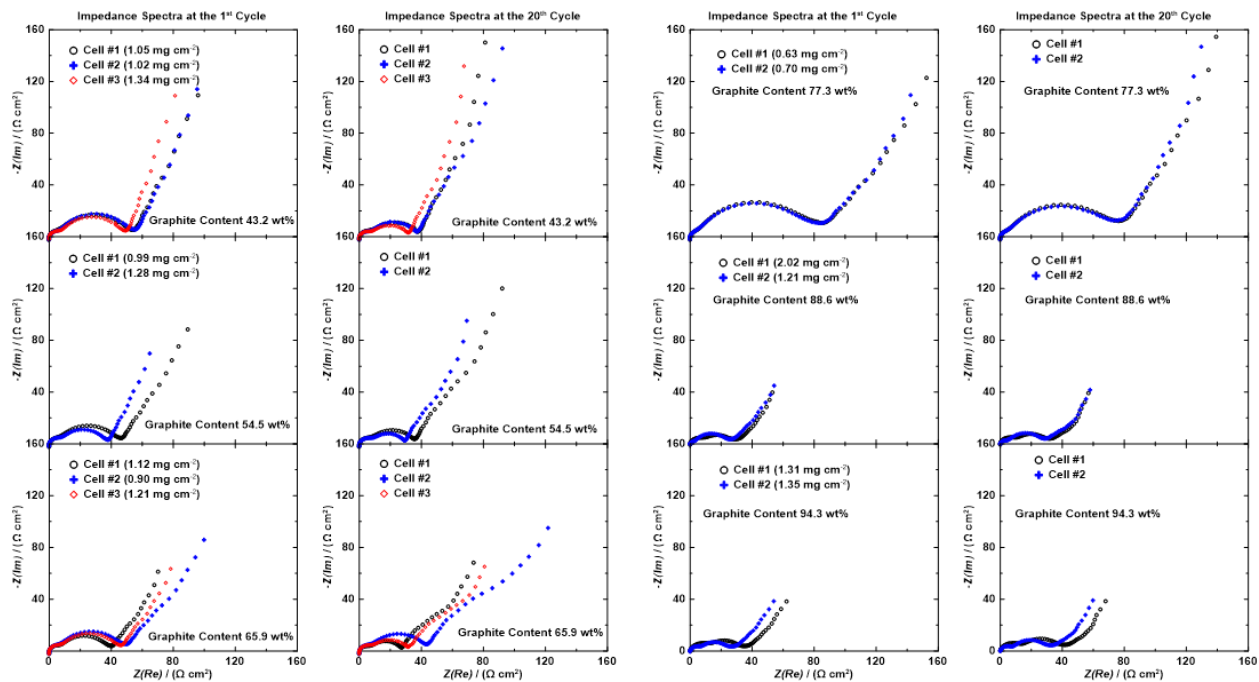


Figure C.6 The Nyquist plot of Si-alloy/graphite blended electrodes with various graphite contents at the 1<sup>st</sup> cycle (left column) and at the 20<sup>th</sup> cycle (right column).

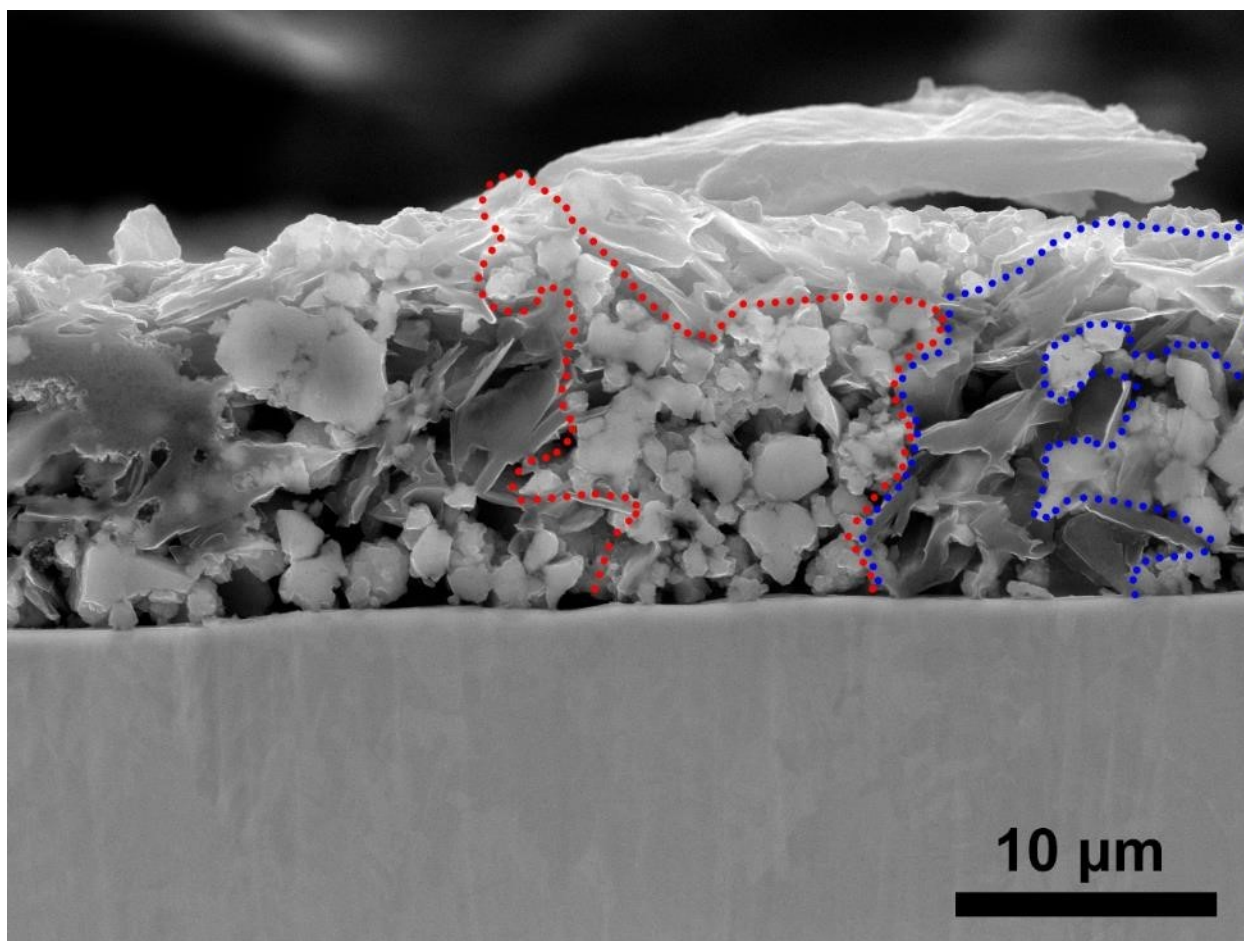


Figure C.7 Cross-section SEM image of a handmixed Si-alloy/graphite blended electrode (54.5 wt.% graphite content) purposely made to have a poor particle distribution. The slurry was hand-mixed about five minutes or just until all the particles were dispersed in water. The bright irregularly-shaped particles are Si-alloy and the dark flake-like particles are graphite. Agglomerations of Si-alloy and graphite particles are shown in the red and blue dotted line regions, respectively.

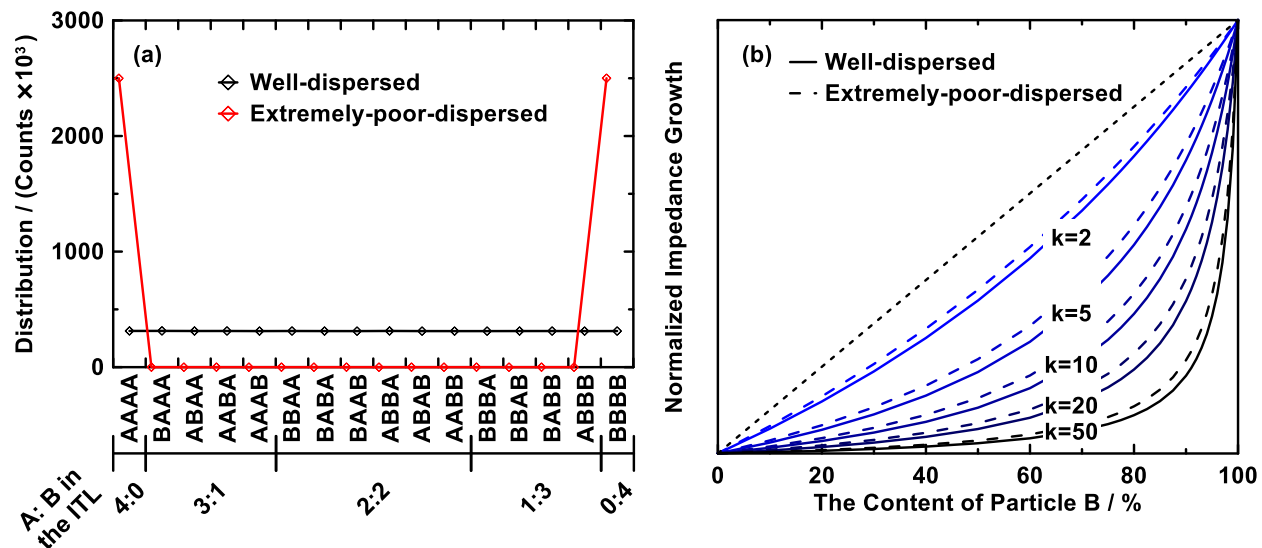


Figure C.8 (a) Simulated distribution of extremely-poor-dispersed electrodes when the content of particle B is 50%, compared to the distribution of well-dispersed electrodes. (b) Normalized overall interfacial impedance growth in extremely-poor-dispersed electrodes, in comparison to well dispersed electrodes.  $k = R_{sB}/R_{sA}$ .

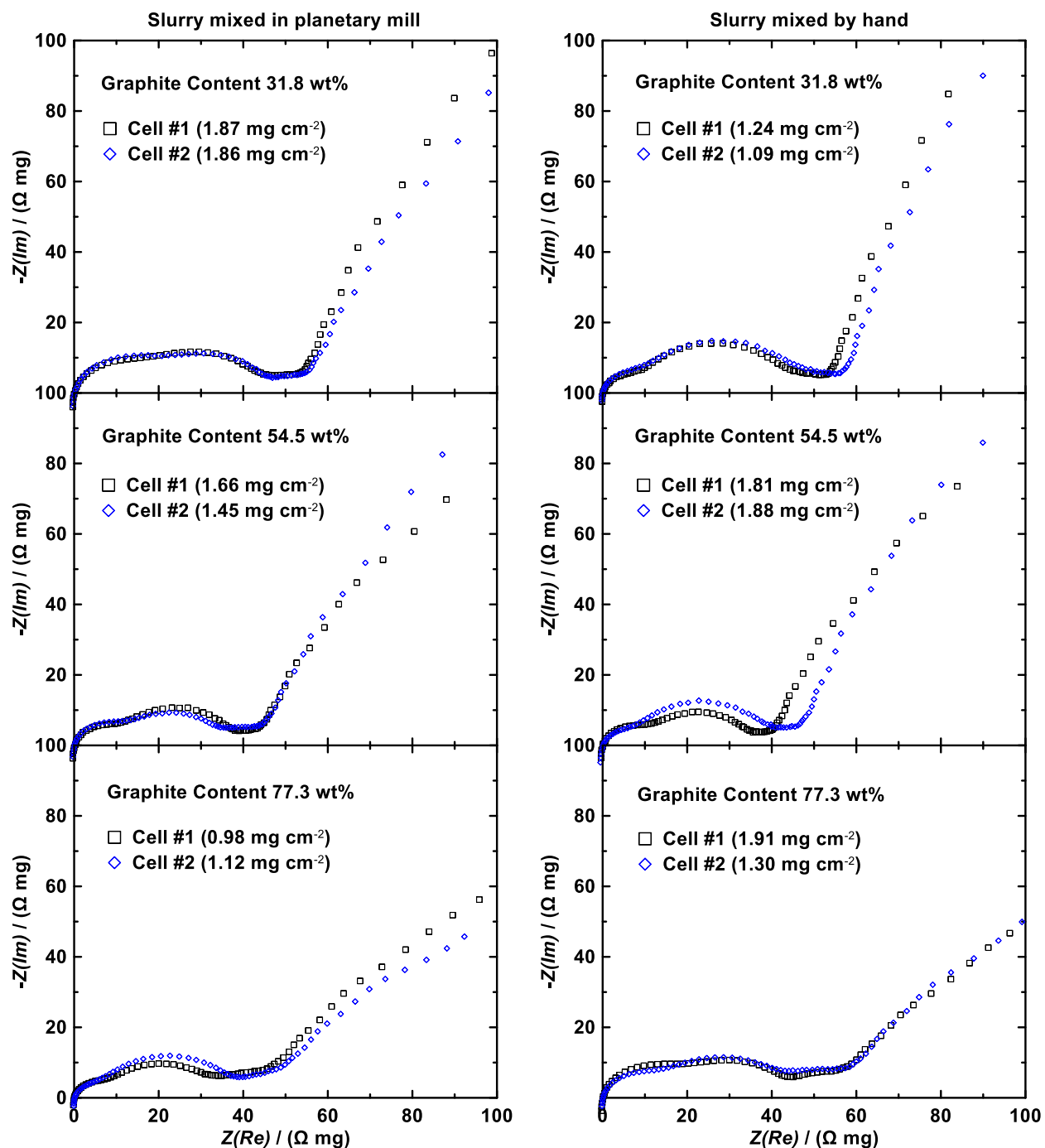


Figure C.9 The Nyquist plots of Si-alloy/graphite blended electrodes made with two different mixing processes: mixed in planetary (left column, good dispersion) and mixed by hand (right column, poor dispersion). The impedance was measured at the first fully discharge state ( $C/20$ ). Electrodes with three different graphite contents were tested. Results show the interfacial impedance between electrodes made with the different mixing processes is similar for electrodes having the same composition. Please note that the axes represents the areal impedance multiplied by the mass loading. The reason for using this type of impedance is to exclude variations caused by the mass loading, as described in the main manuscript.

D- APPENDIX D Supplementary Information for Chapter 5

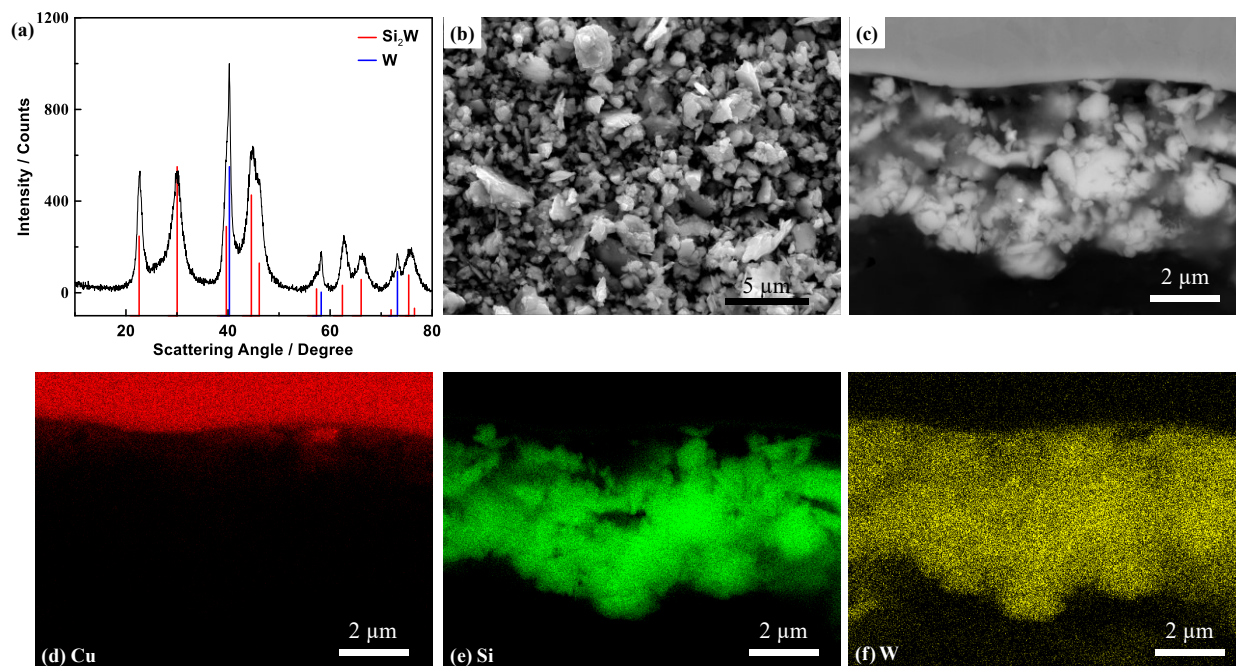


Figure D.1 (a) XRD pattern of synthesized Si<sub>80</sub>W<sub>20</sub>. (b) SEM image of Si<sub>80</sub>W<sub>20</sub>. (c) Cross-sectional SEM image of Si<sub>80</sub>W<sub>20</sub> and corresponding energy-dispersive X-ray spectroscopy (EDS) maps of (d) Cu, (e) Si, and (f) W elements.

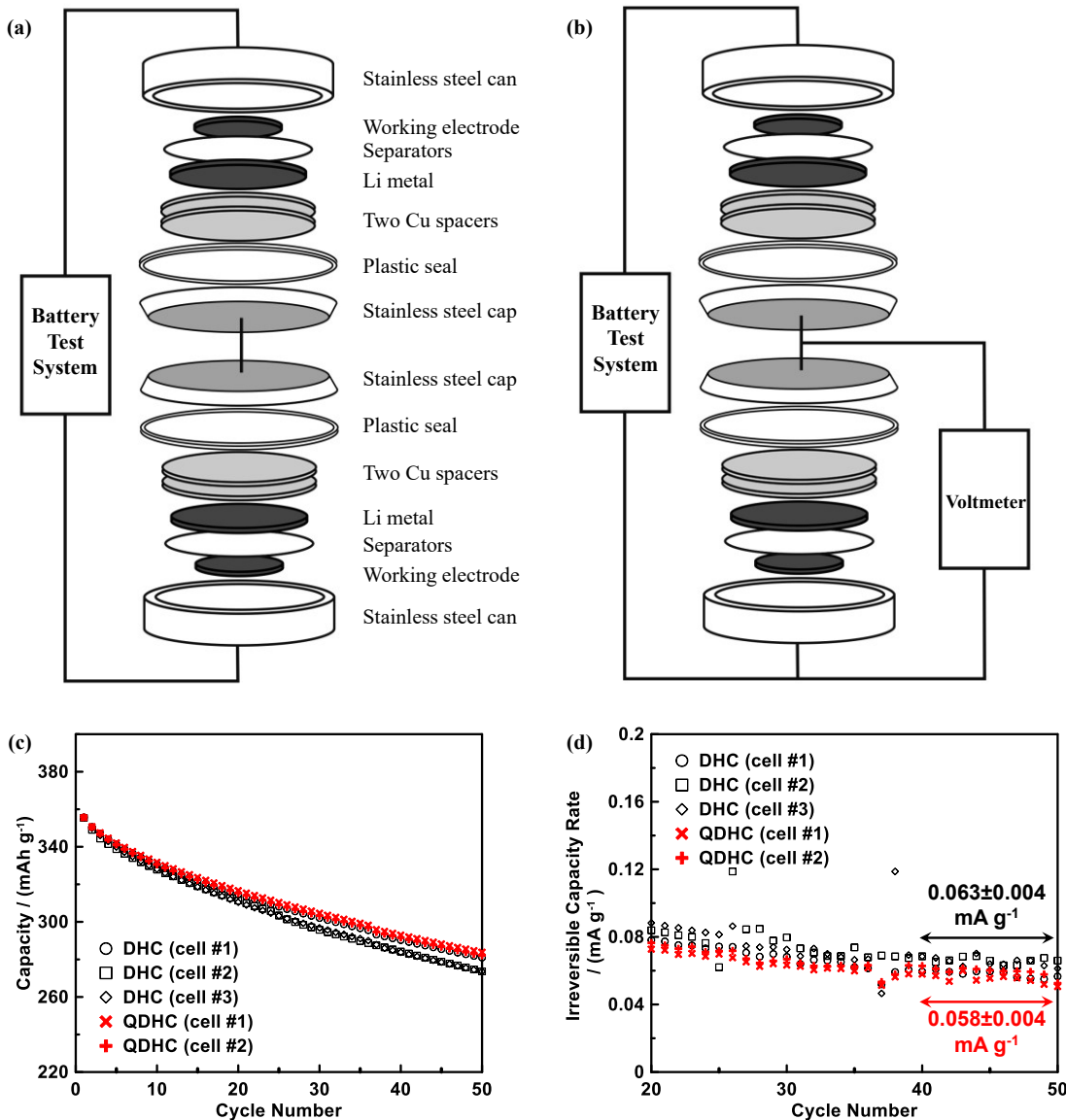


Figure D.2 Exploded views of (a) a DHC and (b) a QDHC with connections to battery test systems. (c) Capacity versus cycle number of graphite electrodes cycled in DHCs and QDHCs. The electrodes were composed of 90 wt% graphite (MAG-E), 2 wt% CB, and 8 wt% poly(vinylidene fluoird) (PVDF) (HSV 900, KYNAR). The mass loading of the graphite electrodes was  $\sim 2.7 \text{ mg cm}^{-2}$ , or  $3.7 \text{ mg per disk electrode}$ . (d) Irreversible capacity rate versus cycle number of the graphite electrodes evaluated in DHCs and QDHCs. The irreversible capacity rate was calculated using the discharge capacity fade between consecutive cycles, per cycle time and per the total electrode mass in each symmetric cell. The average irreversible capacity rates between the 41<sup>th</sup> and the 50<sup>th</sup> cycle measured using DHC and QDHC are shown in (d). The difference in irreversible capacity rates observed for DHCs and QDHCs can also be estimated from the charger system specifications. Considering that the charger's potential sense leads have a high impedance of  $10^{12} \Omega$  and that the average potential of graphite is  $0.1 \text{ V}$ , this corresponds to a leakage current of  $10^{-13} \text{ A}$ . The results indicate the additional connection has a very small, but measurable impact on cell capacity. Nevertheless, caution has been taken in this work by not using QDHCs for coulometric studies.

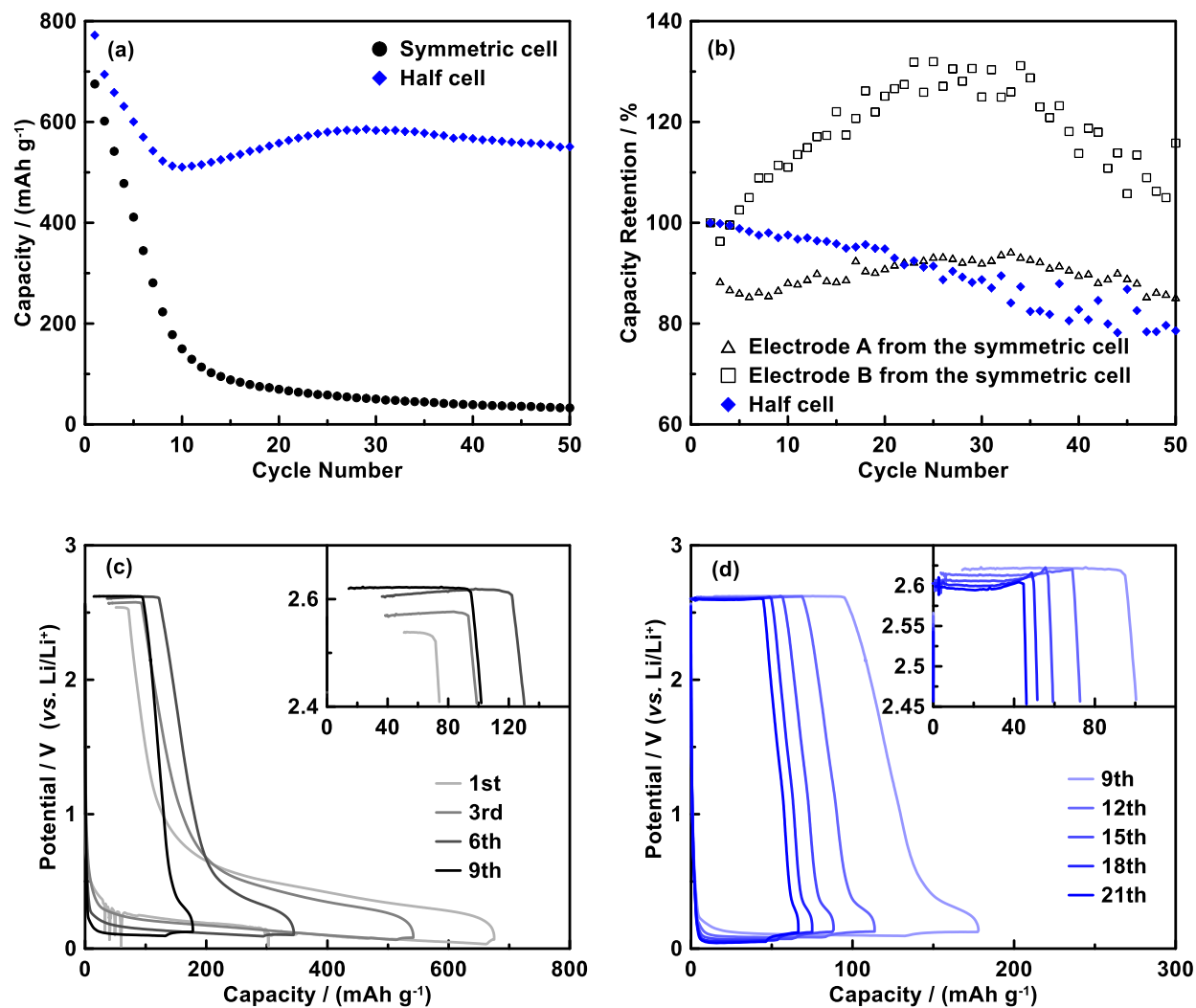


Figure D.3 (a) The specific capacity versus cycle number of  $\text{Si}_{80}\text{W}_{20}$  electrodes in a QDHC (symmetric cell) and a half cell. (b) Capacity retention versus cycle number of aged  $\text{Si}_{80}\text{W}_{20}$  electrodes in half cells. The half cells were cycled between 5 mV and 2.5 V while the QDHCs were cycled between  $\pm 2.5$  V. Potential curves of the prelithiated  $\text{Si}_{80}\text{W}_{20}$  electrode in the QDHC (c) between 1<sup>st</sup> and 9<sup>th</sup> cycles, and (d) between 9<sup>th</sup> and 21<sup>st</sup> cycles. The insets in (c) and (d) show expanded views of the potentials above 2.4 V and 2.45 V, respectively.

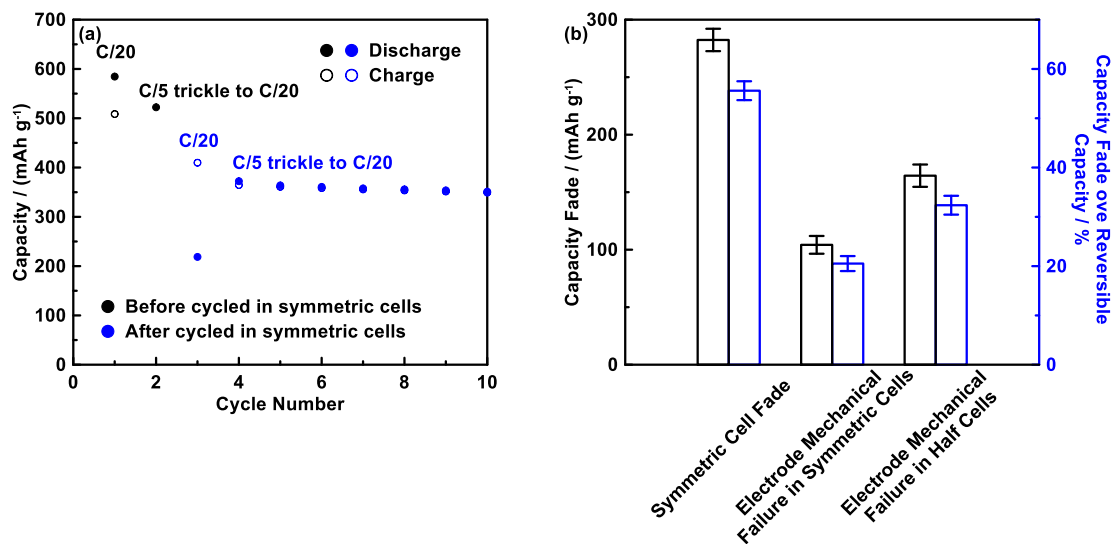


Figure D.4 (a) Capacity of the Si<sub>80</sub>W<sub>20</sub>/G 20/50 electrode before (black) and after (blue) 50 cycles in QDHCs with cut-off potentials of  $\pm 2.5$  V. The capacity before cycling in QDHCs was obtained in the pre-lithiation process for symmetric cell preparation. (b) A summary of capacity fade in QDHCs and mechanical failure of the Si<sub>80</sub>W<sub>20</sub>/G 20/50 electrodes in QDHCs and half cells. The electrode mechanical failure in symmetric cells was determined by conducting an additional discharge/charge cycle on the individual half-cells that make up the QDHCs. The capacity loss due to mechanical failure was then equated to the difference between the charge capacities of the individual half-cells before and after symmetric cell cycling. The capacity loss due to electrode mechanical failure in half cells was determined as the difference in capacities between the initial and the 51<sup>st</sup> cycle charge capacity.

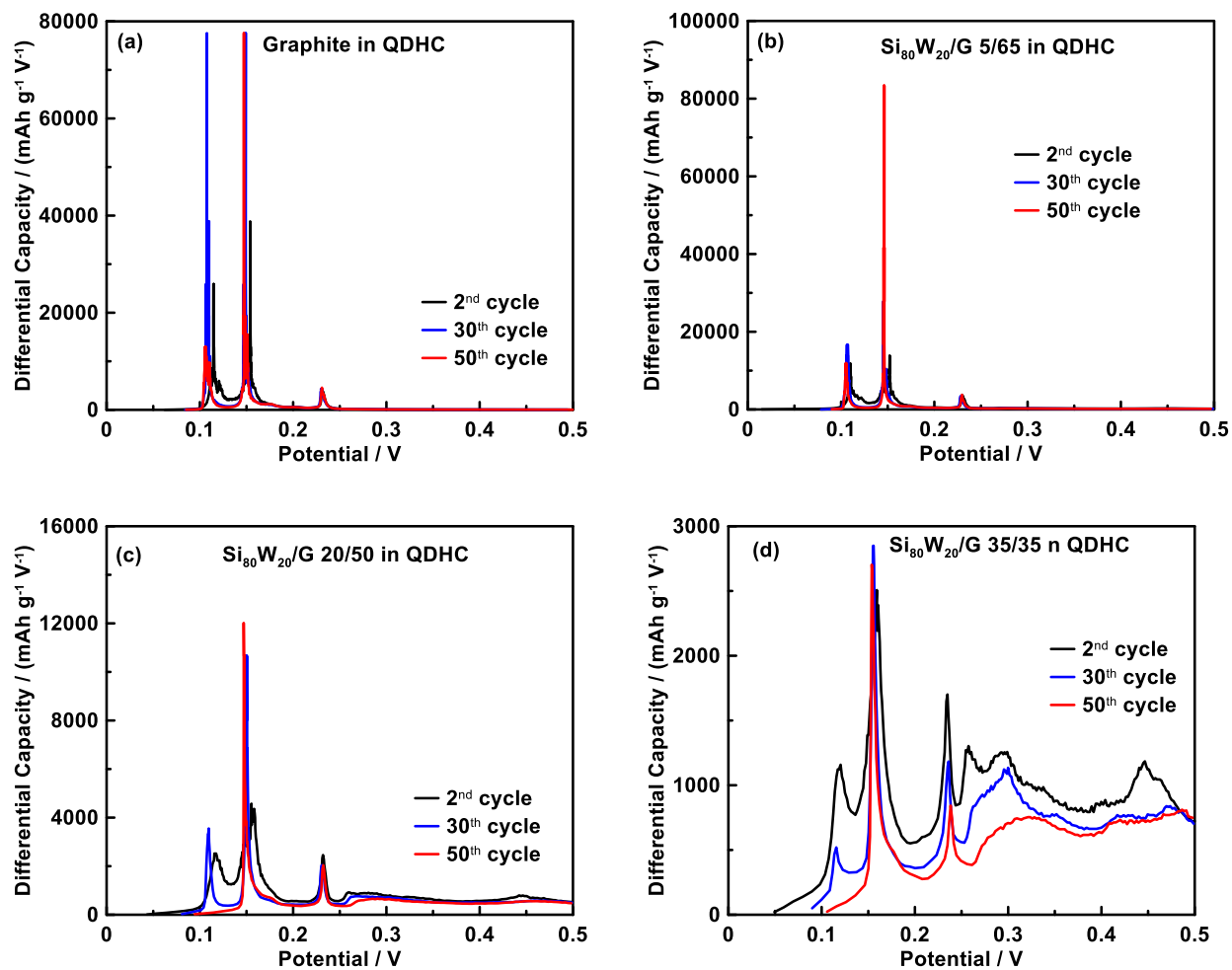


Figure D.5 Differential capacity of (a) graphite, (b) Si<sub>80</sub>W<sub>20</sub>/G 5/65, (c), Si<sub>80</sub>W<sub>20</sub>/G 20/50, and (d) Si<sub>80</sub>W<sub>20</sub>/G 35/35 QDHCs at differential cycles, as indicated.

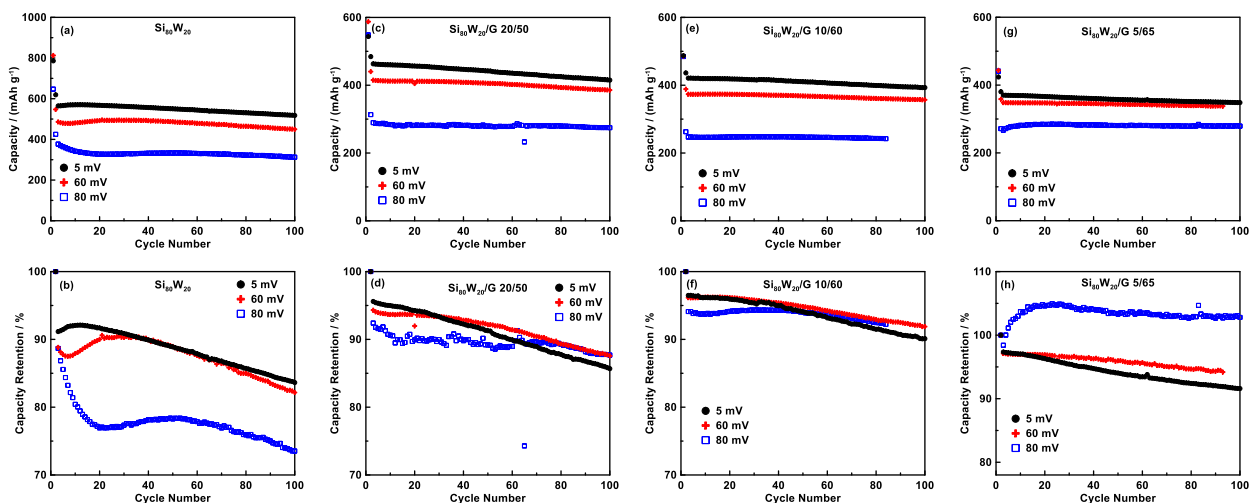


Figure D.6 Capacity versus cycle number of (a)  $\text{Si}_{80}\text{W}_{20}$ , (c)  $\text{Si}_{80}\text{W}_{20}/\text{G}$  20/50, (e)  $\text{Si}_{80}\text{W}_{20}/\text{G}$  10/60, and (g)  $\text{Si}_{80}\text{W}_{20}/\text{G}$  5/65 electrodes cycled in half cells with different lower cutoff potentials, including 5 mV, 60 mV, and 80 mV, while the upper cutoff potential for these cells was set to 0.9 V except for the first cycle. Cells were initially cycled between 5 mV and 1.5 V at C/20 rate, then cycled at C/5 rate, trickled to C/20 for sequent cycles. Corresponding capacity retention versus cycle number for these cells are shown in (b), (d), (f), and (h), respectively. The capacity retention was calculated on the basis of the second cycle discharge capacity.

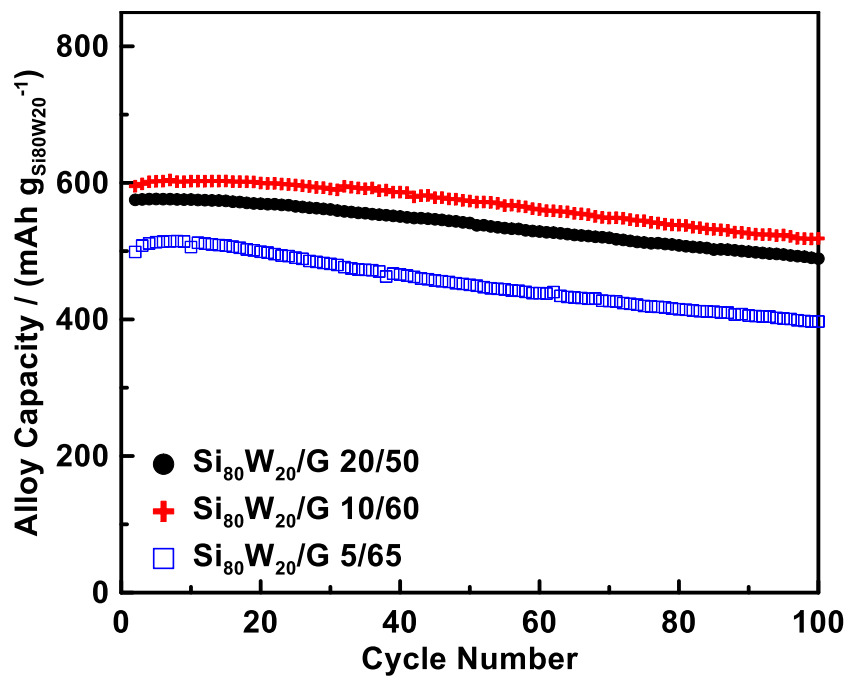


Figure D.7 Alloy capacity versus cycle number of Si<sub>80</sub>W<sub>20</sub> cycled to 5 mV in the blended electrodes as indicated. The data extracted from Figure D.6. The alloy capacity is calculated assuming constant graphite capacities which are 336 mAh g<sup>-1</sup>.

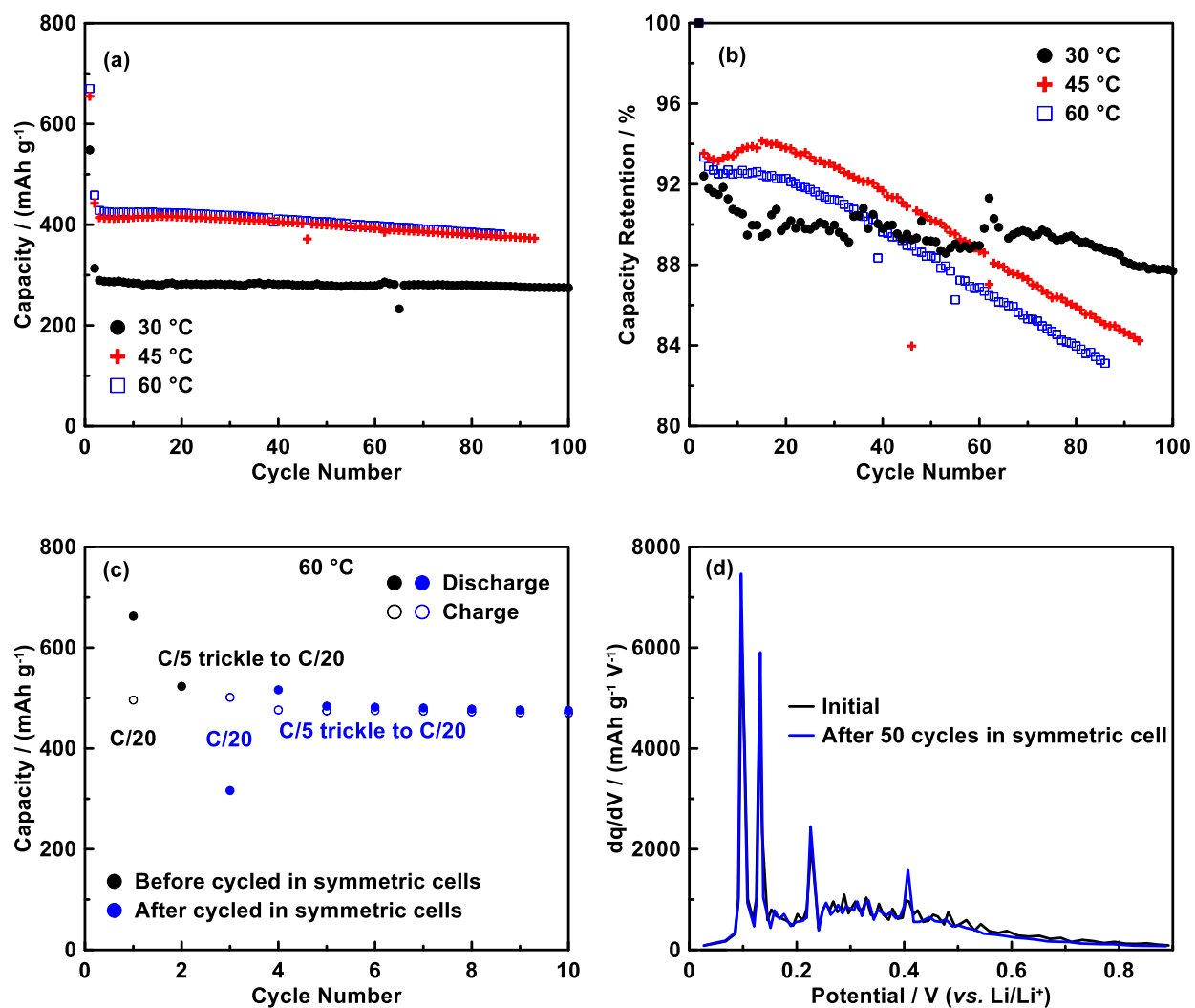


Figure D.8 (a) Capacity and (b) capacity retention versus cycle number of  $\text{Si}_{80}\text{W}_{20}/\text{G}$  20/50 electrodes cycled in half cells with a lower cutoff potential of 80 mV at different temperatures. (c) Capacity of the  $\text{Si}_{80}\text{W}_{20}/\text{G}$  20/50 electrode before (black) and after (blue) 50 cycles in DHCs (symmetric cells) at 60 °C. The capacity before cycling in DHCs was obtained in the pre-lithiation process for symmetric cell preparation. The result indicates no mechanical failure is observed when elevated temperature is applied. (d) Differential capacity curves of  $\text{Si}_{80}\text{W}_{20}/\text{G}$  20/50 electrodes before and after cycling in symmetric cell at 60 °C, showing that little change has occurred after the cycling process.

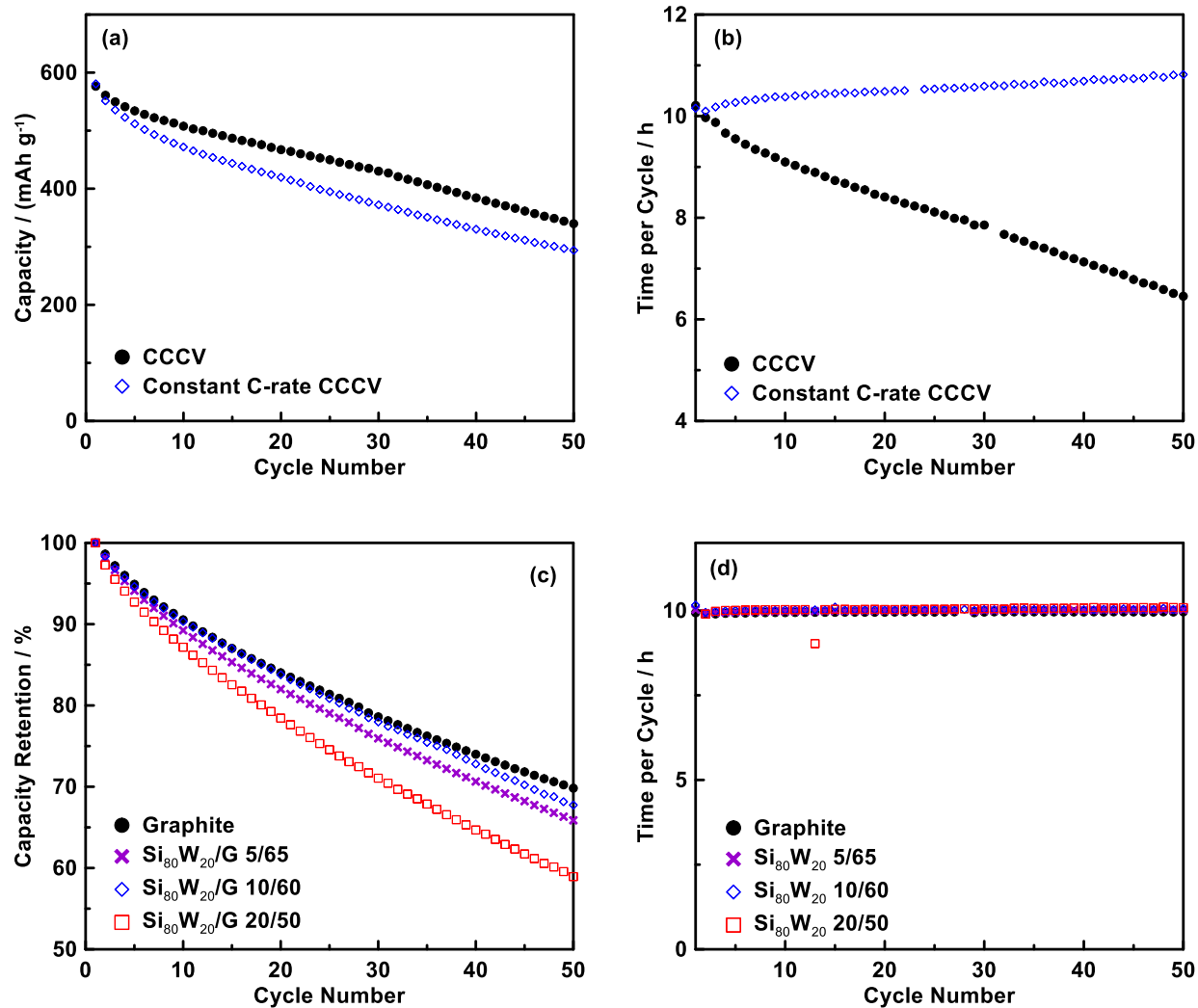


Figure D.9 (a) Capacity and (b) time per cycle versus cycle number of Si<sub>80</sub>W<sub>20</sub> electrodes cycled in DHCs with a constant current constant voltage (CCCV) cycling protocol and a constant C-rate CCCV cycling protocol. (c) Capacity retention and (d) time per cycle versus cycle number of graphite and various ratio of Si<sub>80</sub>W<sub>20</sub>/G electrodes cycled in DHCs with a constant C-rate CCCV protocol.

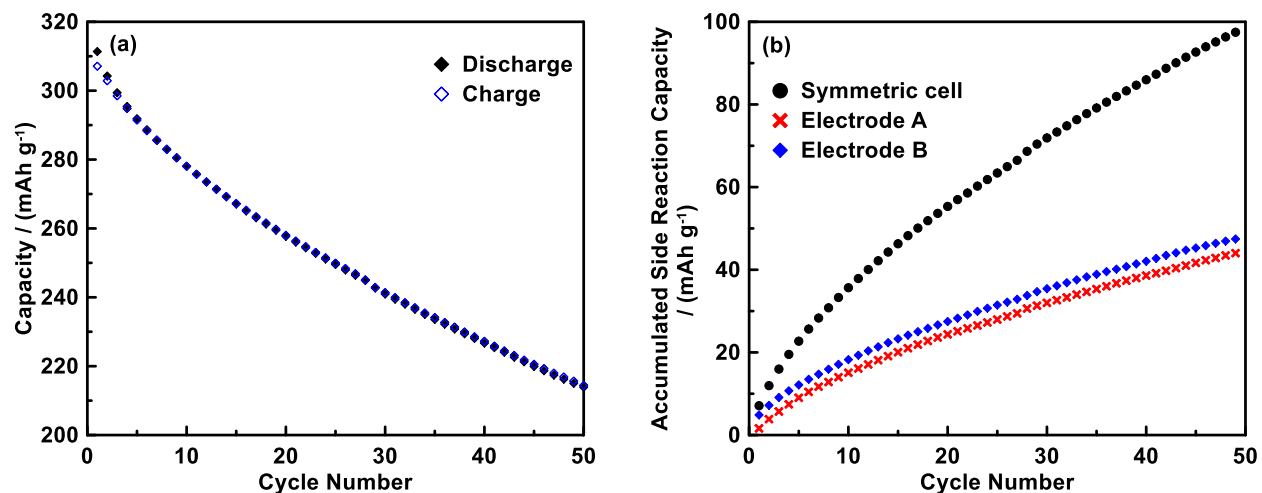


Figure D.10 (a) Charge and discharge capacity versus cycle number of DHC containing graphite electrodes. The constant C-rate CCCV cycling protocol is used. (b) Accumulated side reaction capacity versus cycle number of the graphite/graphite DHC (symmetric cell), pre-lithiated electrode (electrode A), and pre-delithiated electrode (electrode B). The specific capacities of electrode A and B were calculated with respect to their corresponding active material mass, assuming that electrode A and B have achieved the same average specific steady state reaction rate between the 21<sup>st</sup> and 50<sup>th</sup> cycle and have the same average specific reaction rate during these cycles, as applied in equation (5.3).

Table D.1 Specific surface areas (in m<sup>2</sup> g<sup>-1</sup>) of powders used in this study [27]

MAG-E	CB
2.35	62

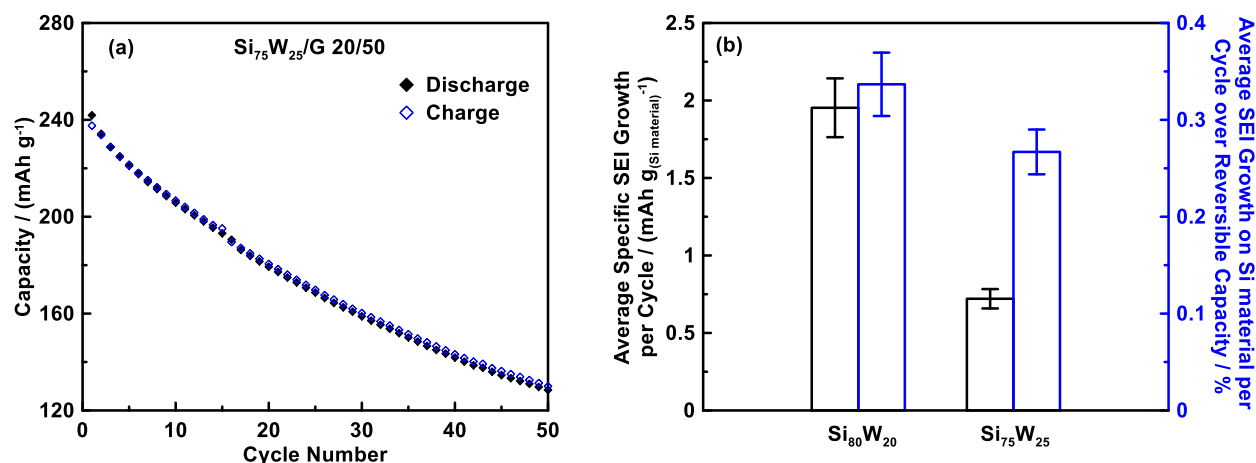


Figure D.11  $\text{Si}_{75}\text{W}_{25}$  was prepared as a similar way for  $\text{Si}_{80}\text{W}_{20}$ , but with different stoichiometric ratio of Si and W. (a) Capacity of  $\text{Si}_{75}\text{W}_{25}/\text{G}$  20/50 electrodes cycled in DHC with the constant C-rate CCCV cycling protocol. (b) A summary of average SEI growth capacity per cycle and average SEI growth capacity per cycle over reversible capacity on  $\text{Si}_{75}\text{W}_{25}$ , with a comparison of  $\text{Si}_{80}\text{W}_{20}$ .

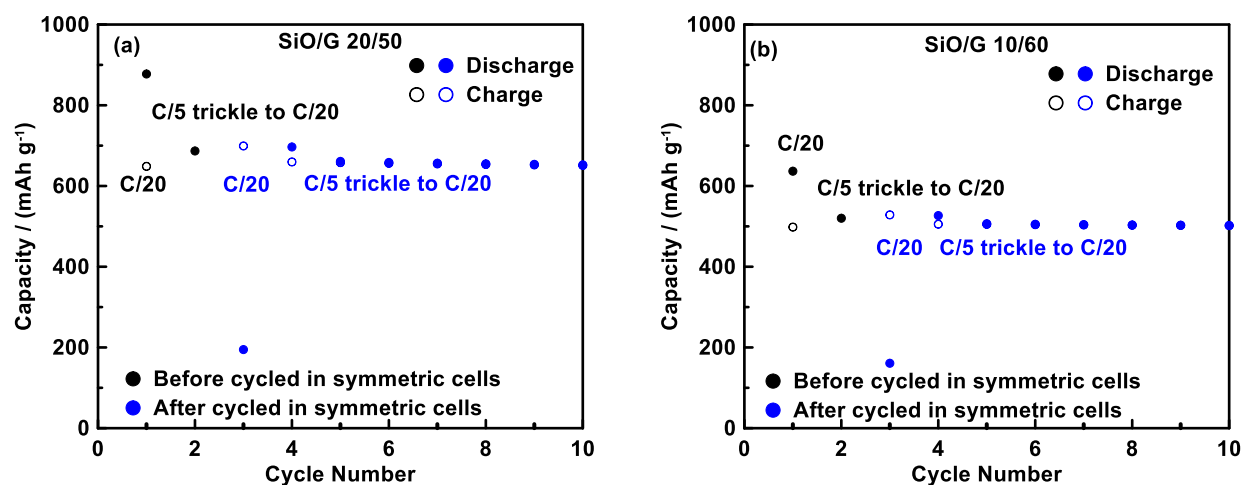


Figure D.12 Capacity of (a)  $\text{SiO}/\text{G}$  20/50 and (b)  $\text{SiO}/\text{G}$  10/60 electrodes before (black) and after (blue) 50 cycles in DHCs (symmetric cells) at 30 °C. The capacity before cycling in DHCs was obtained in the pre-lithiation process for symmetric cell preparation. No mechanical failure is observed for  $\text{SiO}/\text{G}$  20/50 and  $\text{SiO}/\text{G}$  10/60 electrodes when cycled in DHCs.

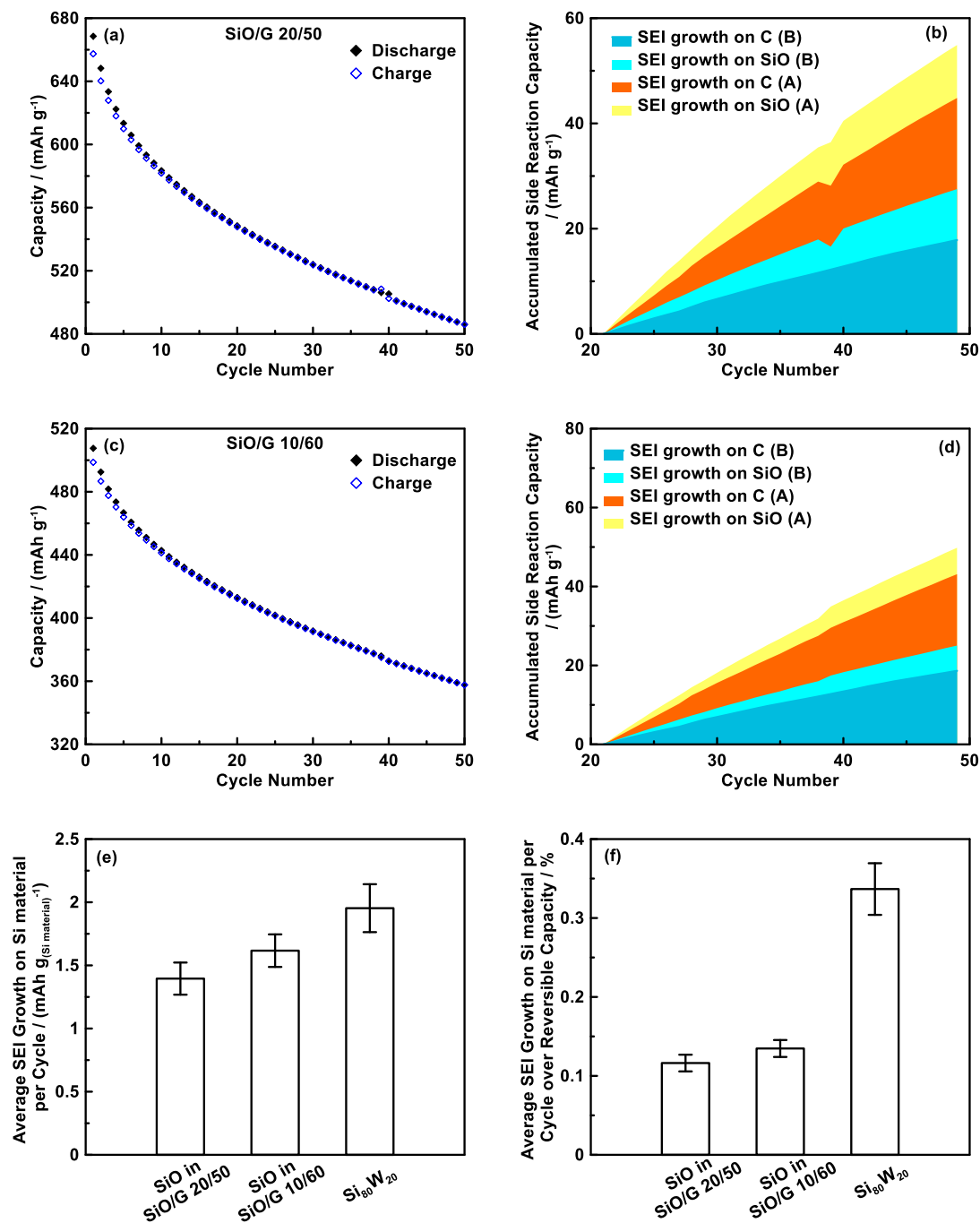


Figure D.13 Capacity of (a) SiO/G 20/50 and (c) SiO/G 10/60 electrodes cycled in DHCs with the constant C-rate CCCV cycling protocol. The corresponding accumulated side reaction capacity was shown in (b) and (d), respectively. A summary of (e) average SEI growth capacity per cycle on SiO and (f) average SEI growth capacity per cycle per SiO reversible capacity. Values for Si<sub>80</sub>W<sub>20</sub> electrodes are shown for comparison.

E- APPENDIX E Supplementary Information for Chapter 6

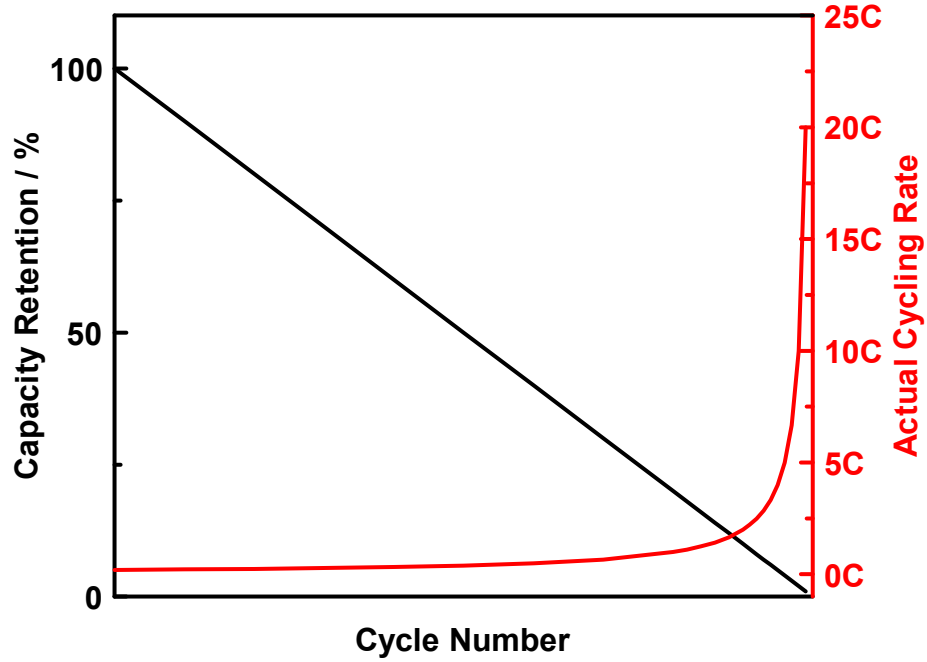


Figure E.1 Illustrated the relationship between the capacity retention and the cycling rate at each cycle, if the cycling current is set to be constant while the cell capacity fades linearly. The initial cycling rate is set to be  $C/5$ .

## Synthesis of LiNiO<sub>2</sub>

LiNiO<sub>2</sub> was prepared as described in Reference [55]. A mixture of Ni(OH)<sub>2</sub> and LiOH·H<sub>2</sub>O with a Li/Ni ratio of 1.02 was prepared by hand milling in a mortar. The sample were heated in a tube furnace under oxygen atmosphere at 485 °C for 3 hours. The sample was taken out from the furnace to further hand milling. The ground powders were heated again in the furnace at 485 °C for 2 hours, then at 700 °C for 20 hours. The heating rate is set at 10 °C per minute.

## Characterization Methods

X-ray diffraction (XRD) patterns of synthesized LiNiO<sub>2</sub> were collected using a Rigaku Ultima IV diffractometer with a Cu K $\alpha$  X ray source, a diffracted beam monochromator, and a scintillation counter detector. Rietveld refinement was conducted using Rietica software.

The morphology of synthesized LiNiO<sub>2</sub> particles was studied using scanning electron microscope (SEM) (TESCAN MIRA3) with an accelerate voltage of 20 kV.

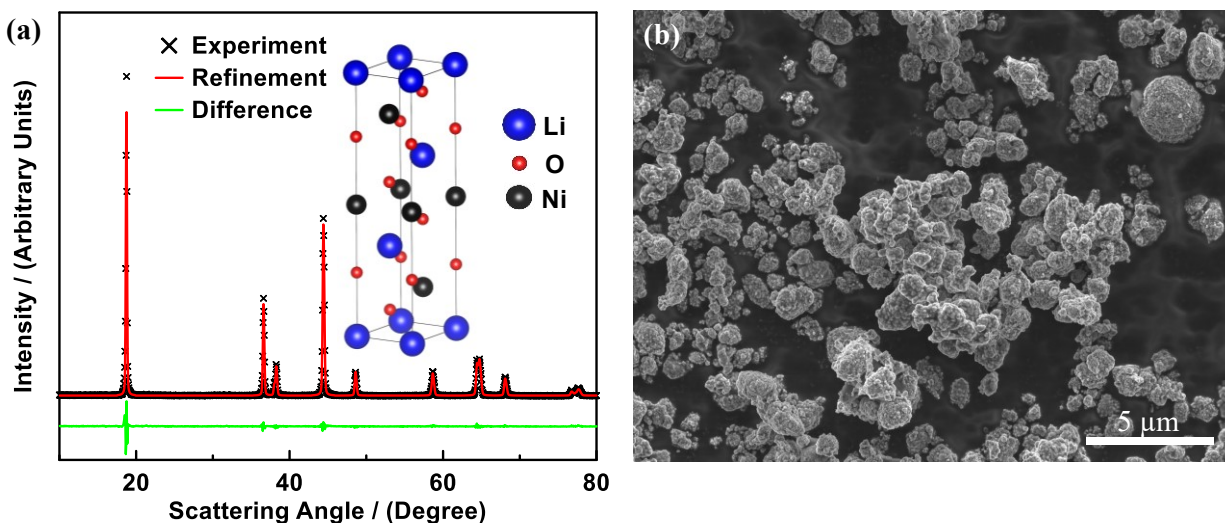


Figure E.2 (a) XRD pattern and Rietveld refinement of synthesized LiNiO<sub>2</sub>. Inset of (a) is crystal structure of the LiNiO<sub>2</sub>. Blue, red, and black balls represent Li, O, and Ni atoms, respectively. (b) SEM image of the synthesized LiNiO<sub>2</sub>.

Table E. 1 Rietveld refinement results for synthesized LiNiO<sub>2</sub>.

Atom	Li(1)	Li(2)	Ni(1)	Ni(2)	O
Site	3a	3b	3a	3b	6c
x	0	0	0	0	0
y	0	0	0	0	0
z	0	0.5	0	0.5	0.2423(3)
Occ	0.977(2)	0.023(2)	0.977(2)	0.023(2)	1
Unit cell: hexagonal R-3m space group (166); a= 2.8767(9) Å, c= 14.196(1) Å; Bragg R factor =1.41.					

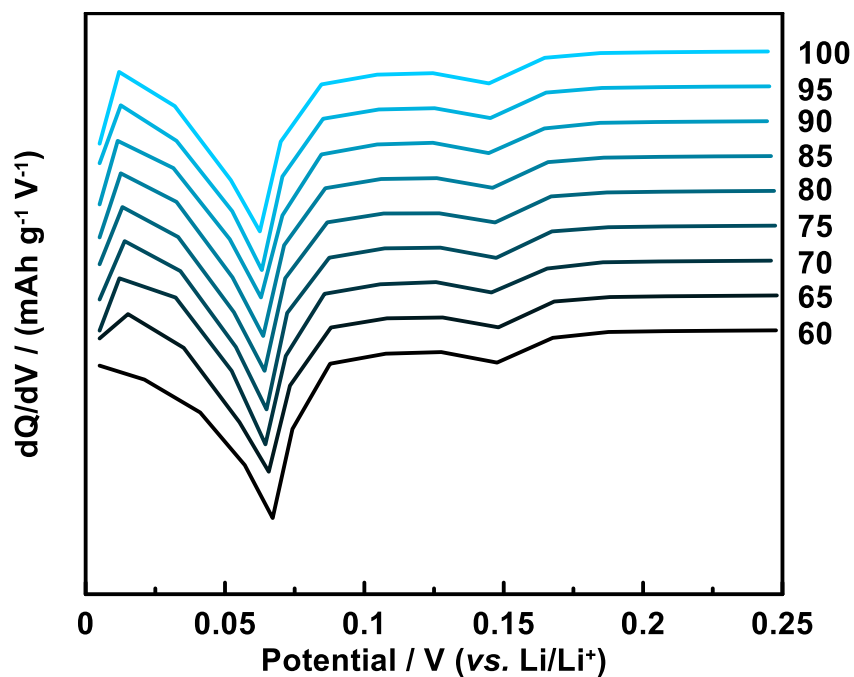


Figure E.3 The dQ/dV curves of the graphite electrodes at indicated cycle number, cycled by TGC protocol.

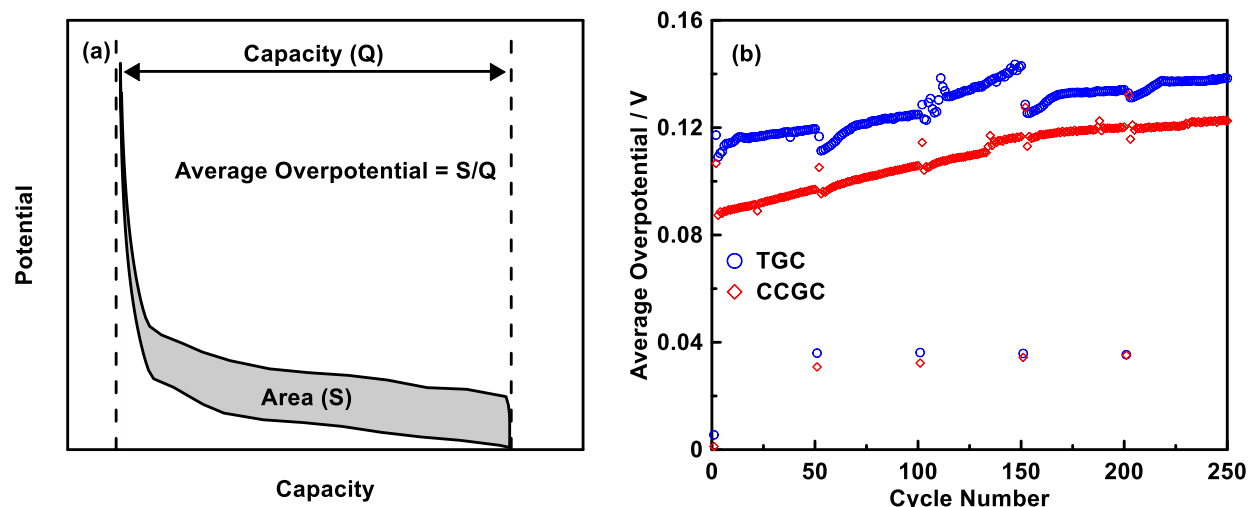


Figure E.4 Illustration of the calculation of the average overpotential at each cycle. (b) The calculated average overpotential of the graphite electrodes cycled under CCGC and TGC. In each 50 cycles, the graphite electrodes were first cycled at the rate of  $C/20$ , followed by 49 cycles at the rate of  $C/3$  between 5 mV and 0.9 V.

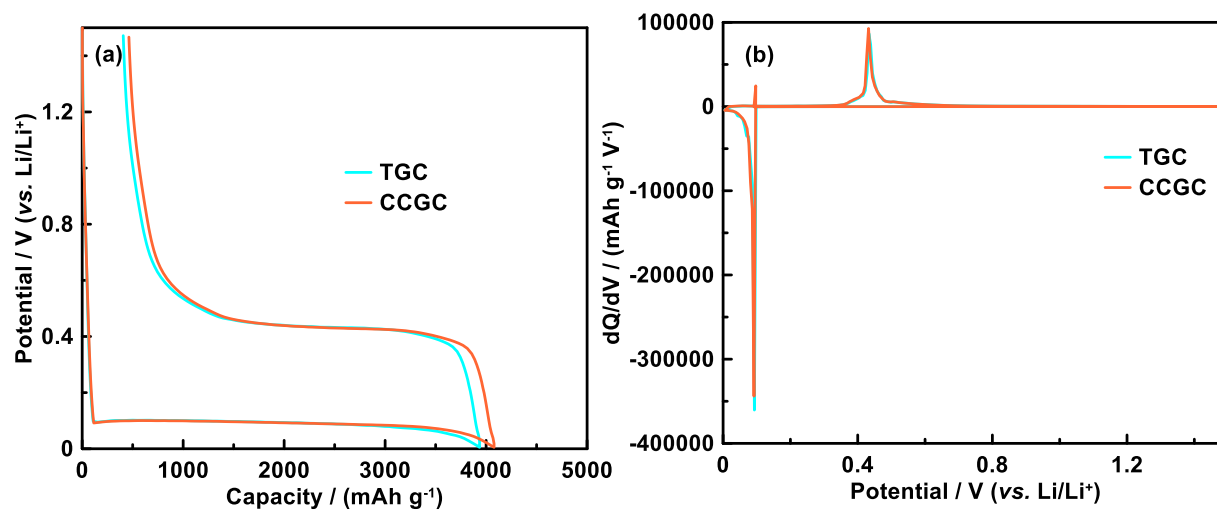


Figure E.5 (a) Initial potential curves and (b) corresponding differential capacity ( $dQ/dV$ ) curves of Si electrodes under CCGC and TGC. The initial cycle was set at the rate of  $C/20$  between 5 mV-1.5 V.

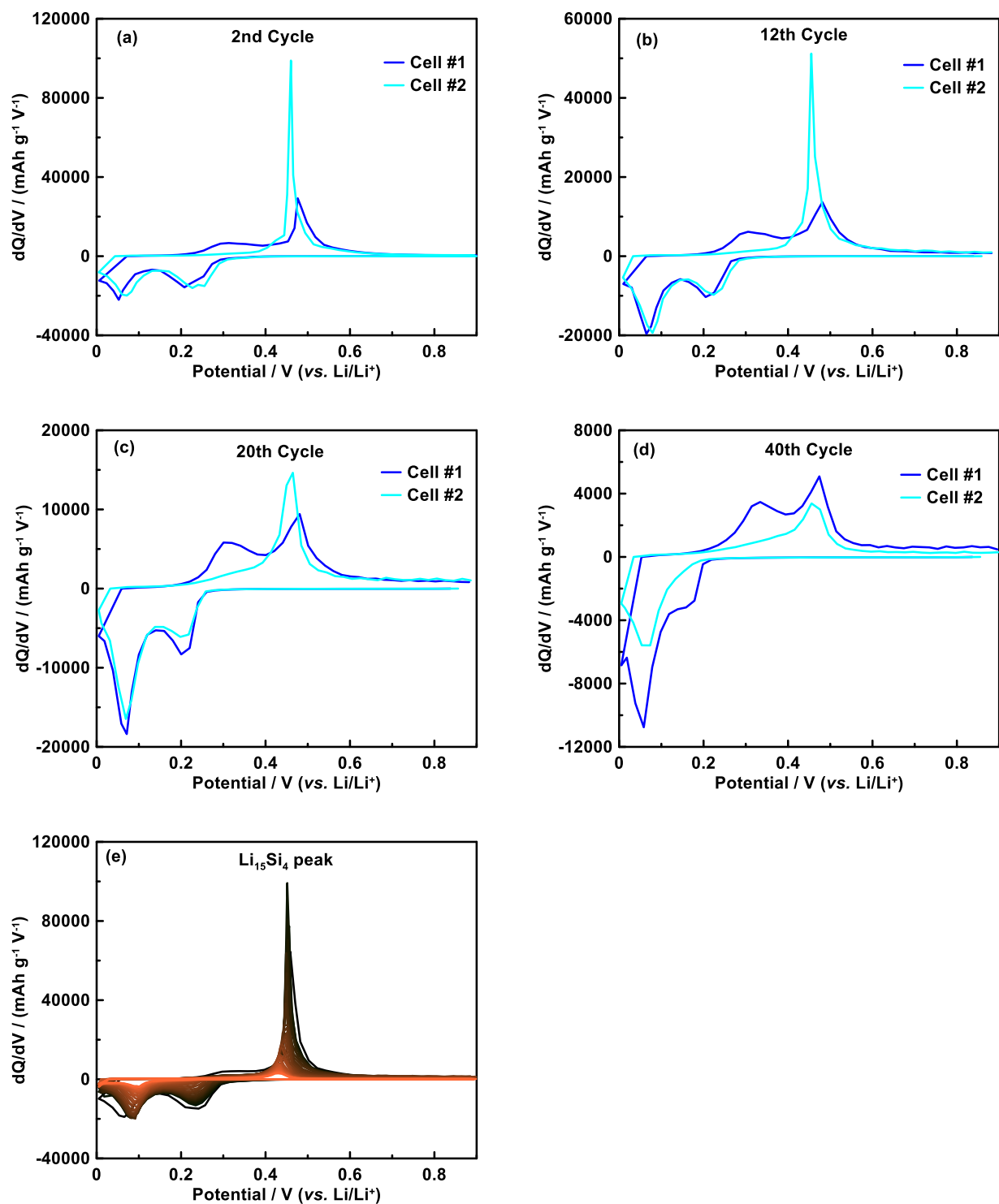


Figure E.6 (a-d) The  $dQ/dV$  curves of two Si electrode cells cycled with TGC at the indicated cycles. (e) The  $dQ/dV$  curves of cycles 1 (black) to 60 (orange) of a Si electrode cell cycled with CCGC. Both CCGC cycled Si electrode cells in this study had nominally identical  $dQ/dV$  curves.

## F- APPENDIX F Copyright Permission



Home



Help



Email Support



Zilai Yan ▾

### Promise and reality of post-lithium-ion batteries with high energy densities

**SPRINGER NATURE**

Author: Jang Wook Choi et al

Publication: Nature Reviews Materials

Publisher: Springer Nature

Date: Mar 31, 2016

Copyright © 2016, Macmillan Publishers Limited

### Order Completed

Thank you for your order.

This Agreement between Dalhousie University -- Zilai Yan ("You") and Springer Nature ("Springer Nature") consists of your license details and the terms and conditions provided by Springer Nature and Copyright Clearance Center.

Your confirmation email will contain your order number for future reference.

License Number 5083920356181

[Printable Details](#)

License date Jun 07, 2021

#### Licensed Content

**Licensed Content Publisher** Springer Nature  
**Licensed Content Publication** Nature Reviews Materials  
**Licensed Content Title** Promise and reality of post-lithium-ion batteries with high energy densities  
**Licensed Content Author** Jang Wook Choi et al  
**Licensed Content Date** Mar 31, 2016

#### Order Details

**Type of Use** Thesis/Dissertation  
**Requestor type** academic/university or research institute  
**Format** print and electronic  
**Portion** figures/tables/illustrations  
**Number of figures/tables/illustrations** 1  
**High-res required** no  
**Will you be translating?** no  
**Circulation/distribution** 50000 or greater  
**Author of this Springer Nature content** no

#### About Your Work

**Title** Evaluating Degradation Mechanisms in Next-generation Electrode Chemistries  
**Institution name** Dalhousie University  
**Expected presentation date** Aug 2021

#### Additional Data

**Portions** Figure 2

## Order Confirmation

Thank you, your order has been placed. An email confirmation has been sent to you. Your order license details and printable licenses will be available within 24 hours. Please access Manage Account for final order details.

This is not an invoice. Please go to manage account to access your order history and invoices.

### CUSTOMER INFORMATION

Payment by invoice: You can cancel your order until the invoice is generated by contacting customer service.

#### Billing Address

Mr. Zilai Yan  
Dalhousie University  
6274 Coburg Road, Halifax  
Halifax, NS B3H 4R2  
Canada  
  
+1 (902) 233-6897  
zilai.yan@dal.ca

#### Customer Location

Mr. Zilai Yan  
Dalhousie University  
6274 Coburg Road, Halifax  
Halifax, NS B3H 4R2  
Canada

#### PO Number (optional)

N/A

#### Payment options

Invoice

### PENDING ORDER CONFIRMATION

Confirmation Number: Pending

Order Date: 07-Jun-2021

#### 1. Journal of the Electrochemical Society

0.00 CAD

Order License ID	Pending	Publisher	IOP Publishing
ISSN	1945-7111	Portion	Image/photo/illustration
Type of Use	Republish in a thesis/dissertation		

#### LICENSED CONTENT

Publication Title	Journal of the Electrochemical Society	Country	United States of America
Author/Editor	Electrochemical Society.	Rightsholder	IOP Publishing, Ltd
Date	01/01/1948	Publication Type	e-Journal
Language	English	URL	http://www.scitation.org/JES

#### REQUEST DETAILS

## Order Confirmation

Thank you, your order has been placed. An email confirmation has been sent to you. Your order license details and printable licenses will be available within 24 hours. Please access Manage Account for final order details.

This is not an invoice. Please go to manage account to access your order history and invoices.

### CUSTOMER INFORMATION

Payment by invoice: You can cancel your order until the invoice is generated by contacting customer service.

#### Billing Address

Mr. Zilai Yan  
Dalhousie University  
6274 Coburg Road, Halifax  
Halifax, NS B3H 4R2  
Canada  
  
+1 (902) 233-6897  
zilai.yan@dal.ca

#### Customer Location

Mr. Zilai Yan  
Dalhousie University  
6274 Coburg Road, Halifax  
Halifax, NS B3H 4R2  
Canada

#### PO Number (optional)

N/A

#### Payment options

Invoice

### PENDING ORDER CONFIRMATION

Confirmation Number: Pending

Order Date: 07-Jun-2021

#### 1. Journal of the Electrochemical Society

0.00 CAD

Order License ID	Pending	Publisher	IOP Publishing
ISSN	1945-7111	Portion	Image/photo/illustration
Type of Use	Republish in a thesis/dissertation		

#### LICENSED CONTENT

Publication Title	Journal of the Electrochemical Society	Country	United States of America
Author/Editor	Electrochemical Society.	Rightsholder	IOP Publishing, Ltd
Date	01/01/1948	Publication Type	e-Journal
Language	English	URL	http://www.scitation.org/JES

#### REQUEST DETAILS

## Order Confirmation

Thank you, your order has been placed. An email confirmation has been sent to you. Your order license details and printable licenses will be available within 24 hours. Please access Manage Account for final order details.

This is not an invoice. Please go to manage account to access your order history and invoices.

### CUSTOMER INFORMATION

Payment by invoice: You can cancel your order until the invoice is generated by contacting customer service.

#### Billing Address

Mr. Zilai Yan  
Dalhousie University  
6274 Coburg Road, Halifax  
Halifax, NS B3H 4R2  
Canada  
  
+1 (902) 233-6897  
zilai.yan@dal.ca

#### Customer Location

Mr. Zilai Yan  
Dalhousie University  
6274 Coburg Road, Halifax  
Halifax, NS B3H 4R2  
Canada

#### PO Number (optional)

N/A

#### Payment options

Invoice

### PENDING ORDER CONFIRMATION

Confirmation Number: Pending

Order Date: 07-Jun-2021

#### 1. Journal of the Electrochemical Society

0.00 CAD

Article: Review—SEI: Past, Present and Future

Order License ID	Pending	Publisher Portion	IOP Publishing
ISSN	1945-7111		Image/photo/illustration
Type of Use	Republish in a thesis/dissertation		

#### LICENSED CONTENT

Publication Title	Journal of the Electrochemical Society	Publication Type	e-Journal
Article Title	Review—SEI: Past, Present and Future	Start Page	A1703
Author/Editor	Electrochemical Society.	End Page	A1719
Date	01/01/1948	Issue	7
		Volume	164

**Characterization of Lithium Alkyl Carbonates by X-ray Photoelectron Spectroscopy: Experimental and Theoretical Study**



Author: R. Dedryvère, L. Gireaud, S. Grugeon, et al

Publication: The Journal of Physical Chemistry B

Publisher: American Chemical Society

Date: Aug 1, 2005

Copyright © 2005, American Chemical Society

**PERMISSION/LICENSE IS GRANTED FOR YOUR ORDER AT NO CHARGE**

This type of permission/license, instead of the standard Terms & Conditions, is sent to you because no fee is being charged for your order. Please note the following:

- Permission is granted for your request in both print and electronic formats, and translations.
  - If figures and/or tables were requested, they may be adapted or used in part.
  - Please print this page for your records and send a copy of it to your publisher/graduate school.
  - Appropriate credit for the requested material should be given as follows: "Reprinted (adapted) with permission from (COMPLETE REFERENCE CITATION). Copyright (YEAR) American Chemical Society." Insert appropriate information in place of the capitalized words.
  - One-time permission is granted only for the use specified in your request. No additional uses are granted (such as derivative works or other editions). For any other uses, please submit a new request.
- If credit is given to another source for the material you requested, permission must be obtained from that source.

[BACK](#)

[CLOSE WINDOW](#)

June 15<sup>th</sup>, 2021 ¶

¶  
Aaron Smith, ¶

¶  
I am preparing my PhD thesis for submission to the Faculty of Graduate Studies at Dalhousie University, Halifax, Nova Scotia, Canada. I am seeking your permission to include Figure 4.2 from the following publication(s) in the thesis. ¶

¶  
[A HIGH-PRECISION STUDY OF LI-ION BATTERIES, Aaron Smith, Dalhousie PhD thesis, 2012] ¶

¶  
Canadian graduate theses are collected and stored online by the Library and Archives of Canada. I am also seeking your permission for the material described above to be stored online with the LAC. Further details about the LAC thesis program are available on the LAC website ([www.bac-lac.gc.ca](http://www.bac-lac.gc.ca)). ¶

¶  
Full publication details and a copy of this permission letter will be included in the thesis. ¶

¶  
Yours sincerely, ¶

¶  
¶  
Zilai Yan ¶

¶  
\_\_\_\_\_  
¶  
Permission is granted for: ¶

- ¶  
a) → the inclusion of the material described above in your thesis. ¶  
¶  
b) → for the material described above to be included in the copy of your thesis that is sent to the Library and Archives of Canada (formerly National Library of Canada) for online storage. ¶

Name: Aaron Smith Title: Dr ¶  
Signature: \_\_\_\_\_ Date: 06/18/21 ¶

¶

## Order Confirmation

Thank you, your order has been placed. An email confirmation has been sent to you. Your order license details and printable licenses will be available within 24 hours. Please access Manage Account for final order details.

This is not an invoice. Please go to manage account to access your order history and invoices.

### CUSTOMER INFORMATION

Payment by invoice: You can cancel your order until the invoice is generated by contacting customer service.

#### Billing Address

Mr. Zilai Yan  
Dalhousie University  
6274 Coburg Road, Halifax  
Halifax, NS B3H 4R2  
Canada

+1 (902) 233-6897  
zilai.yan@dal.ca

#### Customer Location

Mr. Zilai Yan  
Dalhousie University  
6274 Coburg Road, Halifax  
Halifax, NS B3H 4R2  
Canada

#### PO Number (optional)

N/A

#### Payment options

Invoice

### PENDING ORDER CONFIRMATION

Confirmation Number: Pending

Order Date: 08-Jun-2021

#### 1. Journal of power sources

0.00 CAD

Article: Selecting inactive materials with low electrolyte reactivity for lithium-ion cells

Special Terms Apply

Order License ID	Pending	Publisher	ELSEVIER S.A.
ISSN	0378-7753	Portion	Image/photo/illustration
Type of Use	Republish in a thesis/dissertation		

#### LICENSED CONTENT

Publication Title	Journal of power sources	Rightsholder	Elsevier Science & Technology Journals
Article Title	Selecting inactive materials with low electrolyte reactivity for lithium-ion cells	Publication Type	Journal
		Start Page	374
		End Page	381
Date	01/01/1976		



### Quantifying the cost effectiveness of non-aqueous potassium-ion batteries

Author: Zilai Yan, M.N. Obrovac  
Publication: Journal of Power Sources  
Publisher: Elsevier  
Date: 15 July 2020

© 2020 Elsevier B.V. All rights reserved.

#### Journal Author Rights

Please note that, as the author of this Elsevier article, you retain the right to include it in a thesis or dissertation, provided it is not published commercially. Permission is not required, but please ensure that you reference the journal as the original source. For more information on this and on your other retained rights, please visit: <https://www.elsevier.com/about/our-business/policies/copyright#Author-rights>

BACK

CLOSE WINDOW



**Understanding interfacial impedance growth in porous electrodes containing blended active materials**

Author: Zilal Yan, Congxiao Wei, M.N. Obrovac

Publication: Journal of Power Sources

Publisher: Elsevier

Date: 31 October 2019

© 2019 Elsevier B.V. All rights reserved.

**Journal Author Rights**

Please note that, as the author of this Elsevier article, you retain the right to include it in a thesis or dissertation, provided it is not published commercially. Permission is not required, but please ensure that you reference the journal as the original source. For more information on this and on your other retained rights, please visit: <https://www.elsevier.com/about/our-business/policies/copyright#Author-rights>

BACK

CLOSE WINDOW

## Order Confirmation

Thank you, your order has been placed. An email confirmation has been sent to you. Your order license details and printable licenses will be available within 24 hours. Please access Manage Account for final order details.

This is not an invoice. Please go to manage account to access your order history and invoices.

### CUSTOMER INFORMATION

Payment by invoice: You can cancel your order until the invoice is generated by contacting customer service.

#### Billing Address

Mr. Zilal Yan  
Dalhousie University  
6274 Coburg Road, Halifax  
Halifax, NS B3H 4R2  
Canada

+1 (902) 233-6897  
zilal.yan@dal.ca

#### Customer Location

Mr. Zilal Yan  
Dalhousie University  
6274 Coburg Road, Halifax  
Halifax, NS B3H 4R2  
Canada

#### PO Number (optional)

N/A

#### Payment options

Invoice

### PENDING ORDER CONFIRMATION

Confirmation Number: Pending

Order Date: 13-Dec-2021

#### 1. Electrochemical Society. Meeting Abstracts

0.00 USD

Order License ID	Pending	Publisher	IOP Publishing
ISSN	2151-2043	Portion	Image/photo/illustration
Type of Use	Republish in a thesis/dissertation		

#### LICENSED CONTENT

Publication Title	Electrochemical Society. Meeting Abstracts	Country	United States of America
		Rightsholder	IOP Publishing, Ltd
		Publication Type	Journal

---

**From:** Rights DE  
**Sent:** December 14, 2021 8:54 AM  
**To:** Zilai Yan  
**Cc:** Rights DE  
**Subject:** AW: Request permissions

**CAUTION:** The Sender of this email is not from within Dalhousie.

Dear Zilai,

For: preparing your PhD thesis, titled “**Evaluating Degradation Mechanisms in Next-generation Electrode Chemistries**”, for submission to the Faculty of Graduate Studies at Dalhousie University, Halifax, Nova Scotia, Canada

**We hereby grant permission for the requested use ([doi.org/10.1002/batt.202100345](https://doi.org/10.1002/batt.202100345)) expected that due credit is given to the original source.**

If material appears within our work with credit to another source, authorisation from that source must be obtained.

Credit must include the following components:

**- Journals: Author(s) Name(s): Title of the Article. Name of the Journal. Publication year. Volume. Page(s) Copyright Wiley-VCH GmbH. Reproduced with permission.**

If you also wish to publish your thesis in electronic format, you may use the article according to the Copyright transfer agreement:

3. Final Published Version.

Wiley-VCH hereby licenses back to the Contributor the following rights with respect to the final published version of the Contribution:

a. [...]

b. Re-use in other publications. The right to re-use the final Contribution or parts thereof for any publication authored or edited by the Contributor (excluding journal articles) where such re-used material constitutes less than half of the total material in such publication. In such case, any modifications should be accurately noted.

Kind regards

Heike Weller  
Rights Manager  
Rights & Licenses